Characterization of prostate tumor spheroid growth and response to treatment using dynamic optical coherence tomography

by

Steph Swanson

A thesis
presented to the University of Waterloo
in fulfillment of the
thesis requirement for the degree of
Doctor of Philosophy
in
Physics

Waterloo, Ontario, Canada, 2025

© Steph Swanson 2025

Examining Committee Membership

The following served on the Examining Committee for this thesis. The decision of the Examining Committee is by majority vote.

External Examiner:	Yoshiaki Yasuno Professor, Institute of Applied Physics University of Tsukuba
Supervisor(s):	Ernest Osei Adjunct Professor, Department of Physics and Astronomy University of Waterloo Kostadinka Bizheva Professor, Department of Physics and Astronomy University of Waterloo
Internal Member:	Jeff Chen Professor, Department of Physics and Astronomy University of Waterloo
Internal-External Member:	Shawn Wettig Professor, School of Pharmacy University of Waterloo
Other Member(s):	Johnson Darko Adjunct Professor, Department of Physics and Astronomy University of Waterloo

Author's Declaration

This thesis consists of material all of which I authored or co-authored: see Statement of Contributions included in the thesis. This is a true copy of the thesis, including any required final revisions, as accepted by my examiners.

I understand that my thesis may be made electronically available to the public.

Statement of Contributions

Chapters 1, 2, 3, and 7 were authored solely by **Steph Swanson** and have not been previously published.

Chapter 4: **Swanson S**, Chen K, Cheraghi E, Osei E, Bizheva K. "Longitudinal investigation of prostate tumor spheroid proliferation with dynamic line-field optical coherence tomography", to be submitted to *Biomedical Optics Express*, 2025.

- **Kostadinka Bizheva** conceived the study.
- **Ernest Osei** and **Kostadinka Bizheva** provided the study materials.
- **Steph Swanson** and **Keyu Chen** contributed to planning of the study.
- **Steph Swanson** and **Elahe Cheraghi** contributed to culturing tumor spheroids and acquired the proliferation assay and fluorescence microscopy data.
- **Keyu Chen** designed and operated the LF-OCT system, and wrote the algorithm for OCT image generation.
- **Steph Swanson** and **Keyu Chen** contributed to the algorithm for dOCT image generation and acquired the OCT data.
- **Steph Swanson** identified the mathematical shape of the spheroid well, developed a sampling protocol to identify the well location throughout the 3D OCT dataset, and wrote the algorithms for extracting the fit of each well, volumetric spheroid masking, volumetric attenuation compensation, morphological OCT analysis, and dOCT analysis.
- **Steph Swanson** and **Keyu Chen** processed the experimental data.
- **Steph Swanson** analyzed and interpreted the experimental results, performed all statistical analysis, and wrote the first draft of the manuscript.
- **All authors** contributed to the final version in preparation for publication.

Chapter 5: **Swanson S**, Chen K, Cheraghi E, Osei E, Bizheva K. "Comparison of volumetric dynamic optical coherence tomography with biological methods for evaluation of radiation effects in prostate tumor spheroids", to be submitted to *Journal of Biomedical Optics*, 2025.

- **Kostadinka Bizheva** conceived the study.
- **Ernest Osei** and **Kostadinka Bizheva** provided the study materials.
- **Steph Swanson** and **Keyu Chen** contributed to planning of the study.
- **Steph Swanson** and **Elahe Cheraghi** contributed to culturing tumor spheroids and acquired the clonogenic assay, proliferation assay, and fluorescence microscopy data.
- **Steph Swanson** developed and simulated the 3D agent-based model.
- **Keyu Chen** designed and operated the LF-OCT system, and wrote the algorithm for OCT image generation.
- **Steph Swanson** and **Keyu Chen** contributed to the algorithm for dOCT image generation and acquired the OCT data.
- **Steph Swanson** wrote the algorithms for volumetric spheroid masking, morphological OCT analysis, and dOCT analysis.
- **Steph Swanson** and **Keyu Chen** processed the experimental data.
- **Steph Swanson** analyzed and interpreted the experimental results, performed all statistical analysis, and wrote the first draft of the manuscript.
- **All authors** contributed to the final version in preparation for publication.

Chapter 6: **Swanson S**, McKenna C, Cheraghi E, Osei E. "Post-treatment recovery of docetaxel-treated prostate cancer monolayer and spheroid culture", to be submitted to *BMC Cancer*, 2025.

- **Ernest Osei** conceived the study and provided the study materials.
- **Steph Swanson** designed the experiments and planned the study.
- **Steph Swanson**, **Catherine McKenna**, and **Elahe Cheraghi** contributed to culturing spheroid and monolayer culture, and acquired the clonogenic assay, proliferation assay, and fluorescence microscopy data.
- **Steph Swanson** developed and simulated the 3D agent-based model.

- **Steph Swanson** analyzed and interpreted the experimental results, performed all statistical analysis, and wrote the first draft of the manuscript.
- **All authors** contributed to the final version in preparation for publication.

Abstract

Prostate cancer, the most prevalent cancer in North American men, is often treated with radiation and in the case of advanced disease, with the first-line chemotherapeutic docetaxel (DTX). The use of *in vitro* cell culture as a model for *in vivo* patient tumors has been instrumental in understanding the cancer biology underpinning tumor development, progression, and treatment. Conventionally, *in vitro* cells were cultured as 2D monolayers on hard, flat surfaces. However, it has become well understood in the last half-century that the behavior of *in vivo* tumors is better replicated by small 3D aggregates of *in vitro* cancer cells called tumor spheroids. While cells proliferate along the spheroid periphery, the center of the spheroid succumbs to starvation and waste build up. In between forms an intermediate layer of hypoxic and non-proliferative quiescent cells: two characteristics associated with treatment resistance.

Despite the physiological pertinence of spheroid culture, its 3D nature challenges conventional biological methods. Moreover, cell culture geometry influences cell behavior not only during treatment, but in post-treatment recovery and throughout measurement as well. The clonogenic assay is a gold standard method for quantifying cell survival following treatment; however, it requires spheroids to be disaggregated and cultured in 2D for colony formation, which alters the cellular response. Proliferation assays quantify cellular activity inside intact spheroids, but similarly lack spatial resolution. Although fluorescence microscopy (FM) enables spatially resolved spheroid evaluation, it remains largely qualitative rather than quantitative. Proliferation assays and FM also require the addition of exogenous agents that are invasive to the sample and struggle to penetrate large spheroids. Alternatively, optical coherence tomography (OCT) enables non-invasive, high-speed, volumetric imaging of biological tissues with cellular resolution. Analysis of temporal OCT intensity fluctuations generates dynamic OCT (dOCT) images that can provide a quantitative and spatially resolved measurement of cellular activity throughout the spheroid.

Nevertheless, investigating treatment response in spheroids is known to be tedious and time consuming, and some questions of interest cannot be accessed experimentally with adequate accuracy. As such, mathematical *in silico* models of spheroids have become increasingly prevalent. The heterogeneity inherent to *in vivo* tumors and *in vitro* spheroids is recapitulated by discrete *in silico* methods like agent-based modeling (ABM). These methods simulate each cancer cell as an individual "agent" that responds to neighboring cells, nutrients, drugs, and other components of its local environment. In particular, the cellular Potts model (CPM) is a form of ABM with phenomenological utility, given adequate validation to experimental observations. As such, it can describe, visualize, interpolate, and potentially even extrapolate experimental data to guide future experiments.

This dissertation investigated and validated emerging and under-used *in vitro* tools for characterizing prostate tumor spheroid growth and response to treatment with radiation and DTX. First, I created a semi-automated masking process to isolate spheroids from volumetric OCT images for high resolution morphological analysis. For analysis of dynamic motion, I generated dOCT images using a frequency banding method that had only been previously subject to qualitative evaluation. Then, I developed a technique to quantify cellular activity in volumetric dOCT images of masked spheroids. Visual and quantitative comparison of live and formaldehyde-fixed spheroids imaged with dOCT and FM confirmed that dynamic motion measured with the dOCT method was associated with cellular activity. To mitigate influences unrelated to cellular activity, the average measurement of formaldehyde-fixed spheroids was subtracted from quantitative dOCT measurement as background. Post-treatment recovery of prostate tumor spheroids exposed to DTX was investigated with repeated measurement via Alamar Blue (AB) proliferation assay and longitudinal observation of clonogenic assay colony formation.

Excellent agreement was observed between the quantitative dOCT method and AB proliferation assay over two weeks of longitudinal spheroid growth. Volumetric morphological analysis supported the measured cellular activity trends. However, fixation-subtraction could not be performed in a spatially sensitive manner and the dOCT images failed to resolve the longitudinal formation of a necrotic spheroid core that was observed via FM. Nonetheless, dOCT images and quantification of spheroids post-radiation demonstrated good agreement with FM and AB, respectively. Spheroids treated with radiation and DTX demonstrated better survival compared to monolayer culture. Monolayer culture treated with low dose DTX demonstrated higher post-treatment cellular activity and faster colony formation, but clonogenic survival remained lower than the untreated control. This effect was also observed in spheroids, albeit to a lesser extent. Experimental observations were probed with novel *in silico* CPMs of prostate tumor spheroid treatment.

This thesis serves as a step towards validating emerging and under-used *in vitro* tools for spheroid evaluation in well-studied conventional cancer treatments. Once validated, these *in vitro* tools are particularly well suited for discovery and testing of novel targeted cancer treatments since spheroid protein and gene expressions are more physiologically representative than monolayer culture.

Acknowledgements

My graduate experience has been life changing in the most literal sense. I'm overwhelmed with gratitude for all of the people who have had a hand in changing me.

I am tremendously grateful to my supervisors, Dr. Ernest Osei and Dr. Kostadinka Bizheva, for their steadfast belief and high expectations. Ernest, I will be forever thankful that you provided me with such an interesting door to medical physics. I couldn't imagine a more interdisciplinary project to further my learning. You taught me, as you tell everyone: only ever doing what's expected of you is a tragedy. Dida, if this PhD is my door into medical physics, then you graciously provided me with an invaluable window. This thesis would have been impossible without your thoughtful guidance, mentorship, and support. No team of supervisors could have given me more insight and perspective.

I am deeply grateful to my PhD committee members, Dr. Johnson Darko, Dr. Jeff Chen, and Dr. Shawn Wettig for their expertise and encouragement. Johnson, thank you for reminding me that help is always there, if we only reach out and ask for it. As I forged my path, you were someone who watched over me to prevent my path from bending too far away from my destination. I am in awe of your desire to keep your head down and live a quiet life, despite your out-sized impact; I can only hope to follow in your footsteps.

Beyond my PhD committee, I was incredibly lucky to be surrounded by highly qualified people who went out of their way to help me complete my work. Dr. Mohammad Kohandel, you have my sincere thanks for providing a place to keep and culture my cells. Dr. Brian Ingalls, thank you for your microwave, your microscope, and a life changing talk you gave in 2018. Ron Snelgrove, thank you for all of the questions asked and answered. More than anyone else, you've borne the brunt of my curiosity since I walked through your office door as an undergraduate in 2020. Dr. Dorsa Mohammadrezaei and Mohamed Aborig, thank you for patiently and graciously teaching me how to handle cell culture.

Of course, I was also privileged to have worked alongside many generous and thoughtful people. Keyu Chen, thank you for momentarily sharing my brain and eternally sharing my trust; this has been a little bit tricky one, but you did tell me once that dOCT is the best ever technology developed for cellular activity evaluation. Khushmeet Dhaliwal, Nima Abbasi Firoozjah, and Simran Pattar, thank you for making the office such a friendly place. Elahe Cheraghi, thank you for all your help in the lab.

It was my distinct pleasure to help supervise undergraduate students. Catherine McKenna and Saduni Sumithrarachchige Don, you have my heartfelt gratitude for making me strive to be a better person and mentor. Vithushan Aravienthan and Olivia Masella, thank you for your patience in being the first; no two students could have shaped my

perspective on supervision so effectively. And thank you to all the students in between who were a part of my journey: Richard Dong, Ben Giilck, JD Zhu, and Olivia Moluchi.

The people in my personal life have undoubtedly influenced my professional trajectory. Atiyeh Ahmadi, you once asked me if I needed a mirror. You have certainly provided me with a beautiful one, and I couldn't be more ardently grateful. Nadia Dingelstad, you've been a little sister to me. Thank you for all of the laughter. Cindy Karamy, thank you for letting me imagine a future to run not walk towards. Thank you to everyone who had a tremendous impact: Laura Bumbulis, Debbie Bumbulis, Sue Bender, Meaghan Mazurek, Martha Rogers, and many others.

Finally, family is my root. Michael, you have constantly inspired me with your humility and grace. And last but not least, I've learned more from my parents than they ever intended to teach me: unwavering resilience, fierce independence, and the confidence to stand up for myself. These were not easy lessons to learn, but I truly believe that I am a better person for having learned them. I couldn't have asked for better parents. Thank you.

Dedication

This is dedicated to all cancer patients and to the scientists who strive to ask and answer questions in service of their care.

Table of Contents

Examining Committee ii

Author's Declaration iii

Statement of Contributions iv

Abstract vii

Acknowledgements ix

Dedication xi

List of Figures xvii

List of Tables xxiv

List of Abbreviations xxv

1 Introduction 1

1.1 Prostate cancer management 1

1.1.1 Radiation treatment 3

1.1.2 Docetaxel (DTX) chemotherapy 4

1.2 Tumor spheroids 5

1.3 Simulating tumor spheroids . . . 8
1.4 Measuring tumor spheroids with biological methods . . . 10
1.4.1 Proliferation and viability assays . . . 12
1.4.2 Clonogenic assay . . . 13
1.4.3 Fluorescence microscopy (FM) . . . 14
1.5 Thesis organization . . . 15

2 Optical coherence tomography (OCT) 18
2.1 Theory of OCT . . . 18
2.2 OCT system designs . . . 21
2.2.1 Time domain OCT (TD-OCT) . . . 21
2.2.2 Fourier domain OCT (FD-OCT) . . . 22
2.3 Characteristics of FD-OCT systems . . . 23
2.3.1 Axial resolution . . . 24
2.3.2 Lateral resolution . . . 24
2.3.3 Depth of focus (DOF) . . . 25
2.3.4 Scanning range . . . 26
2.3.5 Digital resolution . . . 27
2.3.6 Signal-to-noise ratio (SNR) . . . 27
2.4 OCT imaging Modalities . . . 28
2.4.1 Point-scan OCT (PS-OCT) . . . 28
2.4.2 Line-field OCT (LF-OCT) . . . 29
2.4.3 Full-field OCT (FF-OCT) . . . 30
2.5 Dynamic contrast OCT (dOCT) . . . 31
2.5.1 Subcellular origin of dynamic signal . . . 31
2.5.2 Applications . . . 32
2.5.3 Image acquisition requirements . . . 34
2.5.4 PS-D-DOCT . . . 35
2.5.5 FF-D-DOCT . . . 40
2.5.6 LF-D-DOCT . . . 41

3 Cellular Potts model (CPM) 45

3.1 CPM theory . . . 45

3.1.1 Lattice . . . 46

3.1.2 Multi-scale hybrid modeling . . . 46

3.1.3 Modified Metropolis algorithm . . . 47

3.1.4 Hamiltonian . . . 48

3.1.5 Utility . . . 49

3.1.6 Limitations . . . 50

3.2 CPM implementation . . . 51

4 Longitudinal investigation of prostate tumor spheroid proliferation with dynamic line-field optical coherence tomography 55

4.1 Introduction . . . 55

4.2 Methods . . . 58

4.2.1 OCT setup . . . 58

4.2.2 Cell culture methods . . . 58

4.2.3 OCT Image acquisition . . . 61

4.2.4 Image processing . . . 61

4.2.5 Statistics . . . 63

4.3 Results . . . 63

4.3.1 Morphological OCT . . . 63

4.3.2 Dynamic OCT . . . 64

4.4 Discussion . . . 70

4.4.1 Spheroid seeding and morphology . . . 70

4.4.2 Cyclical proliferation . . . 70

4.4.3 Necrotic spheroid core . . . 71

4.4.4 Origin of dynamic signal . . . 72

4.4.5 LF-dOCT system and dynamic analysis methods . . . 72

4.4.6 Reflection artifacts and pseudo-longitudinal protocol 74
4.4.7 Signal attenuation 75
4.5 Conclusion 76

5 Comparison of volumetric dynamic optical coherence tomography with biological methods for evaluation of radiation effects in prostate tumor spheroids 77
5.1 Introduction 77
5.2 Methods 79
5.2.1 Prostate tumor spheroids 79
5.2.2 Radiation treatment 81
5.2.3 Biological assays 81
5.2.4 Fluorescence microscopy 82
5.2.5 OCT 83
5.2.6 Simulation 84
5.2.7 Statistics 86
5.3 Results 86
5.4 Discussion 90
5.4.1 Morphological measurement of radiation effects 90
5.4.2 Clonogenic measurement of radiation effects 92
5.4.3 Alternative measurement of radiation effects 93
5.4.4 Comparison of causes of cell death 95
5.5 Conclusion 96

6 Post-treatment recovery of docetaxel-treated prostate cancer monolayer and spheroid culture 97
6.1 Introduction 97
6.2 Methods 99
6.2.1 Monolayer and spheroid cultures 99

6.2.2 Docetaxel chemotherapy treatment . . . 99
6.2.3 Clonogenic assay . . . 101
6.2.4 Alamar Blue proliferation assay . . . 102
6.2.5 Fluorescence microscopy . . . 103
6.2.6 Simulation . . . 103
6.2.7 Statistics . . . 104
6.3 Results . . . 105
6.4 Discussion . . . 110
6.4.1 End-of-treatment survival . . . 110
6.4.2 Post-treatment recovery . . . 113
6.4.3 Simulation . . . 114
6.4.4 Limitations . . . 115
6.5 Conclusion . . . 116

7 Conclusion **117**
7.1 Summary . . . 117
7.2 Future work . . . 118

References **120**

APPENDICES **160**

A Prostate tumor spheroid growth CPM **161**

B Prostate tumor spheroid radiation treatment CPM **177**

C Prostate tumor spheroid DTX treatment CPM **195**

List of Figures

1.1 Prostate tumor spheroids (yellow) created with a 3D Petri Dish gel (pink) that was formed by filling an autoclavable silicon micro-mold (green) with molten agarose. Suspended cells fall by gravity and self-assemble into spheroids at the bottom of each well. 7

1.2 Biological methods for measurement of 3D Petri Dish cultured spheroids. (A) AB proliferation assay incubates spheroid-containing gels with blue, non-fluorescent resazurin which is reduced to pink, fluorescent resorufin under cellular metabolism. Culture medium containing the reduced agent is extracted and the fluorescence quantified to produce an average across the spheroids in the gel. (B) Clongogenic assay requires spheroids to be removed from the gel and disaggregated for plating in 2D and longitudinal observation of subsequent colony formation. Colonies are counted and compared with control samples to calculate survival. (C) FM imaging of spheroid-containing gels with a live/dead cell viability assay solution containing green calcein-AM and red PI for identifying live and dead cells, respectively. AB: Alamar Blue; FM: fluorescence microscopy; calcein-AM: calcein acetoxymethyl; PI: propidium iodide. 11

2.1 A representative OCT dataset of a prostate tumor spheroid. (A) An OCT A-scan intensity profile. (B) An OCT B-scan cross-sectional XZ intensity image composed of a set of A-scans. (C) A 3D volumetric OCT image composed of a set of B-scans. 19

2.2 A schematic of a free space OCT system based on a Michelson interferometer. A low coherence light source produces light with electric field component E_i that is split and into the sample and reference arms, which reflect back E_S and E_R, respectively. The detector captures the interference signal. LS: light source; BS: beam splitter; D: detector. 19

2.3 OCT system design schematics. (A) TD-OCT systems adjust the reference arm position to collect depth-resolved data. Rather than manipulating the path length of the reference arm, FD-OCT systems apply a Fourier transform to the detected signal. There are two types of FD-OCT systems: (B) SD-OCT systems utilize a broadband light source and employ a diffraction grating to separate the light by wavelength before detection. (C) SS-OCT systems sweep a narrow band of a tunable-wavelength light source over time to detect each band sequentially. LS: light source; BS: beam splitter; D: detector; TD-OCT: time domain OCT; FD-OCT: Fourier domain OCT; SD-OCT: spectral domain OCT; SS-OCT: swept source OCT. 23

2.4 (A) Objectives with lower NA provide lower lateral resolution δ_x and improved DOF b compared to (B) objectives with higher NA. 26

2.5 (A) Point-scan OCT (PS-OCT) systems focus a narrow, confocal beam onto the imaging plane and acquire one depth-resolved A-scan at each location in the sample. Scanning the beam in each lateral direction allows volumetric acquisition in a point-by-point manner. (B) Line-field OCT (LF-OCT) systems focus the beam into a line onto the imaging plane and acquire A-scans at all lateral positions simultaneously in a cross-sectional image or B-scan. Volumetric acquisition is achieved by scanning the beam in the remaining lateral direction. (C) Full-field OCT (FF-OCT) systems project a parallel beam onto the imaging plane and acquire an enface image in the XY plane without resolving depth. Instead, enface images must be acquired at each depth to achieve volumetric acquisition. 29

3.1 A CPM lattice with cell type τ and index σ indicated by color and number, respectively. The depicted lattice has three cell types (green, yellow, and orange) in addition to the black *Medium*, including two unique cells $\sigma = 1$ and $\sigma = 3$ of different volumes but the same green type. A) The modified Metropolis algorithm performs "copy attempts" by randomly selecting a lattice site i (in red square) and a neighboring site j (in red circle), and proposing that the cell index σ at i becomes that of j. B) The change is accepted if the change in effective energy $\Delta\mathcal{H}$ is reduced. C) Otherwise, the change is accepted with probability $\exp(\Delta\mathcal{H}/T)$. 48

3.2 The simulation parameters were determined phenomenologically by comparing morphology with OCT imaging and masking of cultured prostate tumor spheroids. Cross-section B-scan (top row) and volumetric (bottom row) visualizations of a spheroid 48 hours after seeding generated by simulation (left column) and OCT (right column), with surrounding culture medium and gel removed. Scale bar: 100 μm. 53

4.1 Schematic diagram of setup and processing. (A) Seeding spheroids. Agarose gels, depicted in pink, that each contained an array of wells were filled with a suspension of cells, shown in yellow, to form prostate tumor spheroids at the bottom of each well. (B) Imaging spheroids. Spectral-domain LF-dOCT system with glass Petri dish containing a gel of spheroids. The yellow inset magnifies the gel to show spheroids in the wells. The green inset displays a single spheroid in its well with a volumetric collection of B-scans. The purple inset displays the collection of B-scans acquired at one location over 4 seconds of recording time. (C) OCT processing. Intensity images were used to generate masks by reducing intensity below 3D curve of well inside gel (Eq. 4.1), beyond lateral edges of spheroid, and with Gaussian and Gaussian FFT filters. (D) Volumetric OCT image of live spheroid generated from mask. (E) dOCT processing at each voxel location by FFT in time direction. Integration of spectrum was performed along two frequency bands: red over 0-0.5 Hz and green over 0.5-5 Hz. (F) Volumetric dOCT image of live spheroid. DC: dispersion compensation; FFT: fast Fourier transform; log: base 10 logarithm; ZP: zero-padding; abs: absolute value; A_R: area under red frequency band; A_G: area under green frequency band. 59

4.2 Morphological OCT images of prostate tumor spheroids. Central B-scan OCT images (A) 2, (B) 5, (C) 10, (D) 60, and (E) 120 minutes after cell seeding. Reflection artifact is labeled with red arrow. Masked central B-scan OCT images (F) 1, (G) 2, (H) 6, (I) 10, and (J) 14 days after cell seeding. Masked volumetric OCT images (M) 1, (N) 2, (O) 6, (P) 10, and (Q) 14 days after cell seeding. All scale bars are 100 μm. 65

4.3 Numerical morphological analysis of masked volumetric OCT images of prostate tumor spheroids over 14 days of growth. (A) spheroid volume, (B) internal gap volume, (C) external surface area, and (D) sphericity given by Eq. 4.2. Average measurement of live (black) and fixed (red) spheroids are presented with standard deviation error bar. 66

4.4 Maximum projection OCT, maximum projection dOCT, and FM enface images of prostate tumor spheroids 1, 2, 6, 10, and 14 days after cell seeding. Blue inset in last column shows 4X magnification with 25 μm scale bars. All other scale bars are 100 μm. 68

4.5 Numerical dynamic analysis of masked volumetric dOCT images of prostate tumor spheroids over 14 days of growth. (A) raw dynamic signal of live (black) and fixed (red) spheroids given by Eq. 4.3. (B) normalized dynamic signal given by Eq. 4.4. (C) Volumetric and maximum projection enface images of a live spheroid and the same spheroid after 1 hour of fixation with 4% formaldehyde. (D) Normalized absorbance of AB proliferation assay. Average measurements are presented with standard deviation error bar. All scale bars are 100 μm. 69

5.1 Schematic of experimental and simulated spheroid seeding, irradiation, and measurement. (A) Cells (yellow) seeded into agarose gels (pink) formed prostate tumor spheroids in the bottom of wells. (B) After 24 hours, spheroids in 6-well plates were surrounded by Superflab bolus (yellow) and irradiated with 6 MV radiation at 5 cm depth in Solid Water (brown). Measurement was performed 24 hours post-irradiation. (C) Clonogenic assay disaggregated spheroids for plating 2D cultures that were fixed and stained after two weeks. (D) AB proliferation assay added AB solution to gels that was extracted for absorbance measurement. (E) FM added solution of green calcein acetoxymethyl and red propidium iodide to gels that fluoresced in live and dead cells, respectively, during enface imaging. (F) Volumetric dOCT imaging acquired forty repeated frames per cross-section. Dynamic signals were extracted from intensity fluctuations via an FFT-based algorithm assigning red ($<$0.5 Hz) and green (0.5–5 Hz) frequency bands. (G) 3D agent-based simulation of spheroid seeding, irradiation, and measurement applied experimental LQ survival at treatment. SAD: source-to-axis distance; B: Superflab bolus; SW: Solid Water; AB: Alamar Blue; FM: fluorescence microscopy; dOCT: dynamic optical coherence tomography; FFT: Fast-Fourier transform; LQ: linear-quadratic model. 80

5.2 Morphological OCT and simulated analyses of live control, irradiated (1, 2, 6, and 10 Gy), and formaldehyde-fixed prostate tumor spheroids. Numerical analysis of (A) spheroid volume, (B) internal gap volume, (C) external surface area, and (D) sphericity given by Eq. 5.4. Average OCT-measured (black circle) and simulated (red triangle) values are presented with standard deviation error bar. Simulated data in (B-D) are inset. Asterisks indicate significant differences (10 Gy or fixed vs. live control; Methods Section 5.2.7). Central (third row) masked OCT B-scans and (fourth row) simulated visualizations of live control, irradiated (2 and 10 Gy), and formaldehyde-fixed spheroids. An internal gap is labeled with yellow arrow. Sim: simulation. Scale bars: 100 μm. 88

5.3 Dynamic analysis of live control and irradiated prostate tumor spheroids. (A) Clonogenic assay SF values with LQ model fit line for 3D spheroids (black circle, solid line) and 2D monolayer culture (blue square, dashed line). (B) SF of spheroids measured via normalized dynamic signal from volumetric dOCT images (purple / hatch), normalized absorbance from AB proliferation assay (blue circle hatch), simulated clonogenic assay (orange X hatch), and LQ fit from clonogenic assay (olive // hatch). Data shown are averages with error bars as described in Methods Section 5.2.7. Volumetric dOCT images (second row) and simulated visualizations (third row) of live control and irradiated (2, 6, and 10 Gy) spheroids. A central slice has been cut out of the volumes. Colormaps for dOCT (red: <0.5 Hz, green: 0.5-5 Hz); and simulation (red: *Apoptotic*, orange: *Necrotic*, yellow: *Hypoxic*, green: *Normoxic* cells). SF: survival fraction; LQ: linear-quadratic model; AB: Alamar Blue; Sim: simulation; CL: clonogenic. 89

5.4 OCT maximum projection (first row), dOCT maximum projection (second row), FM (third row), and simulated (fourth row) enface images of live control, irradiated (1, 2, 6, and 10 Gy), and formaldehyde-fixed prostate tumor spheroids. An internal gap is labeled with yellow arrow. Colormaps for dOCT (red: <0.5 Hz, green: 0.5-5 Hz); FM (red: PI, green: calcein-AM); and simulation (red: *Apoptotic*, orange: *Necrotic*, yellow: *Hypoxic*, green: *Normoxic*). FM: fluorescence microscopy; propidium iodide: PI; calcein-AM: calcein acetoxymethyl; Sim: simulation. Scale bars: 100 μm. 91

6.1 (A) Cells (yellow) seeded into agarose gels (pink) created from molds (green) self-assemble into prostate tumor spheroids in the bottom of wells. (B) Spheroids were exposed to 0, 0.1, 1, and 10 nM DTX diluted in saline with a 1:100 ratio of DTX in saline to culture medium and gel for 48 hours. DTX was removed by (C) centrifuging for (D) SF calculation and longitudinal observation via clonogenic assay, or by (E) serial dilution of spheroid-containing gels for (F) AB proliferation assay and (G) FM. (H) 3D ABM of spheroid seeding, DTX treatment, and measurement applied fitted clonogenic survival from experiment during treatment. DTX: docetaxel; SF: survival fraction; AB: Alamar Blue; FM: fluorescence microscopy; ABM: agent-based modeling. 100

6.2 Measurements performed immediately after the 48 hour treatment period with 0, 0.1, 1, and 10 nM DTX. (A) Clonogenic assay SF values with model fit line given by Eq. 6.3 for 3D spheroids (black circle, solid line) and 2D monolayer culture (orange square, dashed line). (B) SF of spheroids calculated via clonogenic assay measurement (purple x hatch), simulated clonogenic assay S_{CL} (orange \\ hatch), normalized absorbance from AB proliferation assay measurement (blue circle hatch), simulated AB proliferation assay S_{AB} (olive / hatch), and simulated growth S_G (grey - hatch). Data shown are averages with error bars as described in Methods Section 6.2.7. DTX: docetaxel; SF: survival fraction; CL: clonogenic assay; AB: Alamar Blue; G: growth. 106

6.3 FM enface (first row), simulated enface (second row), and simulated volumetric (third row) images of spheroids treated with 0, 0.1, 1, and 10 nM DTX. A central slice has been cut out of the volumes. Colormaps for FM (red: PI, green: calcein-AM); and simulation (red: *Apoptotic*, orange: *Necrotic*, yellow: *Hypoxic*, green: *Normoxic*). DTX: docetaxel; FM: fluorescence microscopy; PI: propidium iodide; calcein-AM: calcein acetoxymethyl; Sim: simulation. Scale bars: 100 μm. 107

6.4 Longitudinal observation of post-treatment recovery in cells treated in spheroid culture with 0, 0.1, 1, and 10 nM DTX. Colony formation on day 8 (first row), day 11 (second row), and day 14 (third row) following removal of DTX and plating at low density in 2D on day 3. Normalized AB absorbance (top right) of intact spheroids treated with 0 nM (green circle, solid line), 0.1 nM (blue square, dashed line), 1 nM (purple triangle, dotted line), and 10 nM (orange cross, dot-dashed line) DTX. Exposure to DTX treatment occurred throughout pink shaded region. DTX: docetaxel; AB: Alamar Blue. Scale bars: 100 μm. 108

6.5 Longitudinal observation of post-treatment recovery in cells treated in monolayer culture with 0, 0.1, 1, and 10 nM DTX. Colony formation on day 8 (first row), day 11 (second row), and day 14 (third row) following removal of DTX and plating at low density in 2D on day 3. Normalized AB absorbance (top right) of monolayer culture treated with 0 nM (green circle, solid line), 0.1 nM (blue square, dashed line), 1 nM (purple triangle, dotted line), and 10 nM (orange cross, dot-dashed line) DTX. Exposure to DTX treatment occurred throughout pink shaded region. DTX: docetaxel; AB: Alamar Blue. Scale bars: 100 μm. 109

List of Tables

6.1 Cells seeded AB proliferation assays of monolayer and spheroid cultures per T-25 flask and well in 3D Petri Dish gel, respectively. 102

List of Abbreviations

AB Alamar Blue 12, 16, 43, 44, 99, 117, 118

ABM agent-based modeling 9, 45, 46, 49, 98, 99, 103, 116

ADT androgen deprivation therapy 2, 3, 97

ALIV authentic logarithmic intensity variance 38

AO acridin orange 12

ATP adenosine triphosphate 14, 32, 34, 35, 40

BCR biochemical recurrence 2

CA cellular automata 10

CAFs cancer-associated fibroblasts 6

calcein-AM calcein acetoxymethyl 12, 15, 44

CC3D CompuCell3D 51, 161

COM center of mass 51, 52

CPM cellular Potts model 10, 16, 45–48, 50–52, 54, 118, 161, 177, 178, 195, 203

CRPC castration-resistant prostate cancer 2, 3, 5, 97

CSCs cancer stem cells 6, 45

dB decibel 30, 38, 42

DCIS ductal carcinoma in situ 33

DH dynamic holography 31

dOCT dynamic contrast OCT 16, 18, 31–35, 38, 41–44, 117–119

DOF depth of focus 25, 30, 33, 35, 42

DSBs double-strand breaks 3

DTX docetaxel 2–5, 16, 52, 54, 97, 116–118, 195, 196, 201

EB ethidium bromide 12

ECM extracellular matrix 6, 10

ED eigenvalue decomposition 39

EORTC European Organisation for Research and Treatment of Cancer 2

FD-OCT Fourier domain OCT 21–23, 42

FD-PS-OCT Fourier domain point-scan OCT 34

FDML Fourier domain mode-locked 29, 42

FF-dOCT full-field dOCT 36, 37, 40, 42, 43

FF-OCT full-field OCT 28, 30, 39, 40, 42

FISH fluorescence in situ hybridization 14

FM fluorescence microscopy 15, 16, 43, 44, 99, 118, 119

FOV field of view 14, 27, 28, 30, 42

FWHM full-width at half maximum 24, 25

G6PD glucose-6-phosphate dehydrogenase 12

GGH Glazier-Graner-Hogeweg 45

HSB hue-saturation-brightness 40, 41, 43

HSPC hormone-sensitive prostate cancer 2, 3, 5, 97

HSV hue-saturation-value 40

LDH lactate dehydrogenase release 12

LF-dOCT line-field dOCT 43

LF-OCT line-field OCT 28–30, 43

LGCA lattice gas CA 10

LHRH luteinizing hormone-releasing hormone 2

LIV logarithmic intensity variance 37, 38, 41, 42

LQ linear-quadratic 4, 8, 13

LS-OCT line-scan OCT 29

MAV median adjusted variance 38, 42

mCRPC metastatic CRPC 2, 3, 97

MCS Monte Carlo step 47, 51, 52, 161

mHSPC metastatic HSPC 3

MSCs tumor infiltrating mesenchymal stem cells 6

MTS 3-(4,5-dimethylthiazol-2-yl)-5-(3-carboxymethoxyphenyl)-2-(4-sulfophenyl)-2H-tetrazolium 12

MTT 3-[4,5- dimethylthiazol-2-yl]-2,5 diphenyl tetrazolium bromide 12

NA numerical aperture 25, 30, 35, 42

NCIC CTG/MRC National Cancer Institute of Canada Clinical Trial Group and Medical Research Council 2

OCDS OCT correlation decay speed 38, 39, 41, 42

OCT optical coherence tomography 15, 18, 21, 24–28, 30–43, 52, 117, 118

ODE ordinary differential equation 9, 46

ORG optoretinography 31

OS overall survival 2, 3

PDE partial differential equation 9, 46, 47, 51, 196

PI propidium iodide 12, 15, 44

PR static power ratio 39

PS-dOCT point-scan dOCT 34, 35, 37, 40–43

PS-OCT point-scan OCT 23, 28, 30, 35, 40, 42, 43

PSA prostate-specific antigen 1, 2

PSD power spectral density 36, 37, 39–42

RGB red-green-blue 37, 43, 44

RNFL retinal nerve fiber layer 31

ROI region of interest 36

ROS reactive oxygen species 3, 4

RPE retinal pigment epithelium 32

RTOG Radiation Therapy Oncology Group 2

SD-OCT spectral domain OCT 22, 29, 34

SD-PS-OCT spectral domain point-scan OCT 28, 29, 42

SEM scanning electron microscopy 14

SF survival fraction 4

SNR signal-to-noise ratio 22, 27–30, 42, 43

SPCG-3 Swedish Association for Urological Oncology-3 2

SPCG-7 Scandinavian Prostate Cancer Group Study No. 7 2

SS-FF-OCT swept-source full-field OCT 30

SS-OCT swept-source OCT 22, 29, 30, 34

SS-PS-OCT swept-source point-scan OCT 29, 42

SSBs single-strand breaks 3

STAMPEDE Systemic Therapy in Advancing or Metastatic Prostate Cancer: Evaluation of Drug Efficacy 2

SVD singular value decomposition 39

SWOG 99-16 SWOG Intergroup protocol 99-16 2

TD-FF-OCT time domain full-field OCT 30, 34, 42

TD-OCT time domain OCT 21, 22, 30

TD-PS-OCT time domain point-scan OCT 30

TEM transmission electron microscopy 14

TILs tumor infiltrating lymphocytes 6

TME tumor microenvironment 6–8, 10

TROG Trans-Tasman Radiation Oncology Group 2

TUNEL terminal deoxynucleotidyl transferase (TdT) dUTP Nick-End Labeling 14

WST water soluble tetrazolium 12

XTT 2,3-bis (2-methoxy-4-nitro-5-sulfophenyl)-5-[(phenylamino) carbonyl]-2H-tetrazo-lium hydroxide 12

Chapter 1

Introduction

1.1 Prostate cancer management

Among North American males, prostate cancer is the most commonly diagnosed non-cutaneous cancer [1, 2]. The incidence of prostate cancer significantly increased alongside the aging population in conjunction with widespread use of increasingly sensitive and accessible screening tools such as prostate-specific antigen (PSA) blood tests and ultrasound-directed needle biopsy techniques [3]. Due to its high incidence rate, prostate cancer causes a large number of cancer deaths despite being a relatively indolent cancer with a generally slow progression rate [4]. Nevertheless, prostate cancer is a heterogeneous disease. The American Cancer Society [5] estimated the 5-year survival of prostate cancer to be 97% between 2012 and 2018, yet survival is below 30% in cases with distant metastasis. The dichotomous nature of prostate cancer survival motivates early diagnosis since it is highly manageable as a localized disease and no perfect solution has been developed to control advanced prostate cancer [4]. However, a lack of level one evidence confounds the decision-making process when treating localized prostate cancer [6]; the SPCG-4 study indicated that radical prostatectomy can reduce prostate cancer mortality [7], but the more recent PIVOT study demonstrated only a small benefit to surgery, especially for low-risk disease [8]. Consequently, surgery may provide only marginal survival benefit while potentially causing complications including incontinence and erectile dysfunction [9]. In patients with localized disease that are not suitable for or interested in surgery, delivering radiation treatment with external beam or internally via brachytherapy is a good alternative primary treatment to radical prostatectomy [10].

Although radical prostatectomy and radiation therapy have high cure rates for local-

ized prostate cancer, PSA levels rise in approximately 30% of cases, indicating biochemical recurrence (BCR) associated with local or distant recurrence [11]. Of these patients, approximately one-third exhibit clinical recurrence within 8 years [12]. The standard of care for patients with recurrence, locally advanced prostate cancer that has spread to the seminal vesicles or adjacent organs, or metastatic prostate cancer is castration via androgen deprivation therapy (ADT) [13]. Historically, ADT was accomplished with bilateral orchiectomy, or surgical removal of both testicles, but in the 1980s, medical alternatives such as luteinizing hormone-releasing hormone (LHRH) analogs and anti-androgens were developed [14]. As with other systemic treatments, ADT is thought to be associated with control of micro-metastases in advanced prostate cancer patients [15]. Designed in the late 1980s to late 1990s, several multicenter randomized controlled trials including Radiation Therapy Oncology Group (RTOG) 8531 [16], RTOG 8610 [17], European Organisation for Research and Treatment of Cancer (EORTC) 22863 [18], and Trans-Tasman Radiation Oncology Group (TROG) 9601 [19] suggested that combining ADT with radiation treatment improved clinical outcomes compared to radiation alone. More recently, the National Cancer Institute of Canada Clinical Trial Group and Medical Research Council (NCIC CTG/MRC) trial [20] and Scandinavian Prostate Cancer Group Study No. 7 (SPCG-7)/Swedish Association for Urological Oncology-3 (SPCG-3) trial [21] demonstrated that compared to radiation alone, the combination of ADT and radiation treatment halved rates of BCR and disease-specific mortality, respectively. However, ADT causes numerous side effects that worsen quality of life such as cardiovascular events, sarcopenia, osteopenia, and fractures [22] and the treatment itself incurs substantial cost [13]. Moreover, ADT fails in a median of 18–24 months and patients develop castration-resistant prostate cancer (CRPC) [23].

In 2004, two randomized phase 3 trials, TAX 327 [24] and SWOG Intergroup protocol 99-16 (SWOG 99-16) [25], demonstrated that docetaxel (DTX) chemotherapy provided survival benefit in metastatic CRPC (mCRPC) patients, setting a new standard of care for this population [13]. Prior treatment for patients with mCRPC remained palliative as mitoxantrone and prednisone, the previous standard chemotherapy combination, provided symptom relief but never demonstrated prolonged survival beyond prednisone alone [23]. In light of its success in the mCRPC population, DTX was introduced to hormone-sensitive prostate cancer (HSPC) patients with the intention of improving clinical outcomes by prophylactically eliminating cancer cells insensitive to ADT through pathways alternative to androgen-signaling [13]. However, the GETUGAFU 15 study [26] did not observe improved overall survival (OS) in HSPC patients who received DTX and ADT compared to ADT alone. In contrast, the later CHAARTED [27] and Systemic Therapy in Advancing or Metastatic Prostate Cancer: Evaluation of Drug Efficacy (STAMPEDE) [28] trials both

observed improved OS of combined DTX and ADT compared to ADT alone for HSPC, especially in patients with a high volume of metastatic burden. Given these results, a post-hoc analysis of the GETUGAFU 15 study [29] divided patients into high and low volume disease groups as defined in the CHAARTED trial [27]. The new analysis observed that early DTX chemotherapy did not improve survival in patients with low volume disease, but reduced risk of death by a nonsignificant 20% in the high volume group. While all three trials [26, 27, 28, 29] reported higher rates of febrile neutropenia from DTX treatment in the HSPC setting compared to the CRPC population, the GETUGAFU 15 study [26, 29] demonstrated that prophylactic granulocyte colony-stimulating factor significantly helped to manage the side effect. As such, in addition to being standard of care for mCRPC patients, there is consistent evidence that early DTX chemotherapy with ADT in high-volume metastatic HSPC (mHSPC) patients improves OS.

1.1.1 Radiation treatment

As a cancer treatment, ionizing radiation kills cells by damaging DNA [30]. Ionizing radiation tracks directly damage the sugar backbone of the DNA double helix through single-strand breaks (SSBs) or clustered double-strand breaks (DSBs) [31]. Cells are regularly exposed to DNA damage due to oxidative stress produced through aerobic cellular respiration and have consequently developed various DNA damage repair pathways [32, 33]. Radiation causes significant cell-killing despite producing fewer lesions in DNA than cells experience habitually via respiration, a treatment effect that is largely attributed to DSBs because clustered damage is more complex [32]. As the complexity of the DNA damage increases, the duration of DNA repair increases, as does the likelihood of the damage being irreparable [34, 35]. While cells can survive and recover normal function if the DNA damage is repaired correctly, chronic DNA damage has secondary effects [33]. Radiation-induced DNA damage that is not repaired can activate cell cycle checkpoints and disrupt the cell cycle [33]. In particular, mitosis can be delayed through G2/M phase arrest, in which the G2 phase of the cell cycle is extended [36, 37]. In the case of permanent arrest, cells stop proliferating and remain metabolically active in a state called senescence [38]. However, if the DNA repair mechanisms and cell cycle checkpoints fail to prevent cell division with damaged DNA, aberrant mitosis may occur and cause mitotic catastrophe leading to cell death by some combination of apoptosis or necrosis [38, 39]. Alternatively, radiation deals damage indirectly via oxidative stress by generating reactive oxygen species (ROS) like the superoxide anion, hydroxyl radicals and hydrogen peroxide through the radiolysis of water [39]. Highly reactive and toxic to cells, ROS induce DNA damage and modulate the processes of DNA repair [40]. Radiation can also cause cellular stress by damaging

subcellular organelles like the cytoplasmic membrane, endoplasmic reticulum, ribosomes, mitochondria, and lysosomes [39, 33] and by inducing autophagy, a process in which cells degrade damaged organelles, potentially resulting in cell death similar to necrosis [39, 41].

In 1975, Withers [42] published the 4 Rs of radiobiology that leverage the above radiobiological mechanisms and continue to shape modern radiation treatment: repair, repopulation, redistribution, and reoxygenation. Between treatment fractions, cells repair DNA to regain normal function and the tumor repopulates through proliferation. The efficacy of the next fraction of treatment improves because between fractions, cells redistribute within the cell cycle to more radio-sensitive phases [30] and tumors reoxygenate, which reduces the generation of ROS [43]. Steel et al. [44] later extended the Rs of radiobiology to include radio-sensitivity, which is an intrinsic property that varies by cell type. Fractionation schemes are designed to preferentially kill tumor cells and preserve surrounding tissue by balancing these effects to maximize tumor control [45]. An essential tool for tailoring fractionation schemes to each tumor site is the linear-quadratic (LQ) model of cell killing, which fits the logarithm of the fraction of surviving cells or survival fraction (SF) to a linear and quadratic expression of radiation dose [30]. The LQ model is well validated experimentally and mechanistically characterizes the effects of direct DNA damage by one or two tracks of ionizing radiation via its linear α and quadratic β parameters respectively [46, 47]. In 1982, the Houston [48] and Amsterdam [49] groups introduced the clinical value of the α/β ratio, which captures the curvature of the LQ fit. With a "curvier" LQ fit and smaller α/β ratio of ≈ 3 Gy, late responding tissues demonstrate increased repair and survival at low doses, whereas early-responding tissues have a larger α/β ratio of ≈ 10 Gy and are less sensitive to dose fraction [50]. The α/β ratio is of particular importance for prostate cancer as it, unlike many tumor sites, demonstrates a low α/β ratio and benefits clinically from the high dose per fraction delivered in hypofractionated schemes [51]. Clinical decision-making continues to be guided by α/β ratios [52], which are extracted from survival curves that are measured using *in vitro* cell culture [30].

1.1.2 Docetaxel (DTX) chemotherapy

The history of DTX as a chemotherapeutic agent began in the late 1960s, when cytotoxicity was observed in a crude oil extract from the bark of the Pacific yew, *Taxus brevifolia*, by the National Cancer Institute screening program [53]. In 1971, Wani et al. [54] isolated and characterized the extract's principle, the chemotherapeutic paclitaxel. In 1986, DTX was discovered by semi-synthesis of a non-cytotoxic precursor extracted from the rapidly renewable needles of the *Taxus baccata* yew tree [55]. Both members of the taxane family of chemotherapeutics, DTX differs from paclitaxel by only two chemical modifications,

which make it a stable crystalline white powder [56] that is more active [57]. In contrast, paclitaxel is poorly soluble in water and requires the solubilizing agent cremophor, which causes severe hypersensitivity reactions [58] and nonlinear pharmacokinetics [59]. Similar to paclitaxel, DTX interacts with microtubules, the cellular structures that enable chromosome movement during mitosis, regulate cell morphology, help anchor receptors in cell membranes, and are responsible for cellular motility [56]. Long cylindrical proteins composed of tubulin, microtubules are in constant equilibrium with free tubulin; DTX shifts that equilibrium towards microtubule assembly [57].

Ultimately, microtubule stabilization by DTX prevents depolymerization during mitosis, causing cell cycle arrest in G2/M phase [60, 61, 62]. Taxane induced mitotic arrest occurs at the mitotic spindle-assembly checkpoint, which delays the onset of anaphase if there is incorrect tension in the microtubule-composed mitotic spindle or improper attachment between microtubules and chromosomal structures called kinetochores [63, 64]. Although permanent cell cycle arrest can result in senescence [65], mitotic checkpoint response is often reduced but not absent in tumor cells [66]. Therefore, cell cycle arrest may be transient under excessive damage to the mitotic machinery, and the checkpoint can release without the appropriate repair [67, 68]. Subsequently, the cell may proceed to interphase without splitting into two daughter cells via cytokinesis, a process termed mitotic slippage that results in a tetraploid or "pseudo-G1" phase and eventual apoptosis [64]. Alternatively, aberrant mitosis may result, whereby cell division occurs with improperly segregated chromosomes such that the cell undergoes mitotic catastrophe [69]. While apoptosis has been observed following mitotic catastrophe [70], necrosis-like cell death has also been observed through the development of non-viable cells with nuclear envelopes surrounding individual chromosomes or groups of chromosomes called micronuclei [65]. Additionally, DTX is known to phosphorylate (i.e. inactivate) the anti-apoptotic *BCL2* proto-oncogene [71, 72, 73]. With respect to prostate cancer, immunohistochemistry of prostate biopsy sample has observed Bcl-2 protein levels to be associated with CRPC and undetectable in most HSPC samples [74, 75]. However, evidence has been contradictory as Kraus et al. [76] measured Bcl-2 protein levels in hormone sensitive DU-145 prostate tumors explanted from xenograft mice treated with DTX and concluded that apoptosis was induced through a Bcl-2-independent mechanism.

1.2 Tumor spheroids

In 2000 and 2011, Hanahan and Weinberg [77, 78] famously described the hallmarks of cancer, which are behaviors acquired by tumors during development and progression that

form a blueprint of our foundational understanding of cancer biology. The use of *in vitro* cell culture as a model for *in vivo* tumors has been invaluable in the investigation and observation of these characteristics [79]. Historically, tumors were viewed as a homogeneous collection of cancer cells that could be well understood through investigation of individual cell properties [78]. This view was served well by the conventional technique of culturing *in vitro* cells as 2D monolayers on flat, hard surfaces. However, an abundance of evidence has accumulated to identify the influence of the tumor microenvironment (TME) on cancer cell phenotypes [80]. The TME includes stromal cells that surround and interact with tumors, such as transformed epithelial cells, cancer-associated fibroblasts (CAFs), cancer stem cells (CSCs), tumor infiltrating mesenchymal stem cells (MSCs), tumor infiltrating lymphocytes (TILs), pericytes, and endothelial cells, which have been shown to influence proliferation, metastasis, and treatment response [81, 82]. The TME is also composed of non-cellular components that dictate the complex intercellular interactions between cancerous and surrounding cells as well as the intracellular signaling pathways that underpin cancer cell biology; these components include signaling molecules like growth factors, cytokines, and chemokines as well as structural features such as the extracellular matrix (ECM) and cell adhesion molecules like integrin [78, 83, 84]. While 2D cell culture is efficient, easily scalable, and enables the straightforward application of many biological techniques, the cells lack physiologically relevant cell-cell and cell-environment interactions [85]. Every cell that composes a 2D monolayer has equal and unrestricted access to the oxygen, nutrients, and signal molecules contained in the culture medium. Culturing cells as monolayers also affects cellular polarity and morphology because the cytoskeleton rearranges in response to being stretched, which influences sub-cellular organization, cell signaling, proliferation, and gene and protein expression [86, 87].

The fundamental limitations of 2D monolayers have motivated the development of various 3D cell culture techniques that provide an alternative *in vitro* model for *in vivo* tumors [85]. In 1975, Rheinwald and Green [88] cultured human stratified squamous epithelium in the lab and introduced the concept of organoids, whereby the normal 3D tissue structure is achieved by culturing human stem cells [89]. Organoids are created by embedding tissue-derived adult stem cells into a 3D matrix such that they grow and differentiate into a self-organizing structure composed of various cell types that resemble an organ [90]. Organoid models have been developed for many tumors sites [89], including prostate adenocarinoma [91, 92], but the technique remains limited to tumors of epithelial origin [90]. Additionally, unlike *in vivo* tumors that by nature grow faster than the surrounding healthy tissue, organoids derived from tumors often grow at slower rates than those derived from normal epithelium [93, 94]. While the use of stem cells provides a superior physiological model of heterogeneous patient tumors compared to cancer cell lines, these co-cultures also

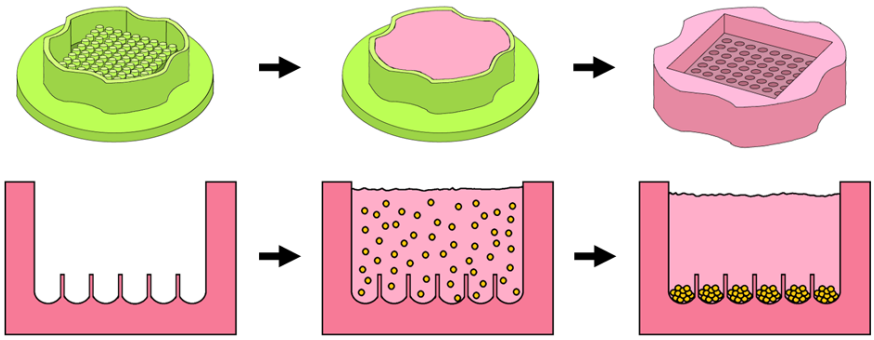


Figure 1.1: Prostate tumor spheroids (yellow) created with a 3D Petri Dish gel (pink) that was formed by filling an autoclavable silicon micro-mold (green) with molten agarose. Suspended cells fall by gravity and self-assemble into spheroids at the bottom of each well.

require significantly more time and resources to culture [90].

Introduced in the early 1970s by Sutherland et al. [95], the most well characterized 3D cell culture model is the multicellular tumor spheroid [96]. Unlike complex 3D organoid co-cultures that are derived from tumor tissue, spheroids are aggregates of cancer cells typically formed from a single cancer cell line that mimic small avascular tumors such as micrometastases [97]. The spatial distribution of cells in tumor spheroids facilitates cell-cell and cell-environment interactions similar to those observed in the TME of *in vivo* tumors, and the cells correspondingly acquire the relevant morphology and behavior [98]. Unlike monolayer culture, heterogeneous cell populations develop within the spheroid as the outer layer of cells are proliferative and surrounded by culture medium, whereas the inner core of the spheroid becomes necrotic and apoptotic due to waste accumulation and limited diffusion of oxygen and nutrients [99]. An intermediate hypoxic layer of non-proliferating quiescent cells also forms [100], which is of particular importance for the investigation of radiation treatment as hypoxia [101, 102] and quiescence [103, 104] are associated with radio-resistance.

A plethora of techniques have been developed to culture tumor spheroids, including in hydrogel scaffolds [105], hanging drops [106], or ultra-low attachment plates [107]. In particular, the 3D Petri Dish technique employed in this thesis uses autoclavable silicon micro-molds distributed by Sigma-Aldrich that may be filled with molten agarose to form a gel containing an array of wells [108] (Fig. 1.1). The agarose gel is seeded with a suspension of cancer cells, which sink to the bottom of each well and self-assemble to form tumor spheroids. With this technique, many spheroids are seeded simultaneously with a

size that may be controlled through the density of the added cell suspension. Therefore, a large sample of spheroids may be cultured easily and efficiently for treatment with radiation or exposure to chemical agents; however, to maintain the concentration of the agent, the volume of the gel must be accounted for. Additionally, because the wells are organized into an array, individual spheroids may be located and examined systematically with ease.

1.3 Simulating tumor spheroids

The inherent complexity of cancer motivated the development of *in vitro* tumor spheroids, and in the same vein, its non-linear and heterogeneous nature has galvanized investigation with *in silico* mathematical methods [109]. A broad range of *in silico* models have been developed to explain and understand the multi-faceted and diverse set of measurements at the molecular, cellular, tissue, and population levels [110, 111, 112]. A century ago, Crowther [113] and Curie [114] laid the foundation for the modern LQ model of radiation cell-killing by explaining ionizing radiation damage with events or "hits" related to dose through a probabilistic distribution [115]. However, statistical methods have also been applied directly to populations. For example, in 1953, Nordling [116] used population level statistics of cancer death rates as a function of age to estimate the absolute number of genetic mutations required for carcinogenesis. Anti-cancer drug regimes are also determined at the population level using pharmacokinetic and pharmacodynamic modeling, sometimes with adjustment at the individual level using statistical methods via therapeutic drug monitoring [117, 118]. More recently, *in silico* models have been applied to the complex and heterotypic biochemical, metabolic, and signaling reaction networks implicated in cancer [110, 111] that were elegantly summarized and integrated by Hanahan and Weinberg [77, 78]. At the transcriptional and signaling levels, attempts to infer causal relationships between genes have generated statistically-inferred networks including signaling related to apoptosis [119], as well as regulatory networks involved in glioma [120] and melanoma [121]. In contrast, stoichiometric or kinetic models of biochemical reaction networks rely on experimental measurements to mechanistically describe interactions between genes, proteins, and metabolites [110]. Beyond molecular and genetic networks, cellular and tissue-level models attempt to capture the crucial influence exerted by the TME on cancer cells [122]. Cell culture geometry shapes the TME through biological and physical processes related to transport of nutrients and wastes, competition for resources, and mechanical forces exchanged between cancer cells and their microenvironment [96]. In light of their experimental accessibility and mimicry of *in vivo* tumors, the mechanical and molecular characteristics of tumor spheroids have been extensively modeled with *in silico*

methods [123].

Classical tissue-level models of tumors described only the tumor volume or number of cancer cells in a homogeneous population over time via deterministic ordinary differential equation (ODE)s [111]. The most well known of these ODE systems is Gompertzian growth, which was introduced in 1825 by Gompertz [124] and adapted to tumor growth by Casey [125] in 1934. The Gompertz curve is sigmoid and suggests that initial tumor growth is slow, then becomes fast, and then stagnates. Introduced by Verhulst in 1845 and then rediscovered by Pearl in 1924 [126], another popular ODE model of tumor growth is the Verhulst-Pearl or logistic equation. Modern iterations of these univariate models include the energy-conserving "Universal Law" proposed by West [127] that is based on the model of biological growth derived by von Bertalanffy [128] in the 1950s. However, ODE models do not consider spatial influences.

Continuum *in silico* methods use partial differential equation (PDE)s and integro-differential equations to describe the spatial distribution of tumors as continuous fields of densities or volume fractions subject to the laws of continuum mechanics [109]. Pioneered by Greenspan in the 1970s [129, 130], continuum techniques accounted for the diffusion and arbitrary spatial distribution of nutrients and other chemicals, as well as interplay between surface tension and cell-cell adhesion. Incremental progress in continuum models additionally accounted for growth regulation by stimulating and inhibitory factors [131], apoptosis [132], necrosis [133, 134], vascularization via angiogenesis [135], and immune response [136]. Historically, continuum models have been limited by simplifying assumptions of spherical geometry [109]; however, recent improvements in numerical techniques have enabled non-linear modeling of complex tumour morphologies [137] in arbitrary 3D geometries [138]. Today, continuum models are solved with efficient numerical solvers, derived from explainable physical laws, and informed fairly directly by experimental measurement [109]. That said, *in silico* continuum techniques describe gross tumor behavior at the tissue-level.

Investigation at the cellular level was enabled by the development of discrete *in silico* methods like agent-based modeling (ABM) [139]. In ABM, each cancer cell is an "agent" that embodies a state described by individualized parameters, capturing the heterogeneity that is inherent to cancer [109]. The behavior of each cell is updated according to a set of biophysical "rules" contingent on its current state and neighboring cells, that may be translated directly from biological observations [122]. Discrete methods are naturally well suited for exploring mechanistic biological hypotheses and resultant emerging behavior [122], particularly in relation to cell-cell interactions or discrete processes involved in carcinogenesis, natural selection, and genetic instability [109].

While purely continuum models struggle to characterize discrete features like distinct vascular morphologies [140] or tumor cell phenotypic transitions [109], discrete methods in isolation fail to incorporate crucial fluid and continuum mechanics relevant to cancer. Consequently, hybrid-modeling frameworks have been developed to combine continuum techniques that describe the distribution of substances (e.g. oxygen, nutrients, signaling molecules, and ECM) with discrete descriptions of cells or cell components that evolve dynamically in response to the complex and multi-faceted local environment [141, 142, 143]. Often referred to as "mutli-scale" models [139], hybrid techniques connect the micrometer and centimeter scales [109] and enable the investigation of genetic, cellular and TME effects on tumor behavior [122].

Discrete models are often implemented on a lattice, or more typically, the discrete component of hybrid models is often lattice-based in conjunction with discretized continuum techniques [139]. The spatial resolution of the lattice specifies the technique: one cell populates a single lattice site in cellular automata (CA) [144]; multiple cells occupy one lattice site in lattice gas CA (LGCA) [145]; or alternatively, each cell is composed of multiple lattice sites in cellular Potts model (CPM)s [146]. Chapter 3 describes the theoretical basis of CPMs and specifies its application in this thesis. Notably, CPMs describe cell morphology with more flexibility, but they are computationally intensive and struggle with calibrating simulated time to physical reality [147]. While lattice-based methods suffer from grid-based artifacts and limited biomechanical realism, lattice-free or off-lattice models that describe arbitrary cell locations are also computationally demanding and burdened with a surplus of parameters to fit [122]. In general, discrete models are limited by computational cost, which quickly increases with the number of modeled cells and limits the spatial and temporal scales [109]. Moreover, the flexibility and cellular level detail of discrete techniques comes at the cost of model parameters that are not easily informed by experimental measurement [147, 109]. Accurate parameter estimates derived from reliable *in vitro* and/or *in vivo* measurements underpin the utility of *in silico* models, which lies less in absolute predictive value and rather in generating new hypotheses, falsifying and refining old ones, and guiding the direction of future experiments [148].

1.4 Measuring tumor spheroids with biological methods

Biological methods to assess cellular health, function, and treatment effect assume many forms and names, including proliferation, clonogenic, viability, or cytotoxicity assays. Generally, these methods attempt to measure cell viability, the number or fraction of healthy cells in a sample, particularly following exposure to toxic agents or processes.

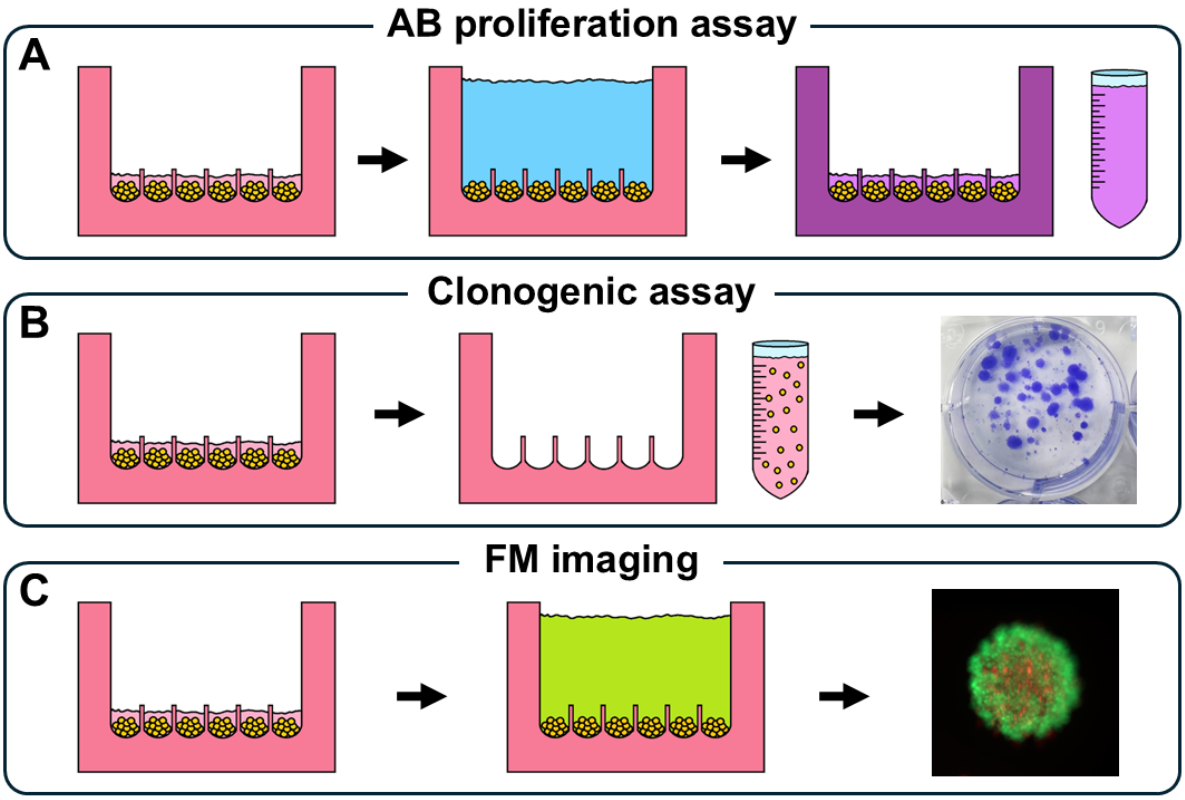


Figure 1.2: Biological methods for measurement of 3D Petri Dish cultured spheroids. (A) AB proliferation assay incubates spheroid-containing gels with blue, non-fluorescent resazurin which is reduced to pink, fluorescent resorufin under cellular metabolism. Culture medium containing the reduced agent is extracted and the fluorescence quantified to produce an average across the spheroids in the gel. (B) Clongogenic assay requires spheroids to be removed from the gel and disaggregated for plating in 2D and longitudinal observation of subsequent colony formation. Colonies are counted and compared with control samples to calculate survival. (C) FM imaging of spheroid-containing gels with a live/dead cell viability assay solution containing green calcein-AM and red PI for identifying live and dead cells, respectively. AB: Alamar Blue; FM: fluorescence microscopy; calcein-AM: calcein acetoxymethyl; PI: propidium iodide.

1.4.1 Proliferation and viability assays

Perhaps the most common method to assess cell viability is by dye exclusion methods that introduce a stain or fluorescent agent that can only enter the damaged membranes of dead cells [149]. The most popular dye exclusion method is Trypan blue, a negatively charged diazo-dye that can only permeate the damaged membrane of dead cells [150]. Its popularity results from its interpretation via bright-field microscopy, which is widely available, but Trypan blue suffers from a lack of sensitivity, as it cannot identify death that leaves the cell membrane intact, and specificity, as it cannot discriminate between necrosis and apoptosis [151]. Other dye exclusion methods include fluorescent stains like propidium iodide (PI), which identifies necrotic cells by permeating compromised plasma membranes and binding to DNA and RNA [152], as well as ethidium bromide (EB) and acridin orange (AO), which identify nuclear changes associated with apoptosis [153]. Other common biological methods include proliferation assays that measure metabolic activity, such as the commonly used tetrazolium salts like 3-[4,5- dimethylthiazol-2-yl]-2,5 diphenyl tetrazolium bromide (MTT), 2,3-bis (2-methoxy-4-nitro-5-sulfophenyl)-5-[(phenylamino) carbonyl]-2H-tetrazo-lium hydroxide (XTT), 3-(4,5-dimethylthiazol-2-yl)-5-(3-carboxymethoxyphenyl)-2-(4-sulfophenyl)-2H-tetrazolium (MTS), and water soluble tetrazolium (WST) that are reduced to formazan crystals by mitochondrial enzymes [151]. Other examples include lactate dehydrogenase release (LDH) and glucose-6-phosphate dehydrogenase (G6PD) assays based on soluble cytoplasmic enzymes, which under membrane disruption are released and involved in the conversion of lactate to pyruvate and NADP+ to NADPH, respectively [154]. The lipid soluble dye calcein acetoxymethyl (calcein-AM) is another measure of metabolic activity in live cells, as it fluoresces under reduction by cytoplasmic esterases [155].

In contrast to the cytotoxic tetrazolium salts [156], Alamar Blue (AB) is a widely used, non-toxic proliferation assay [157] that was employed in this thesis (Fig. 1.2A). The active ingredient of AB, resazurin, was first described in 1929 by Pesch and Simmert [158]. It is a non-toxic and non-fluorescent blue dye that is water-soluble, stable in culture medium, and cell membrane permeable, which enables continuous monitoring of the cell culture [157]. Under reduction by mitochondrial and cytoplasmic enzymes, resazurin is converted to pink and highly fluorescent resorufin [159]. As such, it is a general indicator of cellular metabolism that can be used to qualitatively identify changes in visible color associated with metabolically active cells, or can be measured quantitatively via fluorometric reading [157].

However, the 3D nature of spheroid cultures complicates the implementation and interpretation of these conventional biological methods. Exogenous agents that measure vi-

ability and proliferation can suffer from low accuracy and non-specific labeling [160, 161], as well as limited diffusion into large spheroids [162]. These methods can be sensitive to the concentration of the agent, the incubation time, and the number of cells in the sample [163, 164], which is not straightforward to calculate in many 3D cell culture platforms. Additionally, culturing spheroids in gel formats like hydrogel scaffolds [105] or 3D Petri Dish agarose gels [108] impacts the bioavailability of the agent by diluting it and affecting the exposed cell surface area [164]. These factors complicate interpretation and direct comparison with conventional monolayer culture or different spheroid culture methods. Moreover, fluorescence measurement by dye exclusion do not quantify cellular activity and rather attempt to answer a binary question [151], whereas measurement by proliferation assay provides an average measurement across the spheroid or sample of spheroids [157].

1.4.2 Clonogenic assay

In 1956, Puck and Marcus [165] reported the first survival curve that fit cell survival to radiation dose with a colony forming or clonogenic assay performed with mammalian cells. In contrast to the above cell viability and proliferation assays, clonogenic assay measures the reproductive ability of cells to form 2D colonies through longitudinal observation [166]. As such, it uniquely measures the clonogenic potential of individual cells directly; that is, cells that have undergone reproductive death without suffering physical damage to the cell membrane (e.g. by senescence) are considered dead by clonogenic assay, although they may be considered viable according to many of the cell viability and proliferation assays described in Section 1.4.1. The clonogenic assay has remained the gold standard for measuring radiation survival [167], in part because it accurately identifies the prolonged process of radiation-induced reproductive death, but also because it informs the clinically-relevant LQ model [46, 47]. Beyond its initial and essential role in radiobiological applications, the clonogenic assay is also used to measure cell death following chemotherapeutic and other treatments [166].

The clonogenic assay was first adapted for spheroid culture in the early 1970s by Durand and Sutherland [168]. However, while clonogenic assay is not limited by the addition of an exogenous agent, it requires disaggregation of the spheroid structure to observe longitudinal colony formation (Fig. 1.2B). Consequently, it lacks spatial resolution throughout the 3D spheroid. Moreover, the longitudinal observation takes place in 2D culture, which influences cell phenotype [80] and morphology [86, 87], as discussed in Section 1.2. Lastly, the clonogenic assay is tedious and time-consuming, which has motivated the pursuit of a replacement [169].

1.4.3 Fluorescence microscopy (FM)

Intact spheroids can be evaluated with spatial resolution using imaging techniques [96]. The ideal spheroid imaging technique should provide real-time volumetric imaging with a field of view (FOV) on the order of a millimeter and micrometer-scale resolution throughout the imaging volume, have sensitivity to the tissue and cell functions of interest, and demonstrate little phototoxicity [170]. Bright-field microscopy is readily available in cell culture laboratories and enables real-time imaging, but lacks 3D spatial resolution and functional imaging [171, 96]. Quantitative phase microscopy by digital holography can characterize the morphological structure of near-transparent samples volumetrically, but similarly lacks functional insight [172, 173]. While electron microscopy demonstrates nanometer-scale resolution, sample preparation is complicated, scanning electron microscopy (SEM) cannot visualize the spheroid interior, and functional imaging by transmission electron microscopy (TEM) is millisecond-limited [174]. With contrast generated by higher-order light-matter interactions of multiple photons, multiphoton microscopy is less sensitive to scattering than traditional techniques that employ linear one-photon absorption processes [175]. Nonetheless, although experimental work has imaged to depths of 1 mm [176], usually multiphoton microscopy imaging can only penetrate to a few hundred micrometers [177]. Confocal microscopy generates volumetric imaging via optical sectioning with a detection pinhole whereby all light that does not originate from the plane of focus is rejected [178]; however, the signal strength is particularly impacted by scattering and it also suffers from a penetration limit of a few hundred micrometers [175]. Moreover, volumetric acquisition by confocal microscopy is slow [179], limiting functional investigation [180] and complicating live spheroid imaging due to sample motion [96].

The imaging techniques described above provide morphological information. A common method of generating contrast for functional imaging is with fluorescent labels, or fluorophores [177]. In 1904, Köhler [181] described the first observation of fluorescence via microscopy by illuminating biological material with 275 μm wavelength ultraviolet light. In the century since, fluorescence techniques have flourished to include the detection of a structure of interest with a labeled antibody via immunofluorescence [182] and of specific DNA or RNA sequences in cells with a labeled nucleotide sequence via fluorescence in situ hybridization (FISH) [183].

Fluorescent labels benefit from being highly specific. Relevant to spheroid evaluation, cellular function can be measured fluorescently via intracellular adenosine triphosphate (ATP) concentration [184] and the extensive DNA degradation experienced by apoptotic cells can be detected by terminal deoxynucleotidyl transferase (TdT) dUTP Nick-End Labeling (TUNEL) assay [185]. The most common fluorescence technique for spheroid

evaluation is the live/dead cell viability assay which comprises two fluorophores to identify live and dead cells, typically by calcein-AM and PI, respectively [186, 187, 188] (Fig. 1.2C).

However, fluorescent labels are exogenous agents that must be invasively introduced to the spheroid. Fluorescent labels take time to diffuse throughout the spheroid and penetration into spheroids larger than a few hundred micrometers in diameter is limited [162]. Since labeling is highly specific to the structures or processes of interest, the resulting non-uniform distribution biases the already complicated interpretation of the fluorescent signal within the microenvironment [177]. Moreover, exposure of the excitation light illumination can damage the sample through phototoxicity [189]. While multiple labels can be introduced for the identification of several structures, the complexity and cost of the experiment increases with each label and microscopes have a limited number of fluorescent channels [171]. Specifically, confocal microscopy [190] and two photon microscopy [191] have been widely used for fluorescence microscopy (FM), and confocal FM remains the state-of-the-art for identifying 3D cell distributions [188].

Consequently, generating functional contrast in spheroids with label-free imaging would avoid staining artifacts and phototoxicity, as well as reduce pre-imaging preparation. Additionally, the spheroid is not modified in any way by the introduction of an exogenous agent, enabling the same spheroid to measured again with another method for direct comparison. As described in Chapter 2, optical coherence tomography (OCT) provides a volumetric, non-invasive, quantitative method for spatially resolved evaluation of cellular activity throughout the spheroid [192].

1.5 Thesis organization

This thesis is structured around three journal articles that are currently either under review or being prepared for submission. The Statement of Contributions section details the contributions of the thesis author to each article. The chapters are arranged as follows:

- **Chapter 2**: Optical coherence tomography (OCT)
  - Overview of OCT imaging technology, including the theoretical foundation of low-coherence interferometry, relevant system characteristics, and the various OCT modalities.
  - Extensive review and discussion of recently developed methods to generate dynamic contrast in OCT images.

- **Chapter 3**: Cellular Potts model (CPM)
  - Mathematical introduction to the lattice-based CPM, including the cell lattice, the modified Metropolis algorithm, and Hamiltonian energetics.
  - Discussion of the utility and limitations of the CPM.
  - Implementation details of the CPM of 3D prostate tumor spheroid growth that was developed for this thesis and modified in Chapters 5 and 6 to simulate treatment.
- **Chapter 4**: Longitudinal investigation of prostate tumor spheroid proliferation with dynamic line-field optical coherence tomography
  - Application of a frequency banding dynamic contrast OCT (dOCT) technique to longitudinal tumor spheroid evaluation.
  - Development of a spheroid masking algorithm for quantitative volumetric analysis that reveals the mechanism of longitudinal spheroid growth.
  - Novel algorithm for quantitative dOCT analysis via frequency banding and its comparison to established AB and FM biological methods.
- **Chapter 5**: Comparison of volumetric dynamic optical coherence tomography with biological methods for evaluation of radiation effects in prostate tumor spheroids
  - Novel application of dOCT to irradiated tissue.
  - Development of a CPM for simulating the growth and radiation treatment of tumor spheroids.
  - Comparison of radiation survival in tumor spheroids measured by dOCT to simulation and established clonogenic, AB, and FM biological methods.
- **Chapter 6**: Post-treatment recovery of docetaxel-treated prostate cancer monolayer and spheroid culture
  - Novel clonogenic measurement of spheroid culture treated with DTX chemotherapy and dose-dependent longitudinal observation of post-treatment recovery in prostate cancer monolayer and spheroid culture.
  - Adaptation of the previously developed CPM for simulating DTX treatment of tumor spheroids.
  - Comparison of DTX treatment survival in tumor spheroids via simulation and established clonogenic, AB, and FM biological methods.

- **Chapter 7**: Conclusion
  - A summary of the research performed in the PhD, with particular attention to novel contributions and findings.
  - Discussion of potential future applications of this work.

Chapter 2

Optical coherence tomography (OCT)

Often characterized as the optical analogue of ultrasound imaging, OCT provides non-invasive, high-speed images of biological tissues with cellular resolution [193]. The concept of visualizing highly-scattering biological tissues via optical echoes was conceived in 1971 by Michel Duguay [194], and the invention of OCT soon followed in 1991 [193]. Through low-coherence interferometry, OCT captures the magnitude and echo time delay of light that has been back-scattered from layers at different depths in the sample [193]. Cross-sectional and volumetric images are generated via tomographic reconstruction, as depicted in Fig. 2.1. The fundamental unit of an OCT image is the A-scan, a 1D array that provides a depth-resolved reflectivity profile in the axial or Z-direction (Fig. 2.1A). A series of A-scans in the lateral X-direction forms a 2D cross-sectional B-scan image (Fig. 2.1B) and a collection of B-scans in the lateral Y-direction similarly forms a 3D volumetric image (Fig. 2.1C). This chapter briefly reviews the theoretical basis of OCT, characteristics that describe OCT system performance, the various OCT imaging modalities, as well as dOCT and its application to tumor spheroid imaging.

2.1 Theory of OCT

Fig. 2.2 shows a simplified schematic of a free space OCT system based on a Michelson interferometer. The sample arm of the interferometer behaves as a confocal microscope that undergoes low coherence interference with the reference arm. Assume a low coherence light source generates an electromagnetic field that propagates with an electric field component characterized by:

$$E_i = s\left(k\right) \exp\left\{i\left(kz - \omega t\right)\right\} \tag{2.1}$$

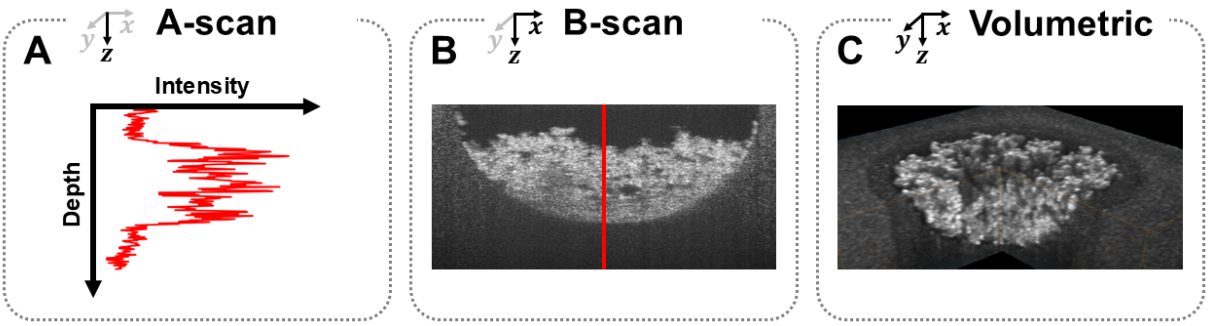


Figure 2.1: A representative OCT dataset of a prostate tumor spheroid. (A) An OCT A-scan intensity profile. (B) An OCT B-scan cross-sectional XZ intensity image composed of a set of A-scans. (C) A 3D volumetric OCT image composed of a set of B-scans.

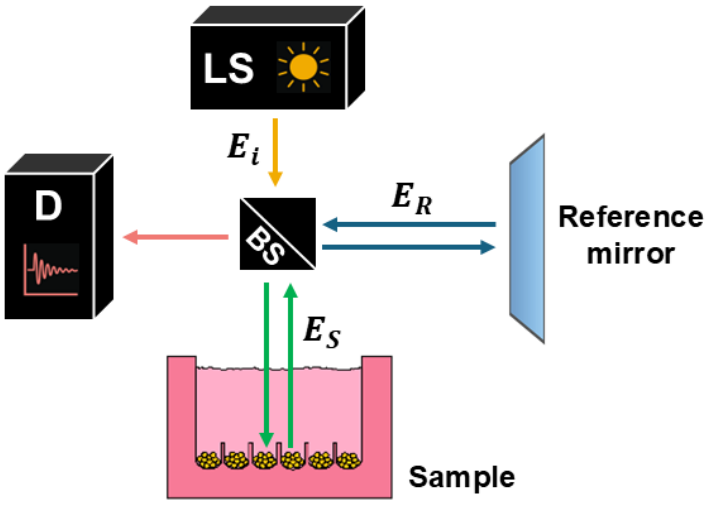


Figure 2.2: A schematic of a free space OCT system based on a Michelson interferometer. A low coherence light source produces light with electric field component E_i that is split and into the sample and reference arms, which reflect back E_S and E_R, respectively. The detector captures the interference signal. LS: light source; BS: beam splitter; D: detector.

where $s(k)$ is the electric field amplitude as a function of the wavenumber $k = \frac{2\pi}{\lambda}$, and ω is the angular frequency. A 50:50 beam-splitter that we assume to be perfect splits the light into two arms: a reference arm that ends with a mirror for back-reflection; and a sample arm that ends with a multi-layer sample. The light reflected by the reference mirror may be expressed by:

$$E_R = \frac{E_i}{\sqrt{2}} r_R \exp(i2kz_R) \tag{2.2}$$

and by the multi-layer sample by:

$$E_S = \frac{E_i}{\sqrt{2}} [r_S(z_S) \circledast \exp(i2kz_S)] \tag{2.3}$$

Here, r_R and $r_S(z_S)$ are respectively the electric field reflectivity of the reference mirror and the multi-layer sample as a function of the individual sample layers, with convolution denoted by $\circledast$. The distances z_R and z_S are from the beam splitter to the reference mirror and to the reflective layers in the sample, respectively. Assuming there are n discrete sample layers, the electric field reflectivity of the i-th layer in the sample may be expressed by:

$$r_S(z_S) = \sum_{i=1}^{n} r_{Si} \delta(z_S - z_{Si}) \tag{2.4}$$

where the depth of the layer is z_{Si} and the Dirac delta function δ identifies the location of each layer.

The electromagnetic field from the reference and sample arms interfere and are collected by the detector. The photocurrent generated by the detector is given by:

$$I(k) = \frac{\rho(k)}{2} \left\langle |E_R + E_S|^2 \right\rangle \tag{2.5}$$

Here, $\rho(k)$ is the detector responsivity and $\langle \cdot \rangle$ indicates integration over the response time of detection. Substitution of Eq. 2.2 and Eq. 2.3 into Eq. 2.5 and considering only the real part yields the following "spectral interferogram":

$$\begin{aligned} Re\{I(k)\} = S(k) \{ r_R^2 + \sum_{i=1}^{n} r_{Si}^2 \; + 2 \sum_{i=1}^{n} \sqrt{r_R r_{Si}} \cos[2k(z_R - z_{Si})] \\ + \sum_{i,j=1, i \neq j}^{n} \sqrt{r_{Si} r_{S,j}} \cos[2k(z_{Si} - z_{S,j})] \; \} \end{aligned} \tag{2.6}$$

Here, $S(k) = \frac{\rho}{4}\langle s^2(k)\rangle$. Eq. 2.6 may be decomposed into three components. The first two terms r_R^2 and $\sum_{i=1}^{n} r_{Si}^2$ comprise the constant or "DC" term I_{DC} and arise from direct reflections from the reference mirror and sample layers respectively, with no interference. Of these, the direct reference mirror reflection is typically characterized before imaging and subtracted from the final result, and the direct sample layer reflection is usually negligible because the sample layer in tissue has much smaller electric field reflectivity compared to the reference mirror (i.e. $r_{Si} \ll r_R$). The second component of Eq. 2.6 is the "cross-correlation" term I_{CC} given by $2\sum_{i=1}^{n}\sqrt{r_R r_{Si}}\cos\left[2k\left(z_R - z_{Si}\right)\right]$. It corresponds to the interference between the sample layers and the reference mirror, and is the term from which low coherence interferometry amplified signals are extracted to form depth-resolved OCT images. Finally, the last term $\sum_{i,j=1,i\neq j}^{n}\sqrt{r_{Si}r_{S,j}}\cos\left[2k\left(z_{Si} - z_{S,j}\right)\right]$ is the "auto-correlation" term I_{AC} that arises from interference between reflections from different sample layers. Due to the small electric field reflectivity of the sample, the "auto-correlation" term is also generally negligible.

2.2 OCT system designs

The interpretation of Eq. 2.6 differs between the two OCT system designs: time domain OCT (TD-OCT) and Fourier domain OCT (FD-OCT) (Fig. 2.3).

2.2.1 Time domain OCT (TD-OCT)

The first OCT systems that were designed fell into the category of TD-OCT. These systems collect information along the axial A-scan direction by physically adjusting the path length z_R of the reference arm to match various depths z_{Si} in the sample (Fig. 2.3A). The reference mirror may be moved with various methods, including linear stages or piezoelectric actuator-based fiber stretchers [195]. Assume the incident light has the following Gaussian wave profile:

$$s(k) = \frac{1}{\Delta k\sqrt{\pi}}\exp\left\{-\left(\frac{k-k_0}{\Delta k}\right)^2\right\} \tag{2.7}$$

Here, $k_0 = \frac{2\pi}{\lambda_0}$ and Δk are the central wavenumber and half-width of the spectrum at $\frac{1}{e}$ intensity of its maximum, respectively. Integrating the cross-correlation term of Eq. 2.6 with respect to all wavenumbers yields:

$$I_{CC}(z_R) = \int_0^\infty I_{CC}(k)dk \propto \sum_{i=1}^{n}\sqrt{r_R r_{Si}}\exp\left\{-\left(z_R - z_{Si}\right)^2\Delta k^2\right\}\cos\left[2k_0\left(z_R - z_{Si}\right)\right] \tag{2.8}$$

The exponential decay of Eq. 2.8 via $\exp\left\{-\left(z_R - z_{Si}\right)^2 \Delta k^2\right\}$ suggests an interference signal that peaks when $z_R = z_{Si}$ and quickly diverges with increasing path length difference. The Fourier transform of $s\left(k\right)$ determines the width of the interference signal.

However, the small exposure time at each depth and movement of mechanical components limits the signal-to-noise ratio (SNR) of TD-OCT systems, which conventionally achieve A-scan rates on the order of a few kHz [195].

2.2.2 Fourier domain OCT (FD-OCT)

Compared to TD-OCT systems, FD-OCT systems offer significantly improved acquisition speeds and SNR [196]. Rather than the TD-OCT approach of integrating Eq. 2.6 with respect to all wavenumbers through moving mechanical components, FD-OCT instead applies a Fourier transform to the signal measured by the detector $I_D\left(k\right)$ [197]. The Fourier transform of the k-space cross-correlation term of Eq. 2.6 is given by:

$$I_{CC}\left(z\right) = \mathcal{F}\left\{I_{CC}\left(k\right)\right\} \propto \gamma\left(z\right) \circledast \sum_{i=1}^{n} \sqrt{r_R r_{Si}} \left\{\delta\left[z \pm 2\left(z_R - z_{Si}\right)\right]\right\} \tag{2.9}$$

where the Fourier transform of $s\left(k\right)$ is the coherence function $\gamma\left(z\right)$. Eq. 2.9 may be further simplified by computing the convolution as follows:

$$I_{CC}\left(z\right) \propto \sum_{i=1}^{n} \sqrt{r_R r_{Si}} \left\{\gamma\left(z\right)\left[2\left(z_R - z_{Si}\right)\right] - \gamma\left(z\right)\left[2\left(z_R + z_{Si}\right)\right]\right\} \tag{2.10}$$

The reflectivity profile of the sample $r_S\left(z_S\right)$ may be directly reconstructed without changing the optical path lengths via Eq. 2.10, which contains information about all of the discrete sample layers within the scanning range of each A-scan.

Consequently, the FD-OCT approach does not require physical manipulation of the reference arm path length, and rather requires a resolved interference k-spectrum for application of the Fourier transform. There are two common methods to achieve the required spectrum: a diffraction grating is placed in front of the camera to separate light from a broadband light source into individual wavelengths that are captured along a line detector [198]; or alternatively, a tunable-wavelength light source sweeps a very narrow band of the spectrum over time and a single detector captures each band sequentially [199]. These FD-OCT approaches are respectively called spectral domain OCT (SD-OCT) (Fig. 2.3B) and swept-source OCT (SS-OCT) (Fig. 2.3C).

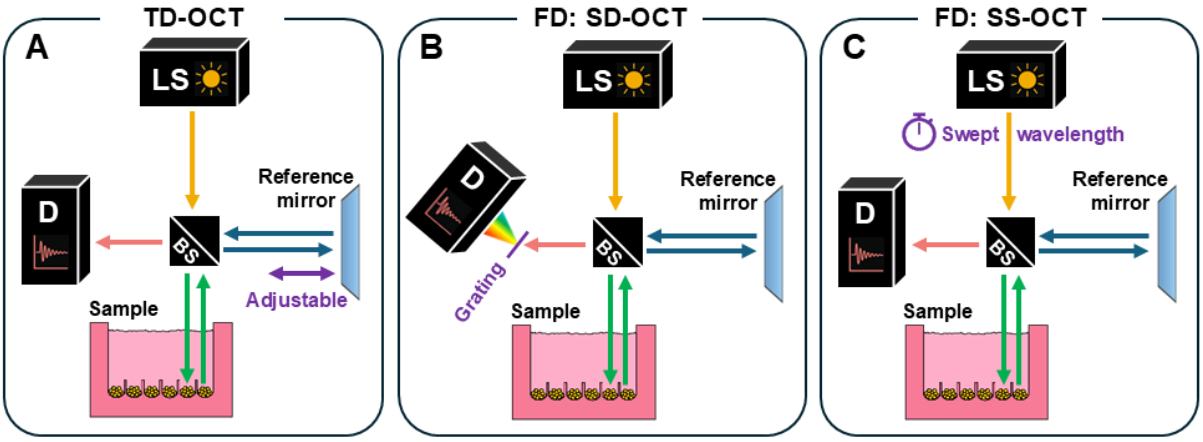


Figure 2.3: OCT system design schematics. (A) TD-OCT systems adjust the reference arm position to collect depth-resolved data. Rather than manipulating the path length of the reference arm, FD-OCT systems apply a Fourier transform to the detected signal. There are two types of FD-OCT systems: (B) SD-OCT systems utilize a broadband light source and employ a diffraction grating to separate the light by wavelength before detection. (C) SS-OCT systems sweep a narrow band of a tunable-wavelength light source over time to detect each band sequentially. LS: light source; BS: beam splitter; D: detector; TD-OCT: time domain OCT; FD-OCT: Fourier domain OCT; SD-OCT: spectral domain OCT; SS-OCT: swept source OCT.

Notably, the symmetric terms $\gamma(z)\left[2\left(z_R - z_{Si}\right)\right]$ and $-\gamma(z)\left[2\left(z_R + z_{Si}\right)\right]$ arise from the mirror artifact of the Fourier transform and create a mirror image of the sample reflectivity profile on the other side of the zero path length. The mirror artifact may be avoided by ensuring the entire sample remains on one side of the zero path length delay. Fourier transforms of the DC and the auto-correlation terms also generate image artifacts, but these are manageable through background subtraction and sufficient reference reflectivity, respectively.

2.3 Characteristics of FD-OCT systems

The following characteristics describe the performance of an FD-OCT system under the assumption of a normalized Gaussian beam profile with electric field amplitude described by Eq. 2.7 and the point-scan OCT (PS-OCT) modality described in section 2.4.1.

2.3.1 Axial resolution

The axial resolution δ_z of an OCT system is its best ability to resolve distinct points in the axial or depth direction. Uniquely, axial resolution is independent of the physical design of the system, and rather depends only on the profile of the light source. The coherence function $\gamma(z)$ of the light source is given by the Fourier transform of the field amplitude $s(k)$ as follows:

$$\gamma(z) = \mathcal{F}\{s(k)\} = \exp\left(-z^2 \Delta k^2\right) \tag{2.11}$$

The axial resolution δ_z, also called the coherence length l_c, is the full-width at half maximum (FWHM) of the coherence function, given by:

$$\delta_z = l_c = \frac{2\sqrt{\ln(2)}}{\Delta k} = \frac{2\ln(2)}{\pi}\frac{\lambda_0^2}{\Delta\lambda} \tag{2.12}$$

where $\lambda_0 = \frac{2\pi}{k_0}$ and $\Delta\lambda$ are respectively the central wavelength and FWHM of the light source wavelength spectrum.

Eq. 2.12 provides a theoretical limit to the axial resolution of an OCT system. In practice, even using light sources with Gaussian beam profiles, the beam profile incident on the sample is not perfectly Gaussian. For non-Gaussian beam profiles, the Fourier transform of the measured beam profile provides a better estimate of axial resolution.

2.3.2 Lateral resolution

The lateral resolution δ_x of an OCT system is the FWHM of the intensity diameter of the beam width at the focal plane. Because of the confocal component of OCT systems, the theoretical lateral resolution δ_x can be characterized by considering light propagating through a confocal microscope [196]. At the focal plane, the light power distribution $I(v)$ can be modeled as follows:

$$I(v) = \left[\frac{2 \cdot J_1(v)}{v}\right]^4 \tag{2.13}$$

where $J_1(v)$ is the first-order Bessel function of the first kind and v is the normalized lateral range parameter given by:

$$v = \frac{2\pi x \sin(\alpha)}{\lambda_0}. \tag{2.14}$$

Here, x is the lateral distance from the light propagation axis, α is the half-angular aperture of the objective, $\sin(\alpha)$ is the numerical aperture (NA) of the microscopic objective, and λ_0 is the central wavelength. Considering the FWHM, the lateral resolution δ_x is given by:

$$\delta_x = \frac{\sqrt{2\ln(2)}}{\pi}\frac{\lambda_0}{\sin(\alpha)} = \frac{\sqrt{2\ln(2)}}{\pi}\frac{\lambda_0}{\mathrm{NA}} \tag{2.15}$$

Therefore, microscopic objectives with higher NA generate smaller focal spot sizes and improve the lateral resolution, as shown in Fig. 2.4. Notably, lateral resolution depends on the central wavelength λ_0 and not the bandwidth $\Delta\lambda$. Consequently, Eq. 2.15 reasonably approximates the lateral resolution of narrow-band OCT systems, but the approximation may not hold well for broadband spectrum input.

2.3.3 Depth of focus (DOF)

The depth of focus (DOF) describes the depth over which the intensity of the beam is sufficient to remain in focus. Assume a propagating Gaussian beam with intensity profile given by:

$$I(r) = I_0 \exp\left\{-\frac{2r^2}{w^2(z)}\right\} \tag{2.16}$$

where z is the distance along the propagation axis such that $z = 0$ locates the focal plane, r is the radial distance from the propagation axis, and $w(z)$ is the radius of the beam at which the intensity falls to $1/e^2$ of I_0. For light at the focal plane, the beam waist w_0 of the Gaussian beam refers to the $1/e^2$ beam radius and is given by:

$$w_0 = \frac{\lambda_0}{\pi \mathrm{NA}} \tag{2.17}$$

The Rayleigh length, or Rayleigh range, Z_{RL} is defined as the axial distance from the beam waist such that $w(z) = \sqrt{2}w_0$. This location is where the beam's cross-sectional area doubles and the intensity falls to $1/e^2$ of its maximum at the beam waist and is given by the following:

$$Z_{RL} = \frac{\pi w_0^2}{\lambda_0} = \frac{\lambda_0}{\pi(\mathrm{NA})^2}. \tag{2.18}$$

The DOF, also called the confocal parameter b, is defined as twice the Rayleigh length:

$$\mathrm{DOF} = b = 2Z_{RL} = \frac{2\pi w_0^2}{\lambda_0} = \frac{2\lambda_0}{\pi(\mathrm{NA})^2} \tag{2.19}$$

Eq. 2.19 reveals that microscopic objectives with higher NA result in a shorter DOF despite improving lateral resolution, as illustrated in Fig. 2.4.

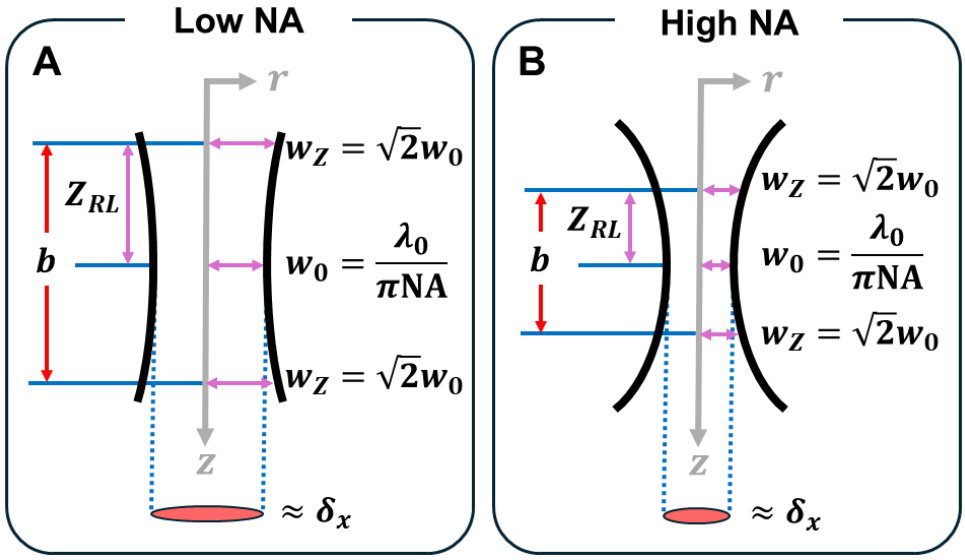


Figure 2.4: (A) Objectives with lower NA provide lower lateral resolution δ_x and improved DOF b compared to (B) objectives with higher NA.

2.3.4 Scanning range

The scanning range z_{max} is the maximum depth from which detector can interpret the OCT interference fringe without aliasing, given the constraints of the detector and broadband light source. Eq. 2.6 reveals the OCT interference fringe to be a sinusoid of the form $\cos\left[2k\left(z_R - z_{Si}\right)\right]$, whereby the frequency of the interference fringe increases with increasing path length difference. Assuming there are N pixels in the detector and the broadband light source has spectrum width $\Delta k = k_{max} - k_{min}$, the Nyquist-Shannon sampling theorem [200] states that the sampling frequency should be at least twice the detected frequency to prevent aliasing as follows:

$$2\Delta k\left(z_R - z_{Si}\right) \leq \frac{N}{2} \times 2\pi \tag{2.20}$$

Thus, the scanning range z_{max} can be extracted by imposing equality to Eq. 2.20, which yields:

$$Z_{max} = \frac{N\pi}{2\left(k_{max} - k_{min}\right)} = \frac{N}{4}\frac{1}{\left(\frac{1}{\lambda_{min}} - \frac{1}{\lambda_{max}}\right)} \tag{2.21}$$

where λ_{min} and λ_{max} represent the wavelengths, corresponding to the maximum and minimum wavenumbers k_{max} and k_{min}, respectively.

2.3.5 Digital resolution

The digital resolution $\widetilde{\delta}$ of the OCT system is the effective resolution of each pixel, given as the ratio of the FOV to the number of pixels that comprise it. The axial digital resolution $\widetilde{\delta_z}$ is determined by the scanning range z_{max} in Eq. 2.21 and the number of camera pixels N as follows:

$$\widetilde{\delta_z} = \frac{z_{max}}{\frac{N}{2}} = \frac{1}{2\left(\frac{1}{\lambda_{min}} - \frac{1}{\lambda_{max}}\right)} \tag{2.22}$$

where the factor of 2 accounts for the mirror artifact from the Fourier transform. The lateral digital resolution $\widetilde{\delta_x}$ is determined by the lateral FOV_x and number of A-scans (i.e. pixels) in the corresponding lateral direction N_x as follows:

$$\widetilde{\delta_x} = \frac{\text{FOV}_x}{N_x} \tag{2.23}$$

The remaining lateral dimension is similarly calculated from the FOV_y and number of A-scans N_y in the y-direction. To prevent aliasing, the Nyquist-Shannon sampling theorem [200] states that each of the actual resolutions of the system should be at least twice that of their digital counterparts.

2.3.6 Signal-to-noise ratio (SNR)

The SNR of an OCT system is defined as the ratio of the mean-square peak signal power $\langle I_D \rangle^2$ incident on the detector to the variance of the noise σ^2:

$$\text{SNR} = \frac{\langle I_D \rangle^2}{\sigma^2} \tag{2.24}$$

Considering only the zero-delay signal at $z_R = z_S$ in the cross-correlation intensity I_{CC} from Eq. 2.6 yields:

$$I_D\left(z_R = z_S\right) = \frac{\rho\left(k\right)}{2} s^2\left(k\right) \sqrt{r_R r_S} \tag{2.25}$$

Assume the detector has an integration time τ and a quantum efficiency η. Then Eq. 2.25 can be expressed using Planck's constant h and the photon frequency ν as follows:

$$I_D = \frac{\eta\tau}{h\nu} s^2\left(k\right) \sqrt{r_R r_S} \tag{2.26}$$

Assume a shot-noise-limited system. Then, the noise on the detector is dominated by back-reflection from the reference arm mirror and its variance follows the Poisson distribution as:

$$\sigma^2 = \frac{\eta\tau}{h\nu} s^2(k)\, r_R \tag{2.27}$$

Thus, the SNR of an OCT system under the assumption of a perfect detector and no additional noise is found by substituting Eq. 2.27 and Eq. 2.25 into Eq. 2.24, which yields:

$$\mathrm{SNR} = \frac{\eta\tau}{h\nu} s^2(k)\, r_S \tag{2.28}$$

As discussed in section 2.3.4, the frequency of OCT interference fringes is depth-dependent. As a consequence of the Nyquist-Shannon sampling theorem [200], high frequency fringes may not be detected as effectively by the detector's finite number of pixels, causing a drop in SNR with depth – a phenomenon known as "SNR roll-off". Although the meaning of the terms "SNR" and "sensitivity" can vary according to the context, they are used interchangeably in this thesis.

2.4 OCT imaging Modalities

There are three categories of OCT imaging modalities characterized by the beam shape on the imaging plane: PS-OCT, line-field OCT (LF-OCT), and full-field OCT (FF-OCT) (Fig. 2.5).

2.4.1 Point-scan OCT (PS-OCT)

PS-OCT systems focus a narrow, confocal beam onto the imaging plane to acquire one depth-resolved A-scan at each location in the sample (Fig. 2.5A). Volumetric datasets are acquired by scanning the beam laterally in a point-by-point manner via two linear scanners or micro-electromechanical system (MEMS) mirrors. Compared to OCT systems that employ the other imaging modalities with equivalent SNR, PS-OCT systems demonstrate improved image quality because each A-scan in the volume is captured separately, so there is reduced crosstalk between A-scans. Nevertheless, PS-OCT systems also generally offer the slowest data acquisition speeds of all imaging modalities because each A-scan exposure takes some period of time. Typical clinical PS-OCT systems demonstrate A-scan rates of approximately 100 kHz, which provide ample opportunity for gross sample motion to introduce artifacts, particularly for imaging with large FOV. Researchers have reported A-scan rates of 600 kHz for a spectral domain point-scan OCT (SD-PS-OCT) system with a

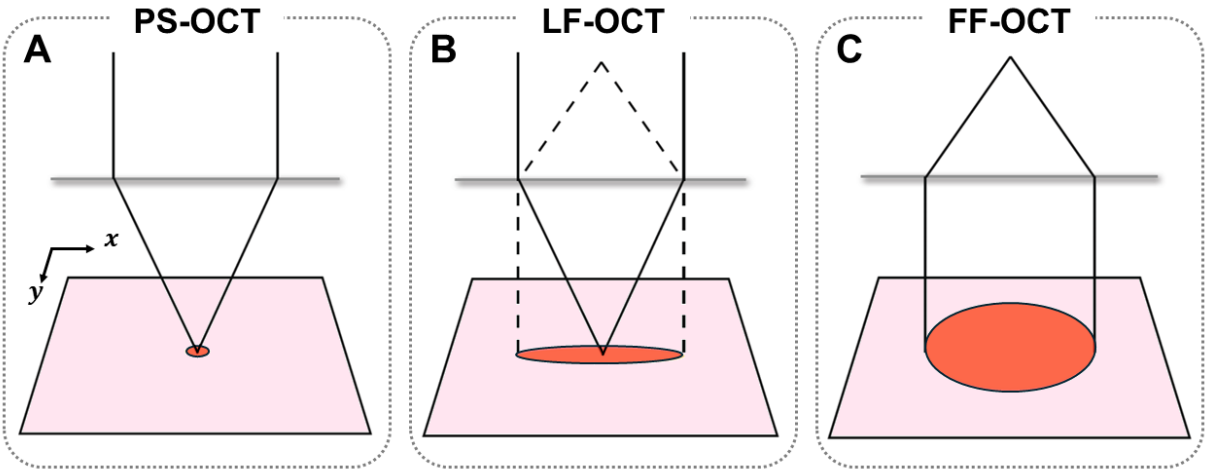


Figure 2.5: (A) Point-scan OCT (PS-OCT) systems focus a narrow, confocal beam onto the imaging plane and acquire one depth-resolved A-scan at each location in the sample. Scanning the beam in each lateral direction allows volumetric acquisition in a point-by-point manner. (B) Line-field OCT (LF-OCT) systems focus the beam into a line onto the imaging plane and acquire A-scans at all lateral positions simultaneously in a cross-sectional image or B-scan. Volumetric acquisition is achieved by scanning the beam in the remaining lateral direction. (C) Full-field OCT (FF-OCT) systems project a parallel beam onto the imaging plane and acquire an enface image in the XY plane without resolving depth. Instead, enface images must be acquired at each depth to achieve volumetric acquisition.

high-speed line camera [201] and 20 MHz for a swept-source point-scan OCT (SS-PS-OCT) system with a Fourier domain mode-locked (FDML) laser [202]. Still, SD-PS-OCT and SS-PS-OCT systems respectively suffer from limited SNR due to shorter A-scan exposure and lower axial resolution due to the swept source light source.

2.4.2 Line-field OCT (LF-OCT)

First reported in 1999 [203], LF-OCT systems, which are also called line-scan OCT (LS-OCT), focus the beam into a line onto the imaging plane to simultaneously acquire A-scans at all lateral positions in a cross-sectional image or B-scan (Fig. 2.5B). LF-OCT systems convert a circular-shaped beam into a line-shaped beam with a 2D lens and capture depth data along the line with a 2D sensor camera in SD-OCT systems or a line camera in SS-OCT systems. Data acquisition speeds are significantly higher in LF-OCT systems

compared to PS-OCT systems, which helps to reduce motion artifacts. Investigators have reported LF-OCT systems with equivalent A-scan rates of several MHz and sufficient SNR for imaging biological tissues [204, 205, 206, 207, 208, 209]. Because each line-scan exposure directly generates one B-scan without any mechanical movement of the system, volumetric acquisition requires a single linear scanner for beam translation. Consequently, B-scans acquired with LF-OCT systems typically offer better phase stability than the other OCT imaging modalities. However, the image quality of LF-OCT systems is limited by the lack of confocal gating in the line direction which causes increased crosstalk between A-scans within each B-scan, and reflection artifacts are prevalent and difficult to mitigate. Moreover, the beam energy is redistributed across the imaging line rather than focused into a point, which limits the FOV in the line direction. While the digital resolution along the line direction is limited by how the imaging line is magnified onto the camera, its physical lateral resolution is subject to the NA that governs the confocally gated lateral resolution. Interference fringe washout poses another impediment to LF-OCT systems due to the longer single-shot camera exposure time. Lastly, the most common method for generating an imaging line in LF-OCT systems is a cylindrical lens, which gives rise to a Gaussian intensity distribution along the imaging line that can cause a 10 decibel (dB) variation in SNR along the line-direction FOV. Chen et al. [207] developed a LF-OCT system with conically-shaped Powell lens that demonstrated a more uniform line-direction SNR distribution, but complicated alignment of the system due to lack of a well-defined focus.

2.4.3 Full-field OCT (FF-OCT)

The concept of FF-OCT was first presented in 2002 [210]. By projecting a parallel beam onto the imaging plane, FF-OCT systems acquire an enface image in the XY plane with a single camera exposure (Fig. 2.5C). Unlike PS-OCT and LF-OCT, FF-OCT systems do not acquire depth information. Rather, to generate volumetric datasets they employ TD-OCT or SS-OCT approaches because collection of a 2D enface image alongside a 1D array of spectrum information would require the impossible feat of a 3D camera sensor. Remarkably, swept-source full-field OCT (SS-FF-OCT) systems have demonstrated acquisition speeds of up to 1.5 MHz [211]. In comparison, time domain full-field OCT (TD-FF-OCT) systems have demonstrated acquisition speeds of up to 250 kHz [212], which remains a marked improvement over the conventional time domain point-scan OCT (TD-PS-OCT) A-scan rates of a few kHz [195]. The utilization of a parallel beam avoids the DOF constraints associated with beam focusing, allowing FF-OCT systems to benefit from high NA objectives that achieve cellular-level lateral resolution throughout the entire scanning

depth. Concomitantly, the lack of confocal gating in any direction also results in crosstalk issues, although various techniques have been developed to reduce these effects, including random phase modulations [213] and multi-mode fibers [214].

2.5 Dynamic contrast OCT (dOCT)

OCT systems rely on reflective layers in the sample that occur when the refractive index changes. Thus far, OCT has widely been used for morphological investigation of the weakly scattering and mostly transparent layers of the retina, leading to its now routine use in clinical eye care [215]. Longitudinal OCT imaging has enabled the characterization of how biological structures move over various time scales, including annual monitoring of retinal nerve fiber layer (RNFL) thickness in glaucoma patients [216], assessment of stroke recovery in the ensuing hours and days [217], and observation of retinal neuronal function via optoretinography (ORG) over milliseconds [218]. From this framework, a functional, non-invasive, and label-free imaging technique called dOCT emerged to elucidate cellular and subcellular mechanisms by repeating OCT acquisition in the same location to characterize temporal behavior [192]. Here, label-free refers to the dynamic contrast arising due to statistically measurable intensity fluctuations in each pixel, as opposed to conventional methods that require an exogenous stain to be introduced to the sample.

Other interferometric imaging techniques like dynamic holography (DH), which is based on the Mach-Zender-like interferometer, have also provided insight into cellular dynamics through the statistical analysis of temporal fluctuations in dynamic speckle [219]. Although DH has been used to investigate the viability [220] and phenotypic drug response [221] of tumor spheroids, it measures the combined dynamics of a population of cells. Unique in the field of label-free dynamic microscopy, dOCT can investigate cellular activity at the level of individual cells through temporal fluctuations associated with subcellular movements [192].

2.5.1 Subcellular origin of dynamic signal

There remains some confusion as to how exactly cellular activity generates the dynamic signal measured by dOCT, as its interpretation is complicated by diffraction-limited spatial filtering and the higher sensitivity of dOCT systems to axial motion [192, 222]. Modulated by the angle of displacement, the dynamic signal arises from the motion of scatterers including cells and their subcellular organelles [223]. Often colloquially referred to as the

"powerhouse of the cell", mitochondria are highly dynamic organelles that are primarily responsible for cell metabolism through continuous production of the cellular energy source, ATP [224]. The motion of mitochondria varies between random Brownian motion and active ATP-consuming motion directed by molecular motors and the cytoskeleton [225]. Depending on temperature, directed mitochondrial motion achieves speeds on the order of several hundred nanometers per second [225, 224].

Using dOCT, Leroux et al. [226] observed increased motion of intracellular components under inhibition of actomyosin contractility, which is known to reduce cytoplasmic stiffness and increase intracellular movement [227]. The dynamic signal measured by OCT systems has also been associated with mitochondria in retinal pigment epithelium (RPE) cells [223], and inhibition of ATP production in rat liver cells revealed that the detected motion is not Brownian in nature [222]. Furthermore, transformation of the cytoskeleton due to cell membrane blebbing during death in cervical epithelial HeLa cells has also been observed to change the frequency and magnitude of the dynamic signal [228]. Nonetheless, these results are difficult to generalize due to the variety of mitochondrial shapes, sizes and motion observed in different cell types and at different times within the same cell [224].

2.5.2 Applications

Conventional *in vitro* cell culture

In its short history, the applications of dOCT have been varied and numerous, extending even to the detection of invasive fungal infections [229]. The early applications of dOCT employed conventional *in vitro* cell culture techniques. In 2010, Van der Meer et al. [230] differentiated between viable, necrotic, and apoptotic human fibroblasts in the first report of cellular dynamics extracted from temporal OCT fluctuations. They cultured the cells in 2D monolayers for treatment with agents that induce cell death before trypsinizing and centrifuging cells into pellets for imaging. Shortly after, Farhat et al. [231] observed that suspension cultures of myeloid leukemia cells undergoing apoptosis demonstrated decreased decorrelation time in temporal scattering signals due to apoptotic cell swelling, which allowed organelles to diffuse more freely. Despite the challenge posed by artifacts in shallow imaging depths, 2D monolayer cultures have also been imaged directly with dOCT systems to investigate human fibroblasts [232], assess the viability of HeLa cells [228, 233], and validate characterization of wound healing in RPE cells to immunohistochemistry [223].

3D *in vitro* cell culture

However, the DOF of OCT systems is particularly well suited for imaging 3D *in vitro* cell cultures, including organoids and tumor spheroids. Motivated by the clinical role of OCT in retinal imaging [215], retinal organoids have been characterized [234] and investigated longitudinally [235] with dOCT. The structure and repair of alveolar organoids have similarly been investigated [236]. The growth of mammary epithelial organoids [237], as well as their response to the chemotherapeutics doxorubicin [238] and the anti-cancer drug paclitaxel [239] have also been quantified through dOCT analysis. The effect of paclitaxel has similarly been investigated in MCF-7 breast adenocarcinoma spheroids [187, 240, 241, 242], in addition to the carcinogenic chemical perfluorooctanoic acid [243]. Gels embedded with spheroids modeling breast ductal carcinoma in situ (DCIS) alongside gold nano-rods have been used to explore the dynamic signature of different classes of light scatterers [180]. The viability of HeLa cervical [244], MCF-7 breast [245], and C3A hepatocyte [246] tumor spheroids were explored with dOCT. Additionally, temporal autocorrelation of OCT signals have been used to investigate intracellular motility in human colorectal adenocarcinoma and murine colon carcinoma spheroids [226]. The distribution and viability of human Jurkat cells in 3D scaffolds has been quantified with dOCT [188]. The motility of cell populations has also been investigated with longitudinal and non-invasive dOCT measurement of breast cancer invasion in paper-based 3D culture [247].

ex vivo tissues

Progress towards the promise of optical biopsy made in 2000 [248] is being made in dOCT analysis of *ex vivo* tissues and biopsy samples [177]. Numerous studies have investigated freshly excised murine tissue samples with dOCT [222, 249, 250, 201, 251, 252, 253, 254, 255]. Liu et al. [256] identified live and dead cells in mouse allograft tumors and liver tissue. Explant macaque retinas [249] and porcine bladder tissue [257] have also been investigated. Human biopsy samples have been analyzed with dOCT methods for characterization of subcellular morphology and activity in esophageal and cervical biopsy samples [258], investigation of gut tissue [259], and evaluation of cilia beating, mucus secretion, and immune function in nasal concha [254]. Cancer diagnosis has also been performed with dOCT using human biopsy samples in breast [260], lung [261], and skin [262].

***in vivo* samples**

The ultimate non-invasive goal of *in vivo* dOCT measurement is complicated by motion artifacts and noise. Investigation of *in vivo* zebrafish larvae emphasized the particularly strong and unwanted signals caused by blood vessels [177]. Nonetheless, *in vivo* dOCT investigation has been performed in mice liver [263], brain [264], and Fallopian tube [265, 266, 267, 268].

2.5.3 Image acquisition requirements

The first reported dOCT study analyzed single B-scans acquired every few minutes [230], but current dOCT studies measure cellular dynamics with much higher temporal resolution [192]. Technological developments have improved acquisition speeds through increased camera frame rates in SD-OCT [201] and TD-FF-OCT [269] systems, and increased wavelength sweeping speeds in SS-OCT systems [211]. To observe cellular activity with dOCT, the acquisition speed should be sufficient to resolve frequencies associated with ATP-consuming processes and the active movement of organelles, which are estimated to be in the range of 0.1 to 20 Hz [270, 271]. The first measurement of ATP-consuming processes via dOCT methods with sufficient temporal resolution to assess the active movement of organelles was reported in 2013 by Oldenburg et al. [180]. By the Nyquist-Shannon sampling theorem [200], the fastest dynamics observable by a dOCT system occur at half the frequency of 2D image acquisition.

In addition to temporal resolution, dOCT systems require phase stability to ensure minuscule scatterer movement translates into measurable variation [192]. Lastly, the axial and lateral resolutions (discussed in sections 2.3.1 and 2.3.2, respectively) must also be sufficient to detect organelle movement through variation in the signal of individual voxels [192]. That said, El-Sadek et al. [187, 240] successfully resolved the necrotic core in breast tumor spheroids with a point-scan dOCT (PS-dOCT) system that demonstrated large axial and lateral resolutions of 14 μm and 19 μm, respectively.

As discussed in section 2.4, these properties of OCT systems depend on the modality. The two main architectures of dOCT systems are Fourier domain point-scan OCT (FD-PS-OCT) and TD-FF-OCT. The dOCT acquisition and analysis of each architecture are described in sections 2.5.4 and 2.5.5, respectively.

2.5.4 PS-D-DOCT

Recall from section 2.4.1 that PS-OCT systems acquire a single depth-resolved A-scan in a camera exposure and the beam is scanned laterally with a linear scanner to produce a 2D B-scan image in the XZ plane. For PS-dOCT, each B-scan is typically acquired in a few dozens of milliseconds [196]. If a time series of PS-OCT signals is acquired by repeating B-scan acquisition, referred to as BM-mode, the PS-dOCT method can resolve dynamics in the range of 0.25 to 90 Hz [192]. If faster dynamics are desired, the acquisition of individual A-scans may be repeated before linear translation of the beam to resolve dynamics in the range of 10 kHz [258, 264]; however, this protocol, referred to as MB-mode, elongates the acquisition of each B-scan. While PS-OCT systems benefit from depth-resolved scanning that leverages all scattered photons in each A-scan, they often have a shallow DOF due to high-NA objectives [250]. Consequently, they demonstrate decreased lateral resolution outside the narrow depth of interest, which may affect the scattering cross section for small organelles [192].

The following discussion of various PS-dOCT metrics assumes the dOCT acquisition was performed by repeating B-scan acquisition across N frames in BM-mode, each collected at regular time intervals Δt. The intensity (i.e. amplitude) of the OCT signal at location (x, z) in the B-scan at the i-th time point t_i is denoted $I(x, z, t_i)$. Time averaging is denoted by $\langle \cdot \rangle$.

Motility coefficient M and autocorrelation

The first reported dOCT measurement of ATP-consuming processes in 2013 by Oldenburg et al. [180] introduced a metric called the motility coefficient M as follows:

$$M(x,z) = \sqrt{\frac{\frac{1}{N}\sum_{i=1}^{N}\left[I(x,z,t_i) - \langle I(x,z,t)\rangle\right]^2}{\langle I(x,z,t)\rangle}} \tag{2.29}$$

As such, $M(x, z)$ identifies shot noise limited speckle fluctuations and may be directly interpreted as the ratio of the standard deviation measured at the pixel located at (x, z) to that expected from shot noise. While $M(x, z)$ gives the amplitude of the fluctuations, Oldenburg et al. [180] also defined a time scale by fitting γ, the normalized temporal autocorrelation of $I(x, z, t_i)$, and the $1/e$ decorrelation time τ as:

$$\log\{\gamma(t)\} = -t\tau + c \tag{2.30}$$

Using a full-field dOCT (FF-dOCT) system, Leroux et al. [226] also investigated autocorrelation of the OCT signal. More recently, Xu et al. [257] fit the autocorrelation to multiple exponential decay functions with the CONTIN method.

Since $M(x, z)$ was found to decay significantly with depth in their breast cancer organoid samples, in a more recent paper Oldenburg et al. [237] described a new motility coefficient M' as follows:

$$M'(x, z) = \frac{\sqrt{\Gamma(x, z, \Delta t) - \langle I(x, z, t)\rangle^2}}{\langle I(x, z, t)\rangle} \tag{2.31}$$

Here, $\Gamma(x, z, \Delta t) = \frac{1}{N}\sum_{i=1}^{N-1}[I(x, z, t_i)I(x, z, t_{i+1})]$ is the temporal autocorrelation of $I(x, z, t_i)$ evaluated at a time delay equal to the acquisition time interval Δt. The improved motility coefficient M' describes OCT signals that persist beyond a single sampling time but shorter than the total measurement period; consequently, it ignores shot noise which decorrelates immediately. They previously found the decorrelation time of cell-driven fluctuations to be approximately 4.8 seconds [180], which informed their minimum sampling time interval of approximately 1.1 seconds [237]. This method was directly employed in later studies [238, 239, 243, 272].

Power spectral density (PSD)

In the same paper, Oldenburg et al. [237] also calculated the power spectral density (PSD) S as the square modulus of the Fourier transform of the intensity:

$$S(x, z, f) = |\mathcal{F}\{I(x, z, t)\}|^2 \tag{2.32}$$

Then, they spatially averaged $S(x, z, f)$ across each region of interest (ROI) and omitted frequencies $f \leq 0$ before fitting the values to the following inverse-power-law model:

$$S(f) = c_0 f^{-\alpha} + n \tag{2.33}$$

where c_0 is the constant of proportionality, α is the power-law exponent, and n is additive white noise. Later work by the same group [238] combined the power-law exponent α and modified motility M' metrics into a new metric called the intracellular kinetic energy E as:

$$E = \alpha M' \tag{2.34}$$

which attempts to describe cellular activity *in toto*.

Frequency banding red-green-blue (RGB) images

Apelian et al. [273] introduced another method that employs the PSD to generate red-green-blue (RGB) images. Rather than fitting the inverse-power-law model, the PSD is integrated over three frequency bands in each voxel as follows:

$$B(x,z) = \int_{f_2}^{f_{\max}} S(x,z,f)df \tag{2.35}$$

$$G(x,z) = \int_{f_1}^{f_2} S(x,z,f)df \tag{2.36}$$

$$R(x,z) = \int_{0}^{f_1} S(x,z,f)df \tag{2.37}$$

Here, the maximum detectable frequency is given by $f_{\max}$, the thresholds of the frequency bands are given by f_1 and f_2, and the normalized result of each integral R, G and B then encodes the red, green, and blue color channels, respectively. In this way, high-frequency motion between f_2 and $f_{\max}$ is represented in a different color (conventionally blue) than low-frequency motion between 0 and f_1 (conventionally red). Intermediate motion is represented in the remaining color (conventionally green). While this method was first employed with a FF-dOCT system [273, 249], it has since been widely used with PS-dOCT systems [258, 254, 250, 201, 251]. Common values of f_1 and f_2 are approximately 0.5 Hz and 5 Hz [249, 250, 254], although Leung et al. [258] employed non adjacent frequency bands of <0.08 Hz, 0.55-0.78 Hz, and 4-20 Hz for red, blue, and green, respectively.

Intensity variance

Kohlfaerber et al. [244] visualized cervical HeLa spheroids in 3D-printed scaffolds by directly calculating the voxel-wise intensity variance $V(x,z)$ as follows:

$$V(x,z) = \frac{1}{N}\sum_{i=1}^{N}\left[I(x,z,t_i) - \langle I(x,z,t)\rangle^2\right] \tag{2.38}$$

This method has been adopted by other investigators to evaluate spheroids [245] and bovine embryos [274].

El-Sadek et al. [187] introduced a similar metric called the logarithmic intensity variance (LIV) that assumes the intensity of the OCT signal $I(x,z,t_i)$ may be decomposed into static and dynamic contributions $I_S(x,z)$ and $I_D(x,z,t_i)$, respectively, as follows:

$$I(x,z,t_i) = I_S(x,z)I_D(x,z,t_i) \tag{2.39}$$

Thus, the logarithm of the intensity (i.e. conversion into dB) may be expressed as:

$$I_{dB}(x,z,i) = 10\log_{10}\{I(x,z,t_i)\} = 10\log_{10}\{I_S(x,z)\} + 10\log_{10}\{I_D(x,z,t_i)\} \tag{2.40}$$

which effectively isolates the static component for subtraction via time averaging. The LIV is then defined as:

$$\mathrm{LIV}(x,z) = \frac{1}{N}\sum_{i=1}^{N}\left[I_{dB}(x,z,t_i) - \langle I_{dB}(x,z,t)\rangle^2\right] \tag{2.41}$$

Substituting Eq. 2.40 into Eq. 2.41 then yields:

$$\mathrm{LIV}(x,z) = \frac{1}{N}\sum_{i=1}^{N}\left[10\log_{10}\{I_D(x,z,t_i)\} - \langle 10\log_{10}\{I_D(x,z,t_i)\}\rangle^2\right] \tag{2.42}$$

The LIV metric depends only on the magnitude of the temporally dynamic OCT signal and does not contain any information about the speed of the observed dynamics. It has been compared with birefringence and attenuation coefficient dOCT metrics [252, 253], as well as histology [236]. A deep-learning neural network was developed to generate LIV images from as few as four OCT images [275].

Morishita et al. [276] recently presented analysis of the saturation of a windowed LIV curve and introduced the new metrics authentic logarithmic intensity variance (ALIV) and swiftness as the saturation level and speed, respectively. Tan et al. [245] developed a similar metric called the median adjusted variance (MAV) by employing the median of the intensity variance rather than a logarithm.

OCT correlation decay speed (OCDS)

To describe the speed of the observed dynamics, El-Sadek et al. [187] introduced another metric called the OCT correlation decay speed (OCDS), which first evaluates ρ, the autocorrelation of the intensity, with time delay $j\Delta t$ as follows:

$$\rho(x,z,j\Delta t) = \frac{\mathrm{Cov}\{I_{dB}(x,z,t_i), I_{dB}(x,z,t_i+j\Delta t)\}}{\mathrm{Var}\{I_{dB}(x,z,t_i)\}\mathrm{Var}\{I_{dB}(x,z,t_i+j\Delta t)\}} \tag{2.43}$$

Here, $\mathrm{Cov}\{\cdot\}$ and $\mathrm{Var}\{\cdot\}$ represent covariance and variance, respectively, and the time delay is computed as a discrete multiple of the sampling interval Δt. At each voxel (x,z), ρ is calculated as a function of different time delays j, and the slope is evaluated in two

regions via linear regression: the "early" OCDS$_e$ is calculated in a short delay region, and the "late" OCDS$_\ell$ is calculated in a long delay region. Because the autocorrelation of quickly oscillating scatterers decays quickly (i.e. the PSD oscillates with a high frequency), cells with fast dynamics have larger OCDS$_e$ than OCDS$_\ell$; otherwise the two metrics are comparable. Later studies have also employed OCDS [240, 241, 242].

Eigenvalue decomposition and static power ratio (PR)

Wei et al. [264] exploited subtle phase changes in the complex OCT signal by applying an eigenvalue decomposition (ED) method previously developed for angiography [277]. The first A-scan at location (x, y) was analyzed pairwise with each subsequent A-scan acquired at (x, y) after a time interval of $j\Delta t$, where $j \in [1, N-1]$. These A-scans are denoted A_1 and A_j, respectively, and clustered as $A_{1j} = \begin{bmatrix} A_1 & A_j \end{bmatrix}$. Then, a 2×2 covariance matrix R_c^j, normalized by the number of depth samples in each A-scan M, is calculated and diagonalized via ED as follows:

$$R_c^j = \frac{1}{M} A_{1j}^\dagger A_{1j} = E^j \Lambda (E^j)^\dagger = E^j \begin{bmatrix} \lambda_1^j & 0 \\ 0 & \lambda_2^j \end{bmatrix} (E^j)^\dagger \tag{2.44}$$

where $\dagger$ indicates the complex conjugate transpose and Λ is the transformed diagonal matrix whose eigenvalues λ_1^j and λ_2^j represent the power of the static and dynamic components of the sample, respectively. The eigenvectors of Λ are contained within the 2×2 matrix E^j. Finally, the static power ratio (PR) for the time interval of $j\Delta t$ is computed as the ratio of static power to total power along the time axis and fit to exponential decay as follows:

$$\mathrm{PR}_j = \frac{\lambda_1^j}{\lambda_1^j + \lambda_2^j} = C \exp(G \cdot j\Delta t) \tag{2.45}$$

Here, C is the peak static power ratio which is approximately 1, and the fitted negative decay coefficient G characterizes the dynamic motion, as G values with smaller magnitude indicate faster decay.

The polarization-sensitive birefringence metric calculated by Mukherjee et al. [252, 253] similarly requires matrix diagonalization. Another similar approach was reported by Scholler [263] and Ammari et al. [278], which instead achieved diagonalization by singular value decomposition (SVD) using a FF-OCT system. Wei et al. [264] and Scholler [263] each applied their decomposition methods to *in vivo* mouse brain and liver, respectively.

2.5.5 FF-D-DOCT

Recall from section 2.4.3 that in FF-OCT systems, each camera exposure acquires a 2D enface image in the XY plane, and cellular-level lateral resolution is maintained throughout the entire scanning depth. Consequently, FF-dOCT acquisition repeats enface imaging at the camera frame rate, which is typically on the order of a few hundred Hz [177]. Then, volumetric analysis may be performed by scanning in the axial direction and repeating acquisition at each enface [222]. Compared to PS-OCT systems, FF-OCT systems demonstrate improved phase stability, however they also suffer from the limited use of scattered photons from the enface plane, which is usually on the order of 1 μm thick, and they demonstrate high sensitivity to axial sample movements and slow acquisition of volumetric data [250].

In contrast to PS-dOCT acquisition, the following discussion of various FF-dOCT metrics assumes N enface frames were acquired at regular time intervals Δt at each depth before scanning to the next axial position. Here, the intensity of the OCT signal at location (x, y) in the enface at the i-th time point t_i is denoted $I(x, y, t_i)$.

Running standard deviation of intensity

Apelian et al. [222] reported the first FF-dOCT analysis by calculating the standard deviation voxel-wise in $N_s = N/n$ subsets of the complete time series of N enface images, then averaging over the subsets as follows:

$$D_n(x,y) = \frac{\sum_{j=1}^{N_s} \sqrt{\frac{1}{n}\sum_{i=1}^{n}\left[I(x,y,t_{i+jN_s}) - \left\{\frac{1}{n}\sum_{i=1}^{n} I(x,y,t_{i+jN_s})\right\}^2\right]}}{N_s} \tag{2.46}$$

They qualitatively compared FF-dOCT images to the static counterpart in *ex vivo* rat liver as cells in the sample died over time to argue that the decrease in dynamic signal was related to the reduction in ATP-consuming processes.

Hue-saturation-brightness (HSB) images

A more recently adopted FF-dOCT method leverages the PSD to form a hue-saturation-brightness (HSB) image, sometimes referred to as a hue-saturation-value (HSV) image [234, 223, 235, 232]. Similar to its definition given in Eq. 2.32, the PSD $S(x, y, f)$ employed by FF-dOCT methods is rather calculated as the square modulus of the Fourier transform

of the enface intensity $I(x, y, t)$. Scholler et al. [234] first developed the HSB technique using three metrics for the three channels of the image: the mean frequency, the inverse of the frequency bandwidth, and the running standard deviation developed by Apelian et al. [222] given by Eq. 2.46. The hue channel represents the fluctuation speed captured by the mean frequency f_{mean}, calculated using N_b frequency bins of the PSD S as follows:

$$f_{\text{mean}}(x, y) = \sum_{i=1}^{N_b} S(x, y, f_i) f_i \tag{2.47}$$

where f_i is the frequency of the i-th bin. Thus, the color of each voxel varies from blue to red with increasing temporal frequency. The saturation channel is computed with the voxel-wise inverse of the frequency bandwidth, calculated using the standard deviation f_{std} of the frequencies as follows:

$$f_{\text{std}}(x, y) = \sum_{i=1}^{N_b} S(x, y, f_i) f_i^2 - \sum_{i=1}^{N_b} \left[S(x, y, f_i) f_i\right]^2 \tag{2.48}$$

Consequently, broader bandwidths that are more representative of white noise appear dull and grayish, whereas narrow bandwidths appear with vivid color. Lastly, the brightness channel encodes information about frequency and intensity variance by directly employing the running standard deviation given by Eq. 2.46 to emphasize intracellular motion. Later studies applied this method directly [223, 235, 232], whereas Liu et al. [256] considered only the mean frequency of the PSD.

Park et al. [228, 233] similarly considered the normalized mean frequency, but calculated the PSD with a windowing method to improve sensitivity to non-Brownian motion and additionally considered the integral of the PSD as a separate metric. Using a PS-dOCT system, Wang et al. [246] adopted the windowing method of Park et al. [228, 233] in conjunction with the HSB method developed by Scholler et al. [234]. Alternatively, El-Sadek et al. [187, 240] used a PS-dOCT system to construct HSB images. They encoded the hue channel with either LIV or OCDS metrics described in sections 2.5.4 and 2.5.4, respectively. Then, they set the saturation channel to 1 in all voxels so all colors remained vivid, and encoded the brightness as the intensity of the OCT signal $I(x, z)$.

2.5.6 LF-D-DOCT

As discussed in section 2.5.3, dOCT analysis requires sufficient temporal resolution, phase stability, and axial and lateral resolution. In addition to sufficiently small Δt between

consecutive enface images in FF-dOCT or A-scans (MB-mode) or B-scans (BM-mode) in PS-dOCT for temporal resolution of dynamic signals, volumetric dOCT analysis practically requires reasonable imaging time of the entire volume. High acquisition speeds can also minimize motion artifacts due to bulk movement of cells and environmental vibrations, as well as effects that arise while imaging *in vitro* cell culture that has been removed from its tightly regulated culture environment.

In general, faster acquisition speeds are achieved at the cost of reduced sensitivity [279], and volumetric acquisition by PS-dOCT is faster than FF-dOCT, which is limited by camera frame rates on the order of 1 ms [177]. Our group demonstrated the first SD-PS-OCT system with an isotropic imaging resolution of approximately 1.5 μm^3 and an imaging speed of 250 kHz [280]. It demonstrated an SNR of 98 dB measured at a depth of 100 μm, with an SNR roll-off of 10 dB over 1.4 mm. Similar resolutions were achieved by Münter et al. [201], who performed dOCT with a SD-PS-OCT system that provided an A-scan rate of 600 kHz, but the system's high acquisition speed limited its sensitivity to 51 dB at a depth of 80 μm. Although an experimental SS-PS-OCT system demonstrated A-scan rates as high as 20 MHz [202], the FDML light source limits the axial resolution to greater than 5 μm. Furthermore, the high NAs employed to achieve subcellular lateral resolutions in PS-OCT systems significantly reduce the DOF, unlike the parallel beams employed in FF-OCT systems. Scholler et al. [234] performed dOCT with a TD-FF-OCT system that demonstrated subcellular axial and lateral resolutions throughout the imaging volume. However, to maintain sufficient SNR, they used a camera frame rate of 100 Hz and it required several minutes to image the total volume with a FOV of 320 $\times$ 320 μm^2 over a 10 μm depth.

Another system characteristic that influences dOCT analysis is SNR. Methods that directly measure variation in the intensity of the OCT signal, such as the motility coefficient, autocorrelation, intensity variance, LIV, MAV, and OCDS described in section 2.5.4, and the running standard deviation described in section 2.5.5, require the signal to be sufficiently resolved from noise. For example, El-Sadek et al. [187] used a SS-PS-OCT system with an SNR of 104 dB to successfully resolve the necrotic spheroid core with both LIV and OCDS, despite axial and lateral resolutions of 14 μm and 19 μm. Similarly, Oldenburg et al. [180] developed the motility coefficient and autocorrelation methods using a SD-PS-OCT system that demonstrated an SNR of 108 dB [281, 272]. In contrast, methods that analyze the PSD benefit from filtering via Fourier transform; this is especially true in the case of frequency banding, which additionally integrates over the spectrum to smooth out noise. Compared to FD-OCT systems, FF-OCT suffers from an approximate 15 dB loss in sensitivity [282]. Notably, the running standard deviation FF-dOCT method was only analyzed qualitatively [222], and later implementations incorporated PSD-calculated

metrcs to form HSB images [234, 223, 235, 232]. FF-dOCT also suffers from the limited use of photons scattered from the enface place and a high sensitivity to sample movement in the axial plane, to which dOCT is especially sensitive. Still, because each enface image is acquired repeatedly with a stationary system and sample, FF-dOCT offers improved phase stability compared to PS-dOCT [250]. That said, PS-OCT systems acquire all axial pixels simultaneously, enabling direct retrieval of the optical phase [177].

One method to increase imaging speed while maintaining depth resolved images is with LF-OCT, which benefits both from scattered photons throughout the entire depth and improved stability due to the reduced mechanical motion from scanning in only one lateral direction. LF-OCT systems have demonstrated equivalent A-scan rates of several MHz with sufficient SNR for resolving cells [204, 205, 206, 207, 208, 209]. Our group developed the first line-field dOCT (LF-dOCT) platform [283], which is described in detail in the longitudinal study in chapter 4. We employed the frequency banding method described in section 2.5.4. Prior to our recent work analyzing tumor spheroids dOCT [283], to the best of our knowledge the frequency banding method has been used exclusively with *ex vivo* samples [273, 249, 258, 254, 250, 201, 251]. While another student, Keyu Chen, designed and built the LF-OCT system, I applied the developed technology to image prostate tumor spheroids in the longitudinal and radiation studies described in chapters 4 and 5 of this thesis, respectively. I made significant contributions to the investigations, including:

- Seeding and culturing the prostate tumor spheroids.
- Developing the protocol to fix spheroids with 4% formaldehyde within their gel.
- Developing the protocol to irradiate spheroids with a clinical linear accelerator.
- Transporting and irradiating spheroids.
- Performing FM, AB proliferation assay, and clonogenic assay.
- Developing, simulating, and interpreting the 3D agent-based model.
- Modifying the spheroid culturing technique to minimize reflection artifacts during OCT imaging.
- Modifying the RGB frequency banding method to employ only two color channels.
- Developing the algorithm for volumetric spheroid masking.
- Developing the algorithms for all numerical analyses of OCT images including the spheroid volume, internal gap volume, external surface area, and sphericity.

- Developing the algorithms for all numerical dOCT analyses including the raw dynamic signal and its normalized counterpart that uses formaldehyde-fixed spheroids for background subtraction.
- Collaborating with Keyu Chen to develop the algorithm for dOCT image generation.
- Interpreting all experimental results.
- Performing all statistical analysis.

In particular, my work uniquely performed quantitative analysis of the dynamic signal measured by RGB frequency banding in comparison with an established biological method, AB proliferation assay. For ease of comparison with conventional measurement of tumor spheroids with FM and clonogenic assay, I adapted the method to consider only two color channels: a green and red channel that measure fast and slow dynamics for direct association with live and dead cell fluorescent staining by green calcein-AM and red PI, respectively. Previous work that employed the method was limited to qualitative comparison with fluorescence imaging [249] and histological staining [258, 254, 250, 251].

Chapter 3

Cellular Potts model (CPM)

Conceptually, the CPM was first introduced in 1992 by Graner and Glazier [284] as an extension of the large-Q Potts model [285], which in turn is a generalization of the Ising model of spins that are arranged in a lattice and subject to nearest-neighbor interactions [286, 287]. Popularized by Hogeweg [288] for the study of morphogenesis, the CPM is also called the Glazier-Graner-Hogeweg (GGH) model and provides a modeling framework more so than it represents a single model [289]. As a consequence of its origin in statistical physics, the foundation of the CPM is a 2D or 3D lattice containing cells subject to a Hamiltonian, which describes all interactions in the model in terms of energy. The CPM is an example of ABM, as cells behave as discrete, individual agents. Its first application was energetic modeling of cell sorting via differential intercellular adhesion [284, 290], but its use has since expanded to describe many phenomena of interest to cancer including CSCs [291], cell migration [292, 293], angiogensis [294, 295, 296], vasculogenesis [297], tumor vascularization [298], and chemotherapy treatment [299]. This chapter briefly reviews the theoretical basis of the CPM in its mathematical formalism, as well as the specific implementation of tumor growth that was developed in this thesis.

3.1 CPM theory

The mathematical formalism of the CPM described below arises directly from the Ising model description of a spin σ located at the i-th position in a 2D or 3D lattice that is comprised of N positions or voxels [286, 287].

3.1.1 Lattice

Rather than spins, the lattice of the CPM is occupied by cells that each behave as an individual agent. Each unique cell is composed of multiple voxels that are assigned the same cell index σ. The surrounding environment or *Medium* is described by $\sigma = 0$, so in a simulation that contains n cells, σ belongs to the set $\{0, 1, ..., n\}$. The volume v of the cell with index σ^* is given in voxels by:

$$v(\sigma^*) = \sum_{i=0}^{N} \delta(\sigma_i, \sigma^*) \tag{3.1}$$

where σ_i denotes the cell index at the i-th position in the lattice and δ denotes the Dirac delta function. Similarly, the surface area s of cell σ^* is calculated in pixels using the interfaces along adjacent cells as follows:

$$s(\sigma^*) = \frac{1}{2} \sum_{i,j \text{ neighbors}} \delta(\sigma_i, \sigma^*) \times [1 - \delta(\sigma_i, \sigma_j)] \tag{3.2}$$

While the cells are internally structureless, the resolution provided by spanning multiple lattice sites enables simulated cell behavior that mimics the membrane fluctuations and pseudopod protrusions that have been observed in biological cells [147]. Cells are grouped into biological cell types τ that have unique type-based attributes and behaviors, allowing for specific categorical phenotypes and morphologies. There are few other cell-based methods for investigating interactions of heterogeneous and non-isotropic cell populations with phenotypic morphologies, including the vertex model [300] and the sub-cellular element model [301].

3.1.2 Multi-scale hybrid modeling

Despite the lack of internal structure, the flexible ABM approach enables intracellular behavior to be implemented via ODEs that describe intrinsic cellular processes, generally arising from kinetic models of the intracellular biochemistry [288, 302, 303, 304, 305]. On the other end of the spatial scale, the CPM is often used to investigate the non-intuitive emergence of tissue-level phenomena from the collective behavior of individual cells [146]. As such, the CPM is considered a multi-scale model due to its combination of multiple spatial and temporal scales [147]. In addition to discrete cells that occupy the lattice, chemical fields governed by continuous PDEs may be discretized to the lattice to describe growth factors [306], signaling molecules [298], extracellular materials [307],

nutrients [306, 298], drugs [299], or any other fluid or chemical of interest. In this way, the CPM also provides a hybrid-modeling framework.

3.1.3 Modified Metropolis algorithm

The spatio-temporal behavior of each chemical field is dictated by its PDE. In contrast, the discrete cellular arrangement in the lattice evolves in time through a stochastic modified Metropolis algorithm [308], which is a Markov chain Monte Carlo method that performs "copy attempts" using the Hamiltonian to represent the effective energy of the lattice (Fig. 3.1). At the start of every copy attempt, a lattice site i and a neighboring site j are chosen at random with uniform distribution. The cell index σ_j of the neighboring lattice site j is copied into position i, then the effective energy before the copy attempt $\mathcal{H}$ is compared with the new effective energy $\mathcal{H}(\sigma_i = \sigma_j)$. A copy attempt is energetically favorable or unfavorable if the change in energy $\Delta\mathcal{H} = \mathcal{H}(\sigma_i = \sigma_j) - \mathcal{H}$ is negative or positive, respectively. Energetically favorable copy attempts are accepted, whereas energetically unfavorable copy attempts are accepted with a Boltzmann probability [309] as follows:

$$P(\sigma_i \to \sigma_j) = \begin{cases} 1 & \Delta\mathcal{H} \leq 0 \\ \exp(\Delta\mathcal{H}/T) & \Delta\mathcal{H} > 0 \end{cases} \tag{3.3}$$

Another remanent of its origin in statistical physics, T is called the temperature of the model, although here it has units of simulated energy. T is also called the amplitude of cell-membrane fluctuations or the cell motility because each successful copy attempt changes a single lattice site along the border of one cell – or two cells if the interface falls along another cell border rather than the medium. Periodic boundary conditions are often imposed to the lattice, and may be thought to map the simulation space onto a torus. That is, cells that fluctuate beyond the edge of the cell lattice appear to enter the lattice on the opposite edge. However, fixed boundary conditions of a confined environment can also be imposed. One Monte Carlo step (MCS) has passed when N copy attempts have been performed on a lattice of N voxels. As such, the MCS demarcates the passage of simulated time.

Note that the ratio $\Delta\mathcal{H}/T$ in Eq. 3.3 controls how frequently cells rearrange. Large $\Delta\mathcal{H}/T$ results in rigid, barely motile cells whereas small $\Delta\mathcal{H}/T$ results in high cell motility and rearrangement. Consequently, simulations that impose a higher temperature T parameter observe higher rates of cellular rearrangement. The nature of those rearrangements, however, is directed by the form of the Hamiltonian $\mathcal{H}$, which embodies the physical and phenomenological forces enacted on the cells.

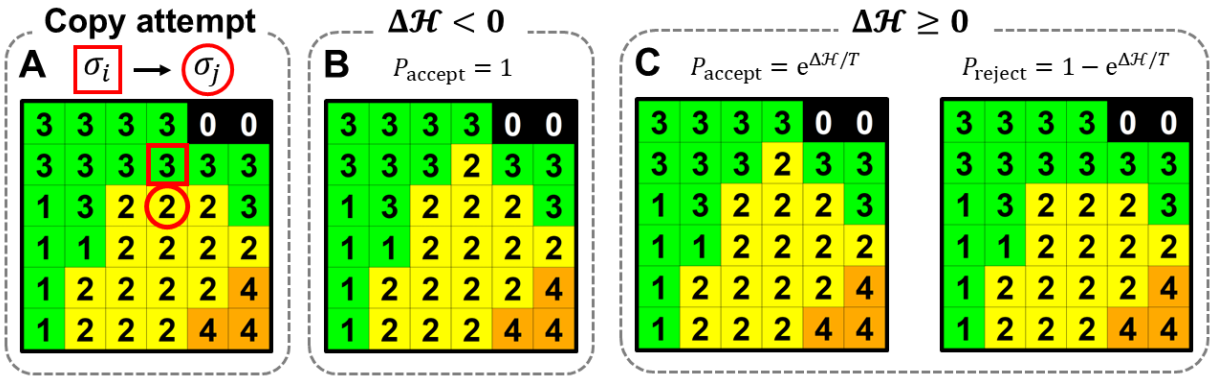


Figure 3.1: A CPM lattice with cell type τ and index σ indicated by color and number, respectively. The depicted lattice has three cell types (green, yellow, and orange) in addition to the black *Medium*, including two unique cells $\sigma = 1$ and $\sigma = 3$ of different volumes but the same green type. A) The modified Metropolis algorithm performs "copy attempts" by randomly selecting a lattice site i (in red square) and a neighboring site j (in red circle), and proposing that the cell index σ at i becomes that of j. B) The change is accepted if the change in effective energy $\Delta\mathcal{H}$ is reduced. C) Otherwise, the change is accepted with probability $\exp(\Delta\mathcal{H}/T)$.

3.1.4 Hamiltonian

The Hamiltonian is the effective energy of the simulation space through which all rules that dictate cellular characteristics and intercellular interactions are ultimately manifested via regulation of cell surface fluctuations. Common components of the CPM Hamiltonian that are relevant to this thesis include contributions from intercellular contact adhesion, cell size, and external forces like gravity:

$$\mathcal{H} = \mathcal{H}_a + \mathcal{H}_v + \mathcal{H}_s + \mathcal{H}_g \tag{3.4}$$

The following sections describe the mathematical form of each of these contributions.

Contact adhesion

The contact adhesion term $\mathcal{H}_a$ describes the energy associated with cell-cell interfaces of adjacent cells through a matrix J that is indexed by cell type τ as follows:

$$\mathcal{H}_a = \sum_{i,j \text{ neighbors}} J\{\tau(\sigma_i), \tau(\sigma_j)\} \times [1 - \delta(\sigma_i, \sigma_j)] \tag{3.5}$$

Thus, the effective energy contribution from contact adhesion sums the cell type specific contact energy between all pairs of neighboring lattice sites i and j that belong to different cells. Contact adhesion models surface tension because $J\{\tau(\sigma_i), \tau(\sigma_j)\}$ is generally positive, in which case the Metropolis algorithm (Eq. 3.3) minimizes the surface area of cells that is shared with other cells or the medium [290].

Cell size

The size of cells is typically determined by assigning each cell a target volume V_t and imposing the following:

$$\mathcal{H}_v = \sum_{\sigma=0}^{n} \lambda_v(\sigma_i) \times [v(\sigma_i) - V_t(\sigma_i)]^2 \tag{3.6}$$

where the cell volume v adheres to its target more strictly with increasing λ_v. Similarly, the cell surface area s is encouraged to achieve a target surface area S_t with strictness λ_s as follows:

$$\mathcal{H}_s = \sum_{\sigma=0}^{n} \lambda_s(\sigma_i) \times [s(\sigma_i) - S_t(\sigma_i)]^2 \tag{3.7}$$

Gravity

Gravity is implemented as follows:

$$\mathcal{H}_g = \sum_{i=0}^{N} \lambda_g(z_{\max} - z_i) \times [1 - \delta(\sigma_i, 0)] \tag{3.8}$$

where z_i is the distance along the z-axis of position i with maximum distance $z_{\max}$ and λ_g mediates the strength of the gravitational field. Notice that only cells experience the gravitational force, with the *Medium* excluded from the calculation.

3.1.5 Utility

ABM can be broadly categorized into two paradigms: mechanistic models and phenomenological models [147]. Mechanistic models focus on rules representative of hypothesized

mechanisms that have been abstracted from biological processes for verification, falsification, or proof-of-principle. The conclusions drawn from mechanistic models are limited by the simplifying assumptions made in the process of abstracting the mechanism of interest. In contrast, models that are phenomenological prioritize empirical or statistical agreement with observed biological behavior over the exact modeling of the relevant mechanism. If the experimental agreement is sound, phenomenological models allow theoretical exploration of conditions similar to those of experiment and enable measured biological data to be described, visualized, summarized, interpolated, or potentially even extrapolated. Phenomenological models can also have utility in guiding future experiments toward interesting behavior, although their predictions are only credible with convincing validation to observation.

Other than the study of cellular phenomena that arise directly from the size, shape, or polarity of cells [303, 310, 311, 304], the exclusive action of the Metropolis algorithm through the shape and fluctuation of the cell membrane described in Section 3.1.3 makes the CPM inherently phenomenological. Consequently, the CPM has ambiguous explanatory power but retains utility in describing and visualizing biological processes in many contexts. Nonetheless, this utility requires model behavior to match experiments [312], which is achieved by parameter tuning. Since the parameters interact with each other in complex non-intuitive ways, parameter fitting a CPM is not a straightforward task [147].

3.1.6 Limitations

Lowengrub et al. [109] described that in general, discrete models have parameters that are not easily informed by experimental measurement. They acquiesced that while discrete techniques are more flexible and detailed at the cellular level, they are also limited by computational burden that increases with the number of simulated cells and ultimately restricts the spatial and temporal scales. Discrete methods have been highlighted for the exploration of mechanistic biological hypotheses and resultant emerging behavior [122]. However, the flexibility in cellular morphology in CPM is provided at the cost of convoluted control over cellular behavior and intercellular interactions that reduces its mechanistic utility. Moreover, the nature of the modified Metropolis algorithm complicates its temporal calibration to physical reality, altough it has been argued that in biologically-meaningful situations, simulated and experimental time are proportional [313]. Voss [147] derived with rigorous mathematical detail numerous limitations of the CPM through comparison with the multi-type voter model [314], which predicts that cells consecutively die out in the long-time limit. This is due to the modification to the Metropolis algorithm. The standard Metropolis algorithm is a Markov chain Monte Carlo method that, after starting

from an arbitrary initial configuration, arrives at the equilibrium model that corresponds to the Hamiltonian $\mathcal{H}$ after a sufficiently long period of time [315]. However, regardless of the form of $\mathcal{H}$, long-time behavior of the modified Metropolis algorithm is rather to become trapped in an absorbing state [147]. This is related to the non-zero probability that a cell composed of a single lattice position disappears in a copy attempt, but the probability of reappearance is zero. In their introduction of the method, Glazier and Graner [290] acknowledged that there is energy loss due to cell elimination. Therefore, the initial time period is of interest in CPMs, as the long term evolution tends not towards energy minimization, but towards consecutive cell death.

Every tool has its strengths and limitations. Experimental *in vitro* methods benefit from comparison with complementary techniques, and similarly, complementary *in silico* methods operating at different levels of complexity may help validate conclusions drawn from the CPM. In particular, mechanistic CPM investigation of phenomena that do not emphasize cell size and shape could benefit from comparison with continuous tissue-scale methods [316] or other discrete cell-based techniques with lower resolution, such as interacting particle systems [317] or discrete random walk models [318].

3.2 CPM implementation

In this thesis, three CPMs were developed and implemented with the CompuCell3D (CC3D) platform [313]. The first model developed for the thesis models prostate tumor spheroid growth via the 3D Petri Dish method described in Section 1.2. It directly employs the Hamiltonian given by Eq. 3.4.

In addition to the *Medium* and *Gel* cell types that describe the culture medium and agarose gel, respectively, there are three tumor cell types: *Normoxic*, *Hypoxic*, and *Necrotic*. These tumor cell types are updated every 10 MCS using the partial pressure of oxygen P_O at the center of mass (COM) of the cell i_{COM}. A tumour cell is *Normoxic*, *Hypoxic*, or *Necrotic* if its partial pressure of oxygen is respectively above, between, or below the hypoxic and necrotic oxygen thresholds of 5 mmHg and 1 mmHg. While transitions between the *Normoxic* and *Hypoxic* cell types are reversible, conversion to the *Necrotic* type indicates irreversible cell death due by starvation.

Oxygen is maintained at a constant partial pressure in *Medium* and modeled with a reaction-diffusion PDE as follows:

$$\frac{\partial P_O(i,t)}{\partial t} = D_O \nabla^2 P_O(i,t) - f_{\text{uptake}}(i,t) \times \delta(\tau(\sigma_i), \tau_{\text{tum}}) \tag{3.9}$$

where the diffusion coefficient D_O is 3440 pixel^2/MCS and roughly corresponds to 1200 μm^2/s, which is slightly more than half the diffusion constant of oxygen in water [298] under the assumption that the physical size of each simulated voxel is (5 μm)^3 or 125 μm^3. The function f_{uptake} describes the consumption of oxygen per MCS within living *Normoxic* and *Hypoxic* tumor cell types, denoted collectively as τ_{tum}, through the following piecewise linear approximation to a Michaelis-Menten saturation curve:

$$f_{\text{uptake}}(i,t) = \begin{cases} \alpha P_O(i,t) & P_O(i,t) < P_{\text{O, max}} \\ \alpha P_{\text{O, max}} & P_O(i,t) \geq P_{\text{O, max}} \end{cases} \tag{3.10}$$

Here, α is the fraction of the local oxygen that is consumed until saturation at the maximum partial pressure $P_{\text{O, max}}$.

In conjunction with consumption, the partial pressure of oxygen at the COM of each living cell i_{COM} also increases its target volume V_t via the following Michaelis-Menten saturation curve:

$$\frac{dV_t}{dt} = \frac{V_{\text{max}} \times P_O(i_{\text{COM}}, t)}{K_V + P_O(i_{\text{COM}}, t)} \tag{3.11}$$

where V_{max} and K_V denote the maximum growth rate and half saturation oxygenation, respectively. Similarly, the cell's target surface area S_t grows with maximum growth rate S_{max} and half saturation oxygenation K_S as follows:

$$\frac{dS_t}{dt} = \frac{S_{\text{max}} \times P_O(i_{\text{COM}}, t)}{K_S + P_O(i_{\text{COM}}, t)} \tag{3.12}$$

Once *Normoxic* and *Hypoxic* cells have achieved a sufficient volume called the mitotic volume, they undergo mitosis and split along a random direction into two identical cells that are assigned post-mitotic target volumes and surface areas.

The simulation parameters were determined phenomenologically by comparison with quantitative measurement of the size and shape of the prostate tumor spheroid and its containing well inside the agarose gel via volumetric OCT imaging (Fig. 3.2). These measurements also determined the temporal calibration of 1200 MCS to 24 hours, as we assume simulated and physical time are proportional [313]. To replicate the gaps observed throughout the spheroid in accordance with the CPM contact adhesion implementation, a phenomenological *Gap* cell type was developed to mimic pockets of culture medium trapped inside the spheroid.

The CPM of prostate tumor spheroid growth described above was modified to implement radiation and DTX chemotherapy treatments, as described in Chapters 5 and 6,

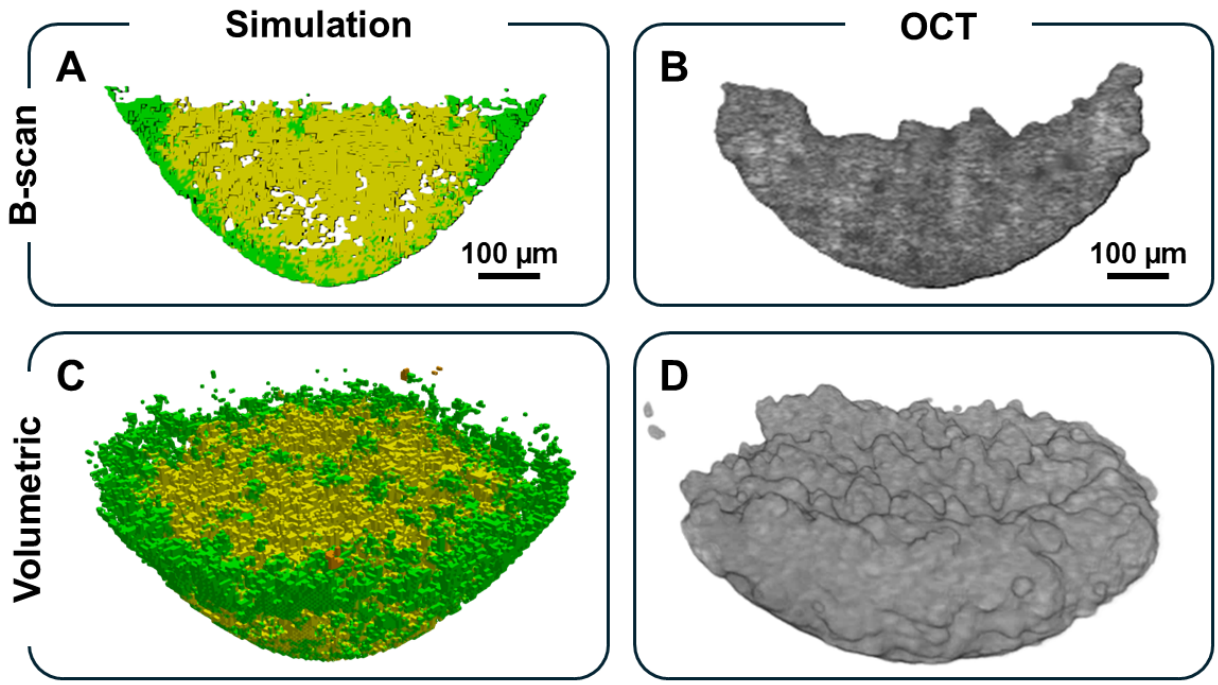


Figure 3.2: The simulation parameters were determined phenomenologically by comparing morphology with OCT imaging and masking of cultured prostate tumor spheroids. Cross-section B-scan (top row) and volumetric (bottom row) visualizations of a spheroid 48 hours after seeding generated by simulation (left column) and OCT (right column), with surrounding culture medium and gel removed. Scale bar: 100 μm.

respectively. The full code of the CPMs modeling prostate tumor spheroid growth, radiation treatment, and DTX treatment can be found in Appendices A, B, and C respectively, and on Github at https://github.com/skswanso/CPM.git.

Chapter 4

Longitudinal investigation of prostate tumor spheroid proliferation with dynamic line-field optical coherence tomography

4.1 Introduction

Prostate cancer is the most commonly diagnosed cancer among North American men [1, 2]. The use of *in vitro* cell culture has been invaluable in the investigation of tumor cell biology and cancer progression [79]. Historically, tumors were thought to be composed of a homogeneous population of cancer cells [78], which was a perspective well-suited to the conventional practice of culturing cells *in vitro* as 2D monolayers on flat, rigid surfaces. In a 2D monolayer, each cell has equal and unrestricted access to oxygen, nutrients, and signaling molecules available in the culture medium. However, cancer cell behavior is influenced by its surrounding environment [80], including nearby cells [81], signaling molecules [78], and structural features such as the extracellular matrix (ECM) [84] and cell adhesion molecules like integrin [83]. Although 2D cell culture methods are efficient, scalable, and compatible with many biological assays, cells grown as monolayers lack physiologically relevant cell-cell and cell-environment interactions [85]. These interactions critically influence cellular signaling, proliferation, and gene and protein expression [86, 87]. In recent decades, it has been demonstrated that culturing cancer cells as small, 3D aggregates, known as tumor spheroids, provides improved physiological relevance [319, 96]. The increased cell-

to-cell contact and spatial organization within *in vitro* tumor spheroids promote cellular morphologies and characteristics that more closely resemble those found in *in vivo* tumors [320, 321]. Unlike the homogeneous environment in monolayer cultures, diffusion-limited nutrient distribution in tumor spheroids gives rise to heterogeneous cell populations: proliferative cells form the outer layer in contact with the culture medium, whereas the inner core accumulates metabolic waste and contains necrotic and apoptotic cells [99].

Nevertheless, the 3D nature of tumor spheroids challenges conventional biological tools, which typically destroy spatial information either by averaging signals across a population of cells or by requiring disaggregation of cellular structures into cell suspensions. For example, a common method of assessing cellular activity is the non-toxic Alamar Blue (AB) proliferation assay, which measures cellular metabolism through the reduction of the blue, non-fluorescent dye resazurin to the pink, highly fluorescent resorufin [157]. However, the fluorescence measured in this assay directly quantifies the total amount of resorufin produced within the spheroid, providing only an average metric [164]. Another widely used method for spheroid assessment is fluorescence microscopy (FM). Although this modality preserves spatial information and does not require spheroid disaggregation, fluorescence measurements remain qualitative rather than quantitative. Additionally, introducing fluorophores into the sample is invasive and precludes true longitudinal investigation.

Optical coherence tomography (OCT) is a non-invasive optical imaging modality that relies on low-coherence interferometry to generate volumetric images of biological samples with micrometer-scale resolution [193, 322]. Previous studies have employed OCT to provide insights into the 3D structure of tumor spheroids [323, 324, 186, 325, 326]. The application of OCT has expanded beyond static morphological imaging to dynamic OCT (dOCT), which analyzes temporal fluctuations in repeated OCT acquisition [192]. Unlike contrast derived from exogenous fluorophores or stains, the contrast in dOCT images is generated non-invasively by quantitative statistical analysis of the intensity fluctuations of the optical beam registered at each pixel of the OCT detector. dOCT has enhanced investigations of various 3D cell culture models, including tumor spheroids [180, 226, 244, 187, 240, 241, 242, 243, 272, 245, 283, 246], organoids [237, 238, 239, 234, 235, 236], paper-based 3D culture [247], and 3D scaffolds [188]. Furthermore, dOCT has also been utilized for cancer diagnosis in human biopsy samples from lung [261], breast [260], and skin [262] tissues.

While OCT was initially used to study particle dynamics (Brownian motion) in microsphere suspensions [327, 328], the idea of using temporal fluctuations in the OCT signal generated by light scattered from single cells to study cell apoptosis was first proposed in 2010 by Van der Meer et al. [230]. Since then, numerous dOCT approaches have been developed for the different designs of high speed OCT technology: spectral domain OCT

(SD-OCT) [180, 237, 257, 250, 201, 251, 244, 254, 258, 245, 246], swept source OCT (SS-OCT) [187, 240, 241, 242, 276], full field OCT (FF-OCT) [222, 226, 273, 249, 234, 223, 235, 232, 228, 233], and line-field OCT (LF-OCT) [283]. Furthermore, various dOCT methods for analysis and interpretation of the OCT interferogram itself have been employed, including a standard-deviation metric termed motility [180, 237], running standard deviation [222], autocorrelation [237, 226, 257], OCT correlation decay speed (OCDS) [187], intensity variance [244], logarithmic intensity variance (LIV) [187] and its modifications [276], and median adjusted variance (MAV) [245]. Other methods have characterized the spectrum of the OCT interferogram by fitting the power spectral density (PSD) to an inverse-power-law model [237], integrating it over discrete frequency bands to generate red-green-blue (RGB) images [273, 249, 258, 254, 250, 201, 251, 283], or computing the mean frequency and inverse frequency bandwidth to generate hue-saturation-brightness (HSB) images [234, 223, 235, 232, 228, 233, 246]. Many dOCT assessments of 3D cell cultures have been qualitatively compared with established biological techniques, including FM [187, 240, 241, 242], immunohistochemistry [234], TUNEL assay [235], histological staining [236], and luciferase-based ATP luminescence assay and live/dead cell counting via nuclear staining [188]. However, direct and quantitative validation of the dOCT measurements against standard biological methods has been limited and exclusively performed with point-scanning (PSc) OCT. These studies analyzed fluctuations in the OCT intensity signal itself through motility and the inverse-power-law [238, 247] or MAV [245], or analyzed its spectrum via the HSB method [246] or the mean frequency alone [256]. Compared to FF-OCT systems, PSc-OCT offers an approximate 15 dB sensitivity gain [282] and faster dOCT volumetric acquisition [250], which is required for the investigation of 3D cell culture. Nevertheless, extended data acquisition times have limited previous studies to cross-sectional imaging or temporally sparse volumetric data collection. To bridge this gap, we recently developed a high-speed spectral-domain LF-OCT system for volumetric dOCT imaging[283]. We adapted the frequency banding technique [273], which to the best of our knowledge, has never been quantitatively validated to an established biological method.

In this study, we employed the LF-dOCT technology and analytical method to longitudinally investigate qualitative and quantitative morphological and dynamic changes in prostate tumor spheroids at the cellular level over two weeks of growth.

4.2 Methods

4.2.1 OCT setup

In this study, we employed a high-speed spectral-domain LF-dOCT system [283] for both morphological and dynamic imaging of tumor spheroids. The system utilizes a broadband superluminescent diode (SLD) light source (cBLMD-T-850-HP, Superlum, Ireland) with a central wavelength of 842 nm and a full-width-at-half-maximum (FWHM) spectral bandwidth of 179 nm, resulting in an axial OCT resolution of 2.6 μm in air, equivalent to 1.9 µm in biological tissue assuming an average refractive index of 1.38. A high-speed area CMOS camera (FASTCAM NOVA S9, Photron) is used at the detection end of the LF-OCT system to acquire B-scans at a maximum rate of 2,500 fps. Utilizing 1024 camera pixels in the spectral direction, the system achieves an axial scanning range of approximately 1 mm. With a microscope objective (M Plan APO, Mitutoyo, Japan) of 5x magnification power in the LF-OCT imaging probe, the system's lateral resolution is 6.4 μm in air. For an optical power of 3.5 mW incident on the imaged object and an imaging rate of 2,000 fps, the system's sensitivity was approximately 93 dB. A detailed description of the system's design and performance can be found in [283].

4.2.2 Cell culture methods

Spheroid culture

PC3 cells were cultured in RPMI 1640 (Sigma-Aldrich, USA) supplemented with 10% fetal bovine serum (Thermo Fisher Scientific, USA) and 1% penicillin (Thermo Fisher Scientific, USA). Cells were maintained at 37°C with 5% CO_2 in a humidified atmosphere. Prostate tumor spheroids were created and cultured in a 3D Petri Dish (MicroTissues Inc., USA) made of 2% agarose gel and containing a 9×9 array of wells that were each seeded with approximately 1,000 cells (Fig. 4.1A). Here, one 3D Petri Dish is referred to as a gel. Culture medium in each gel was exchanged every other day.

Pseudo-longitudinal protocol

OCT imaging of the cell seeding process began immediately after the cell suspension was introduced into the well. Without moving the imaging stage of the LF-OCT system, images were acquired regularly for two hours as cells settled to the bottom of the well. Longitudinal

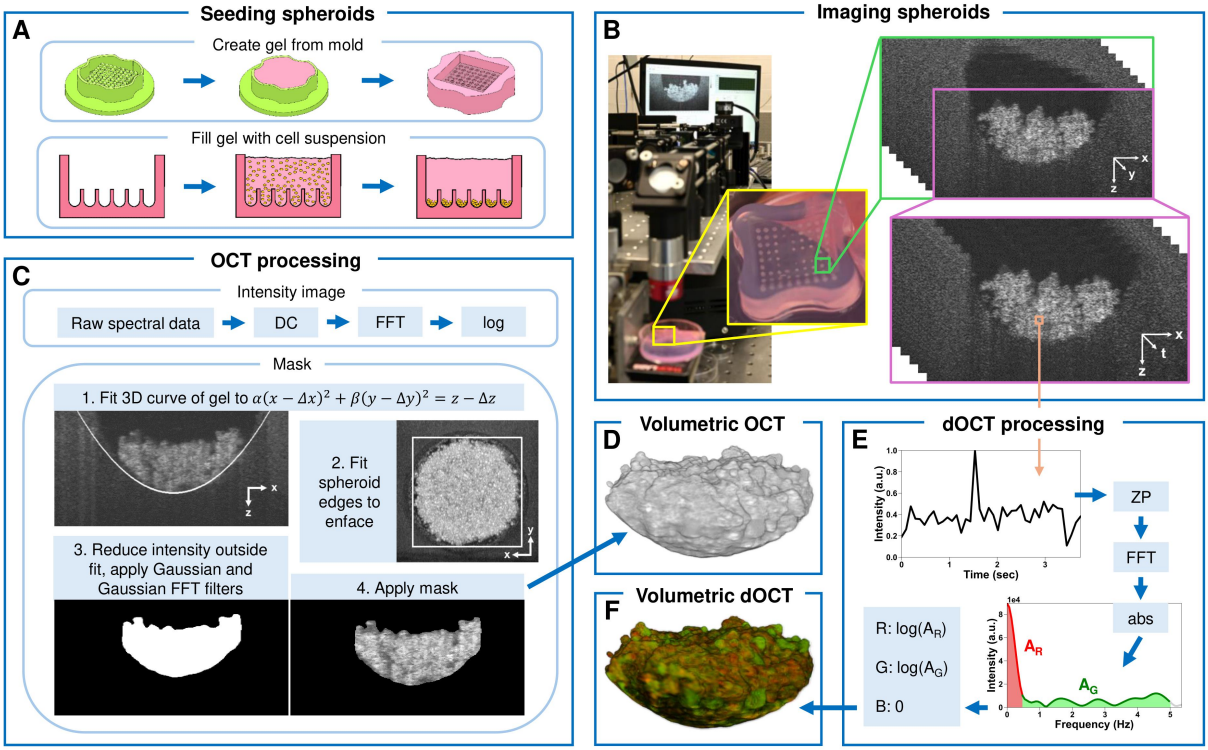


Figure 4.1: Schematic diagram of setup and processing. (A) Seeding spheroids. Agarose gels, depicted in pink, that each contained an array of wells were filled with a suspension of cells, shown in yellow, to form prostate tumor spheroids at the bottom of each well. (B) Imaging spheroids. Spectral-domain LF-dOCT system with glass Petri dish containing a gel of spheroids. The yellow inset magnifies the gel to show spheroids in the wells. The green inset displays a single spheroid in its well with a volumetric collection of B-scans. The purple inset displays the collection of B-scans acquired at one location over 4 seconds of recording time. (C) OCT processing. Intensity images were used to generate masks by reducing intensity below 3D curve of well inside gel (Eq. 4.1), beyond lateral edges of spheroid, and with Gaussian and Gaussian FFT filters. (D) Volumetric OCT image of live spheroid generated from mask. (E) dOCT processing at each voxel location by FFT in time direction. Integration of spectrum was performed along two frequency bands: red over 0-0.5 Hz and green over 0.5-5 Hz. (F) Volumetric dOCT image of live spheroid. DC: dispersion compensation; FFT: fast Fourier transform; log: base 10 logarithm; ZP: zero-padding; abs: absolute value; A_R: area under red frequency band; A_G: area under green frequency band.

dOCT image acquisition of spheroid growth began 24 hours after seeding and was repeated every 24 hours for two weeks. During each imaging session, 15 live tumor spheroids were imaged, then fixed with 4% formaldehyde (Thermo Fisher Scientific, USA) in PBS (Wisent Inc., Canada) for 1 hour to remove metabolic activity and subsequently maintained at 4°C for ∼24 hours to reduce motion induced during the fixing process. Afterward, 15 of the spheroids fixed during the previous day's imaging session were also imaged. During imaging, spheroids were kept at 21°C without CO_2 supply. As spheroids were sacrificed by fixation after each imaging session, 42 gels were seeded at the beginning of the experiment, with three gels allocated for each of the 14 days of imaging.

Alamar Blue proliferation assay

Average cellular proliferation within the tumor spheroids was measured via AB proliferation assay. At each measurement time, culture medium was removed from three gels of spheroids and replaced with 34.5 μL of AB (Sigma-Aldrich, USA) and 156 μL of RPMI to achieve 5% concentration throughout each 500 μL gel. Samples were then incubated for 3 hours at 37°C with 5% CO_2 in a humidified atmosphere before intensity was recorded using a BioTek Synergy H1 microplate reader at 570 nm. Gels containing no cells were treated identically and measured as background. The average background intensity was subtracted from the measurement of gels containing spheroids. After background subtraction, AB absorbance was normalized relative to the absorbance measured on day 1.

Live/dead fluorescence microscopy

FM was used to spatially assess cell death within spheroids using a Live/Dead Cell Viability assay (Sigma-Aldrich, USA) comprising two fluorophores. The first, calcein acetoxymethyl (calcein-AM), is a cell-permeant dye that identifies live cells through conversion to fluorescent green calcein by intracellular processes [155]. The second, propidium iodide (PI), is not permeant to live cells and thus instead identifies dead cells by fluorescing red upon binding with DNA or RNA [152]. Culture medium was removed from each gel and replaced with a solution of 0.2875 μL calcein-AM, 1.15 μL PI, 95 μL RPMI, and 95 μL PBS. Gels were incubated for one hour at 37°C with 5% CO_2 in a humidified atmosphere before transfer to cover slip-bottomed Petri dishes that were placed on the stage of a Zeiss Axio Observer widefield microscope. The microscope was operated by ZEN2 Blue Edition and equipped with an Axiocam 506 mono camera. Fluorescent images were acquired with a FOV of 1.25 mm by 1 mm and a lateral resolution of 0.908 μm using a Plan-Apochromat 63/1.4 Oil

Ph3 M27 objective (Carl Zeiss Microscopy-LLC, NY, USA). Temperature was maintained at 37°C throughout imaging using an incubating plate (PECON, Erbach, Germany).

4.2.3 OCT Image acquisition

Both morphological and dynamic OCT images were acquired with the LF-dOCT system at a B-scan rate of 2,000 fps. Each B-scan frame consisted of 400 A-scans, and one 3D volume comprised 400 B-scans. For cell seeding, only morphological OCT data were acquired. At each time point, 5 repeated volumes were acquired consecutively and averaged to improve image contrast. For longitudinal dynamic imaging, each dOCT volume was divided into four sub-volumes, with 40 repetitions per sub-volume, corresponding to approximately four seconds of recording time, resulting in a sub-volume rate of 10.7 Hz. This sub-volume acquisition frequency was approximately half of the theoretical rate given the camera speed due to the non-linear behavior of the scanner, as described in detail in [283]. To address the scanner's non-linearity, 20 additional frames were acquired and discarded at the ends of each sub-volume and the rest time of the scanner was equal to 50% of the acquisition time for a proper reset. The total dOCT recording time for one tumor spheroid was approximately 16 seconds.

4.2.4 Image processing

Morphological

Morphological OCT images were generated using a standard OCT image reconstruction process. The resulting images were digitally dispersion-compensated and displayed on a logarithmic scale. In this work, we developed a novel masking protocol to isolate the spheroid from the surrounding gel (Fig. 4.1C). To generate the mask, the 3D curve of the well containing the spheroid within the gel was first fit to the curve:

$$\alpha(x - \Delta x)^2 + \beta(y - \Delta y)^2 = z - \Delta z \tag{4.1}$$

where x and z are respectively the lateral and depth positions in each B-scan, y is the position along the lateral scanning direction, and the location of the bottom of the well is given by (Δx, Δy, Δz). The steepness of the well in the x and y directions is given by α and β, respectively. Then, the intensity was reduced below the 3D curve of the well and beyond a manually selected lateral rectangular region of interest (ROI) on the maximum intensity projection enface, chosen to contain the spheroid. Intensity far from the center of

the spheroid was further reduced using a large Gaussian filter with FWHM comparable to the width of each B-scan. Finally, a Gaussian FFT filter with $\sigma = 25$ was applied, and a volumetric mask was generated by removing all pixels with zero intensity. In particularly dense spheroids, incident light did not penetrate well to the bottom, resulting in much lower intensity. In these cases, the masks were adjusted to include portions of the spheroid that the filters had removed.

Then, a newly developed numerical morphological analysis on the volumetric masks was carried out. The volume V_{sph} and external surface area S of each spheroid were estimated directly as the volume of non-zero pixels in the mask and the externally bounding surface area, respectively. The volume of internal gaps V_{gap} was estimated as the volume of zero intensity pixels within the external surface area. The surfaces of internal gaps were not included in the external surface area. To compare the external surface area of each spheroid to the volume it enclosed, the following sphericity metric was developed:

$$\text{Sphericity} = \frac{(V_{\text{sph}} + V_{\text{gap}})^{2/3}}{(4/9\pi)^{1/3} S} \tag{4.2}$$

Since the ratio $V^{2/3}/S$ of a solid sphere is $(4/9\pi)^{1/3}$, sphericity achieves a maximum of 1 for any sphere, regardless of whether the sphere is hollow or full.

Dynamic

The dOCT algorithm employed in this study investigates motion of cells in tumor spheroids using frequency banding [273] (Fig. 4.1E). To generate dOCT B-scans, a Hann window function was first applied to the linearly scaled OCT intensity values at each voxel location in the time dimension to reduce sidelobe artifacts and frequency leakage after FFT. Following zero-padding to improve digital resolution, FFT was applied along the time-axis at each location. For ease of comparison with live/dead FM, integrals along two frequency bands of interest were calculated: a red band of slow frequencies below 0.5 Hz and a green band of fast frequencies between 0.5 and 5 Hz. Logarithmic scaling was applied to each of the red and green dOCT channels to recalibrate the intensity distribution. To mitigate random variations in the recorded signal and background intensities, a uniform intensity baseline was achieved by subtracting the sum of the average and standard deviation of the intensity within a small region of culture medium above each spheroid in a central B-scan. Unlike in our previous work [283], to display the combined channels as a color image, each masked channel was independently normalized to those of a representative spheroid. Here, to reduce random noise and improve image quality, a Gaussian FFT filter with $\sigma_R = 90$

and $\sigma_G = 65$ to the red and green channels, respectively, was also applied, followed by the previously utilized 3×3 median filter.

In our newly developed numerical dynamic analysis, the above process was followed with the exception of normalization to a representative spheroid. A raw dynamic signal metric was developed for a given spheroid as:

$$D_{\text{raw}} = \frac{\sum_{\text{mask}} I_G}{\sum_{\text{mask}} I_R + \sum_{\text{mask}} I_G} \tag{4.3}$$

where I_R and I_G represent the red and green intensity channels, respectively, and $\sum_{\text{mask}}$ is a voxel-wise sum over the masked spheroid. To account for the lower intensity in dense spheroids, the intensity above the 3D curve of the well and within the lateral ROI was used to exclude C-scans from numerical analysis whose average intensity was lower than the volume-wide median. The average raw dynamic signal of each day's fixed spheroids was subtracted from that of the corresponding live spheroids, and the result was normalized relative to day 1 as:

$$D_{\text{norm}}(t) = \frac{D^l_{\text{raw}}(t) - D^f_{\text{raw}}(t)}{D^l_{\text{raw}}(t_1) - D^f_{\text{raw}}(t_1)} \tag{4.4}$$

Here, $D^l_{\text{raw}}(t)$ and $D^f_{\text{raw}}(t)$ are respectively the live and fixed raw dynamic signal on the day given by t, with day 1 given by t_1.

4.2.5 Statistics

All measurements are presented as averages with standard deviation. Numerical OCT and dOCT measurements that fell outside of the interquartile range were excluded.

4.3 Results

4.3.1 Morphological OCT

Figure 4.2 summarizes results from the morphological OCT imaging. The first row displays unmasked central B-scans of spheroid formation 2, 5, 10, 60, and 120 minutes after seeding. The culture medium inside the well appears dark, while the agarose gel exhibits faint speckles due to its relatively low reflectivity. Cells appear suspended in the culture medium

at 2 minutes after seeding (Fig. 4.2A) but by 5 minutes they have settled at the bottom of the well (Fig. 4.2B). Subsequently, cells self-assemble into spheroids by forming clumps that condense and gradually pull away from the gel at 10, 60, and 120 minutes after seeding (Fig. 4.2C-E).

The second and third rows of Figure 4.2 show central B-scans and corresponding volumetric OCT images of representative spheroids on days 1, 2, 6, 10, and 14, respectively. The gel and culture medium surrounding each spheroid have been masked. Despite the spheroids appearing quite flat 120 minutes after seeding (Fig. 4.2E), as they grow, their upper portions became more spherical while the bottom portion retained the parabolic shape of their containing well. On day 1, the central region of the spheroids appeared collapsed (Fig. 4.2F) whereas the periphery grew diffusely along the slope of the well (Fig. 4.2K), similar to the cellular arrangement immediately following seeding. In contrast, on day 2 the spheroids appeared less diffuse (Fig. 4.2G) and were flatter at the top (Fig. 4.2L). As the cells proliferated and the spheroids became larger, internal gaps formed within the spheroid bulk by day 6 (Fig. 4.2H), although these gaps were not visible externally (Fig. 4.2M). Despite the presence of internal gaps, attenuation due to spheroid density reduced the OCT signal from deeper regions (Fig. 4.2H). After 10 and 14 days, culture media contained many suspended cells, and volumetric images revealed individual cells along the slope of the gel (Fig. 4.2N,O).

The average spheroid volume, internal gap volume, external surface area, and sphericity of live and fixed spheroids over 14 days of growth are shown in Figure 4.3. Generally, we observed similar morphological trends in both live and fixed spheroids. The spheroid volume, internal gap volume, and external surface area of live spheroids all initially decreased following cell seeding, reached a minimum on day 4, then increased and repeated this trend twice more (Fig. 4.3A-C). However, sphericity continued to increase until it peaked on day 7 (Fig. 4.3D).

4.3.2 Dynamic OCT

Figure 4.4 compares OCT, dOCT, and FM enface images of spheroids on days 1, 2, 6, 10, and 14. The first and second rows respectively display OCT and corresponding dOCT maximum projection enface images of the same spheroids shown in Figure 4.2, while the third row shows FM enface images of separately imaged spheroids.

While the OCT enface images resolved individual cells and did not vary significantly over 14 days, the dOCT enface images resolved cells equally well while also indicating dynamic changes over time. Overall, the dOCT green channel intensity increased throughout

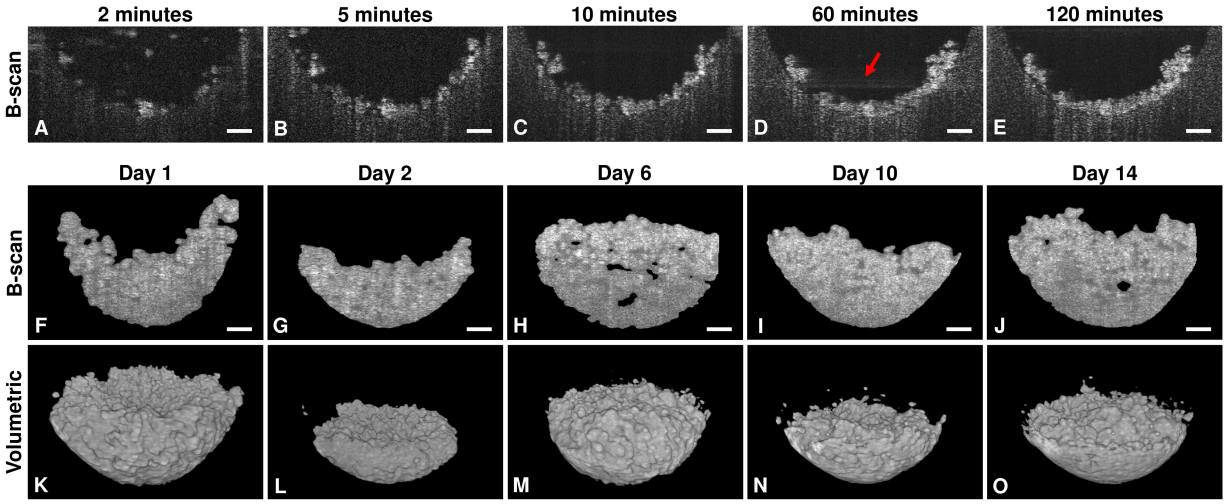


Figure 4.2: Morphological OCT images of prostate tumor spheroids. Central B-scan OCT images (A) 2, (B) 5, (C) 10, (D) 60, and (E) 120 minutes after cell seeding. Reflection artifact is labeled with red arrow. Masked central B-scan OCT images (F) 1, (G) 2, (H) 6, (I) 10, and (J) 14 days after cell seeding. Masked volumetric OCT images (M) 1, (N) 2, (O) 6, (P) 10, and (Q) 14 days after cell seeding. All scale bars are 100 μm.

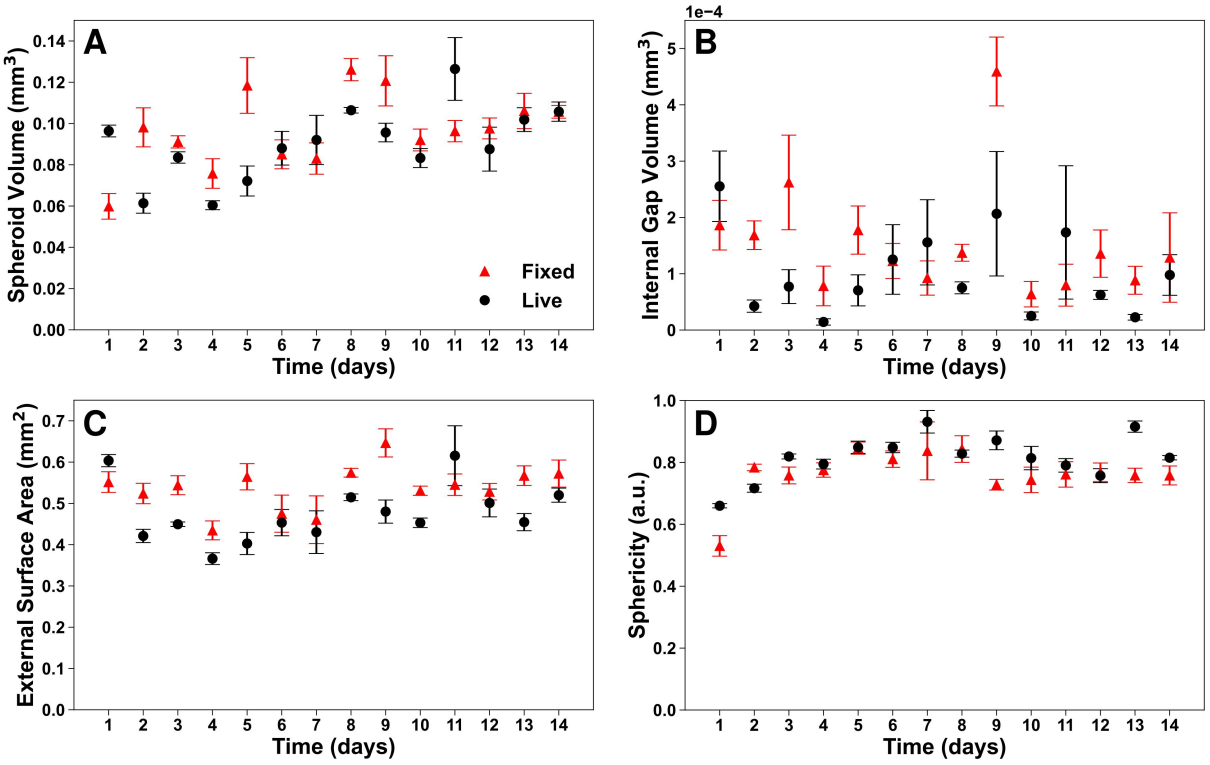


Figure 4.3: Numerical morphological analysis of masked volumetric OCT images of prostate tumor spheroids over 14 days of growth. (A) spheroid volume, (B) internal gap volume, (C) external surface area, and (D) sphericity given by Eq. 4.2. Average measurement of live (black) and fixed (red) spheroids are presented with standard deviation error bar.

the 14-day period. On day 1, the dOCT red channel intensity was higher at the spheroid periphery, whereas the green channel exhibited higher intensity in the central region (Fig. 4.4G). By day 2, the dOCT green channel intensity increased and extended to cover a larger area, although the red channel intensity remained higher along the periphery (Fig. 4.4H). On days 6, 10, and 14, both the dOCT red and green channel intensities were more uniformly dispersed across the enface image (Fig. 4.4I-K).

In contrast, on day 1, FM showed predominantly live (green channel) intensity at the spheroid periphery, some central red channel intensity indicating dead cells, and dark regions suggesting a diffuse cellular arrangement (Fig. 4.4M). By day 2, the spheroid had condensed, and a central yellow hue emerged due to the overlap of green and red channel intensities (Fig. 4.4N). Subsequently, the coverage of the central red channel intensity expanded on day 6 (Fig. 4.4O), filled the spheroid's cross-sectional area by day 10 (Fig. 4.4P), and overwhelmed the green channel intensity by day 14 (Fig. 4.4Q).

The last column of Figure 4.4 shows 4× enlarged cutouts of each day 14 enface image, demonstrating the improved resolution of the OCT system compared to the fluorescent microscope. Notably, localized regions of high intensity in the OCT enface (Fig. 4.4F) correspond to either the green or red channel intensities in the dOCT enface (Fig. 4.4L).

Figure 4.5 summarizes the numerical dOCT analysis. The raw dynamic signal of live and fixed spheroids, as well as the normalized dynamic signal of live spheroids over 14 days of growth, are shown in Figure 4.5A and B, respectively. The top row of Figure 4.5C shows volumetric and enface dOCT images of a live spheroid, and the bottom row shows volumetric and enface dOCT images of the same spheroid immediately after it was fixed for one hour with 4% formaldehyde. The raw dynamic signal of live spheroids remained consistently larger than that of fixed spheroids, however the raw dynamic signal of fixed spheroids was not negligible, and both signals increased gradually over 14 days (Fig. 4.5A). Correspondingly, although the spheroid appears more red after one hour of fixing, some cells in the fixed spheroid still appear intensely green (Fig. 4.5C). Figure 4.5D shows the normalized AB absorbance over 14 days of growth. After normalization, the dynamic signal and AB absorbance of live spheroids both initially increased, decreased on day 5, and then increased and decreased once more (Fig. 4.5B,D).

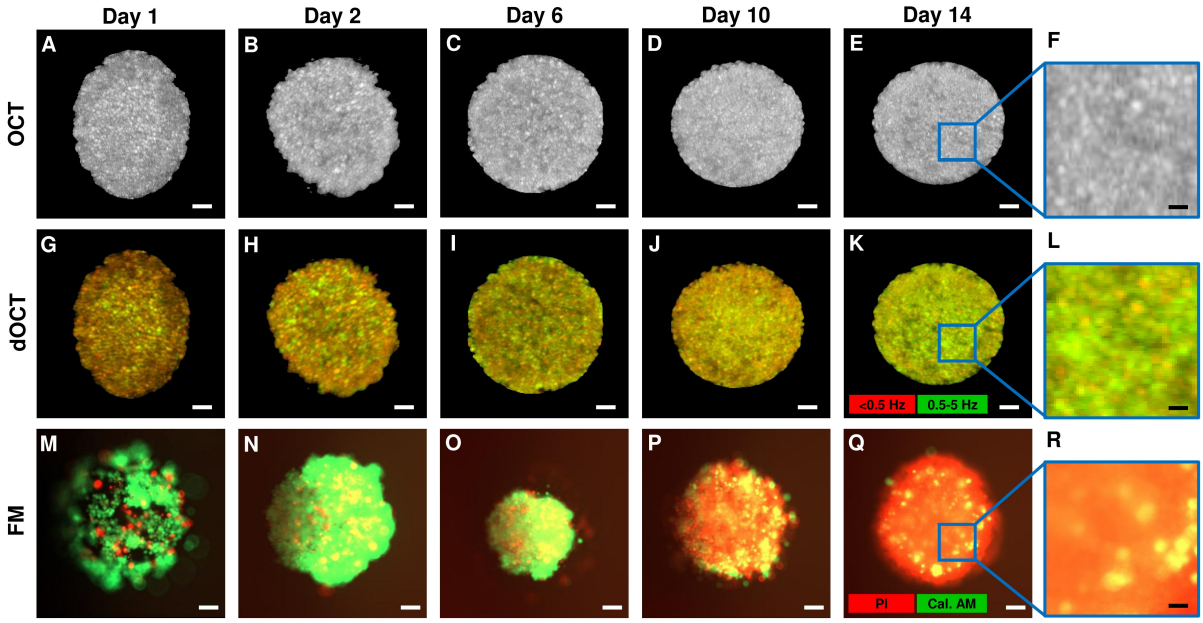


Figure 4.4: Maximum projection OCT, maximum projection dOCT, and FM enface images of prostate tumor spheroids 1, 2, 6, 10, and 14 days after cell seeding. Blue inset in last column shows 4X magnification with 25 μm scale bars. All other scale bars are 100 μm.

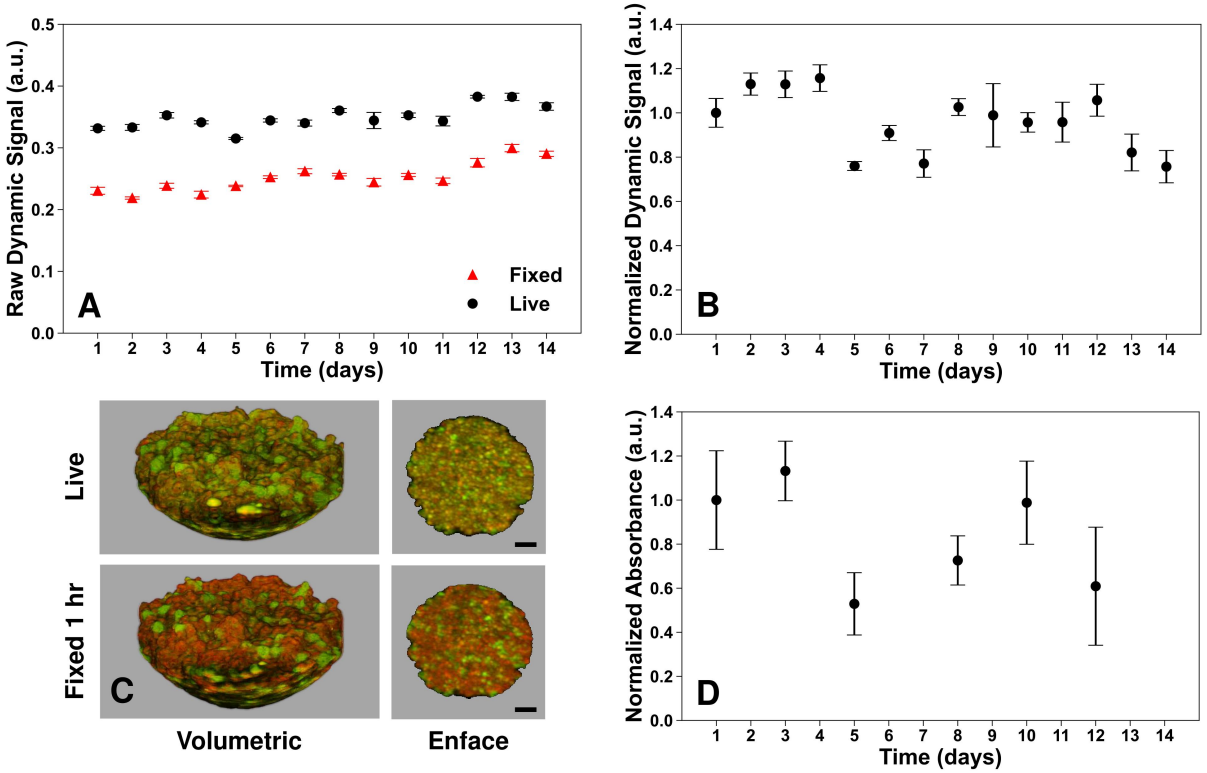


Figure 4.5: Numerical dynamic analysis of masked volumetric dOCT images of prostate tumor spheroids over 14 days of growth. (A) raw dynamic signal of live (black) and fixed (red) spheroids given by Eq. 4.3. (B) normalized dynamic signal given by Eq. 4.4. (C) Volumetric and maximum projection enface images of a live spheroid and the same spheroid after 1 hour of fixation with 4% formaldehyde. (D) Normalized absorbance of AB proliferation assay. Average measurements are presented with standard deviation error bar. All scale bars are 100 μm.

4.4 Discussion

4.4.1 Spheroid seeding and morphology

While 3D tumor spheroids are widely recognized as a more physiological *in vitro* model of tumor behavior than 2D monolayer cultures [319, 96], the "3D Petri Dish" is not a conventional technique for spheroid seeding and cultivation. Comparison between various spheroid formation methods is complicated by the influence of both cell-to-cell adherence, which varies by cell type, and the 3D culture environment on cellular arrangement [107, 329]. Previous studies have used OCT to investigate tumor spheroids formed in low-attachment well-plates [187, 240, 241, 242, 245, 325, 246], by hanging-drop [323], in microfluidic systems [226], or embedded in a collagen or gel matrix [180, 243, 272, 244]. The PC3 cells employed in our study adhere loosely [107] and preferentially to neighboring cells over the agarose gel, as demonstrated by the cell clumping observed within 5 minutes of seeding (Fig. 4.2B). After cell seeding, we observed that initially diffuse spheroids condensed before their volume generally increased, albeit with some fluctuations (Fig. 4.3A). Similar trends were noted by Sharma et al. [323] and Tartagni et al. [330], though without voxel-wise masking that characterized internal gaps. While we observed that sphericity peaked at nearly 1 on day 7 (Fig. 4.3D), the spheroids did not appear "spherical" in most volumetric images (Fig. 4.2K-O), a finding consistent with previous visual [323] and numerical observations [243].

4.4.2 Cyclical proliferation

We observed similar trends in the dynamic signal and AB absorbance after normalization. Both metrics increased approximately 15% from the initial day 1 measurement by day 3 (Fig. 4.5B, D). Despite the AB proliferation assay suggesting an increase in cell number over this period, on day 4, the volume and external surface area of live spheroids had decreased to approximately two-thirds of their initial day 1 values (Fig. 4.3A, C). However, the internal gap volume similarly decreased and reached a minimum on day 4 (Fig. 4.3B), suggesting that the initially large volume and surface area in newly seeded spheroids arose from dispersed cells that subsequently condensed into more tightly aggregated structures. After this compaction, the spheroid volume, internal gap volume, and external surface area all increased (Fig. 4.3A-C). We propose that once cells became tightly aggregated, some died due to insufficient nutrition and detached from their neighbors. As a result, the spheroid partially dispersed, allowing central cells better access to nutrients and thus improved growth. This interpretation is supported by the normalized dynamic signal and

AB absorbance, which both reached a minimum on day 5, then increased once again (Fig. 4.5B, D). The subsequent period of mostly increasing spheroid volume, internal gap volume, external surface area, and normalized dynamic signal continued until approximately day 8. Then, the pattern repeated: the three morphological metrics decreased until approximately day 10 before increasing on day 11 (Fig. 4.3A-C). Lagging by a day, the normalized dynamic signal decreased until day 11 before increasing on day 12 (Fig. 4.5B). Although less frequent measurements complicate direct comparison, normalized AB absorbance also rose again before subsequently decreasing (Fig. 4.5D). The increase in spheroid volume, internal gap volume, and external surface area on day 14 (Fig. 4.3A-C) indicates cell death and detachment within the spheroids, which is further supported by the low normalized dynamic signal (Fig. 4.5B) and high FM red channel intensity (Fig. 4.4Q) observed on day 14.

4.4.3 Necrotic spheroid core

FM revealed a predominantly green spheroid periphery with central red intensity that increased over time, suggesting the formation of a necrotic core of dead cells surrounded by proliferating live cells (Fig. 4.4M-Q). This is an established phenomenon previously observed both by conventional biological methods [319, 96] and dOCT [187, 240]. In contrast, dOCT images showed increasing green channel intensity throughout the 14-day period (Fig. 4.4G-K) and the raw dynamic signal measured via dOCT in live spheroids did not follow the trend observed with AB (Fig. 4.5B,D). Notably, the raw dynamic signal in spheroids killed by formaldehyde fixation also increased throughout the experiment (Fig. 4.5A). We assume that the dynamic motion observed in fixed spheroids did not change over the two-week experimental period because an identical fixing procedure was followed each day. Therefore, the variation in fixed dynamic signal over time suggests that the system's performance or the influence of factors unrelated to cellular metabolism also varied with time. To correct for these factors external to the sample, the dynamic signal of fixed spheroids was subtracted as background from live spheroids, and the subsequent normalized dynamic signal measured via dOCT agreed well numerically with AB proliferation assay (Fig. 4.5B,D). However, dOCT images visually represent the raw dynamic signal before averaging and subtraction of the corresponding fixed measurement. Since spheroids were maintained at 4°C for approximately 24 hours post-fixation, the dOCT images of fixed spheroids were not registered to their live counterparts. Consequently, the dOCT images could not be similarly fixation-subtracted for an improved qualitative comparison to FM.

4.4.4 Origin of dynamic signal

We observed that dOCT images of live spheroids were significantly more green than fixed spheroids (Fig. 4.5A). As fixation eliminates metabolic activity by killing cells without damaging the spheroid structure, this differentiation suggests that the LF-dOCT system could distinguish temporal intensity fluctuations due to cellular metabolism. Furthermore, the average dynamic signal throughout the spheroid bulk, once fixation-subtracted and normalized, demonstrated excellent agreement with AB (Fig. 4.5B), a well-established indicator of cellular metabolism [157]. However, the longitudinal development of a necrotic spheroid core revealed by FM (Fig. 4.4M-Q) was not spatially well-resolved in dOCT images, which instead showed higher green intensity in the spheroid core (Fig. 4.4G-K). While AB is specific to cellular activity and becomes fluorescent through reduction by cytoplasmic and mitochondrial enzymes [331, 332, 333], the sub-cellular motion measured by dOCT may also arise from physical changes in cell morphology and volume. Cells undergoing necrosis exhibit physical changes, such as cell swelling, nuclear disintegration called karyolysis, and ultimately degradation of the cellular membrane and leakage of cellular contents [334, 38]. Following necrosis, these cellular fragments may have been subject to Brownian motion and further contributed to the high frequency motion detected in the spheroid core.

Unlike necrotic cell death due to competition for resources in a confined space, formaldehyde fixation kills cells quickly and efficiently, preserving spheroid structure by cross-linking proteins through a process completed within 24 to 48 hours [335]. Fixed spheroids were maintained at 4°C for approximately 24 hours to reduce motion caused by the cross-linking process. Nevertheless, some cells throughout the spheroid bulk remained intensely green in dOCT images after fixation (Fig. 4.5C). While some of these cells may have survived the fixing process, the localized high frequency motion measured by dOCT in fixed spheroids could also be due to non-metabolic motion. Although cells killed by fixation are expected to remain tightly adhered to neighbors, some cells may have died by necrosis before fixation and the resulting cell bodies and fragments may have experienced Brownian motion.

4.4.5 LF-dOCT system and dynamic analysis methods

The current system achieves a sensitivity of 93 dB, using a 2,000 fps camera speed and 3.5 mW of incident power at the imaging plane. This represents approximately a 3 dB improvement in sensitivity compared to the initial report of the dOCT platform [283], which can be attributed to finer alignments. Our imaging protocol acquired each sub-volume at a rate of 10.7 Hz. By the Nyquist-Shannon sampling theorem [200], the fastest

dynamics observable to our method occurred at just over 5 Hz: the maximum threshold of our green frequency band. While our system and method appear sufficient for numerically accurate extraction of spatially-averaged and fixation-subtracted dynamic signals (Fig. 4.5B,D), the spheroid's necrotic core is not visually resolved (Fig. 4.4). The following section discusses various system characteristics that may have contributed.

Temporal resolution

To observe cellular activity with dOCT, there must be sufficient temporal resolution of the OCT signal. Dynamic contrast is provided by ATP-consuming processes and the active movement of organelles [192], which are estimated to be in the range of 0.1 to 20 Hz [270, 271]. By detecting frequencies up to 28 Hz, Wang et al. [246] visually resolved the necrotic spheroid core. They generated HSB images using the mean frequency, inverse frequency bandwidth, and running standard deviation technique developed by Scholler et al. [234]. The frequency banding method we employed similarly analyzes the OCT spectrum and has been used to detect frequencies up to 12 Hz [201], 20 Hz [258], or 25 HZ [254, 250, 251]. Nevertheless, Liu et al. [256] used mean frequencies limited to the range of 0.16 Hz to 1 Hz to distinguish live and dead cells in mouse allograft tumors. In fact, the first reported dOCT study differentiated between viable, necrotic, and apoptotic human fibroblasts with single B-scans acquired every few minutes [230]. Consequently, while our maximum detectable frequency of 5 Hz may have contributed to the inability to resolve the necrotic spheroid core, it was likely not the most significant factor.

Sensitivity

The limited sensitivity of our LF-dOCT platform may have also contributed to the undistinguished necrotic core. Because dOCT analysis relies on OCT intensity fluctuations, a higher system sensitivity should allow for more accurate extraction of dynamic signals. In general, acquisition speed is increased at the cost of reduced sensitivity [279]. The maximum frequency thresholds of 12 Hz [201], and 25 HZ [254, 251] discussed in section 4.4.5 were achieved with a PSc-OCT system that demonstrated a sensitivity of 51 dB at a depth of 80 μm. Alternatively, the studies by El-Sadek et al. [187, 240, 241, 242] successfully resolved the necrotic core in human breast adenocarcinoma (MCF-7) spheroids by employing a PSc-OCT system with a sensitivity of 104 dB. Compared to our system, their 11 dB higher system sensitivity enabled them to directly evaluate OCT intensity fluctuations via the LIV and OCDS metrics. Likewise, Tan et al. [245] implemented MAV, another direct variation method, to investigate MCF-7 spheroids with a commercial PSc-OCT

system. However, akin to our results, they did not observe a necrotic spheroid core and demonstrated quantitative agreement with viability measured by Trypan Blue, a biological method similar to AB that provides an average measurement across many spheroids.

Frequency band thresholds

In contrast to these methods, to mitigate the strong influence of noise inherent in direct variation methods, we addressed our reduced sensitivity by employing the frequency banding technique introduced by Apelian et al. [273]. By integrating the spectrum of OCT intensity fluctuations, this approach effectively averages over a range of signals, thereby diminishing the impact of random noise. Previous work has qualitatively compared this technique to fluorescence imaging [249] and histological staining [258, 254, 250, 251] to differentiate various cellular and intracellular morphological structures. However, to the best of our knowledge, the work we describe here is the first to quantitatively validate it to an established biological method. Meanwhile, the HSB spectrum-based method [234] has been used to assess the viability of HeLA cervical cancer cells cultured in 2D monolayers and qualitatively compared with Trypan Blue, which stains cells with broken cell membranes [228]. The mean frequency computed in this method has also been quantitatively validated using FM images captured by confocal laser scanning microscopy [246] or multiphoton microscopy with registration to the OCT equivalent [256]. Since Wang et al. [246] successfully resolved the necrotic spheroid core with a spectrum-based dOCT method, perhaps the thresholds imposed by our frequency banding approach contributed to our undistinguished necrotic core. Future studies should quantitatively investigate how differences in system sensitivity, the threshold between the red and green frequency bands, and the removal of a blue frequency band impact the accuracy of dOCT signal extraction.

4.4.6 Reflection artifacts and pseudo-longitudinal protocol

As is common in OCT systems, reflection artifacts were prevalent and difficult to mitigate. This issue is particularly pronounced in LF-OCT systems due to the absence of confocal gating that is leveraged by PSc-OCT systems. While imaging the seeding process, the sample was not adjusted; however, an artifact that was not present at 10 minutes after seeding (Fig. 4.2D) appeared at 60 minutes (Fig. 4.2D, red arrow). The sudden appearance of the artifact was likely due to the evaporation of the culture medium over the course of imaging, which altered the angle of the liquid surface. Reflection artifacts were minimized in regions of the gel where the liquid surface was slightly curved due to surface tension, resulting in fewer direct reflections reaching the camera. Consequently, spheroids located in these edge

areas were selected more frequently for imaging. However, location within the 9×9 well array inside the gel influences spheroid size, as seen in the yellow inset in Figure 4.1B. Although 15 live and fixed spheroids were imaged each day to form a representative sample, this selection process likely introduced some bias into the morphological measurements. Future work is encouraged to record spheroid location and identify its statistical impact.

Additionally, the Petri dish's top cover introduced significant reflection artifacts and was therefore removed during imaging, potentially exposing the cell culture to contamination. As a result, samples were not returned to the sterile incubator and we employed a suboptimal pseudo-longitudinal protocol that imaged different spheroids over the 14-day growth period. To conduct a truly non-invasive longitudinal study, imaging should be performed through the Petri dish cover, or more ideally, with an incubator integrated into the OCT imaging stage. Such integration would not only prevent the need for spheroid transportation – a mechanically stressful process that may alter cellular arrangement – but also enable the growth of individual spheroids to be monitored over time. Even in this integrated scenario, we suggest including a subset of spheroids that are fixed and imaged during each live imaging session. This would create a relevant metabolic control and establish a baseline of system performance for comparison. Numerical analysis of our pseudo-longitudinal protocol, which fixed spheroids at the time of each live imaging session, revealed significant changes in fixed spheroids over time (Fig. 4.3). These changes may influence the dynamic response to non-metabolic motion. A limitation of our study is that, since each nominal day of fixed spheroid measurement was acquired the following day, fixed subtraction in the normalized dynamic signal does not precisely account for the system performance on the exact day of live spheroid imaging. However, because imaging occurred every 24 hours, the system performance is not expected to undergo significant changes within that time frame.

4.4.7 Signal attenuation

Another factor complicating the interpretation of dOCT results was attenuation caused by spheroid condensation and growth beyond the system's 260 μm depth of focus (DOF) in conjunction with the signal-to-noise ratio (SNR) roll-off inherent to the spectral domain dOCT platform. Although intensity was notably reduced in the lower portions of large spheroids in the morphological images (Fig. 4.2H), the spheroid masks were manually extended to include these attenuated regions in the morphological analysis. However, the dynamic signals could no longer be accurately extracted, and we excluded the low-intensity regions of the dOCT data using the intensity filter described in Methods Section 4.2.4. To address this issue, several approaches could be considered: reducing the lateral resolution

further to increase the DOF; switching from a spectral domain to a swept-source OCT system to avoid SNR roll-off; or using a longer central wavelength light source, such as 1310 nm, to enhance penetration depth and improve overall performance.

4.5 Conclusion

In conclusion, we acquired volumetric dOCT images of prostate tumor spheroids with a spectral-domain LF-dOCT system to characterize structural morphology and cellular dynamics over two weeks of growth. By comparing live spheroids with those killed by formaldehyde fixation, we confirmed that the system's sensitivity was sufficient to detect dynamic signal variations associated with cellular metabolism. Numerical analysis of dOCT images was in excellent agreement with results from AB proliferation assay. In future work, we plan to further improve the system's sensitivity to enhance the reliability of the dOCT platform and to incorporate an incubator for truly non-invasive, repeatable cellular dOCT measurements.

Chapter 5

Comparison of volumetric dynamic optical coherence tomography with biological methods for evaluation of radiation effects in prostate tumor spheroids

5.1 Introduction

Prostate cancer is the most prevalent cancer in North American males [1, 2] and is commonly treated with radiation therapy [336]. Clinically, modern radiation treatments are delivered through fractionation schemes that leverage distinct radiobiological behavior exhibited by different tumor types and their surrounding tissues [42, 44, 45]. Our foundational radiobiological understanding of cellular responses to radiation was formed through conventional 2D monolayer cell culture methods [52, 30]. In 1956, Puck and Marcus [165] irradiated mammalian cells cultured in 2D monolayers and published the first radiation survival curve that fit cell survival to radiation dose using a colony-forming or clonogenic assay. Since then, the clonogenic assay has remained the gold standard for measuring radiation survival [169], in part because it informs the extensively validated linear-quadratic (LQ) model [46, 47]. In the LQ model, the linear α and quadratic β parameters mechanistically describe cell killing due to one or two radiation tracks, respectively [31]. The α/β ratios obtained from conventional 2D monolayer cell culture experiments continue to

guide clinical decision-making [52]. However, a growing body of evidence in recent decades has demonstrated that *in vitro* cells cultured in 2D monolayers on flat, hard surfaces do not accurately replicate the behavior of *in vivo* tumors [98, 337]. In contrast, cancer cells cultured in small 3D aggregates called tumor spheroids exhibit more physiologically relevant behavior due to increased cell-to-cell contact and diffusion-limited distributions of oxygen and nutrients [96, 320, 319]. This heterogeneous distribution leads to the formation of a hypoxic spheroid core of non-proliferative or quiescent cells[337]. It has been widely observed that radiation survival differs significantly between *in vitro* cancer cells cultured in 2D monolayers and those cultured in 3D spheroids [168, 103, 338].

Cell culture geometry is suspected to influence the effects of radiation through biological and physical processes related to nutrient and waste transport, resource competition, and mechanical forces exchanged between cancer cells and their microenvironment [168, 339, 104]. Mathematical *in silico* models that simulate these biological and physical processes have become increasingly prevalent as tools to elucidate the mechanisms underlying tumor growth and treatment response [340, 341]. In particular, *in silico* methods have been utilized to investigate the mechanical and molecular characteristics of tumor spheroids [123]. Conventional *in silico* approaches, such as continuum models described by partial differential equations (PDEs), are mathematically well-characterized and computationally efficient; however, these models struggle to accurately capture the inherent cellular heterogeneity and diversity present within patient tumors and tumor spheroids [342]. In contrast, discrete *in silico* methods such as agent-based models address these limitations by simulating each cancer cell as an individual "agent" that evolves through time by responding to its local environment, including neighboring cells and nutrient availability [340, 343]. The utility of *in silico* models for falsifying hypotheses and generating novel insights depends critically upon the accuracy of their parameter estimates, which are derived from *in vitro* and/or *in vivo* measurements [148].

However, the 3D structure of tumor spheroids poses challenges for measurement by conventional biological techniques. Clonogenic assay can be adapted for evaluating radiation survival in spheroid cultures by disaggregating the 3D cellular structures into a cell suspension for 2D plating and longitudinal observation of colony formation. Nevertheless, the geometry of cell culture following radiation treatment itself influences cellular survival and response [103]. Alternative methods, such as proliferation assays, avoid the need for spheroid disaggregation and have also been utilized to estimate clonogenic radiation survival [344]. For instance, the Alamar Blue (AB) proliferation assay is a common technique that measures cellular metabolism by detecting the reduction of non-fluorescent, blue resazurin to fluorescent pink resorufin [157]. Although the AB proliferation assay has been adapted for spheroid cultures [164], the fluorescence measurement reflects only an averaged

response across the entire cell population within the spheroid and does not distinguish the treatment effect in the hypoxic core from the spheroid periphery. Fluorescence microscopy (FM) is widely employed to evaluate spheroids with spatial resolution [103, 345, 346]; however, these assessments remain qualitative rather than quantitative.

In contrast, optical coherence tomography (OCT) enables the quantitative evaluation of 3D tumor spheroids through non-invasive, high-resolution volumetric imaging [323, 193]. Recently, dynamic OCT (dOCT) methods have been developed, which involve repeatedly acquiring OCT images at each spatial location to estimate cellular activity from temporal OCT intensity signal fluctuations [192]. Previously, dOCT has been employed to investigate spheroids [240, 187, 245, 239] as well as other types of 3D cell cultures [239, 347, 235, 236]. Quantitative analysis of tumor spheroids using dOCT has been conducted following chemotherapy treatment [240, 187] and exposure to perfluorooctanoic acid [239]; however, the effects of radiation treatment have not yet been explored with this method. Although the clonogenic assay remains the gold standard for measuring cell survival after radiation exposure, there has been sustained interest in adapting alternative methods, such as proliferation assays, to circumvent the long experiment duration and labor-intensive colony counting required by clonogenic assays [348, 349, 344]. Given prior suggestions that dOCT can quantify cellular activity and viability [240, 245], it may also provide another feasible alternative to the clonogenic assay. In this study, we employed a previously described high-speed spectral-domain line-field (LF) dOCT system [283] to image prostate tumor spheroids after radiation treatment and performed qualitative and quantitative comparisons with established biological methods and computational simulation.

5.2 Methods

5.2.1 Prostate tumor spheroids

PC3 cells (human prostate adenocarcinoma) were cultured in RPMI 1640 (Sigma-Aldrich, USA) supplemented with 1% penicillin (Thermo Fisher Scientific, USA) and 10% fetal bovine serum (Thermo Fisher Scientific, USA). Cells were incubated at 37°C with 5% CO_2 in a humidified atmosphere. Monolayer cell culture was plated in T-25 culture flasks. Prostate tumor spheroids were seeded and cultured in a 3D Petri Dish (MicroTissues Inc., USA) composed of 2% agarose gel. Each agarose gel contained a 9×9 array of wells and was seeded to form spheroids composed of approximately 1,000 cells in each well (Fig. 5.1A).

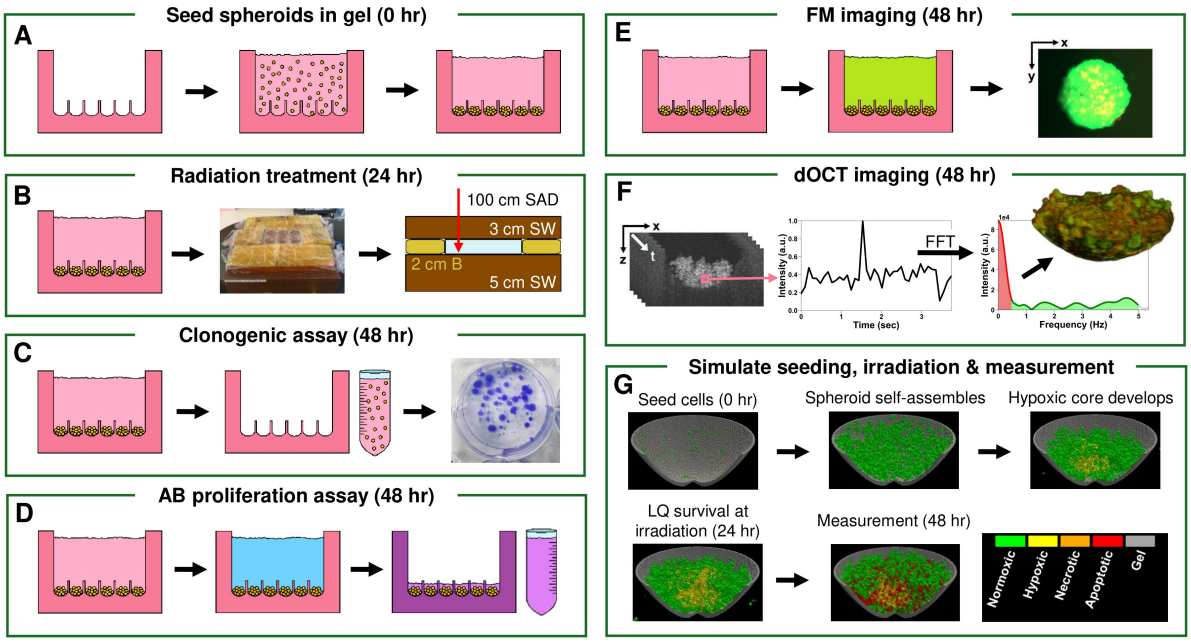


Figure 5.1: Schematic of experimental and simulated spheroid seeding, irradiation, and measurement. (A) Cells (yellow) seeded into agarose gels (pink) formed prostate tumor spheroids in the bottom of wells. (B) After 24 hours, spheroids in 6-well plates were surrounded by Superflab bolus (yellow) and irradiated with 6 MV radiation at 5 cm depth in Solid Water (brown). Measurement was performed 24 hours post-irradiation. (C) Clonogenic assay disaggregated spheroids for plating 2D cultures that were fixed and stained after two weeks. (D) AB proliferation assay added AB solution to gels that was extracted for absorbance measurement. (E) FM added solution of green calcein acetoxymethyl and red propidium iodide to gels that fluoresced in live and dead cells, respectively, during enface imaging. (F) Volumetric dOCT imaging acquired forty repeated frames per cross-section. Dynamic signals were extracted from intensity fluctuations via an FFT-based algorithm assigning red (<0.5 Hz) and green (0.5–5 Hz) frequency bands. (G) 3D agent-based simulation of spheroid seeding, irradiation, and measurement applied experimental LQ survival at treatment. SAD: source-to-axis distance; B: Superflab bolus; SW: Solid Water; AB: Alamar Blue; FM: fluorescence microscopy; dOCT: dynamic optical coherence tomography; FFT: Fast-Fourier transform; LQ: linear-quadratic model.

5.2.2 Radiation treatment

A Varian TrueBeam linear accelerator was used to deliver 1, 2, 4, 6, 8, or 10 Gy to monolayer and spheroid cultures with a 6 MV beam 24 hours after seeding (Fig. 5.1B). Each 6-well plate containing gels with spheroids was positioned at a source-to-axis distance (SAD) of 100 cm, at a depth of 5 cm within Gammex 457-CTG Solid Water, and surrounded by Superflab bolus for scatter conditions. Nonetheless, we expect a delivered dose with an uncertainty in the range of 10%. T-25 culture flasks of monolayer culture were similarly situated and treated. Live control spheroids, which were not exposed to radiation, were removed from incubation and handled identically to treated samples. At the time of treatment, a subset of live control spheroids were fixed with 4% formaldehyde (Thermo Fisher Scientific, USA) in PBS (Wisent Inc., Canada) for 1 hour to eliminate metabolic activity. These fixed spheroids were subsequently stored at 4°C for approximately 24 hours before measurement to minimize dOCT motion artifacts induced by fixation.

5.2.3 Biological assays

Clonogenic assay

Clonogenic assay was performed with monolayer and spheroid cultures 24 hours post-irradiation to measure clonogenic survival (Fig. 5.1C). To disaggregate spheroids for clonogenic plating, spheroids were aggressively flushed out of the wells with their surrounding media and transferred into a falcon tube for mechanical vortexing, followed by incubation for two hours to allow cells to settle by gravity. The supernatant was then removed and replaced with at least twice the remaining volume in 0.25% trypsin-EDTA (Thermo Fisher Scientific, USA). After incubation for ten minutes, the trypsin solution was mechanically vortexed again and centrifuged for subsequent cell counting. For monolayer culture, cells were incubated in 0.25% trypsin-EDTA for 3 minutes, then centrifuged for counting. Following cell counting, cells from each experimental condition were plated into 6-well plates at low densities and allowed to grow for approximately two weeks. Colonies were then fixed with 4% formaldehyde in PBS for 1 hour and subsequently stained with 0.5% crystal violet (Thermo Fisher Scientific, USA) dissolved in water for 30 minutes. Stained colonies were counted, and the plating efficiency (PE) was calculated in live control samples as follows:

$$\mathrm{PE} = \frac{N_{\mathrm{colonies}}}{N_{\mathrm{plated}}} \tag{5.1}$$

where N_{colonies} is the number of colonies counted and N_{plated} is the number of cells plated. Then, in treated samples, survival fraction (SF) was calculated as follows:

$$\text{SF} = \frac{N_{\text{colonies}}}{N_{\text{plated}} \times \text{PE}} \tag{5.2}$$

The linear and quadratic parameters α and β were extracted by least-squares fitting of SF values for each treated dose d to the LQ model:

$$\text{SF} = \exp(-\alpha d - \beta d^2) \tag{5.3}$$

Alamar Blue proliferation assay

AB proliferation assay was performed 24 hours post-irradiation to measure the average cellular proliferation within the tumor spheroids (Fig. 5.1D). To achieve a final AB concentration of 5% within each 500 μL gel, 34.5 μL of AB (Sigma-Aldrich, USA) and 156 μL of RPMI were added drop-wise to each gel after careful removal of the culture medium in 10 μL increments. Samples were incubated for 3 hours at 37°C with 5% CO_2 in a humidified atmosphere. Following incubation, the absorbance intensity of the extracted solution was recorded at 570 nm using a BioTek Synergy H1 microplate reader. Three gels containing spheroids were measured for each experimental condition. Gels without cells were processed identically and measured to determine background absorbance. For each measurement of gels containing spheroids, the average background intensity was subtracted, and the resulting AB absorbance was normalized relative to the absorbance measured in the live control samples.

5.2.4 Fluorescence microscopy

FM was performed 24 hours post-irradiation to visualize cell death within spheroids using the Live/Dead Cell Viability assay (Sigma-Aldrich, USA). Live cells were labeled using calcein acetoxymethyl (calcein-AM), which fluoresces green through intracellular processes [155]. Dead cells were labeled using propidium iodide (PI), which fluoresces red upon binding with DNA or RNA that is inaccessible in live cells [152]. After careful removal of culture medium, a solution containing 0.2875 μL calcein-AM, 1.15 μL PI, 95 μL RPMI, and 95 μL PBS was added to each gel. Samples were then incubated for one hour at 37°C with 5% CO_2 in a humidified atmosphere. Following incubation, gels were transferred to coverslip-bottomed Petri dishes and imaged using a Zeiss Axio Observer widefield microscope that was operated by ZEN2 Blue Edition software and equipped with an Axiocam

506 mono camera. A Plan-Apochromat 63/1.4 Oil Ph3 M27 objective (Carl Zeiss Microscopy LLC, USA) was used to acquire fluorescent images, while an incubation plate (PECON, Germany) maintained the temperature at 37°C during imaging.

5.2.5 OCT

Tumor spheroids were imaged with the LF-dOCT system 24 hours post-irradiation (Fig. 5.1F). A detailed description of the system design and performance can be found in [283]. Briefly, the system employed a broadband superluminescent diode (SLD) light source (cBLMD-T-850-HP, Superlum, Ireland) with a central wavelength of 842 nm and a full-width-at-half-maximum (FWHM) spectral bandwidth of 179 nm, achieving an axial resolution of 2.6 μm in air. A 5× microscope objective (M Plan APO, Mitutoyo, Japan) provided a lateral resolution of 6.4 μm. The system operated at an image acquisition speed of 2,000 frames per second (fps), and had approximately 93 dB sensitivity, measured with an incident power of 3.5 mW at the image plane.

Volumetric dOCT images were acquired and processed following methods previously described in Chapter 4. Each dOCT volume consisted of 400 B-scans, with each B-scan composed of 400 A-scans. The dOCT volume acquisition was divided into four sub-volumes, each imaged with 40 repetitions at a repetition rate of 10.7 Hz. OCT images of 15 tumor spheroids per experimental condition were acquired, with each spheroid imaged for approximately 16 seconds during dOCT recording. Spheroids were maintained at 21°C without CO_2 supply during imaging. All OCT and dOCT images presented for each experimental condition were generated from the same representative spheroid, whereas different spheroids were used for FM.

Morphological OCT images were generated using a standard OCT image reconstruction process and are displayed in logarithmic scale with the surrounding gel masked. Volumetric OCT masks were analyzed numerically to estimate the volume V_{sph} and external surface area S of each spheroid, as well as the volume of internal gaps V_{gap} enclosed by that surface area. Sphericity, which reaches a maximum value of 1 for a perfect sphere, was calculated to compare the external surface area of each spheroid to the volume it enclosed as follows:

$$\text{Sphericity} = \frac{(V_{\text{sph}} + V_{\text{gap}})^{2/3}}{(4/9\pi)^{1/3} S} \tag{5.4}$$

To generate dOCT images, a Hann window function was first applied along the time direction to the linearly scaled OCT intensity values at each pixel location. Following zero-padding of the data, a Fast Fourier Transform (FFT) was performed along the time-axis

[249, 250]. Next, integrals were calculated over two distinct frequency bands: a lower-frequency ("slow") red band below 0.5 Hz and a higher-frequency ("fast") green band between 0.5 and 5 Hz. After applying logarithmic scaling to each of the red and green dOCT channels, a small region of culture medium located above each spheroid in a central B-scan was selected. The sum of the mean and standard deviation of the intensity within this reference region was subtracted from each pixel location. To quantitatively analyze dynamic activity, a raw dynamic signal metric was computed for each masked spheroid as follows:

$$D_{\text{raw}} = \frac{\sum_{\text{mask}} I_G}{\sum_{\text{mask}} I_R + \sum_{\text{mask}} I_G} \tag{5.5}$$

Here, I_R and I_G represent the intensity values of the red and green channels, respectively. The average raw dynamic signal measured in the formaldehyde-fixed spheroids was subtracted from the corresponding signal measured in live spheroids, and the resulting value was normalized relative to live control as follows:

$$D_{\text{norm}}(d) = \frac{D_{\text{raw}}(d) - D^f_{\text{raw}}}{D_{\text{raw}}(0) - D^f_{\text{raw}}} \tag{5.6}$$

Here, $D_{\text{raw}}(d)$ and D^f_{raw} represent the raw dynamic signals measured in spheroids treated with radiation dose d (Gy) and formaldehyde-fixed spheroids, respectively. Due to attenuation with depth caused by spheroid density, the numerical analysis excluded any enface (lateral view) planes whose average intensity was lower than the median intensity across the entire volume. To display dOCT images, the masked red and green channels were independently normalized to those of a representative spheroid before a Gaussian FFT filter was applied with $\sigma_R = 90$ and $\sigma_G = 65$ respectively. Finally, a 3×3 median filter was applied to each channel before combining them into an RGB color image.

5.2.6 Simulation

For this study, we also developed an agent-based computer model of 3D tumor spheroid growth and radiation treatment using the software CompuCell3D [313] (Fig. 5.1G). Simulated time evolved according to a Monte-Carlo method, which minimized the effective energy of the 3D lattice containing the spheroid. Each simulation began with a suspension of 1,000 well oxygenated *Normoxic* tumor cells placed randomly inside the gel within a curved well described by:

$$\alpha[(x - \Delta x)^2 + (y - \Delta y)^2] = z - \Delta z \tag{5.7}$$

Here, as extracted from OCT images, $\alpha = 0.0025\ \mu\text{m}^{-1}$, and $(\Delta x, \Delta y, \Delta z)$ positioned the bottom of the well at the center of the bottom surface inside a simulation space measuring 810 μm across and 405 μm deep with 5 μm voxels. Initially suspended cells settle under gravity and self-assemble into a spheroid, driven by the energetic preference of live cells to be in contact with other live cells rather than the surrounding gel or culture medium. Oxygen, governed by a PDE, was maintained at a constant partial pressure in the culture medium, and diffused through the spheroid with a diffusion coefficient approximately equivalent to half that of oxygen in water. Simulated cells consumed oxygen, and their growth rate depended on the local partial pressure of oxygen according to a Michaelis-Menten saturation curve. When a cell grew to a sufficient volume, it divided into two daughter cells of equal volume. Due to competition and limited oxygen diffusion within the spheroid bulk, *Normoxic* cells reversibly became *Hypoxic* when oxygen-deprived, and irreversibly became *Necrotic* upon severe oxygen deficiency. The simulation time scale was calibrated so that *Normoxic* cells divided approximately every 24 hours, and spheroid dimensions were comparable to those measured in Chapter 4 by longitudinal OCT imaging 24 hours after seeding.

Radiation treatment was simulated 24 hours after seeding. At the treatment time, each cell within the spheroid probabilistically survived according to the LQ curve derived from spheroid clonogenic experiments. Cells killed by radiation irreversibly became *Apoptotic* only upon attempted cell division. The simulation explicitly distinguished cell death due to necrosis by nutrient deprivation from radiation-induced apoptosis. However, *Necrotic* and *Apoptotic* cells behaved identically and, unlike *Normoxic* and *Hypoxic* cells, did not preferentially adhere to neighboring cells. Formaldehyde fixation was not explicitly simulated; instead, it was approximated by assuming all cells in the live control simulation became *Apoptotic* at the time of treatment.

Numerical morphological and dynamic analysis of simulated live control spheroids and spheroids irradiated with 1, 2, 6, and 10 Gy were performed 24 hours post-irradiation. Morphological metrics including spheroid volume, surface area, and internal gap volume were calculated voxel-wise using the 3D lattice and were subsequently used to compute sphericity according to Eq. 5.4. Simulated SF was calculated using Eq. 5.2 by estimating N_{colonies} and N_{plated} as the number of living cells and the total number of cells in the spheroid, respectively. Due to the stochastic nature of the Monte Carlo simulation, each condition was simulated ten times. A detailed mathematical description of the simulation can be found in Chapter 3 and Appendix B.

5.2.7 Statistics

All measurements are presented as averages with corresponding error bars. Clonogenic SF error was estimated by Fieller's theorem with a 95% confidence interval from a Poisson distribution, as described by Gupta et al. [350]. For comparison with alternative SF measurements, clonogenic SF was presented using the LQ fit. The upper (lower) LQ error bounds were calculated using LQ parameters, α and β, that were fit to experimental clonogenic SF values plus (minus) the SF error estimated by Fieller's theorem. All other error bars represent standard deviation.

Numerical OCT and dOCT measurements that fell outside of the interquartile range were excluded from the analysis. In the numerical morphological analysis, one-way ANOVA tests were performed to compare live control spheroids with spheroids irradiated with 10 Gy and those fixed with formaldehyde for each metric. If the omnibus ANOVA test was significant, independent Welch's t-tests were conducted to compare each tested condition individually against the live control spheroids. In the numerical dynamic analysis, independent Welch's t-tests were performed to compare the normalized SF measured by dOCT and AB proliferation assay for each dose of radiation. A significance level α of 0.05 was employed and t-tests were Bonferroni-corrected. Statistically significant t-test results are indicated on the relevant plots with an asterisk.

5.3 Results

Figure 5.2 summarizes the volumetric OCT and simulated morphological analyses of live control, irradiated, and formaldehyde-fixed spheroids. The first and second rows of Figure 5.2 present the average spheroid volume, internal gap volume, external surface area, and sphericity calculated voxel-wise in masked volumetric OCT images and simulation. As the radiation dose increased from 0 Gy to 6 Gy, simulations predicted reductions in spheroid volume, internal gap volume, and surface area, alongside an increase in sphericity (Fig. 5.2A-D). All simulated morphological metrics then plateaued between 6 Gy and 10 Gy, with 10 Gy significantly different from live control (Fig. 5.2A-D). Compared to the OCT measurements, simulated gap volumes (Fig. 5.2B) were three orders of magnitude larger, while surface area (Fig. 5.2C) and sphericity (Fig. 5.2D) values were one order of magnitude larger and smaller, respectively. Despite these differences in magnitude, the general trends of the morphological metrics observed by volumetric OCT were consistent with simulated results for radiation doses between 0 Gy and 2 Gy (Fig. 5.2A-D). However, in the OCT analysis, spheroid volume, gap volume and surface area increased at 6 Gy, then

plateaued at 10 Gy, and further increased in formaldehyde-fixed spheroids (Fig. 5.2A-C). Notably, the surface area of formaldehyde-fixed spheroids was significantly larger than that of live control spheroids (Fig. 5.2C). In contrast, after minimal changes between 2 Gy and 6 Gy, both simulated and OCT-measured sphericity achieved a maximum at 10 Gy and minimum in formaldehyde-fixed spheroids; both extremes were significantly different from the live control spheroids (Fig. 5.2D).

The third and fourth rows of Figure 5.2 show central cross-sectional masked OCT images and corresponding simulated visualizations, respectively. OCT images exemplify the smaller volume and surface area of spheroids treated with 2 Gy (Fig. 5.2F) compared to 10 Gy (Fig. 5.2G), which is of a comparable size to live control (Fig. 5.2E). An internal gap can be observed in the OCT image of a formaldehyde-fixed spheroid (Fig. 5.2H, yellow arrow), which otherwise resembles the live control and irradiated spheroids. In contrast, simulated spheroids display largely uniform cross-sectional shapes and sizes across all radiation doses (Fig. 5.2I-K). However, simulated formaldehyde-fixed spheroids similarly contain more internal gaps than both control and irradiated spheroids (Fig. 5.2L).

Figure 5.3 summarizes the dynamic analysis. Clonogenic SF of prostate cancer cells cultured in 3D spheroids and conventional 2D monolayers are presented in Figure 5.3A. Compared to 2D monolayer culture, cells cultured in spheroids demonstrated higher radioresistance with approximately 6% and 2% clonogenic survival after irradiation with 6 Gy and 10 Gy, respectively (Fig. 5.3A). Figure 5.3B compares the SF of spheroids measured via normalized dynamic signals derived from masked volumetric dOCT images, normalized absorbance from AB proliferation assay, simulations, and clonogenic assay. Generally, SF values measured by dOCT were larger than those measured by AB but the differences were not statistically significant; initially increasing slightly with radiation dose from live control, SF values measured by both methods then decreased and subsequently reached a maximum at 10 Gy (Fig. 5.3B). In contrast, clonogenic and simulated SF values consistently decreased with increasing dose, with clonogenic SF decreasing at a faster rate (Fig. 5.3B). The second and third rows of Figure 5.3 show volumetric dOCT images and simulated spheroids irradiated with 1, 2, 6, and 10 Gy, respectively. In dOCT volumetric images, high frequency (green channel) intensity was predominantly observed throughout the spheroid bulk across all radiation doses, reaching its maximum intensity in the spheroid treated with 10 Gy (Fig. 5.3C-F). Conversely, simulated volumetric images demonstrated a distinct hypoxic core in the live control spheroids (Fig. 5.3G), with an increasing proportion of *Apoptotic cells* distributed throughout the spheroid bulk as radiation dose increased (Fig. 5.3H-J).

Figure 5.4 compares OCT, dOCT, FM, and simulated enface images of live control, irradiated, and formaldehyde-fixed spheroids. OCT, dOCT, and FM enface images showed

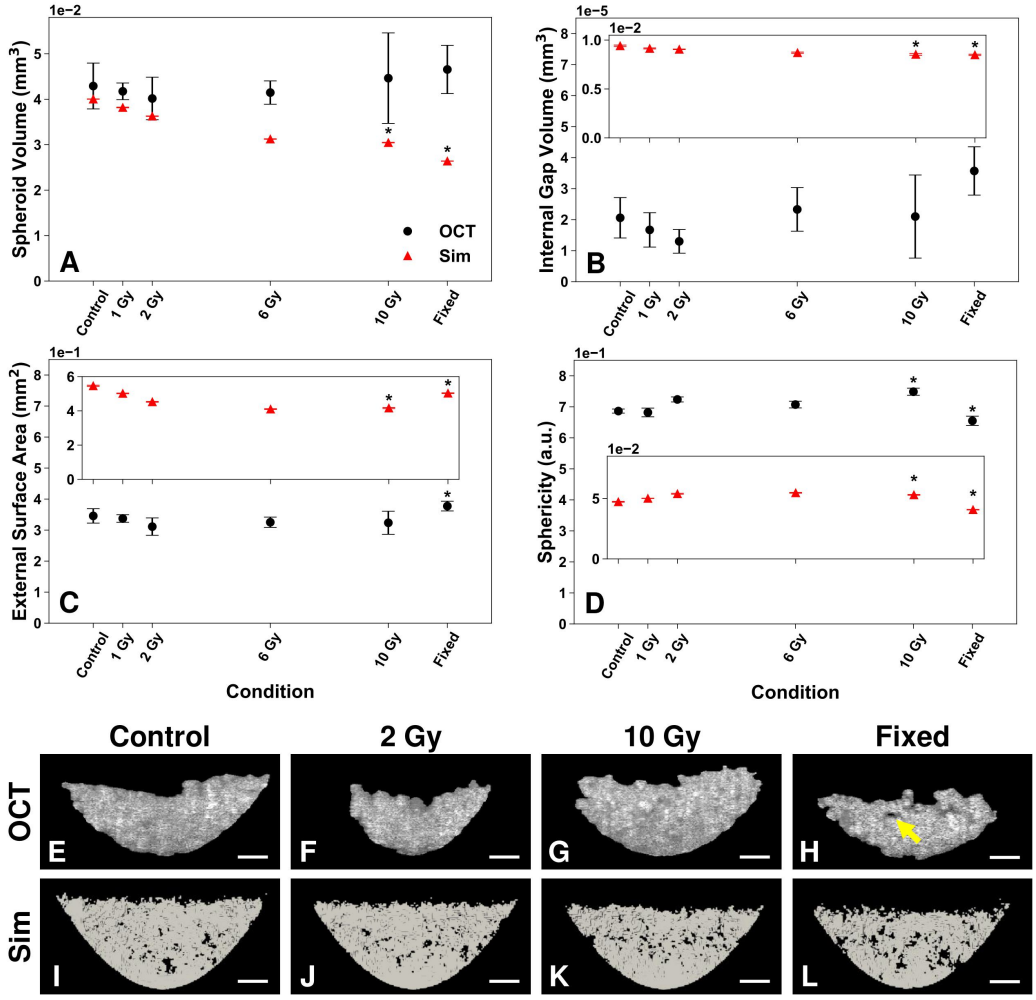


Figure 5.2: Morphological OCT and simulated analyses of live control, irradiated (1, 2, 6, and 10 Gy), and formaldehyde-fixed prostate tumor spheroids. Numerical analysis of (A) spheroid volume, (B) internal gap volume, (C) external surface area, and (D) sphericity given by Eq. 5.4. Average OCT-measured (black circle) and simulated (red triangle) values are presented with standard deviation error bar. Simulated data in (B-D) are inset. Asterisks indicate significant differences (10 Gy or fixed vs. live control; Methods Section 5.2.7). Central (third row) masked OCT B-scans and (fourth row) simulated visualizations of live control, irradiated (2 and 10 Gy), and formaldehyde-fixed spheroids. An internal gap is labeled with yellow arrow. Sim: simulation. Scale bars: 100 μm.

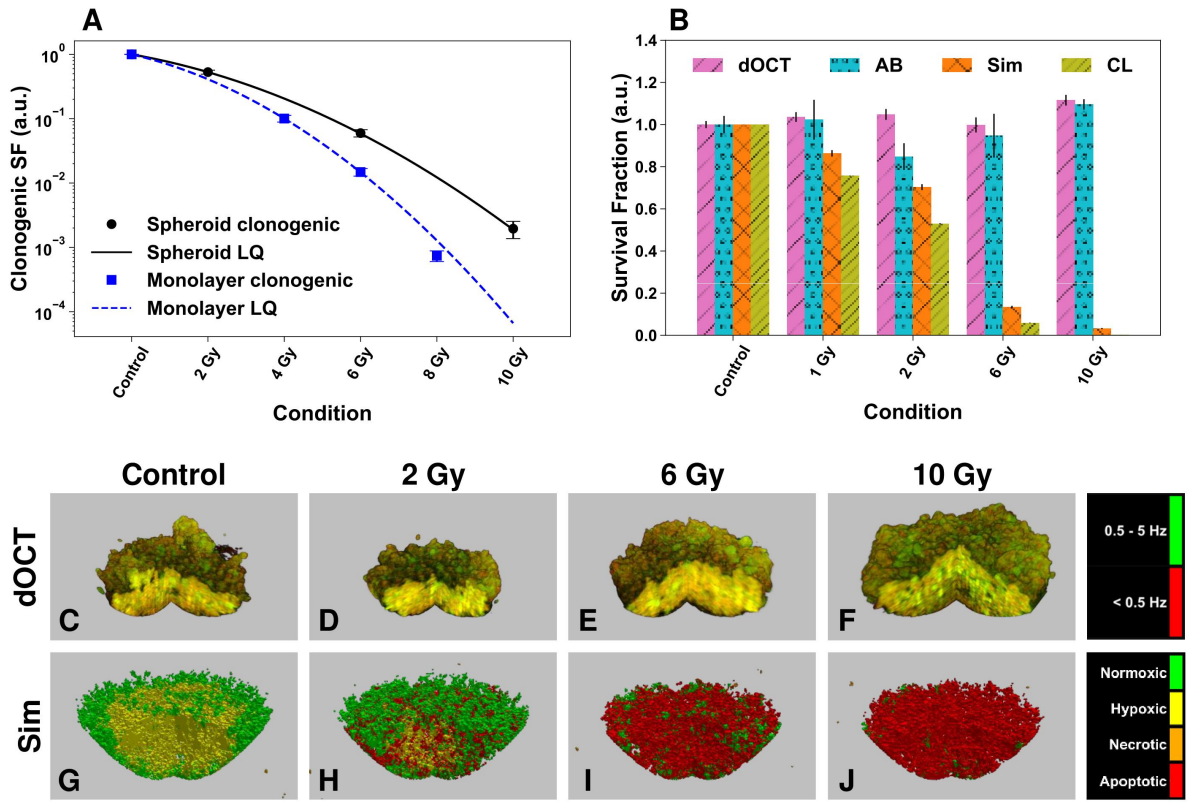


Figure 5.3: Dynamic analysis of live control and irradiated prostate tumor spheroids. (A) Clonogenic assay SF values with LQ model fit line for 3D spheroids (black circle, solid line) and 2D monolayer culture (blue square, dashed line). (B) SF of spheroids measured via normalized dynamic signal from volumetric dOCT images (purple / hatch), normalized absorbance from AB proliferation assay (blue circle hatch), simulated clonogenic assay (orange X hatch), and LQ fit from clonogenic assay (olive // hatch). Data shown are averages with error bars as described in Methods Section 5.2.7. Volumetric dOCT images (second row) and simulated visualizations (third row) of live control and irradiated (2, 6, and 10 Gy) spheroids. A central slice has been cut out of the volumes. Colormaps for dOCT (red: <0.5 Hz, green: 0.5-5 Hz); and simulation (red: *Apoptotic*, orange: *Necrotic*, yellow: *Hypoxic*, green: *Normoxic* cells). SF: survival fraction; LQ: linear-quadratic model; AB: Alamar Blue; Sim: simulation; CL: clonogenic.

minimal variation between live control spheroids and those treated with radiation; however, live control and irradiated spheroids appeared significantly different from formaldehyde-fixed spheroids (Fig. 5.4). Individual cells could be resolved in OCT enface images, with live control and irradiated spheroids appearing generally compact (Fig. 5.4A-E), whereas formaldehyde-fixed spheroids displayed noticeable internal gaps (Fig. 5.4F, yellow arrow). Similarly, individual cells and gaps were clearly resolved in dOCT images (Fig. 5.4G-L, yellow arrow). In dOCT images, green channel intensity was higher at the spheroid periphery and increased slightly with increasing radiation dose in live control and irradiated spheroids (Fig. 5.4G-K). In contrast, formaldehyde-fixed spheroids exhibited ubiquitous red channel intensity with only a few individual cells appearing green (Fig. 5.4L). In FM enface images, the live control and irradiated spheroids appeared predominantly green, with some central red fluorescence (Fig. 5.4M-Q). However, after formaldehyde fixation, the FM image was dominated by red fluorescence and exhibited minimal central green fluorescence (Fig. 5.4R). Unlike OCT, dOCT, and FM images, simulated spheroids were comprised of a progressively increasing proportion of red *Apoptotic* cells as radiation dose increased (Fig. 5.4S-W) and appeared entirely red following simulated fixation (Fig. 5.4X).

5.4 Discussion

5.4.1 Morphological measurement of radiation effects

Simulations provide a platform for visualizing and precisely quantifying the outcomes of logical experiments conducted under perfectly understood, albeit oversimplified, biological conditions [123]. Our 3D agent-based simulation assumed the spheroid grew within a symmetric paraboloid-shaped well (Eq. 5.7) embedded in an agarose gel, with uniform oxygen diffusion and uniform oxygen consumption per unit volume of living cells. At the time of simulated radiation treatment, each cell survived irradiation with a probability equal to the SF given by the experimentally derived spheroid LQ curve shown in Figure 5.3A. Under these assumptions, we observed that simulated spheroid volume (Fig. 5.2A), internal gap volume (Fig. 5.2B), and external surface area (Fig. 5.2C) decreased with increasing radiation dose, subsequently plateauing between 6 Gy and 10 Gy. According to the LQ model, the probability of cell death increased exponentially with increasing dose (Fig. 5.3A), resulting in a corresponding increase in the number of simulated *Apoptotic* cells at 24 hours after treatment (Fig. 5.4S-W). Simulated *Apoptotic* cells failed to undergo cell division; thus, spheroids treated with lower doses exhibited larger volume and surface area due to a greater number of successful cell divisions occurring between treatment and analysis.

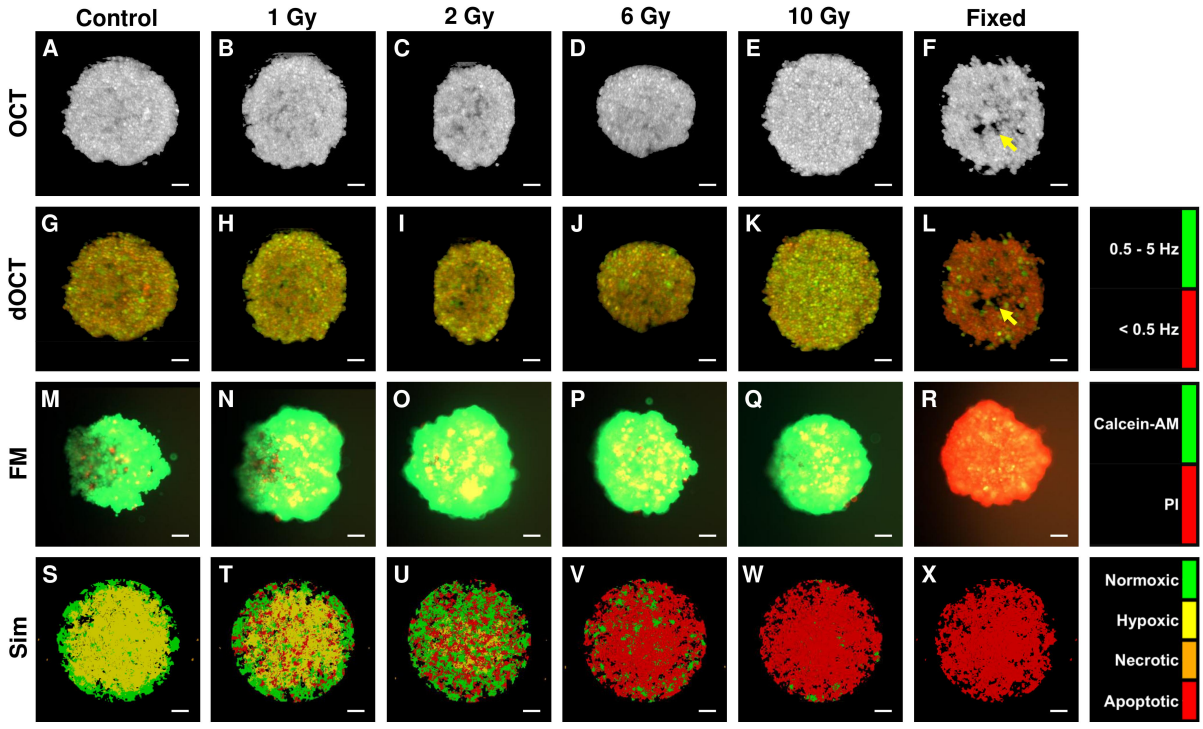


Figure 5.4: OCT maximum projection (first row), dOCT maximum projection (second row), FM (third row), and simulated (fourth row) enface images of live control, irradiated (1, 2, 6, and 10 Gy), and formaldehyde-fixed prostate tumor spheroids. An internal gap is labeled with yellow arrow. Colormaps for dOCT (red: <0.5 Hz, green: 0.5-5 Hz); FM (red: PI, green: calcein-AM); and simulation (red: *Apoptotic*, orange: *Necrotic*, yellow: *Hypoxic*, green: *Normoxic*). FM: fluorescence microscopy; propidium iodide: PI; calcein-AM: calcein acetoxymethyl; Sim: simulation. Scale bars: 100 μm.

The reduced internal gap volume in simulated spheroids treated with higher doses resulted from structural collapse caused by an increased proportion of non-adherent *Apoptotic* cells. Simulated sphericity increased with dose due to its higher sensitivity to surface area (Eq. 5.4), which decreased faster than the combined spheroid and internal gap volumes (Fig. 5.2A-D). Despite a 10% decrease in simulated SF between 6 Gy and 10 Gy (Fig. 5.3B), the corresponding morphological changes were negligible (Fig. 5.2C-D) because the simulated spheroids irradiated with 6 Gy were already predominantly composed of *Apoptotic* cells (Fig. 5.4V).

Simulated surface areas and internal gap volumes were significantly larger than those measured with volumetric OCT masks (Fig. 5.2B-C). Simulations precisely quantified these metrics with a voxel resolution of 5 μm, whereas noise and an imperfect masking process complicated interpretation of the OCT measurements, despite our system demonstrating similar axial and lateral resolutions of 2.6 μm and 6.4 μm, respectively. The observed discrepancy in surface area illustrates the coastline paradox, wherein using higher resolutions to measure fractal-like surfaces, such as coastlines or spheroid surfaces, paradoxically increases the measured value. Rather than improving accuracy, the higher resolution of the simulation merely accounts for increasingly smaller surface features that the OCT mask smooths out. Furthermore, because OCT masks prioritize containing all cells within the spheroid, the smoothing process preferentially reduces internal gap volume and consequently overestimates spheroid volume. Underestimation of gap volume by OCT masking resulted in greater discrepancy with simulation compared to its overestimation of spheroid volume since the volume affected represents a substantially larger fraction of total gap volume than of total spheroid volume (Fig. 5.2A-B).

Despite these differences in absolute magnitude, morphological trends observed in simulated spheroids irradiated with low doses corresponded well with OCT analysis. Raitanen et al. [338] similarly observed no significant size differences in PC3 spheroids irradiated with doses up to 8 Gy after 3 days. However, morphological discrepancies between simulation and OCT increased with increasing dose. Agreement was strongest for live control spheroids because the simulation was calibrated to untreated spheroid dimensions measured in Chapter 4. With higher doses, the simplified mechanism of cell death and unrealistically instantaneous apoptotic process in the simulation diverged increasingly from the complex biological processes observed experimentally.

5.4.2 Clonogenic measurement of radiation effects

In reality, radiation-induced cell death is neither instantaneous nor straightforward. Radiation damages DNA indirectly via reactive oxygen species (ROS) and directly via ionizing

tracks that create single-strand breaks (SSBs) and more lethal double-strand breaks (DSBs) [30, 40, 39]. DNA damage triggers various signaling pathways that instigate DNA repair [33, 32], the duration of which increases with the complexity of the damage and may extend beyond 24 hours [34, 35]. Radiation exposure also induces G2/M phase arrest, delaying the onset of mitosis by prolonging the G2 phase of the cell cycle, thus preventing cell division with damaged DNA [36, 37]. Persistent cell cycle arrest leads to senescence, a state in which cells stop proliferating but can remain metabolically active [38]. Cells with irreparable DNA damage may undergo mitotic catastrophe and subsequently die through some combination of apoptosis and necrosis [30, 38, 39, 33]. Thus, radiation results in clonogenic death by preventing cells from successfully performing cell division, although cells can be observed to remain metabolically active for some time after treatment [338, 345].

Consequently, the clonogenic assay remains the gold standard method for measuring cell survival after irradiation, as it directly assesses the clonogenic potential of individual cells. We measured higher clonogenic SF in prostate cancer cells cultured in 3D spheroids compared to conventional 2D monolayer culture (Fig. 5.3A). The improved clonogenic survival of spheroids compared to monolayer culture was first reported by Durand and Sutherland [168] who attributed this phenomenon to increased cell-to-cell contact and it has since been documented across various cell lines [338, 103, 351, 352, 345, 353, 354]. Additionally, irradiated spheroids exhibit reduced DNA damage [353, 338] and apoptosis [354] compared to monolayer culture. It has been suggested that the increased survival observed in spheroids may result from the presence of a quiescent hypoxic core, which has been widely documented [355, 103, 345, 339, 104]. Clinically, hypoxia significantly contributes to tumor radio-resistance, in part due to the radio-sensitizing effect of oxygen [101, 102, 43]. Cells have been observed to become quiescent under stress such as hypoxia [356, 104], and quiescence itself is known to confer radio-resistance [103, 104]. However, PC3 cells form spheroids as loose aggregates that are not tightly adherent [107, 357], and our FM results showed only a small necrotic core within live control spheroids (Fig. 5.4M). Therefore, compared to other cells lines, the contribution of a quiescent hypoxic core to the increased radio-resistance observed in PC3 spheroids relative to monolayer culture might be relatively minor.

5.4.3 Alternative measurement of radiation effects

A rapid, simple, and reliable alternative to the clonogenic assay for measuring radiation survival has long been sought [348]. The search for alternative methods is particularly salient for 3D spheroid culture, given the observation by Onozato et al. [103] that the spheroid disaggregation required for clonogenic assay can itself influence radiation response.

Our study explored dOCT as another potential alternative alongside proliferation assay for assessing radiation effects in intact spheroids.

We observed that the normalized SF values measured by dOCT were consistently higher than AB proliferation assay at each radiation dose, although these differences did not reach statistical significance (Fig. 5.3B). The dOCT method effectively distinguished intensity fluctuations due to cellular metabolism, clearly differentiating between control (Fig. 5.4G) and formaldehyde-fixed spheroids (Fig. 5.4L). Similarly, AB reduction is a well-established indicator of cellular metabolism [157]. However, the SF values measured by both dOCT and AB were substantially higher than those determined by clonogenic assay (Fig. 5.3B). While dOCT imaging and AB proliferation assay are more straightforward and efficient to perform than clonogenic assay, they capture cellular activity at only a single time point, which limits their detection of delayed radiation effects [33, 338, 345]. Indeed, the numerous signaling pathways activated by radiation repair [33, 32] and subsequent cell death [38, 334, 358] may increase cellular activity observed with dOCT and AB in the first 24 hours following irradiation. Furthermore, radiation has been reported to activate invasive and proliferative pathways mediated through epidermal growth factor receptor (EGFR) [359], integrins [360], and hypoxia inducible factor (HIF) [361], potentially increasing measured cellular activity. Moreover, dOCT measurements are sensitive not only to metabolic activity but also to physical changes in cell morphology and volume. Apoptotic cells undergo characteristic physical transformations, including shrinking, surface blebbing, and chromatin condensation (pyknosis), before nucleus fragmentation (karyorrhexis) [334]. In contrast, necrotic cells exhibit cell swelling, undergo nuclear disintegration (karyolysis), and ultimately degrade, releasing their contents [334, 38]. These physical transformations could explain the higher SF measured by dOCT compared to AB; however, the investigation of post-radiation physical changes such as blebbing and pyknosis would benefit from higher-resolution OCT imaging focused on specific regions rather than the entire spheroid volume. Additionally, high-frequency motion detected by dOCT could also reflect motion artifacts unrelated to cellular behavior, such as Brownian motion, or external scanner and camera noise.

To accurately estimate clonogenic survival with proliferation assay, Nikzad and Hashemi [169] recommended continuous measurement for several days following irradiation to characterize the radiation-induced growth delay. Future work should similarly include multiple dOCT measurements in the week following treatment to assess the delayed effect of radiation. Such growth-delay characterization could then be directly compared with clonogenic SF measurements, analogous to the approach by Buch et al. [344] using MTT proliferation assay.

The simulated SF values were lower than those measured by dOCT and AB prolifera-

tion assay, despite all methods estimating instantaneous survival at a single time point 24 hours post-irradiation (Fig. 5.3B). The discrepancy is likely due to the simplified model of radiation-induced cell death. In our model, hypoxia indirectly delayed radiation effects by slowing cellular growth, delaying attempted cell division, and consequently delaying apoptosis. However, during simulated irradiation, *Hypoxic* cells did not exhibit radio-resistance. In contrast, other models have explicitly included oxygen effects on radiation survival by modifying LQ survival with an oxygen saturation curve [362, 363]. Various investigators have also explicitly modeled the process of DNA damage repair [364, 365, 363], growth delay and cell cycle arrest [363, 366], as well as the effect of cell cycle phase on radiation survival [367, 368, 369, 370, 371]. In this regard, agent-based models provide a particularly effective platform to characterize tumor heterogeneity and explore its implications in radiation treatment.

The clonogenic assay inherently integrates these complex biological factors into a binary probability of long-term clonogenic survival, which we simulated probabilistically at the time of treatment. However, simulated SF remained higher than clonogenic SF for all doses (Fig. 5.3B) because not all cells killed by radiation had attempted cell division and become *Apoptotic* by the measurement time point, 24 hours post-irradiation. Additionally, our model assumed instantaneous cell death without explicitly modeling the duration of apoptosis, a process estimated to take approximately 24 hours [358]. At the measurement time point, many cells classified as *Apoptotic* in the simulation would realistically still be undergoing the physically and metabolically dynamic process of cell death, potentially contributing to the elevated SF values observed by both dOCT and AB proliferation assay.

5.4.4 Comparison of causes of cell death

Our study investigated multiple causes of cell death. At the time of radiation treatment, live control spheroids were also fixed with 4% formaldehyde to eliminate metabolic activity. Clonogenic assay demonstrated approximately 2% clonogenic survival in spheroids irradiated with 10 Gy (Fig. 5.3B), and FM revealed widespread cell death in formaldehyde-fixed spheroids (Fig. 5.4R). However, dOCT and FM images of control and irradiated spheroids both showed higher green channel intensity along the spheroid periphery with some central red channel intensity, whereas formaldehyde-fixed spheroids appeared almost entirely red in color (Fig. 5.4G-R). Both imaging techniques were applied 24 hours after treatment, at a time when irradiated cells remained metabolically active and structurally intact [33, 338, 345]. In contrast, fixation-induced cell death occurred quickly and efficiently. Thus, dOCT accurately detected the metabolically inactive, fixed spheroids as dynamically static, consistent with the extensive cell death observed by FM.

Morphologically, formaldehyde fixation preserved spheroid structure without significant tissue shrinkage by cross-linking proteins [335], effectively arresting spheroid morphology at the treatment time. Due to the simplified nature of our simulation, fixation was not directly simulated; instead, we approximated fixation by assuming all cells in live control spheroids at the treatment time were *Apoptotic* (Fig. 5.4X). At the time of treatment and fixation, 24 hours after seeding, the spheroids were still condensing to become more tightly aggregated (see Chapter 4). This process is reflected in the larger OCT-measured spheroid volume (Fig. 5.2A), internal gap volume (Fig. 5.2B), and external surface area (Fig. 5.2C) of formaldehyde-fixed spheroids compared to live control, although the difference was only statistically significant for surface area. In contrast, the simulated formaldehyde-fixed spheroids had significantly smaller volume (Fig. 5.2A), internal gap volume (Fig. 5.2B), and external surface area (Fig. 5.2C) compared to live control spheroids. The morphological difference between OCT measurement and simulation is likely due to the simplified modeling of the complicated and prolonged process of spheroid aggregation. Consequently, simulated spheroids were smaller and more tightly aggregated at the time of treatment and fixation, and they remained so in the complete absence of simulated cell division and growth in the 24-hour interval between fixation and analysis.

5.5 Conclusion

In conclusion, we employed a spectral-domain LF-dOCT system to acquire volumetric dOCT images of prostate tumor spheroids 24 hours following radiation treatment. Morphological trends measured by volumetric OCT analysis aligned with simulations of a novel 3D agent-based model of radiation treatment whose parameters were informed by experimental clonogenic assay data. The effects of radiation measured using dOCT showed excellent quantitative and qualitative agreement with conventional biological techniques, AB proliferation assay and FM, respectively. The strong agreement between dOCT and AB proliferation assay suggests that a longer duration of repeated dOCT measurement in tumor spheroids following radiation treatment could offer a non-invasive alternative to the clonogenic assay, eliminating the need for spheroid disaggregation.

Chapter 6

Post-treatment recovery of docetaxel-treated prostate cancer monolayer and spheroid culture

6.1 Introduction

The most prevalent cancer among North American men [1, 2], prostate cancer is clinically heterogeneous. Patients generally present with an indolent and localized disease that has a high cure rate and 5-year survival [5], but a subset of patients exhibit aggressive disease with progression and metastasis [372]. The standard of care for patients with recurrent, locally advanced, or metastatic prostate cancer is medical castration via ADT [13]. However, ADT fails in a median of 18–24 months and patients inevitably develop CRPC [23]. With the publication of two randomized phase 3 trials in 2004 [24, 25], DTX chemotherapy emerged as a new standard of care for mCRPC patients. Subsequently, DTX treatment was additionally investigated in HSPC patients and found to benefit those with high-volume metastatic disease [27, 28, 29]. As such, DTX is the first-line chemotherapeutic drug in advanced prostate cancer [13].

Following the observation of paclitaxel cytotoxicity in the late 1960s [53], DTX was discovered in 1986 via extraction from the *Taxus baccata* yew tree [55] as another member of the chemotherapeutic taxane family. Both taxanes stabilize microtubules, which prevents depolymerization during mitosis and causes cell cycle arrest in the G2/M phase via the mitotic spindle-assembly checkpoint [60, 64]. Senescence can arise from permanent cell cycle arrest [65], but arrest can also be transient if the checkpoint releases without the necessary

repair [68]. In this case, cells can experience mitotic slippage and enter a tetraploid or "pseudo-G1" phase without physically splitting into two daughter cells, leading to eventual apoptosis [64]. If cell division occurs with improperly segregated chromosomes, aberrant mitosis leads to mitotic catastrophe [69]. These non-viable cells can undergo a necrosis-like cell death after developing micronuclei as nuclear envelopes surround individual or groups of chromosomes [65]. That said, apoptosis has also been observed following mitotic catastrophe [70].

The mechanism of DTX-induced cell death has been largely observed through conventional 2D monolayer cell culture. However, cell-cell and cell-environment interactions in small 3D aggregates of cancer cells called tumor spheroids are more physiologically representative of patient tumors compared to monolayer architectures [96, 85]. Unlike the homogeneous nature of monolayer culture, heterogeneous cell populations arise in spheroids due to diffusion-limited nutrient and waste distributions [319]. These factors influence cellular morphology [162], signaling [320], proliferation [87], gene and protein expression [86], as well as drug pharmacokinetics [373], delivery [321], and resistance [82]. Consequently, there has been significant interest in using spheroid culture as an *in vitro* platform for drug discovery, testing and characterization [374, 99, 321, 373, 162, 375].

Nevertheless, the use of tumor spheroids for drug investigation is known to be tedious and time consuming [374]. Drug testing in spheroid cultures also suffers from sensitivity to spheroid size [375] and lack of reproducibility [99]. As such, thorough investigation requires analysis of different drug dosages, spheroid sizes, drug penetration into the spheroid, and impact of the spheroid environment on drug delivery. Moreover, some questions of interest cannot be accessed experimentally with adequate accuracy, particularly those related to the behavior of individual cells within the spheroid structure. This laborious combinatorial experiment design and experimental inaccessibility motivates the supplemental use of well informed *in silico* models [376]. Drug efficacy is influenced by mechanical and molecular tumor spheroid characteristics, which have been extensively modeled mathematically with *in silico* methods [123]. ABM, a discrete *in silico* method, simulates these characteristics by considering each cancer cell as an individual "agent" that responds to its local environment, including neighboring cells, nutrients, and drugs [340, 343]. The rule-based structure of ABM is well suited for performing logical experiments with perfectly understood biological mechanisms. Under the assumption of accurate parameter estimates informed by *in vitro* and/or *in vivo* measurements, *in silico* models have particular utility in mechanistic hypothesis testing and falsification [148]. With respect to chemotherapy investigation, *in silico* methods also reduce exposure to dangerous chemicals.

There has been substantial work elucidating the mechanism of DTX [60, 61, 62]. More recent work has thoroughly characterized end-of-treatment survival in prostate cancer

monolayers by proliferation assay [377, 378, 379], and to a lesser extent, clonogenic assay [380, 381, 382]. DTX-treated prostate cancer spheroids have also been investigated via proliferation assay [383, 384]. However, post-treatment recovery in the week following DTX exposure has received little investigation, despite the sometimes delayed outcomes associated with DTX-induced cell cycle arrest. Proliferation assays like the widely used, non-toxic AB measure fluorescence produced by enzyme activity associated with cellular metabolism [157]. Often employed directly at end-of-treatment, proliferation assays can also monitor longitudinal changes in cellular activity. In contrast, clonogenic assay plates cells at low density to identify those capable of colony formation via continuous reproduction and thus, directly measures clonogenic potential [166]. Clonogenic assay is typically employed to quantitatively estimate survival fraction by colony counting, but post-treatment behavior can also be qualitatively investigated through longitudinal observation of colony formation. Here, we assessed end-of-treatment survival and post-treatment recovery of DTX-treated PC3 prostate cancer cells cultured in monolayers and spheroids to measure immediate and delayed effects of DTX treatment. Measurements were performed with clonogenic and AB proliferation assays to assess cell viability and activity, respectively. Qualitative and quantitative results were compared with FM and ABM simulations.

6.2 Methods

6.2.1 Monolayer and spheroid cultures

PC3 cells (human prostate adenocarcinoma) were cultured in RPMI 1640 (Sigma-Aldrich, USA) culture medium supplemented with 10% fetal bovine serum (Thermo Fisher Scientific, USA) and 1% penicillin (Thermo Fisher Scientific, USA) and incubated in a humidified atmosphere at 37°C and 5% CO_2. On day 0 of the experiment, monolayer cell culture was plated in T-25 culture flasks. Concurrently, prostate tumor spheroids were seeded and cultured in 2% agarose 3D Petri Dish (MicroTissues Inc., USA) gels. The 9×9 array of wells contained in each agarose gel was seeded with a suspension of PC3 cells such that spheroids of approximately 1,000 cells formed in each well (Fig. 6.1A).

6.2.2 Docetaxel chemotherapy treatment

24 hours post-seeding, monolayer and spheroid cultures were exposed to 0, 0.1, 1, and 10 nM DTX diluted in 0.9% NaCl in water (saline) for a duration of 48 hours (Fig. 6.1B).

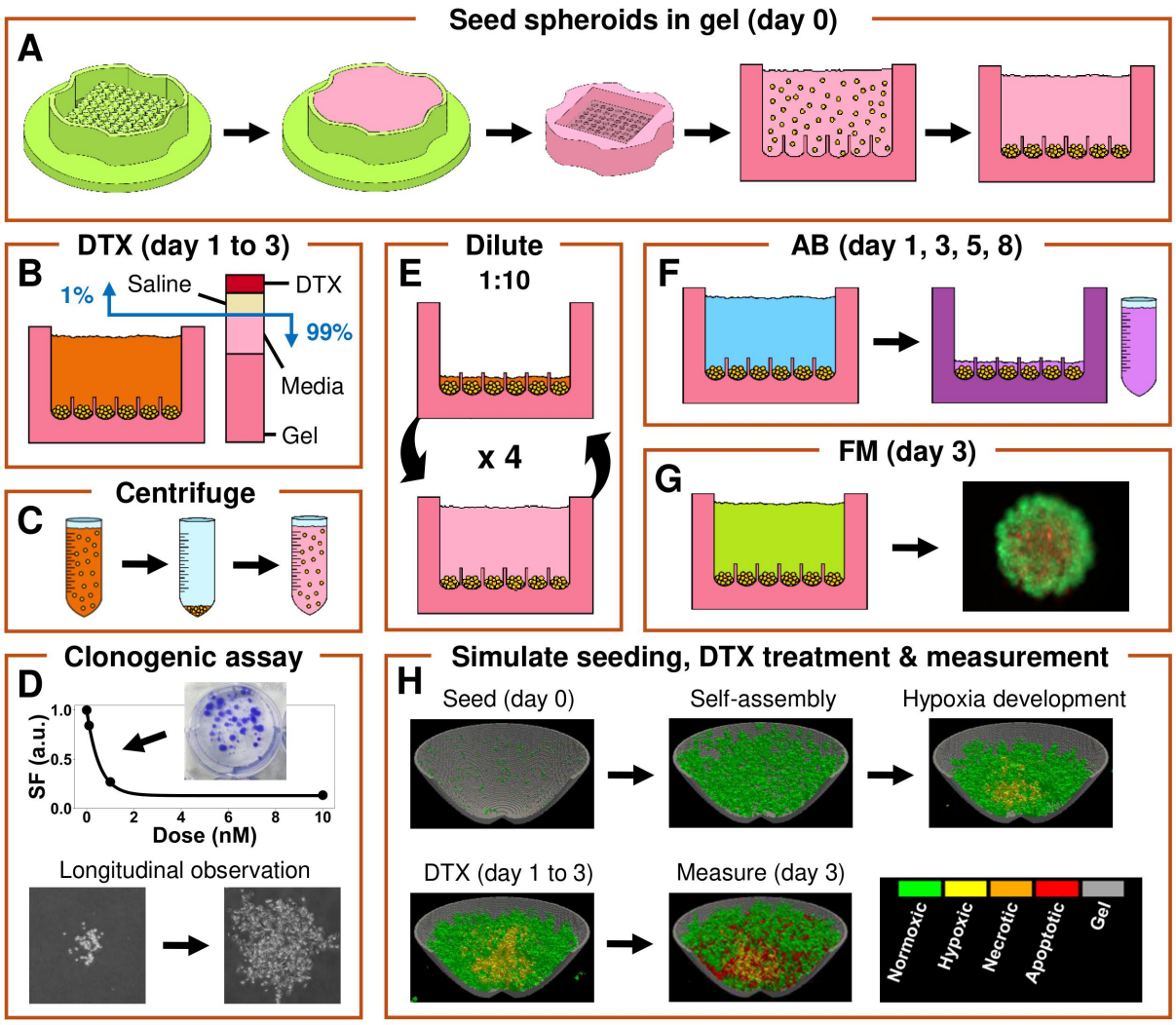


Figure 6.1: (A) Cells (yellow) seeded into agarose gels (pink) created from molds (green) self-assemble into prostate tumor spheroids in the bottom of wells. (B) Spheroids were exposed to 0, 0.1, 1, and 10 nM DTX diluted in saline with a 1:100 ratio of DTX in saline to culture medium and gel for 48 hours. DTX was removed by (C) centrifuging for (D) SF calculation and longitudinal observation via clonogenic assay, or by (E) serial dilution of spheroid-containing gels for (F) AB proliferation assay and (G) FM. (H) 3D ABM of spheroid seeding, DTX treatment, and measurement applied fitted clonogenic survival from experiment during treatment. DTX: docetaxel; SF: survival fraction; AB: Alamar Blue; FM: fluorescence microscopy; ABM: agent-based modeling.

At each dose, a 1:100 ratio of DTX in saline to culture medium was maintained, with control samples exposed to 1:100 of saline to culture medium. In spheroid culture, the 500 μL gel was included in the culture medium volume for calculating treatment concentration. After the 48 hour treatment period, measurement was performed. For monolayer culture, DTX treatment solution was removed from culture flasks which were washed with PBS (Wisent Inc., Canada) before replacement with supplemented culture medium. For spheroid culture, the DTX removal process depended on the measurement. For clonongenic assay, which requires spheroids to be disaggregated into a cell suspension, DTX was removed by centrifuge (Fig. 6.1C). However, AB proliferation assay and FM require intact spheroids to remain in the agarose gel, which retains its concentration of DTX after removal of surrounding treatment media. As such, DTX removal for these methods was achieved by serial dilution (Fig. 6.1E): all liquid was carefully removed from around and inside the gel and replaced drop-wise with 5 mL of RPMI, then gels were left to soak for one hour. The process was repeated four times so that the DTX in each 500 μL gel was diluted by a factor of 10,000. In the final dilution before incubation, spheroid gels received supplemented culture medium.

6.2.3 Clonogenic assay

Clonogenic assay was performed with monolayer and spheroid cultures immediately after the 48 hour treatment period to measure clonogenic survival and observe longitudinal colony formation (Fig. 6.1D). Our detailed protocol for spheroid disaggregation is described in Chapter 5. Briefly, for each dose of DTX, all spheroids were transferred from gels into a falcon tube for mechanical vortexing and incubation for two hours. Then, supernatant was removed and replaced with 0.25% trypsin-EDTA (Thermo Fisher Scientific, USA) before ten minutes of incubation, mechanical vortexing, and centrifuging for cell counting. Monolayer culture was incubated with 0.25% trypsin-EDTA for 3 minutes then centrifuged for cell counting. Counted cells from each dose were plated at low densities in 6-well plates for approximately two weeks of growth. Bright-field microscopy images of plated colony formation were taken regularly with an Olympus CKX53 inverted microscope. For colony counting, plates were fixed with 4% formaldehyde (Thermo Fisher Scientific, USA) in PBS for 1 hour then stained with 0.5% crystal violet (Thermo Fisher Scientific, USA) dissolved in water for 30 minutes. The plating efficiency (PE) was calculated using control samples as follows:

$$\mathrm{PE} = \frac{N_{\mathrm{colonies}}}{N_{\mathrm{plated}}} \tag{6.1}$$

DTX dose	Cells/monolayer (per T-25 flask)	Cells/spheroid (per well)
Control	13,000	1,000
0.1 nM	13,000	1,000
1 nM	19,000	1,000
10 nM	400,000	1,000

Table 6.1: Cells seeded AB proliferation assays of monolayer and spheroid cultures per T-25 flask and well in 3D Petri Dish gel, respectively.

Here, N_{colonies} and N_{plated} are the number of colonies counted and plated, respectively. Survival fraction (SF) was calculated using PE as follows:

$$\text{SF} = \frac{N_{\text{colonies}}}{N_{\text{plated}} \times \text{PE}} \tag{6.2}$$

We developed the following novel model for least-squares fitting of SF values for each dose d:

$$\text{SF} = \alpha \exp(-\beta d) + \gamma \tag{6.3}$$

with parameters α, β, and γ extracted separately for monolayer and spheroid cultures, under the assumption that $\alpha + \gamma = 1$. That is, the fitted curve is assumed to predict a SF of 1 at zero dose.

6.2.4 Alamar Blue proliferation assay

AB proliferation assay was performed with monolayer and spheroid cultures to measure average cellular proliferation pre-treatment on day 1, immediately after the 48 hour treatment period on day 3, and throughout post-treatment recovery on days 5 and 8 (Fig. 6.1F). Cells were not removed from their culturing vessels between treatment and AB measurement. Therefore, T-25 culture flasks for AB readings of monolayer culture were seeded according to dose (Table 6.1). Control samples were seeded as sparsely as possible to prevent the monolayer from becoming confluent by day 8, while ensuring a sufficient sample of cells for the pre-treatment measurement. Monolayers treated with the highest dose of 10 nM were seeded as densely as possible to ensure a sufficient number of cells remained adhered post-treatment, while still preventing confluency at the pre-treatment measurement. In contrast, all spheroids were formed of approximately 1,000 cells.

Prior to each AB measurement, samples were incubated in 5% AB (Sigma-Aldrich, USA) in RPMI for 3 hours at 37°C with 5% CO_2 in a humidified atmosphere. For spheroids, culture medium was first removed from around and inside the gel, then 190 μL of AB solution in RPMI was added to achieve the 5% concentration throughout the 500 μL gel. Following incubation, AB solution was extracted and its absorbance intensity recorded at 570 nm using a BioTek Synergy H1 microplate reader. For each experimental condition, three 100 μL aliquots of AB solution were removed from one monolayer-containing T-25 flasks and three spheroid-containing gels. Each AB measurement day, T-25 flasks and gels without cells were processed identically and measured to determine background absorbance, which was subtracted from that day's monolayer and spheroid measurements, respectively. Due to the different seeding conditions, each experimental condition was then normalized to its day 1 measurement.

6.2.5 Fluorescence microscopy

FM was performed immediately after the 48 hour treatment period to visualize cell death within spheroids using the Live/Dead Cell Viability assay (Sigma-Aldrich, USA) (Fig. 6.1G). Live cells were labeled green with calcein acetoxymethyl (calcein-AM) [155] and dead cells were labeled red using propidium iodide (PI) [152]. Each gel was carefully emptied of culture medium and incubated for one hour with 0.2875 μL calcein-AM, 1.15 μL PI, 95 μL RPMI, and 95 μL PBS. Then, a Zeiss Axio Observer widefield microscope was used to capture fluorescent images of spheroids in gels that had been transferred to coverslip-bottomed Petri dishes. The microscope was operated by ZEN2 Blue Edition software and equipped with an Axiocam 506 mono camera and a Plan-Apochromat 63/1.4 Oil Ph3 M27 objective (Carl Zeiss Microscopy LLC, USA). An incubation plate (PECON, Germany) maintained the temperature at 37°C during imaging.

6.2.6 Simulation

In this study, the ABM of 3D tumor spheroid growth developed in Chapter 5 was adapted to simulate DTX treatment (Fig. 6.1H). Briefly, 1,000 well oxygenated *Normoxic* tumor cells were placed randomly within a curved well inside the agarose gel. The cells fell to the bottom of the well under gravity and, as living cells energetically prefer contact with other living cells, self-assembled into a spheroid. A constant partial pressure of oxygen was maintained in the culture medium. Controlled through a PDE, oxygen diffused through the spheroid and was consumed by cells. The local partial pressure of oxygen determined

cell growth, with volume increasing according to a Michaelis-Menten saturation curve. Once a cell achieved a sufficient volume, it performed cell division. Oxygen-deprivation due to diffusion-limited oxygenation and competition caused *Normoxic* cells to reversibly become *Hypoxic*. Under severe oxygen deficiency, cells irreversibly became *Necrotic*. The 5 μm-voxelized simulation space was 810 μm across and 405 μm deep, and the simulation time scale was determined such that *Normoxic* cells performed cell division approximately every 24 hours. The shape of the curved well and dimensions of simulated spheroids after 24 hours were calibrated to those in OCT images in Chapter 4. Then, 24 hours post-seeding, DTX treatment was simulated through a new PDE that was added to the model. Throughout the 48 hour treatment period, the simulated dose was maintained in the culture medium and gel and diffused through the spheroid with a diffusion coefficient of 256 $\mu m^2 \cdot s^{-1}$ employed by Lai and Friedman [385] and Gordon [386]. During treatment, when cells attempted to perform cell division, they succeeded probabilistically according to the fitted curve (Eq. 6.3) derived from spheroid clonogenic experiments. Cells that failed to divide irreversibly became *Apoptotic*.

Following the 48 hour treatment period, numerical analysis of simulated spheroids treated with 0, 0.1, 1, and 10 nM DTX was performed. Simulated clonogenic SF was calculated using Eq. 6.2 by estimating N_{colonies} and N_{plated} as the number of living cells and the total number of cells in the spheroid, respectively. Simulated AB SF was calculated by estimating cellular activity of living and dying cells and normalizing to control. Living cells contributed to the calculation through the sum of each cell's oxygenation. *Apoptotic* cells were assumed to be in cell cycle arrest for 24 hours following failed cell division [69], before undergoing the active process of apoptosis for 24 hours [334]. Cells actively undergoing apoptosis contributed to the AB estimation by assuming an equivalent level of activity as a fully oxygenated living cell. Simulated growth was estimated as the sum of each cell's oxygenation normalized to that of control, and thus represents the simulated AB SF value without the contribution of active apoptosis.

Each dose was simulated ten times for statistical analysis, as the Monte Carlo simulation is stochastic in nature. A detailed mathematical description of the model can be found in Chapter 3 and Appendix C.

6.2.7 Statistics

For comparison with clonogenic SF measurements, post-treatment day 3 AB absorbance was further normalized to that day's control measurement. As AB measurements were performed in triplicate, individual values with obviously high leverage (i.e. that exerted

undue influence on two similar values) were removed. All measurements are presented as averages with error bars. As described by Gupta et al. [350], clonogenic SF error was estimated by Fieller's theorem using a 95% confidence interval from a Poisson distribution. All other error bars depict standard deviation. Clongenic EC_{50} values for monolayer and spheroid cultures were determined by identifying the dose that yielded a SF of 0.50 according to the model fit given by Eq. 6.3.

6.3 Results

Figure 6.2 summarizes end-of-treatment survival measurements performed immediately after the 48 hour DTX treatment period. Figure 6.2A shows that compared to monolayer culture, clonogenic survival of spheroid culture was comparable at 0.1 nM DTX, lower at 1 nM DTX, and higher at 10 nM DTX, with good fit to Eq. 6.3 for each culture type. Clonogenic EC_{50} was 0.76 nM and 0.45 nM DTX in monolayer and spheroid culture, respectively. Experimental and simulated clonogenic and AB spheroid measurements immediately post-treatment period are given in Figure 6.2B. Simulated spheroid clonogenic survival agrees well with experimental measurement and both significantly decrease with increasing dose. In contrast, we observed that with increasing DTX dose, experimental and simulated AB measurement increased before decreasing to minima of 87% and 89% of control at 10 nM, respectively (Fig. 6.2B). Simulated growth, which removes the contribution of apoptotic activity from the simulated AB calculation, is comparable to simulated clonogenic survival (Fig. 6.2B).

Figure 6.3 shows FM and simulated images of spheroids immediately post-treatment. In the first row, FM enface images of all DTX doses reveal peripheral green intensity with a faint central red spheroid core in control that increases with dose (Fig. 6.3A-D). The second and third rows of Figure 6.3 show simulated enface and volumetric images, respectively. The simulated control spheroid contains a yellow hypoxic core surrounding green proliferating *Normoxic* cells (Fig. 6.3E,I). In the simulated spheroid treated with 0.1 nM DTX, red *Apoptotic* cells appear sparsely throughout the hypoxic spheroid bulk (Fig. 6.3F,J). At higher doses of 1 nM and 10 nM DTX, there is no hypoxia and the majority of the spheroid is comprised of red *Apoptotic* cells with few green *Normoxic* cells throughout (Fig. 6.3G-H,K-L).

The longitudinal observation of post-treatment recovery in spheroid and monolayer cultures are shown in Figures 6.4 and 6.5, respectively. AB measurement was performed pre-treatment on day 1, immediately post-treatment on day 3, and throughout treatment

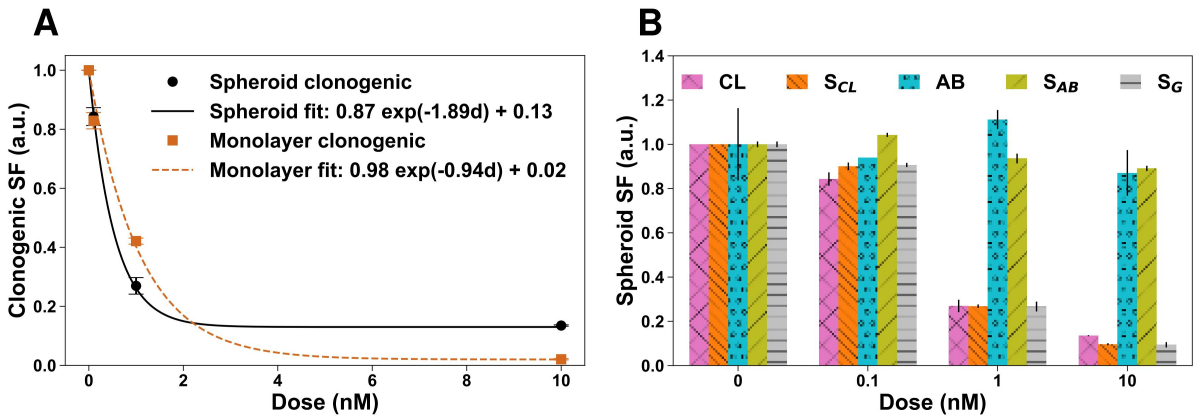


Figure 6.2: Measurements performed immediately after the 48 hour treatment period with 0, 0.1, 1, and 10 nM DTX. (A) Clonogenic assay SF values with model fit line given by Eq. 6.3 for 3D spheroids (black circle, solid line) and 2D monolayer culture (orange square, dashed line). (B) SF of spheroids calculated via clonogenic assay measurement (purple x hatch), simulated clonogenic assay S_{CL} (orange \\ hatch), normalized absorbance from AB proliferation assay measurement (blue circle hatch), simulated AB proliferation assay S_{AB} (olive / hatch), and simulated growth S_G (grey - hatch). Data shown are averages with error bars as described in Methods Section 6.2.7. DTX: docetaxel; SF: survival fraction; CL: clonogenic assay; AB: Alamar Blue; G: growth.

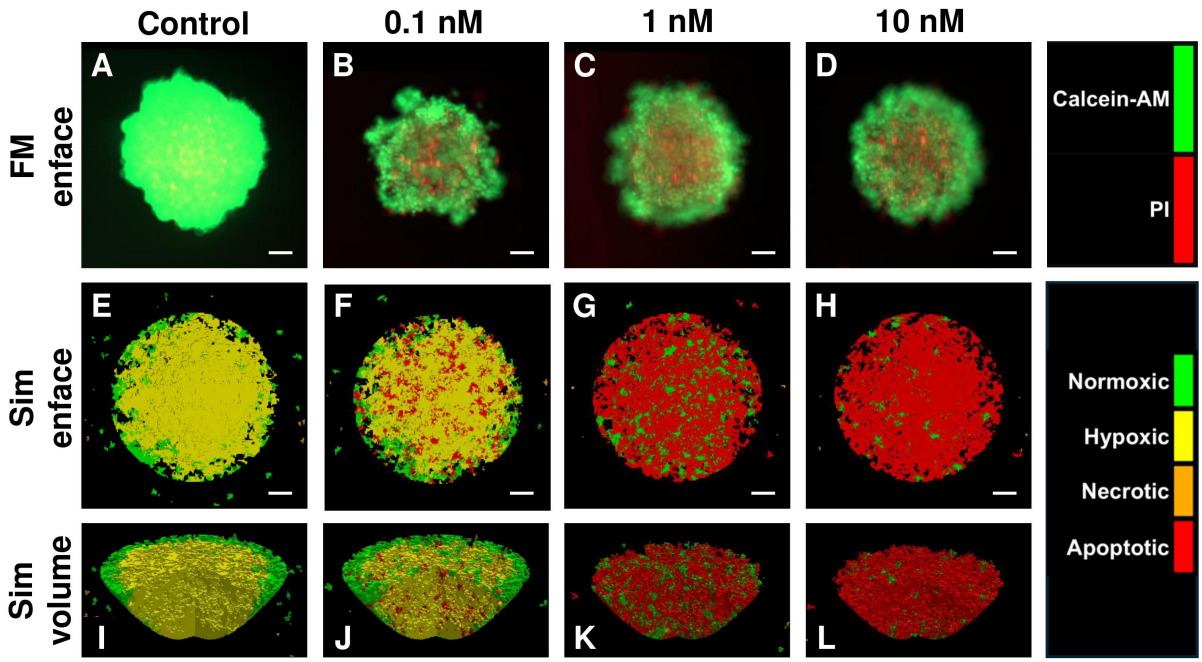


Figure 6.3: FM enface (first row), simulated enface (second row), and simulated volumetric (third row) images of spheroids treated with 0, 0.1, 1, and 10 nM DTX. A central slice has been cut out of the volumes. Colormaps for FM (red: PI, green: calcein-AM); and simulation (red: *Apoptotic*, orange: *Necrotic*, yellow: *Hypoxic*, green: *Normoxic*). DTX: docetaxel; FM: fluorescence microscopy; PI: propidium iodide; calcein-AM: calcein acetoxymethyl; Sim: simulation. Scale bars: 100 μm.

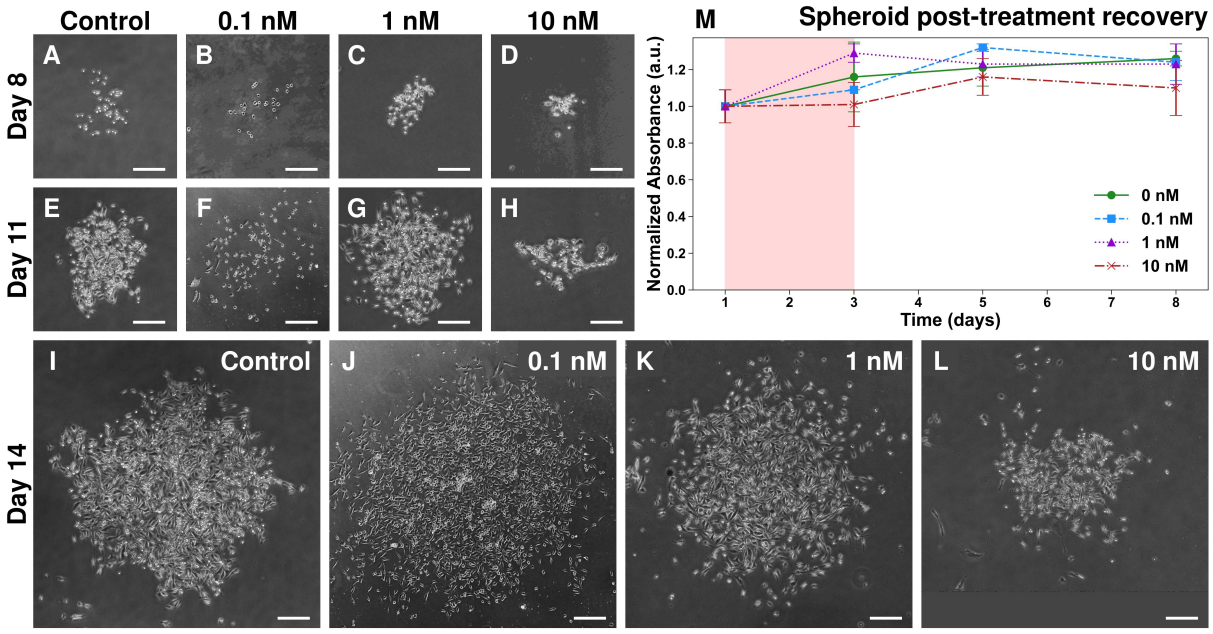


Figure 6.4: Longitudinal observation of post-treatment recovery in cells treated in spheroid culture with 0, 0.1, 1, and 10 nM DTX. Colony formation on day 8 (first row), day 11 (second row), and day 14 (third row) following removal of DTX and plating at low density in 2D on day 3. Normalized AB absorbance (top right) of intact spheroids treated with 0 nM (green circle, solid line), 0.1 nM (blue square, dashed line), 1 nM (purple triangle, dotted line), and 10 nM (orange cross, dot-dashed line) DTX. Exposure to DTX treatment occurred throughout pink shaded region. DTX: docetaxel; AB: Alamar Blue. Scale bars: 100 μm.

recovery on days 5 and 8. In spheroid culture, normalized AB absorbance fluctuated between 87% and 132% of the pre-treatment absorbance (Fig. 6.4M), whereas corresponding measurements in monolayer culture had much larger variations between 49% and 1225% (Fig. 6.5M). Normalized AB absorbance in control spheroids and those treated with lower DTX doses of 0.1 nM and 1 nM DTX were largely comparable, with each dose achieving the highest measurement on a different day and colony formation appearing largely similar (Fig. 6.4). In contrast, normalized AB absorbance in spheroids treated with 10 nM DTX was slightly lower than all other doses but remained higher than pre-treatment levels at each measurement time (Fig. 6.4M). Clonogenic plating of cells from spheroids treated with 10 nM DTX revealed colonies that were recognizable but smaller than all other doses each day (Fig. 6.4D,H,L). In monolayer culture, control and 1 nM DTX treated cells had

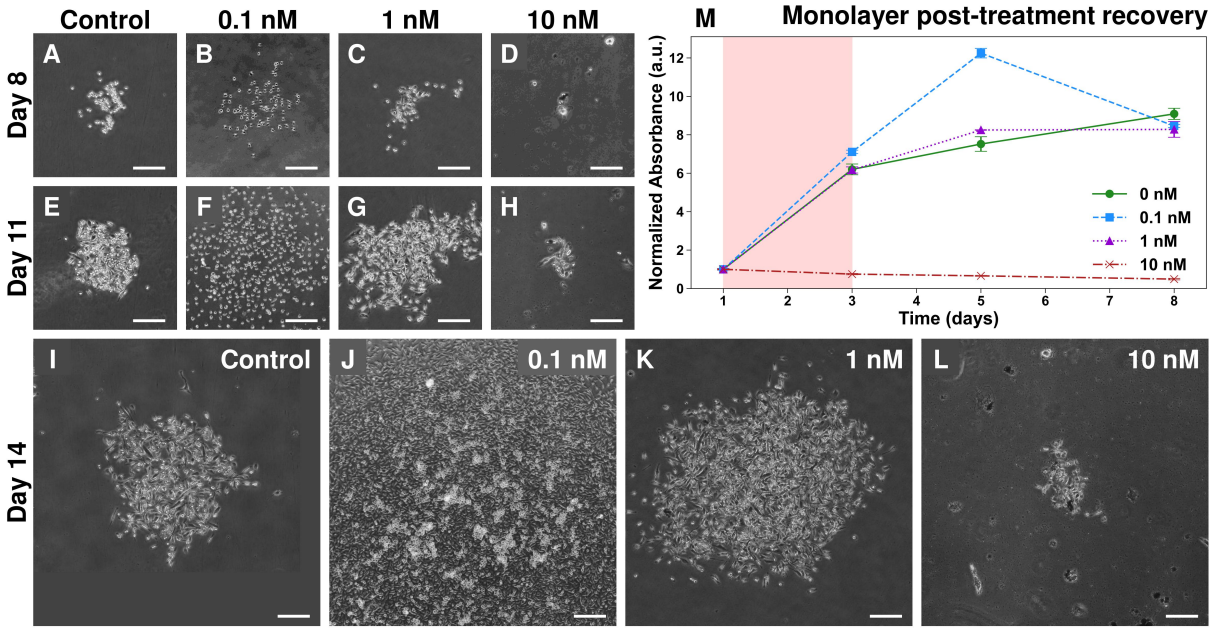


Figure 6.5: Longitudinal observation of post-treatment recovery in cells treated in monolayer culture with 0, 0.1, 1, and 10 nM DTX. Colony formation on day 8 (first row), day 11 (second row), and day 14 (third row) following removal of DTX and plating at low density in 2D on day 3. Normalized AB absorbance (top right) of monolayer culture treated with 0 nM (green circle, solid line), 0.1 nM (blue square, dashed line), 1 nM (purple triangle, dotted line), and 10 nM (orange cross, dot-dashed line) DTX. Exposure to DTX treatment occurred throughout pink shaded region. DTX: docetaxel; AB: Alamar Blue. Scale bars: 100 μm.

comparable normalized AB absorbance, but on days 3 and 5 cells treated with 0.1 nM DTX had much larger values before falling to a value between control and 1 nM DTX by day 8 (Fig. 6.5M). Nonetheless, colony formation by 0.1 nM DTX treated monolayer cells was significantly faster and larger than all other conditions (Fig. 6.5B,F,J). AB absorbance measured in monolayer cells treated with 10 nM DTX decreased from pre-treatment AB absorbance levels throughout the measurement period (Fig. 6.5M) and barely formed colonies by day 14 (Fig. 6.5L).

6.4 Discussion

Clinically, prostate cancer patients are prescribed DTX according to body surface area, typically at 75 mg/m^2 delivered by 1 hour of IV every three weeks [387]. Pharmacokinetic and pharmacodynamic study of this DTX regime observed an average peak plasma concentration of 4 μM (3.26 μg/mL) with an average 2.41 hour exposure to doses above 200 nM (0.16 μg/mL) [388]. However, this dynamic delivery is difficult to reproduce with *in vitro* experiments, which generally expose cells to a constant DTX concentration for some period of time. Moreover, the dose limiting factor in DTX treatment is primarily hematologic toxicity [23]; as such, *in vitro* experiment cannot inform clinical delivery or dosage, but rather may be used to characterize and investigate the cellular response. Previous *in vitro* investigations treating prostate cancer cells with DTX have employed a wide variety of exposure times between 2 hours [389] and three weeks [390], with DTX doses ranging seven orders of magnitude from 6.4 pM [391] to 96 μM [392]. Here, we exposed PC3 cells cultured in monolayers and spheroids to 0.1, 1, and 10 nM DTX for 48 hours. We assessed end-of-treatment survival and post-treatment recovery with clonogenic assay and AB proliferation assay.

6.4.1 End-of-treatment survival

As a disease, cancer is defined by uncontrolled cellular proliferation [393]. Since clonogenic assay directly and uniquely measures the ability of treated cells to continually divide successfully, it is particularly well suited for evaluating the success of cancer treatment. Clonogenic assay was first used to measure radiation effect in the field of radiobiology, where it remains the gold standard [167]. That said, its use has broadened to measure the effect of chemotherapies and other drug treatments [166]. Nonetheless, there has been limited clonogenic investigation of DTX-treated monolayers of prostate cancer cells, and to the best of our knowledge, none with spheroids.

We observed a higher clonogenic EC_{50} of 0.76 nM DTX in PC3 monolayer culture compared to 0.45 nM DTX in spheroid culture. However, cells cultured in monolayers were more susceptible to high doses of DTX and demonstrated approximately 2% clonogenic survival at 10 nM (Fig. 6.2A). Counterintuitively, after a longer exposure of three or four days compared to our 48 hours, Lange et al. [380] found a larger clonogenic EC_{50} of 1 nM DTX in PC3 cells cultured in monolayer. Likewise, clonogenic survival of PC3 monolayer culture treated with DTX for longer durations has yielded larger SF values of 93% at 0.1 nM after 10 days [381] and 57% at 1 nM after 72 hours [382], compared to our observations of 83% and 42% at 0.1 nM and 1 nM, respectively (Fig. 6.2A). However, by treating suspension culture of PC3 cells with DTX 2 hours, Karshafian et al. [389] and Almasri and Karshafian [394] observed similar clonogenic SF values at 0.1 nM of 81% and 75%, respectively. Linke et al. [395] observed equivalently low clonogenic survival of PC3 monolayers at 10 nM, albeit with 24 hours of post-treatment recovery before clonogenic plating. As with variation in measured survival within PC3 cell culture experiments, survival has also been found to vary by prostate cancer cell line [382, 380]. In particular, clonogenic assay has also been performed with DTX-treated monolayer cultures of LNCaP [396, 382, 380], LNCaP-derived C4-2 [397] and C4-2B [390], DU145 [398, 382, 380, 399, 395], VCaP [396], RWPE-2 [400], and 22Rv1 [401] prostate cancer cell lines. Notably, comparison between cell lines may be complicated as investigation of breast cancer cell lines has revealed cell-line-specific variation in the mechanism of DTX-induced cell death [402], potentially due to differences in regulation of proliferation, contact inhibition, or cell cycle checkpoints.

For comparison with clonogenic assay, one of our AB measurement times was at end-of-treatment. Similar investigations of PC3 monolayers treated for 48 hours with DTX have observed a wide range of EC_{50} values using various proliferation assays, including 0.984 nM [403] and approximately 10 nM [404] via MTT, and 33.89 nM via CCK-8 [405]. Monteverde et al. [403] identified a minimum survival of 10% at 2 nM DTX by MTT relative to control, whereas we found end-of-treatment normalized AB absorbance in monolayers was 12% at 10 nM and comparable to control at 1 nM (Fig. 6.5 M). In comparison, end-of-treatment AB measurement fluctuated much less in spheroid culture and spheroids treated with 10 nM DTX demonstrated 87% absorbance compared to control. Pereira et al. [406] similarly evaluated PC3 spheroids treated with DTX for 48 hours by AB and observed approximately 55% absorbance at 1 nM and 10 nM compared to control. Other investigators have similarly performed proliferation assay and observed higher DTX survival in spheroids compared to monolayers with LNCaP [407, 408], DU145 [409, 392, 408], and PC3 [408] cell lines.

Investigations of DTX-treated prostate cancer cells via proliferation assay far outnumber those via clonogenic assay. We suspect one reason for the disparity is that, even for investigation of monolayer culture, clonogenic assay is an arduous method that demands

trial and error. Moreover, we could not find a single investigation that performed clonogenic assay of DTX-treated prostate cancer spheroids, likely because the nature of 3D cell culture makes clonogenic assay much harder to perform. While AB measurement is performed with intact spheroids, longitudinal observation of colony formation by clonogenic assay requires spheroid disaggregation by a physically stressful process involving aggressive enzymatic dissociation by trypsin, mechanical vortexing, and centrifuging.

Furthermore, it is experimentally challenging to employ clonogenic and proliferation assays with the same doses of DTX. Experiments employing clonogenic assay have exposed PC3 monolayers to DTX concentrations up to 0.1 nM [394], 0.5 nM [381], 5 nM [380], 9 nM [389], and 10 nM [382]; in comparison, proliferation assays performed with PC3 monolayers used much larger maximal DTX concentrations of 10 nM [404], 62.5 nM [405], 100 nM [403], 250 nM [410], and 1 μM [395]. Proliferation assays of PC3 spheroids have employed even higher concentrations of 200 nM [408], 2.5 μM [410], and 10 μM [406]. The discrepancy in DTX dosage required to differentiate the effect of treatment via clonogenic and proliferation assays may be due to treated cells that lack reproductive viability while remaining metabolically active, for example by senescence. Moreover, longitudinal observation via clonogenic assay isolates viability measurement to the initial population of cells. In contrast, longitudinal proliferation assay measurements are complicated by detecting the cellular activity of both the initially surviving cells as well as their progeny.

For example, Zemskova et al. [400] performed clonogenic assay with RWPE-2 monolayers with doses up to 20 nM DTX, but all proliferation assays were performed via MTT with 100 nM DTX. Fujiike et al. [392] attempted to investigate DTX treatment of monolayer and spheroid DU-145 culture with both AB and clonogenic assay. By AB proliferation assay, they found that EC_{50} values were approximately 10-fold higher in spheroids compared to monolayer culture. However, they observed no colony formation via clonogenic assay by plating 300 viable cells in 6-well plates after 24 hours of treatment with doses ranging from 1 to 96 μM DTX. In contrast, to perform clonogenic assay for 10 nM monolayer-treated and spheroid-treated cells, we plated 2,400 cells and 12,000 cells in 6-well plates, respectively. Despite the higher SF of spheroid culture at 10 nM, the process of disaggregation lowers spheroid PE such that a higher number of cells must be plated to produce a statistically sound number of colonies. This restricts the upper dose limit accessible to analysis by clonogenic assay, especially for spheroid culture. Potentially, our AB analysis was limited by imposing maximum doses that were also feasible for clonogenic assay, resulting in little variation with dose in spheroids at end-of-treatment (Fig. 6.2B). Nonetheless, long exposure time to higher doses is not clinically achievable [388]; rather, here we are interested in the recovery and clonogenic potential of prostate cancer cells following treatment.

6.4.2 Post-treatment recovery

In addition to pre-treatment and end-of-treatment measurements on days 1 and 3, we also measured AB absorbance of monolayer (Fig. 6.5M) and spheroid (Fig. 6.4M) cultures in their treatment vessels throughout post-treatment recovery on days 5 and 8. After plating clonogenic assay at end-of-treatment, we documented longitudinal colony formation for qualitative comparison with AB trends (Fig. 6.4, 6.5). Some post-treatment measurements have been made previously in DTX-treated PC3 monolayers at 24 hours [395] and 48 hours [411, 410] post-treatment, and with C4-2B cells after 72 hours [390]. However, these post-treatment measurements were not designed to investigate recovery, but rather are a byproduct of sensitization agent delivery [411] or observing drug synergism [390]. Bromma et al. [391] performed longitudinal post-treatment observation of 24 hour DTX-treated LNCaP monolayer and spheroids using CellTiter-Glo 3D proliferation assay at 2 days post-treatment and at 6 and 13 days post-treatment, respectively. They estimated spheroid volume regularly from enface bright-field microscopy images, but they only investigated one dose of DTX and did not measure proliferation assay at pre-treatment or end-of-treatment.

We observed better post-treatment recovery in spheroids, with little fluctuation in AB measurement by DTX dose (Fig. 6.4M) and higher clonogenic survival at higher doses (Fig. 6.2A). In contrast, 10 nM treated monolayer culture never recovered to pre-treatment AB measurement (Fig. 6.5M). Not only was monolayer culture more susceptible to high doses, but a low dose of 0.1 nM appeared to stimulate rather than inhibit monolayer growth (Fig. 6.5M). We observed a similar effect to a lesser extent in spheroid culture (Fig. 6.4M). Colony formation occurred faster in 0.1 nM treated monolayer cells than any other condition, followed by 0.1 nM treated spheroids (Fig. 6.4, 6.5). Despite demonstrating an increased speed of colony formation, monolayer and spheroid culture treated with 0.1 nM DTX produced fewer colonies than control (Fig. 6.2). Compared to untreated monolayers, other investigations of prostate cancer cells have observed higher proliferation after treatment for 48 hours with doses 0.1 nM DTX and lower in PC3 monolayers [404, 403, 410] and 24 hours with doses 1 nM DTX and lower in RWPE-2 monolayers [400].

These observations are consistent with a controversial phenomenon called hormesis [412], whereby an agent exhibits a biphasic dose response with growth inhibition at high doses and growth stimulation at low doses. The concept of hormesis was introduced in the 1880s by Schulz [413] and coined in 1943 by Southam and Ehrlich [414]. It has since been extensively documented and debated [415, 416], particularly in the area of radiobiology [417, 418]. However, chemotherapeutic hormesis has not been well characterized, especially outside of immortalized cell lines [419]. In post hoc analysis of their previous work [420], Yoshimasu et al. [421] identified negative inhibition rates of DTX with *in vitro* histoculture

drug response assay (HDRA) of samples from patients with non-small-cell lung cancer (NSCLC). They suggested hormesis as the cause, but employed a large dose of 124 μM (100 μg/mL) DTX for a duration of 7 days. They analyzed the same specimens with a range of paclitaxel doses and observed growth stimulation at low doses [422], but had not designed the experiment around the low dose range required to validate hormetic behavior [421]. Chang et al. [419] observed paclitaxel-induced hormesis by MTS in NOS3 ovarian cancer cell monolayers, but did not perform clonogenic assay for comparison. In general, hormesis has been widely demonstrated in cell culture [415], but investigations have been critiqued for lacking appropriate experimental controls or sufficient sample of doses [416]. Our study was also not designed to reveal DTX hormesis, but may suggest the first measurement of its kind in prostate cancer spheroid culture, which motivates further investigation.

6.4.3 Simulation

At end-of-treatment, simulated clonogenic and AB values were similar to experiment (Fig. 6.2B). Notably, simulated AB also demonstrated hormesis with higher simulated proliferation observed at 0.1 nM DTX compared to control; however, simulated and experimental clonogenic results agreed well and decreased monotonically with dose (Fig. 6.2B). In this way, simulated spheroids visually indicated cells that are destined for reproductive death, whereas FM images reveal transient cellular health that rather visualizes AB proliferation (Fig. 6.3). As suggested in Chapter 5, cellular activity may be increased following treatment due to the numerous signaling pathways activated by cell repair [423] and death [334, 358]. Simulated AB values were calculated under the assumption that following an inactive period of cell cycle arrest, successfully treated cells undergo an active apoptotic process. However, these cells have lost clonogenic potential and thus do not contribute to simulated clonogenic survival. Removing transient apoptotic activity from simulated AB calculations to represent growth alone removes the hormetic effect and calls into the question the mechanism of higher measured AB proliferation under low DTX dose (Fig. 6.2B). The low dose growth stimulation measured by proliferation assay may be a byproduct of cellular activity associated with DTX-induced cell death or ineffectual repair.

Using a PDE model, Hinow et al. [424] explored drug-specific parameters and similarly observed increased proliferation in a simulated *in vivo* tumor following treatment with a DTX-like drug. However, the growth stimulation was caused by an imbalance of drug-induced cell killing and drug decay rather than a hormetic effect of low dose. DTX-specific simulations have been performed with an ABM of monolayer culture [425], an optimal control framework [426], and a PDE model [385]. Kaura et al. [299] investigated paclitaxel

treatment with a 2D CPM based on the spheroid model developed previously by the authors [376]. They observed FM [376] and simulated [299, 376] images with increased paclitaxel effect along the spheroid periphery, in contrast to the cell death observed centrally in our FM and throughout our simulated images (Fig. 6.3). Similar to the wide range of conflicting experimental *in vitro* DTX measurements, ABM simulations of chemotherapy treatment have made contradictory conclusions that periodic drug administration [427] or constant dosing [428] is more effective.

6.4.4 Limitations

To the best of our knowledge, there has not been previous clonogenic measurement of DTX-treated spheroid culture or longitudinal observation of post-treatment DTX-dose dependent effects in prostate cancer monolayer or spheroid culture. Still, the time scale of our observation was limited by monolayer culture becoming confluent by day 8 of the experiment. To ensure a sufficient number of cells at each AB measurement, we seeded monolayer culture at different cell densities by dose (Table 6.1), and normalized each dose to its own pre-treatment measurement. Unlike many other investigations that diluted DTX in cytotoxic DMSO, we employed 0.9% saline for our dilutions, but as with the other studies, we present normalized results that we expect to remove any effect of dilution medium. While the upper dose limit was restricted by clonogenic plating of spheroid culture, AB measurement limited the number of doses investigated due to the laborious process of removing DTX from spheroid culture gels by four serial dilutions. For each dilution of each gel, 5 mL of RPMI was added dropwise to avoid mechanically agitating the spheroids. Nevertheless, cell loss was unavoidable, but increased post-treatment AB absorbance from pre-treatment levels indicated spheroids continued to grow (Fig. 6.4M). However, interpretation of longitudinal AB absorbance in spheroids may be complicated by our previous observation of cyclical AB measurements described in Chapter 4. Clonogenic plating of spheroid culture is also limited by removing the cells from the spheroid structure, which changes their phenotype [319, 96] and potentially their post-treatment response to DTX.

In contrast to our *in silico* model, previous models of chemotherapy treatment have simulated cell cycle phases and arrest [429], repair [376], and resistance [427]. Nonetheless, our model incorporates clonogenic survival measurements made in spheroid culture that integrate these complicated biological phenomena into a binary probability of reproductive survival or death. A direction for future work involving the model could include the evaluation of drug synergy and combination therapies, as has been previously simulated with DTX and other chemotherapeutics [299, 376], anti-angiogenic agent [385], ADT [426],

targeted therapy [430], and immunotherapy [431]. Combination therapy with radiation is of particular interest because DTX arrests and synchronizes cells in G2-M [60], which is the most radiosensitive phase in the cell cycle [432].

6.5 Conclusion

In conclusion, we assessed end-of-treatment survival and post-treatment recovery via proliferation and clonogenic assays in PC3 cells cultured in monolayers and spheroids that were exposed to 0.1, 1, and 10 nM DTX for 48 hours. To the best of our knowledge, we performed the first clonogenic measurement of DTX-treated prostate tumor spheroids and dose-dependent longitudinal observation of post-treatment recovery. We observed growth stimulation by low dose DTX in monolayer and, to a lesser extent, spheroid culture via AB proliferation assay. While clonogenic assay did not measure improved survival under low dose treatment, observation of colony formation demonstrated faster and larger colony formation by surviving cells. With parameters informed by experimental clonogenic assay data, simulation of a novel 3D ABM of DTX treatment suggested the hormetic effect measured by proliferation assay may have been influenced by the active process of apoptosis. Future work exploring DTX hormesis should sample a sufficient number of doses with careful attention to experimental controls.

Chapter 7

Conclusion

7.1 Summary

This dissertation investigated and validated emerging and under-used *in vitro* tools for characterizing prostate tumor spheroid growth and response to treatment. To this end, spheroids were observed throughout two weeks of growth and following treatment with radiation and DTX chemotherapy.

I modified a previously developed dOCT frequency banding technique and for the first time, quantified and validated it to conventional biological methods for measuring cellular activity. Quantitative dOCT measurement of spheroids that were fixed with formaldehyde to remove metabolic activity varied each day, indicating bias from external noise or variable system performance. I mitigated these effects in live spheroid measurement with background subtraction of the average dOCT-measured activity in formaldehyde-fixed spheroids each day. However, dOCT images could not be similarly standardized in a spatially sensitive manner, which complicated qualitative interpretation. Fixing the spheroid in place and performing a registered voxel-by-voxel fixation subtraction could standardize the dOCT images, but only at the cost of violating the non-invasive nature of the technique.

Alongside AB proliferation assay, fixation-subtracted dOCT measurement revealed a cyclic longitudinal growth pattern in prostate tumor spheroids cultured via 3D Petri Dish gels. I isolated spheroids from the surrounding culture medium and gel in volumetric OCT images by developing a novel semi-automated masking process. Morphological analysis of masked OCT images of spheroids supported the proposed mechanism that the cyclic

activity was due to fluctuating spheroid compaction and concomitant nutrient access. In contrast to FM, dOCT failed to resolve the progressive development of a necrotic spheroid core. One potential reason for the disagreement could be the lack of specificity demonstrated by the dOCT method. Following treatment with radiation, dOCT demonstrated excellent quantitative and qualitative agreement with AB proliferation assay and FM, respectively. The differential agreement of dOCT with post-radiation FM suggests that the method may be better suited for measuring the tidy nature of apoptotic cell death.

To the best of my knowledge, I performed the first clonogenic analysis of DTX-treated spheroids in conjunction with the first dose-dependent post-treatment recovery analysis of DTX-treated prostate cancer cells. The gold standard method for measuring cell survival following radiation treatment is the clonogenic assay, although its use has also expanded to assess the efficacy of drug treatment. It quantifies the delayed effects of treatment by directly identifying cells capable of sustained reproduction through colony formation. However, performing clonogenic assay with spheroids is challenging as it requires spheroids to be disaggregated and plated in 2D, which changes the post-treatment behavior of the cells and decreases plating efficient, consequently reducing experiment feasibility. Moreover, quantification of colonies is provided at the cost of more nuanced characterization. Qualitative observation of colony formation in parallel with post-treatment AB proliferation assay found low-dose stimulated growth rates indicative of DTX hormesis, but with no survival benefit. The effect was observed in monolayer culture as well as in spheroids, albeit to a lesser extent.

The discussed mechanisms and experimental observations were questioned by novel *in silico* CPMs of prostate tumor spheroid treatment. They enabled interpolation and visualization of experiment conditions for the purpose of understanding previous measurements and informing future experimental exploration. As a primarily phenomenological modeling platform, the CPMs were validated to experiment via volumetric OCT images and clonogenic assay.

7.2 Future work

Despite being applied to characterize response to conventional cancer treatments here, the future of these *in vitro* tools is brightest in the area of novel personalized cancer treatments. As a 3D micro-metastasis model, spheroids recapitulate *in vivo* morphology and gene and protein profiles better, albeit imperfectly, compared to conventional monolayer culture. As such, tumor spheroids enable initial investigations of targeted treatments that act on specific molecular targets unique to cancer cells. Bridging the gap between conventional

in vitro monolayer culture and the *in vivo* patient tumor environment in this manner can potentially reduce and replace some animal studies in the process of novel treatment development. However, many of the gold standard conventional *in vitro* methods, like FM and clonogenic assay, are challenged by the 3D nature of tumor spheroids. Capitalizing on the benefits provided by spheroids requires an updated set of *in vitro* tools for use by multi-disciplinary teams in the development of research questions and the design of experiments that attempt to answer them.

Our tools must thoughtfully address our questions. With respect to measuring the efficacy of cancer treatments, post-treatment proliferation and capacity for tumor repopulation require different measurement techniques. In particular, many treatment effects are delayed and require longitudinal measurement with thoughtful controls. Moreover, cell geometry impacts treatment response not only during treatment but also throughout post-treatment recovery and measurement. Experimental techniques that modify the sample, either by introducing an exogenous agent or by disagreggating a 3D structure, can impact the measurement. dOCT provides a volumetric, non-invasive, quantitative method for spatially resolved evaluation of cellular activity throughout tumor spheroids. In addition to directly measuring the effect of novel cancer treatments on *in vitro* cellular morphology and activity, dOCT could also find utility in surgical tumor resection. Given its demonstrated capacity for differentiating cell types, post-operative or even intra-operative dOCT could complement or substitute histology in identifying if surgical margins are positive for cancer. The work contained in this thesis is a first step towards validating emerging and under-used tools with the goal of generating trust for their use in never-before measured contexts.

References

[1] Siegel RL, Kratzer TB, Giaquinto AN, Sung H, Jemal A. Cancer statistics, 2025. Ca. 2025;75(1):10.

[2] Brenner DR, Gillis J, Demers AA, Ellison LF, Billette JM, Zhang SX, et al. Projected estimates of cancer in Canada in 2024. CMAJ. 2024 May;196(18):E615-23. Available from: https://www.cmaj.ca/content/196/18/E615.

[3] Izes JK, McBride TP. In: Overview and Active Surveillance of Prostate Cancer. Cham: Springer International Publishing; 2021. p. 7-19. Available from: https://doi.org/10.1007/978-3-030-52021-2_2.

[4] Kim CS, et al. Management of advanced prostate cancer. Springer; 2018.

[5] Siegel RL, Miller KD, Wagle NS, Jemal A. Cancer statistics, 2023. CA: A Cancer Journal for Clinicians. 2023;73(1):17-48. Available from: https://onlinelibrary.wiley.com/doi/abs/10.3322/caac.21763.

[6] Smith NJ, Cross WR. Counseling the Patient with Newly Diagnosed Prostate Cancer, Stage by Stage. Prostate Cancer: Diagnosis and clinical management. 2014:116-35.

[7] Bill-Axelson A, Holmberg L, Garmo H, Rider JR, Taari K, Busch C, et al. Radical prostatectomy or watchful waiting in early prostate cancer. New England Journal of Medicine. 2014;370(10):932-42.

[8] Wilt TJ, Vo TN, Langsetmo L, Dahm P, Wheeler T, Aronson WJ, et al. Radical prostatectomy or observation for clinically localized prostate cancer: extended follow-up of the Prostate Cancer Intervention Versus Observation Trial (PIVOT). European urology. 2020;77(6):713-24.

[9] Kim JJ, Hong SK. Identifying the Best Candidate for Radical Prostatectomy in High-Risk Prostate Cancer. Management of Advanced Prostate Cancer. 2018:11-9.

[10] Kim JH. Adjuvant Therapy in Locally Advanced Prostate Cancer. Management of Advanced Prostate Cancer. 2018:51-7.

[11] Freedland SJ, Humphreys EB, Mangold LA, Eisenberger M, Dorey FJ, Walsh PC, et al. Risk of prostate cancer–specific mortality following biochemical recurrence after radical prostatectomy. Jama. 2005;294(4):433-9.

[12] Pound CR, Partin AW, Eisenberger MA, Chan DW, Pearson JD, Walsh PC. Natural history of progression after PSA elevation following radical prostatectomy. Jama. 1999;281(17):1591-7.

[13] Moon KT, Yoo TK. Systemic Chemotherapy for Metastatic Hormone-Sensitive Prostate Cancer. In: Management of Advanced Prostate Cancer. Springer; 2018. p. 159-65.

[14] Lee SU, Cho KH. The Roles of Radiotherapy, Androgen Deprivation Therapy, and Their Combination for Locally Advanced Prostate Cancer. Management of Advanced Prostate Cancer. 2018:67-76.

[15] McLaughlin PW, Liss AL, Nguyen PL, Assimos DG, D'Amico AV, Gottschalk AR, et al. ACR appropriateness criteria® locally advanced, high-risk prostate cancer. American Journal of Clinical Oncology. 2017;40(1):1-10.

[16] Pilepich MV, Winter K, Lawton CA, Krisch RE, Wolkov HB, Movsas B, et al. Androgen suppression adjuvant to definitive radiotherapy in prostate carcinoma—long-term results of phase III RTOG 85–31. International Journal of Radiation Oncology* Biology* Physics. 2005;61(5):1285-90.

[17] Roach III M, Bae K, Speight J, Wolkov HB, Rubin P, Lee RJ, et al. Short-term neoadjuvant androgen deprivation therapy and external-beam radiotherapy for locally advanced prostate cancer: long-term results of RTOG 8610. Journal of Clinical Oncology. 2008;26(4):585-91.

[18] Bolla M, Van Tienhoven G, Warde P, Dubois JB, Mirimanoff RO, Storme G, et al. External irradiation with or without long-term androgen suppression for prostate cancer with high metastatic risk: 10-year results of an EORTC randomised study. The lancet oncology. 2010;11(11):1066-73.

[19] Denham JW, Steigler A, Lamb DS, Joseph D, Turner S, Matthews J, et al. Short-term neoadjuvant androgen deprivation and radiotherapy for locally advanced prostate

cancer: 10-year data from the TROG 96.01 randomised trial. The lancet oncology. 2011;12(5):451-9.

[20] Mason MD, Parulekar WR, Sydes MR, Brundage M, Kirkbride P, Gospodarowicz M, et al. Final report of the intergroup randomized study of combined androgen-deprivation therapy plus radiotherapy versus androgen-deprivation therapy alone in locally advanced prostate cancer. Journal of Clinical Oncology. 2015;33(19):2143-50.

[21] Widmark A, Klepp O, Solberg A, Damber JE, Angelsen A, Fransson P, et al. Endocrine treatment, with or without radiotherapy, in locally advanced prostate cancer (SPCG-7/SFUO-3): an open randomised phase III trial. The Lancet. 2009;373(9660):301-8.

[22] Freedland S, Eastham J, Shore N. Androgen deprivation therapy and estrogen deficiency induced adverse effects in the treatment of prostate cancer. Prostate cancer and prostatic diseases. 2009;12(4):333-8.

[23] Phillips CK, Petrylak DP. Docetaxel. Drug Management of Prostate Cancer. 2010:133-46.

[24] Tannock IF, De Wit R, Berry WR, Horti J, Pluzanska A, Chi KN, et al. Docetaxel plus prednisone or mitoxantrone plus prednisone for advanced prostate cancer. New England Journal of Medicine. 2004;351(15):1502-12.

[25] Petrylak DP, Tangen CM, Hussain MH, Lara Jr PN, Jones JA, Taplin ME, et al. Docetaxel and estramustine compared with mitoxantrone and prednisone for advanced refractory prostate cancer. New England Journal of Medicine. 2004;351(15):1513-20.

[26] Gravis G, Fizazi K, Joly F, Oudard S, Priou F, Esterni B, et al. Androgen-deprivation therapy alone or with docetaxel in non-castrate metastatic prostate cancer (GETUG-AFU 15): a randomised, open-label, phase 3 trial. The lancet oncology. 2013;14(2):149-58.

[27] Sweeney CJ, Chen YH, Carducci M, Liu G, Jarrard DF, Eisenberger M, et al. Chemohormonal therapy in metastatic hormone-sensitive prostate cancer. New England Journal of Medicine. 2015;373(8):737-46.

[28] James ND, Sydes MR, Clarke NW, Mason MD, Dearnaley DP, Spears MR, et al. Addition of docetaxel, zoledronic acid, or both to first-line long-term hormone therapy in prostate cancer (STAMPEDE): survival results from an adaptive, multiarm,

multistage, platform randomised controlled trial. The Lancet. 2016;387(10024):1163-77.

[29] Gravis G, Boher JM, Joly F, Soulié M, Albiges L, Priou F, et al. Androgen deprivation therapy (ADT) plus docetaxel versus ADT alone in metastatic non castrate prostate cancer: impact of metastatic burden and long-term survival analysis of the randomized phase 3 GETUG-AFU15 trial. European urology. 2016;70(2):256-62.

[30] Hall E. Radiobiology for the radiologist. Lippincott Williams & Wilkins; 2006.

[31] Carlson DJ, Stewart RD, Semenenko VA, Sandison GA. Combined use of Monte Carlo DNA damage simulations and deterministic repair models to examine putative mechanisms of cell killing. Radiation research. 2008;169(4):447-59.

[32] Lomax ME, Folkes LK, O'Neill P. Biological Consequences of Radiation-induced DNA Damage: Relevance to Radiotherapy. Clinical Oncology. 2013 Oct;25(10):578-85. Available from: https://www.clinicaloncologyonline.net/article/S0936-6555(13)00247-1/fulltext.

[33] Wang JS, Wang HJ, Qian HL. Biological effects of radiation on cancer cells. Mil Med Res. 2018 Jun;5(1):20.

[34] Reynolds P, Anderson JA, Harper JV, Hill MA, Botchway SW, Parker AW, et al. The dynamics of Ku70/80 and DNA-PKcs at DSBs induced by ionizing radiation is dependent on the complexity of damage. Nucleic acids research. 2012;40(21):10821-31.

[35] Schmid TE, Dollinger G, Beisker W, Hable V, Greubel C, Auer S, et al. Differences in the kinetics of γ-H2AX fluorescence decay after exposure to low and high LET radiation. International journal of radiation biology. 2010;86(8):682-91.

[36] O'Connell MJ, Walworth NC, Carr AM. The G2-phase DNA-damage checkpoint. Trends in cell biology. 2000;10(7):296-303.

[37] Rainey M, Black E, Zachos G, Gillespie D. Chk2 is required for optimal mitotic delay in response to irradiation-induced DNA damage incurred in G2 phase. Oncogene. 2008;27(7):896-906.

[38] Lauber K, Ernst A, Orth M, Herrmann M, Belka C. Dying cell clearance and its impact on the outcome of tumor radiotherapy. Frontiers in oncology. 2012;2:116.

[39] Kim W, Lee S, Seo D, Kim D, Kim K, Kim E, et al. Cellular stress responses in radiotherapy. Cells. 2019;8(9):1105.

[40] Srinivas US, Tan BW, Vellayappan BA, Jeyasekharan AD. ROS and the DNA damage response in cancer. Redox biology. 2019;25:101084.

[41] Taylor MA, Das BC, Ray SK. Targeting autophagy for combating chemoresistance and radioresistance in glioblastoma. Apoptosis. 2018;23(11):563-75.

[42] Withers HR. The four R's of radiotherapy. In: Advances in radiation biology. vol. 5. Elsevier; 1975. p. 241-71.

[43] Rey S, Schito L, Koritzinsky M, Wouters BG. Molecular targeting of hypoxia in radiotherapy. Advanced Drug Delivery Reviews. 2017;109:45-62.

[44] Steel GG, McMillan TJ, Peacock J. The 5Rs of radiobiology. International journal of radiation biology. 1989;56(6):1045-8.

[45] Brown JM, Carlson DJ, Brenner DJ. The tumor radiobiology of SRS and SBRT: are more than the 5 Rs involved? International Journal of Radiation Oncology* Biology* Physics. 2014;88(2):254-62.

[46] K SACHS PH, DJ BRENNER R. Review the link between low-LET dose-response relations and the underlying kinetics of damage production/repair/misrepair. International journal of radiation biology. 1997;72(4):351-74.

[47] Brenner DJ, Hlatky L, Hahnfeldt P, Huang Y, Sachs R. The linear-quadratic model and most other common radiobiological models result in similar predictions of time-dose relationships. Radiation research. 1998;150(1):83-91.

[48] Thames Jr HD, Withers HR, Peters LJ, Fletcher GH. Changes in early and late radiation responses with altered dose fractionation: implications for dose-survival relationships. International Journal of Radiation Oncology* Biology* Physics. 1982;8(2):219-26.

[49] Barendsen G. Dose fractionation, dose rate and iso-effect relationships for normal tissue responses. International Journal of Radiation Oncology* Biology* Physics. 1982;8(11):1981-97.

[50] Dörr W. Radiobiology of tissue reactions. Annals of the ICRP. 2015;44(1_suppl):58-68.

[51] Yeoh EE, Botten RJ, Butters J, Di Matteo AC, Holloway RH, Fowler J. Hypofractionated versus conventionally fractionated radiotherapy for prostate carcinoma: final results of phase III randomized trial. International Journal of Radiation Oncology* Biology* Physics. 2011;81(5):1271-8.

[52] Brenner DJ, Sachs RK, Peters LJ, Withers HR, Hall EJ. We forget at our peril the lessons built into the α/β model. International journal of radiation oncology, biology, physics. 2012;82(4):1312-4.

[53] Douros J, Suffness M. New natural products under development at the National Cancer Institute. In: New Drugs in Cancer Chemotherapy. Springer; 1981. p. 153-75.

[54] Wani MC, Taylor HL, Wall ME, Coggon P, McPhail AT. Plant antitumor agents. VI. Isolation and structure of taxol, a novel antileukemic and antitumor agent from Taxus brevifolia. Journal of the American Chemical Society. 1971;93(9):2325-7.

[55] Lavelle F, Gueritte-Voegelein F, Guenard D. Taxotere: from yew's needles to clinical practice. Bulletin du cancer. 1993;80(4):326-38.

[56] Bissery MC, Nohynek G, Sanderink GJ, Lavelie F. Docetaxel (Taxotere®) a review of preclinical and clinical experience. Part I: preclinical experience. Anti-cancer drugs. 1995;6(3):339-55.

[57] Ringel I, Horwitz SB. Studies with RP 56976 (taxotere): a semisynthetic analogue of taxol. JNCI: Journal of the National Cancer Institute. 1991;83(4):288-91.

[58] Webster LK, Woodcock DM, Rischin D, Millward MJ. Cremophor: Pharmacological activity of an" inert" solubiliser. Journal of Oncology Pharmacy Practice. 1997;3(4):186-92.

[59] Van Tellingen O, Huizing M, Panday V, Schellens J, Nooijen W, Beijnen J. Cremophor EL causes (pseudo-) non-linear pharmacokinetics of paclitaxel in patients. British journal of cancer. 1999;81(2):330-5.

[60] Parness J, Horwitz SB. Taxol binds to polymerized tubulin in vitro. The Journal of cell biology. 1981;91(2):479-87.

[61] Schiff PB, Fant J, Horwitz SB. Promotion of microtubule assembly in vitro by taxol. Nature. 1979;277(5698):665-7.

[62] Schiff PB, Horwitz SB. Taxol stabilizes microtubules in mouse fibroblast cells. Proceedings of the National Academy of Sciences. 1980;77(3):1561-5.

[63] Chan GK, Yen TJ. The mitotic checkpoint: a signaling pathway that allows a single unattached kinetochore to inhibit mitotic exit. PROGRESS IN CELL CYCLE RESEARCH. 2003;5:431-40.

[64] Tao W. The mitotic checkpoint in cancer therapy. Cell Cycle. 2005;4(11):1495-9.

[65] Roninson IB, Broude EV, Chang BD. If not apoptosis, then what? Treatment-induced senescence and mitotic catastrophe in tumor cells. Drug Resistance Updates. 2001;4(5):303-13.

[66] Kops GJ, Weaver BA, Cleveland DW. On the road to cancer: aneuploidy and the mitotic checkpoint. Nature Reviews Cancer. 2005;5(10):773-85.

[67] Lanni JS, Jacks T. Characterization of the p53-dependent postmitotic checkpoint following spindle disruption. Molecular and cellular biology. 1998;18(2):1055-64.

[68] Vogel C, Kienitz A, Hofmann I, Müller R, Bastians H. Crosstalk of the mitotic spindle assembly checkpoint with p53 to prevent polyploidy. Oncogene. 2004;23(41):6845-53.

[69] Morse DL, Gray H, Payne CM, Gillies RJ. Docetaxel induces cell death through mitotic catastrophe in human breast cancer cells. Molecular cancer therapeutics. 2005;4(10):1495-504.

[70] Jordan MA, Wendell K, Gardiner S, Brent Derry W, Copp H, Wilson L. Mitotic block induced in HeLa cells by low concentrations of paclitaxel (Taxol) results in abnormal mitotic exit and apoptotic cell death. Cancer research. 1996;56(4):816-25.

[71] Haldar S, Chintapalli J, Croce CM. Taxol induces bcl-2 phosphorylation and death of prostate cancer cells. Cancer research. 1996;56(6):1253-5.

[72] Stein C. Mechanisms of action of taxanes in prostate cancer. In: Seminars in oncology. vol. 26; 1999. p. 3-7.

[73] Pienta KJ. Preclinical mechanisms of action of docetaxel and docetaxel combinations in prostate cancer. In: Seminars in oncology. vol. 28. Elsevier; 2001. p. 3-7.

[74] McDonnell TJ, Troncoso P, Brisbay SM, Logothetis C, Chung LW, Hsieh JT, et al. Expression of the protooncogene bcl-2 in the prostate and its association with emergence of androgen-independent prostate cancer. Cancer research. 1992;52(24):6940-4.

[75] Colombel M, Symmans F, Gil S, O'Toole KM, Chopin D, Benson M, et al. Detection of the apoptosis-suppressing oncoprotein bc1-2 in hormone-refractory human prostate cancers. The American journal of pathology. 1993;143(2):390.

[76] Kraus LA, Samuel SK, Schmid SM, Dykes DJ, Waud WR, Bissery MC. The mechanism of action of docetaxel (Taxotere®) in xenograft models is not limited to bcl-2 phosphorylation. Investigational new drugs. 2003;21:259-68.

[77] Hanahan D, Weinberg RA. The hallmarks of cancer. cell. 2000;100(1):57-70.

[78] Hanahan D, Weinberg RA. Hallmarks of cancer: the next generation. cell. 2011;144(5):646-74.

[79] Langdon SP, Langdon SP. Cancer cell culture. Springer; 2003.

[80] Quail DF, Joyce JA. Microenvironmental regulation of tumor progression and metastasis. Nature medicine. 2013;19(11):1423-37.

[81] Hanahan D, Coussens LM. Accessories to the crime: functions of cells recruited to the tumor microenvironment. Cancer cell. 2012;21(3):309-22.

[82] Fedorenko IV, Smalley KS. The complexity of microenvironment-mediated drug resistance. Genes & cancer. 2015;6(9-10):367.

[83] Levental KR, Yu H, Kass L, Lakins JN, Egeblad M, Erler JT, et al. Matrix crosslinking forces tumor progression by enhancing integrin signaling. Cell. 2009;139(5):891-906.

[84] Lu P, Weaver VM, Werb Z. The extracellular matrix: a dynamic niche in cancer progression. Journal of cell biology. 2012;196(4):395-406.

[85] Kapałczyńska M, Kolenda T, Przybyła W, Zajączkowska M, Teresiak A, Filas V, et al. 2D and 3D cell cultures–a comparison of different types of cancer cell cultures. Archives of medical science. 2018;14(4):910-9.

[86] Nelson CM, Bissell MJ. Of extracellular matrix, scaffolds, and signaling: tissue architecture regulates development, homeostasis, and cancer. Annu Rev Cell Dev Biol. 2006;22(1):287-309.

[87] Delarue M, Montel F, Vignjevic D, Prost J, Joanny JF, Cappello G. Compressive stress inhibits proliferation in tumor spheroids through a volume limitation. Biophysical journal. 2014;107(8):1821-8.

[88] Rheinwatd JG, Green H. Seria cultivation of strains of human epidemal keratinocytes: the formation keratinizin colonies from single cell is. Cell. 1975;6(3):331-43.

[89] Clevers H. Modeling development and disease with organoids. Cell. 2016;165(7):1586-97.

[90] Drost J, Clevers H. Organoids in cancer research. Nature Reviews Cancer. 2018;18(7):407-18.

[91] Karthaus WR, Iaquinta PJ, Drost J, Gracanin A, Van Boxtel R, Wongvipat J, et al. Identification of multipotent luminal progenitor cells in human prostate organoid cultures. Cell. 2014;159(1):163-75.

[92] Chua CW, Shibata M, Lei M, Toivanen R, Barlow LJ, Bergren SK, et al. Single luminal epithelial progenitors can generate prostate organoids in culture. Nature cell biology. 2014;16(10):951-61.

[93] Drost J, Van Jaarsveld RH, Ponsioen B, Zimberlin C, Van Boxtel R, Buijs A, et al. Sequential cancer mutations in cultured human intestinal stem cells. Nature. 2015;521(7550):43-7.

[94] Verissimo CS, Overmeer RM, Ponsioen B, Drost J, Mertens S, Verlaan-Klink I, et al. Targeting mutant RAS in patient-derived colorectal cancer organoids by combinatorial drug screening. elife. 2016;5:e18489.

[95] Sutherland RM, McCredie JA, Inch WR. Growth of multicell spheroids in tissue culture as a model of nodular carcinomas. Journal of the National Cancer Institute. 1971;46(1):113-20.

[96] Nath S, Devi GR. Three-dimensional culture systems in cancer research: Focus on tumor spheroid model. Pharmacology & Therapeutics. 2016 Jul;163:94-108. Available from: https://www.sciencedirect.com/science/article/pii/S0163725816300213.

[97] Gunti S, Hoke AT, Vu KP, London Jr NR. Organoid and spheroid tumor models: techniques and applications. Cancers. 2021;13(4):874.

[98] Pampaloni F, Reynaud EG, Stelzer EH. The third dimension bridges the gap between cell culture and live tissue. Nature reviews Molecular cell biology. 2007;8(10):839-45.

[99] Mehta G, Hsiao AY, Ingram M, Luker GD, Takayama S. Opportunities and challenges for use of tumor spheroids as models to test drug delivery and efficacy. Journal of controlled release. 2012;164(2):192-204.

[100] Hirschhaeuser F, Menne H, Dittfeld C, West J, Mueller-Klieser W, Kunz-Schughart LA. Multicellular tumor spheroids: an underestimated tool is catching up again. Journal of biotechnology. 2010;148(1):3-15.

[101] Horsman MR, Overgaard J. The impact of hypoxia and its modification of the outcome of radiotherapy. Journal of radiation research. 2016;57(S1):i90-8.

[102] Jordan BF, Sonveaux P. Targeting tumor perfusion and oxygenation to improve the outcome of anticancer therapy. Frontiers in pharmacology. 2012;3:94.

[103] Onozato Y, Kaida A, Harada H, Miura M. Radiosensitivity of quiescent and proliferating cells grown as multicellular tumor spheroids. Cancer science. 2017;108(4):704-12.

[104] Menegakis A, Klompmaker R, Vennin C, Arbusà A, Damen M, van den Broek B, et al. Resistance of hypoxic cells to ionizing radiation is mediated in part via hypoxia-induced quiescence. Cells. 2021;10(3):610.

[105] Ingeson-Carlsson C, Martinez-Monleon A, Nilsson M. Differential effects of MAPK pathway inhibitors on migration and invasiveness of BRAFV600E mutant thyroid cancer cells in 2D and 3D culture. Experimental cell research. 2015;338(2):127-35.

[106] Jørgensen A, Young J, Nielsen J, Joensen UN, Toft BG, Meyts RD, et al. Hanging drop cultures of human testis and testis cancer samples: a model used to investigate activin treatment effects in a preserved niche. British journal of cancer. 2014;110(10):2604-14.

[107] Vinci M, Gowan S, Boxall F, Patterson L, Zimmermann M, Court W, et al. Advances in establishment and analysis of three-dimensional tumor spheroid-based functional assays for target validation and drug evaluation. BMC Biology. 2012 Mar;10(1):29. Available from: https://doi.org/10.1186/1741-7007-10-29.

[108] Leary E, Curran S, Susienka M, Manning KL, Blakely AM, Morgan JR. Micromoulded non-adhesive hydrogels to form multicellular microtissues–the 3D Petri Dish®. Technology Platforms for 3D Cell Culture: A User's Guide. 2017:97-122.

[109] Lowengrub JS, Frieboes HB, Jin F, Chuang YL, Li X, Macklin P, et al. Nonlinear modelling of cancer: bridging the gap between cells and tumours. Nonlinearity. 2009;23(1):R1.

[110] Edelman LB, Eddy JA, Price ND. In silico models of cancer. Wiley Interdisciplinary Reviews: Systems Biology and Medicine. 2010;2(4):438-59.

[111] Bekisz S, Geris L. Cancer modeling: From mechanistic to data-driven approaches, and from fundamental insights to clinical applications. Journal of Computational Science. 2020;46:101198.

[112] Gondal MN, Chaudhary SU. Navigating multi-scale cancer systems biology towards model-driven clinical oncology and its applications in personalized therapeutics. Frontiers in Oncology. 2021;11:712505.

[113] Crowther J. Some considerations relative to the action of X-rays on tissue cells. Proceedings of the Royal Society of London Series B, Containing Papers of a Biological Character. 1924;96(674):207-11.

[114] Curie M. Sur l'étude des courbes de probabilité relatives à l'action des rayons X sur les bacilles. Comptes rendus l'Académie des Sci. 1929;188:202-4.

[115] McMahon SJ. The linear quadratic model: usage, interpretation and challenges. Physics in Medicine & Biology. 2018;64(1):01TR01.

[116] Nordling C. A new theory on the cancer-inducing mechanism. British journal of cancer. 1953;7(1):68.

[117] Barbolosi D, Ciccolini J, Lacarelle B, Barlési F, André N. Computational oncology—mathematical modelling of drug regimens for precision medicine. Nature reviews Clinical oncology. 2016;13(4):242-54.

[118] Rousseau A, Marquet P. Application of pharmacokinetic modelling to the routine therapeutic drug monitoring of anticancer drugs. Fundamental & clinical pharmacology. 2002;16(4):253-62.

[119] Janes KA, Albeck JG, Gaudet S, Sorger PK, Lauffenburger DA, Yaffe MB. A systems model of signaling identifies a molecular basis set for cytokine-induced apoptosis. Science. 2005;310(5754):1646-53.

[120] Hashimoto RF, Kim S, Shmulevich I, Zhang W, Bittner ML, Dougherty ER. Growing genetic regulatory networks from seed genes. Bioinformatics. 2004;20(8):1241-7.

[121] Pal R, Datta A, Bittner ML, Dougherty ER. Intervention in context-sensitive probabilistic Boolean networks. Bioinformatics. 2005;21(7):1211-8.

[122] Metzcar J, Wang Y, Heiland R, Macklin P. A review of cell-based computational modeling in cancer biology. JCO clinical cancer informatics. 2019;2:1-13.

[123] Loessner D, Little JP, Pettet GJ, Hutmacher DW. A multiscale road map of cancer spheroids–incorporating experimental and mathematical modelling to understand cancer progression. Journal of cell science. 2013;126(13):2761-71.

[124] Gompertz B. XXIV. On the nature of the function expressive of the law of human mortality, and on a new mode of determining the value of life contingencies. In a letter to Francis Baily, Esq. FRS &c. Philosophical transactions of the Royal Society of London. 1825;(115):513-83.

[125] Casey AE. The experimental alteration of malignancy with an homologous mammalian tumor material: I. results with intratesticular inoculation. The American Journal of Cancer. 1934;21(4):760-75.

[126] Swan G. Tumor cell population dynamics. In: Some Current Mathematical Topics in Cancer Research. University Microfilms International, Ann Arbor, Michigan; 1977. p. 1-8.

[127] West GB, Brown JH, Enquist BJ. A general model for ontogenetic growth. Nature. 2001;413(6856):628-31.

[128] Von Bertalanffy L. Quantitative laws in metabolism and growth. The quarterly review of biology. 1957;32(3):217-31.

[129] Greenspan HP. Models for the growth of a solid tumor by diffusion. Studies in Applied Mathematics. 1972;51(4):317-40.

[130] Greenspan HP. On the growth and stability of cell cultures and solid tumors. Journal of theoretical biology. 1976;56(1):229-42.

[131] Shymko R, Glass L. Cellular and geometric control of tissue growth and mitotic instability. Journal of Theoretical biology. 1976;63(2):355-74.

[132] McElwain D, Morris L. Apoptosis as a volume loss mechanism in mathematical models of solid tumor growth. Mathematical Biosciences. 1978;39(1-2):147-57.

[133] Byrne H, Chaplain MAJ. Growth of nonnecrotic tumors in the presence and absence of inhibitors. Mathematical biosciences. 1995;130(2):151-81.

[134] Byrne HM, Chaplain M. Growth of necrotic tumors in the presence and absence of inhibitors. Mathematical biosciences. 1996;135(2):187-216.

[135] Chaplain MA. Avascular growth, angiogenesis and vascular growth in solid tumours: The mathematical modelling of the stages of tumour development. Mathematical and computer modelling. 1996;23(6):47-87.

[136] Adam JA. General aspects of modeling tumor growth and immune response. In: A survey of models for tumor-immune system dynamics. Springer; 1997. p. 15-87.

[137] Cristini V, Li X, Lowengrub JS, Wise SM. Nonlinear simulations of solid tumor growth using a mixture model: invasion and branching. Journal of mathematical biology. 2009;58:723-63.

[138] Li X, Cristini V, Nie Q, Lowengrub JS. Nonlinear three-dimensional simulation of solid tumor growth. DISCRETE AND CONTINUOUS DYNAMICAL SYSTEMS SERIES B. 2007;7(3):581.

[139] Zhang L, Wang Z, Sagotsky JA, Deisboeck TS. Multiscale agent-based cancer modeling. Journal of mathematical biology. 2009;58:545-59.

[140] Orme M, Chaplain M. Two-dimensional models of tumour angiogenesis and anti-angiogenesis strategies. Mathematical Medicine and Biology: A Journal of the IMA. 1997;14(3):189-205.

[141] Kim Y, Stolarska MA, Othmer HG. A hybrid model for tumor spheroid growth in vitro I: theoretical development and early results. Mathematical Models and Methods in Applied Sciences. 2007;17(supp01):1773-98.

[142] Bearer EL, Lowengrub JS, Frieboes HB, Chuang YL, Jin F, Wise SM, et al. Multiparameter computational modeling of tumor invasion. Cancer research. 2009;69(10):4493-501.

[143] Stolarska MA, Kim Y, Othmer HG. Multi-scale models of cell and tissue dynamics. Philosophical Transactions of the Royal Society A: Mathematical, Physical and Engineering Sciences. 2009;367(1902):3525-53.

[144] Macklin P, Edgerton ME. Discrete cell modeling. In: Multiscale modeling of cancer: an integrated experimental and mathematical modeling approach. Cambridge University Press; 2010. p. 88-122.

[145] Wolf-Gladrow DA. Lattice-gas cellular automata and lattice Boltzmann models: an introduction. Springer; 2004.

[146] Szabó A, Merks RM. Cellular potts modeling of tumor growth, tumor invasion, and tumor evolution. Frontiers in oncology. 2013;3:87.

[147] Voss-Böhme A. Multi-scale modeling in morphogenesis: a critical analysis of the cellular Potts model. PLoS ONE. 2012;7(9):e42852.

[148] Altrock PM, Liu LL, Michor F. The mathematics of cancer: integrating quantitative models. Nature Reviews Cancer. 2015;15(12):730-45.

[149] Ude A, Afi-Leslie K, Okeke K, Ogbodo E. Trypan blue exclusion assay, neutral red, acridine orange and propidium iodide. In: Cytotoxicity-Understanding Cellular Damage and Response. IntechOpen; 2022. .

[150] Strober W. Trypan blue exclusion test of cell viability. Current protocols in immunology. 1997;21(1):A-3B.

[151] Adan A, Kiraz Y, Baran Y. Cell proliferation and cytotoxicity assays. Current pharmaceutical biotechnology. 2016;17(14):1213-21.

[152] Crowley LC, Scott AP, Marfell BJ, Boughaba JA, Chojnowski G, Waterhouse NJ. Measuring Cell Death by Propidium Iodide Uptake and Flow Cytometry. Cold Spring Harbor protocols. 2016;2016(7).

[153] Baskić D, Popović S, Ristić P, Arsenijević NN. Analysis of cycloheximide-induced apoptosis in human leukocytes: Fluorescence microscopy using annexin V/propidium iodide versus acridin orange/ethidium bromide. Cell biology international. 2006;30(11):924-32.

[154] Sumantran VN. Cellular chemosensitivity assays: an overview. Cancer Cell Culture: Methods and Protocols. 2011:219-36.

[155] Bratosin D, Mitrofan L, Palii C, Estaquier J, Montreuil J. Novel fluorescence assay using calcein-AM for the determination of human erythrocyte viability and aging. Cytometry Part A: the journal of the International Society for Analytical Cytology. 2005;66(1):78-84.

[156] Mosmann T. Rapid colorimetric assay for cellular growth and survival: application to proliferation and cytotoxicity assays. Journal of immunological methods. 1983;65(1-2):55-63.

[157] Rampersad SN. Multiple applications of Alamar Blue as an indicator of metabolic function and cellular health in cell viability bioassays. Sensors. 2012;12(9):12347-60.

[158] Pesch K, Simmert U. Combined assays for lactose and galactose by enzymatic reactions. Kieler Milchwirtschaftliche Forschungsberichte. 1929;8(551).

[159] Page B, PAGE M, NOEL C. A new fluorometric assay for cytotoxicity measurements in-vitro. International journal of oncology. 1993;3(3):473-6.

[160] Riccardi C, Nicoletti I. Analysis of apoptosis by propidium iodide staining and flow cytometry. Nature protocols. 2006;1(3):1458-61.

[161] Rosenberg M, Azevedo NF, Ivask A. Propidium iodide staining underestimates viability of adherent bacterial cells. Scientific reports. 2019;9(1):6483.

[162] Sirenko O, Mitlo T, Hesley J, Luke S, Owens W, Cromwell EF. High-content assays for characterizing the viability and morphology of 3D cancer spheroid cultures. Assay and drug development technologies. 2015;13(7):402-14.

[163] Ghasemi M, Turnbull T, Sebastian S, Kempson I. The MTT assay: utility, limitations, pitfalls, and interpretation in bulk and single-cell analysis. International journal of molecular sciences. 2021;22(23):12827.

[164] Bonnier F, Keating ME, Wróbel TP, Majzner K, Baranska M, Garcia-Munoz A, et al. Cell viability assessment using the Alamar blue assay: A comparison of 2D and 3D cell culture models. Toxicology in Vitro. 2015 Feb;29(1):124-31. Available from: https://www.sciencedirect.com/science/article/pii/S0887233314001878.

[165] Puck TT, Marcus PI. Action of x-rays on mammalian cells. The Journal of experimental medicine. 1956;103(5):653-66.

[166] Munshi A, Hobbs M, Meyn RE. Clonogenic cell survival assay. Chemosensitivity: Volume 1 In Vitro Assays. 2005:21-8.

[167] Harrington K, Billingham L, Brunner T, Burnet N, Chan C, Hoskin P, et al. Guidelines for preclinical and early phase clinical assessment of novel radiosensitisers. British journal of cancer. 2011;105(5):628-39.

[168] Durand R, Sutherland R. Effects of intercellular contact on repair of radiation damage. Experimental cell research. 1972;71(1):75-80.

[169] Nikzad S, Hashemi B. MTT assay instead of the clonogenic assay in measuring the response of cells to ionizing radiation. J Radiobiol. 2014;1(1):3-8.

[170] Fei K, Zhang J, Yuan J, Xiao P. Present application and perspectives of organoid imaging technology. Bioengineering. 2022;9(3):121.

[171] Selinummi J, Ruusuvuori P, Podolsky I, Ozinsky A, Gold E, Yli-Harja O, et al. Bright field microscopy as an alternative to whole cell fluorescence in automated analysis of macrophage images. PloS one. 2009;4(10):e7497.

[172] Kim MK. Principles and techniques of digital holographic microscopy. SPIE reviews. 2010;1(1):018005.

[173] Nguyen TL, Pradeep S, Judson-Torres RL, Reed J, Teitell MA, Zangle TA. Quantitative phase imaging: recent advances and expanding potential in biomedicine. ACS nano. 2022;16(8):11516-44.

[174] Zewail AH. Four-dimensional electron microscopy. science. 2010;328(5975):187-93.

[175] Helmchen F, Denk W. Deep tissue two-photon microscopy. Nature methods. 2005;2(12):932-40.

[176] Theer P, Hasan MT, Denk W. Two-photon imaging to a depth of 1000 μm in living brains by use of a Ti: Al_2O_3 regenerative amplifier. Optics letters. 2003;28(12):1022-4.

[177] Thouvenin O, Apelian C, Nahas A, Fink M, Boccara C. Full-field optical coherence tomography as a diagnosis tool: recent progress with multimodal imaging. Applied Sciences. 2017;7(3):236.

[178] Paddock SW, Eliceiri KW. Laser scanning confocal microscopy: history, applications, and related optical sectioning techniques. Confocal microscopy: Methods and protocols. 2014:9-47.

[179] Artigas R. Imaging confocal microscopy. In: Optical measurement of surface topography. Springer; 2011. p. 237-86.

[180] Oldenburg AL, Chhetri RK, Cooper JM, Wu WC, Troester MA, Tracy JB. Motility-, autocorrelation-, and polarization-sensitive optical coherence tomography discriminates cells and gold nanorods within 3D tissue cultures. Optics letters. 2013;38(15):2923-6.

[181] Hicks J, Matthaei E. Fluorescence in histology. The Journal of Pathology and Bacteriology. 1955;70(1):1-12.

[182] Bancroft JD, Gamble M. Theory and practice of histological techniques. Elsevier health sciences; 2008.

[183] Volpi EV, Bridger JM. FISH glossary: an overview of the fluorescence in situ hybridization technique. Biotechniques. 2008;45(4):385-409.

[184] Imamura H, Huynh Nhat KP, Togawa H, Saito K, Iino R, Kato-Yamada Y, et al. Visualization of ATP levels inside single living cells with fluorescence resonance energy transfer-based genetically encoded indicators. Proceedings of the National Academy of Sciences. 2009;106(37):15651-6.

[185] Kyrylkova K, Kyryachenko S, Leid M, Kioussi C. Detection of apoptosis by TUNEL assay. Odontogenesis: methods and protocols. 2012:41-7.

[186] Jung Y, Klein OJ, Wang H, Evans CL. Longitudinal, label-free, quantitative tracking of cell death and viability in a 3D tumor model with OCT. Scientific reports. 2016;6(1):27017.

[187] El-Sadek IA, Miyazawa A, Shen LTW, Makita S, Fukuda S, Yamashita T, et al. Optical coherence tomography-based tissue dynamics imaging for longitudinal and drug response evaluation of tumor spheroids. Biomedical Optics Express. 2020 Nov;11(11):6231-48. Available from: https://opg.optica.org/boe/abstract.cfm?uri=boe-11-11-6231.

[188] Babakhanova G, Agrawal A, Arora D, Horenberg A, Budhathoki JB, Dunkers JP, et al. Three-dimensional, label-free cell viability measurements in tissue engineering scaffolds using optical coherence tomography. Journal of Biomedical Materials Research Part A. 2023;111(8):1279-91.

[189] Icha J, Weber M, Waters JC, Norden C. Phototoxicity in live fluorescence microscopy, and how to avoid it. BioEssays. 2017;39(8):1700003.

[190] Transidico P, Bianchi M, Capra M, Pelicci PG, Faretta M. From cells to tissues: fluorescence confocal microscopy in the study of histological samples. Microscopy research and technique. 2004;64(2):89-95.

[191] Yuste R. Fluorescence microscopy today. Nature methods. 2005;2(12):902-4.

[192] Azzollini S, Monfort T, Thouvenin O, Grieve K. Dynamic optical coherence tomography for cell analysis. Biomedical optics express. 2023;14(7):3362-79.

[193] Huang D, Swanson EA, Lin CP, Schuman JS, Stinson WG, Chang W, et al. Optical coherence tomography. science. 1991;254(5035):1178-81.

[194] Duquay MA. Light photographed in flight. American Scientist. 1971;59(5):550-6.

[195] Leitgeb R, Hitzenberger C, Fercher AF. Performance of fourier domain vs. time domain optical coherence tomography. Optics express. 2003;11(8):889-94.

[196] Aumann S, Donner S, Fischer J, Müller F. Optical coherence tomography (OCT): principle and technical realization. High resolution imaging in microscopy and ophthalmology: new frontiers in biomedical optics. 2019:59-85.

[197] de Boer JF. Spectral/Fourier domain optical coherence tomography. In: Optical coherence tomography: technology and applications. Springer; 2008. p. 147-75.

[198] Fercher AF, Hitzenberger CK, Kamp G, El-Zaiat SY. Measurement of intraocular distances by backscattering spectral interferometry. Optics communications. 1995;117(1-2):43-8.

[199] Yun SH, Tearney GJ, de Boer JF, Iftimia N, Bouma BE. High-speed optical frequency-domain imaging. Optics express. 2003;11(22):2953-63.

[200] Shannon CE. A mathematical theory of communication. The Bell system technical journal. 1948;27(3):379-423.

[201] Münter M, Pieper M, Kohlfaerber T, Bodenstorfer E, Ahrens M, Winter C, et al. Microscopic optical coherence tomography (mOCT) at 600 kHz for 4D volumetric imaging and dynamic contrast. Biomedical Optics Express. 2021;12(10):6024-39.

[202] Wieser W, Biedermann BR, Klein T, Eigenwillig CM, Huber R. Multi-megahertz OCT: High quality 3D imaging at 20 million A-scans and 4.5 GVoxels per second. Optics express. 2010;18(14):14685-704.

[203] Zuluaga AF, Richards-Kortum R. Spatially resolved spectral interferometry for determination of subsurface structure. Optics letters. 1999;24(8):519-21.

[204] Fechtig DJ, Grajciar B, Schmoll T, Blatter C, Werkmeister RM, Drexler W, et al. Line-field parallel swept source MHz OCT for structural and functional retinal imaging. Biomedical optics express. 2015;6(3):716-35.

[205] Pandiyan VP, Jiang X, Kuchenbecker JA, Sabesan R. Reflective mirror-based line-scan adaptive optics OCT for imaging retinal structure and function. Biomedical optics express. 2021;12(9):5865-80.

[206] Han L, Tan B, Hosseinaee Z, Chen LK, Hileeto D, Bizheva K. Line-scanning SD-OCT for in-vivo, non-contact, volumetric, cellular resolution imaging of the human cornea and limbus. Biomedical Optics Express. 2022;13(7):4007-20.

[207] Chen K, Song W, Han L, Bizheva K. Powell lens-based line-field spectral domain optical coherence tomography system for cellular resolution imaging of biological tissue. Biomedical Optics Express. 2023;14(5):2003-14.

[208] Zhang Z, Yang X, Zhao Z, Zeng F, Ye S, Baldock SJ, et al. Rapid imaging and product screening with low-cost line-field Fourier domain optical coherence tomography. Scientific reports. 2023;13(1):10809.

[209] Neuhaus K, Khan S, Thaware O, Ni S, Aga M, Jia Y, et al. Real-time line-field optical coherence tomography for cellular resolution imaging of biological tissue. Biomedical Optics Express. 2024;15(2):1059-73.

[210] Vabre L, Dubois A, Boccara AC. Thermal-light full-field optical coherence tomography. Optics letters. 2002;27(7):530-2.

[211] Bonin T, Franke G, Hagen-Eggert M, Koch P, Hüttmann G. In vivo Fourier-domain full-field OCT of the human retina with 1.5 million A-lines/s. Optics letters. 2010;35(20):3432-4.

[212] Grieve K, Dubois A, Simonutti M, Paques M, Sahel J, Le Gargasson JF, et al. In vivo anterior segment imaging in the rat eye with high speed white light full-field optical coherence tomography. Optics Express. 2005;13(16):6286-95.

[213] Stremplewski P, Auksorius E, Wnuk P, Kozoń Ł, Garstecki P, Wojtkowski M. In vivo volumetric imaging by crosstalk-free full-field OCT. Optica. 2019;6(5):608-17.

[214] Auksorius E, Borycki D, Wegrzyn P, Žičkienė I, Adomavičius K, Sikorski BL, et al. Multimode fiber as a tool to reduce cross talk in Fourier-domain full-field optical coherence tomography. Optics Letters. 2022;47(4):838-41.

[215] Fujimoto J, Huang D. Foreword: 25 years of optical coherence tomography. Investigative ophthalmology & visual science. 2016;57(9):OCTi-OCTii.

[216] Wessel JM, Horn FK, Tornow RP, Schmid M, Mardin CY, Kruse FE, et al. Longitudinal analysis of progression in glaucoma using spectral-domain optical coherence tomography. Investigative ophthalmology & visual science. 2013;54(5):3613-20.

[217] Srinivasan VJ, Mandeville ET, Can A, Blasi F, Climov M, Daneshmand A, et al. Multiparametric, longitudinal optical coherence tomography imaging reveals acute injury and chronic recovery in experimental ischemic stroke. PloS one. 2013;8(8):e71478.

[218] Bizheva K, Pflug R, Hermann B, Považay B, Sattmann H, Qiu P, et al. Optophysiology: depth-resolved probing of retinal physiology with functional ultrahigh-resolution optical coherence tomography. Proceedings of the national academy of sciences. 2006;103(13):5066-71.

[219] Nolte DD, An R, Turek J, Jeong K. Holographic tissue dynamics spectroscopy. Journal of Biomedical Optics. 2011;16(8):087004-4.

[220] An R, Turek J, Matei DE, Nolte D. Live tissue viability and chemosensitivity assays using digital holographic motility contrast imaging. Applied optics. 2013;52(1):A300-9.

[221] An R, Merrill D, Avramova L, Sturgis J, Tsiper M, Robinson JP, et al. Phenotypic profiling of Raf inhibitors and mitochondrial toxicity in 3D tissue using biodynamic imaging. Journal Of Biomolecular Screening. 2014;19(4):526-37.

[222] Apelian C, Harms F, Thouvenin O, Boccara AC. Dynamic full field optical coherence tomography: subcellular metabolic contrast revealed in tissues by interferometric signals temporal analysis. Biomedical Optics Express. 2016 Apr;7(4):1511-24. Available from: https://opg.optica.org/boe/abstract.cfm?uri=boe-7-4-1511.

[223] Groux K, Verschueren A, Nanteau C, Clémençon M, Fink M, Sahel JA, et al. Dynamic full-field optical coherence tomography allows live imaging of retinal pigment epithelium stress model. Communications Biology. 2022;5(1):575.

[224] McCarron JG, Wilson C, Sandison ME, Olson ML, Girkin JM, Saunter C, et al. From structure to function: mitochondrial morphology, motion and shaping in vascular smooth muscle. Journal of vascular research. 2013;50(5):357-71.

[225] Saunter CD, Der Perng M, Love GD, Quinlan RA. Stochastically determined directed movement explains the dominant small-scale mitochondrial movements within non-neuronal tissue culture cells. FEBS letters. 2009;583(8):1267-73.

[226] Leroux CE, Bertillot F, Thouvenin O, Boccara AC. Intracellular dynamics measurements with full field optical coherence tomography suggest hindering effect of actomyosin contractility on organelle transport. Biomedical Optics Express. 2016;7(11):4501-13.

[227] Guo M, Ehrlicher AJ, Jensen MH, Renz M, Moore JR, Goldman RD, et al. Probing the stochastic, motor-driven properties of the cytoplasm using force spectrum microscopy. Cell. 2014;158(4):822-32.

[228] Park S, Nguyen T, Benoit E, Sackett DL, Garmendia-Cedillos M, Pursley R, et al. Quantitative evaluation of the dynamic activity of HeLa cells in different viability states using dynamic full-field optical coherence microscopy. Biomedical Optics Express. 2021;12(10):6431-41.

[229] Maldiney T, Chassot JM, Boccara C, Blot M, Piroth L, Charles PE, et al. Dynamic full-field optical coherence tomography as complementary tool in fungal diagnostics. Journal of Medical Mycology. 2022;32(4):101303.

[230] van der Meer FJ, Faber DJ, Aalders MC, Poot AA, Vermes I, van Leeuwen TG. Apoptosis-and necrosis-induced changes in light attenuation measured by optical coherence tomography. Lasers in medical science. 2010;25:259-67.

[231] Farhat G, Mariampillai A, Yang VX, Czarnota GJ, Kolios MC. Detecting apoptosis using dynamic light scattering with optical coherence tomography. Journal of biomedical optics. 2011;16(7):070505-5.

[232] Monfort T, Azzollini S, Ben Yacoub T, Audo I, Reichman S, Grieve K, et al. Interface self-referenced dynamic full-field optical coherence tomography. Biomedical optics express. 2023;14(7):3491-505.

[233] Park S, Veluvolu V, Martin WS, Nguyen T, Park J, Sackett DL, et al. Label-free, non-invasive, and repeatable cell viability bioassay using dynamic full-field optical

coherence microscopy and supervised machine learning. Biomedical Optics Express. 2022;13(6):3187-94.

[234] Scholler J, Groux K, Goureau O, Sahel JA, Fink M, Reichman S, et al. Dynamic full-field optical coherence tomography: 3D live-imaging of retinal organoids. Light: Science & Applications. 2020;9(1):140.

[235] Monfort T, Azzollini S, Brogard J, Clémençon M, Slembrouck-Brec A, Forster V, et al. Dynamic full-field optical coherence tomography module adapted to commercial microscopes allows longitudinal in vitro cell culture study. Communications Biology. 2023;6(1):992.

[236] Morishita R, Suzuki T, Mukherjee P, Abd El-Sadek I, Lim Y, Lichtenegger A, et al. Label-free intratissue activity imaging of alveolar organoids with dynamic optical coherence tomography. Biomedical Optics Express. 2023;14(5):2333-51.

[237] Oldenburg AL, Yu X, Gilliss T, Alabi O, Taylor RM, Troester MA. Inverse-power-law behavior of cellular motility reveals stromal–epithelial cell interactions in 3D co-culture by OCT fluctuation spectroscopy. Optica. 2015;2(10):877-85.

[238] Yu X, Fuller AM, Blackmon R, Troester MA, Oldenburg AL. Quantification of the effect of toxicants on the intracellular kinetic energy and cross-sectional area of mammary epithelial organoids by OCT fluctuation spectroscopy. Toxicological Sciences. 2018;162(1):234-40.

[239] Yang L, Yu X, Fuller AM, Troester MA, Oldenburg AL. Characterizing optical coherence tomography speckle fluctuation spectra of mammary organoids during suppression of intracellular motility. Quantitative Imaging in Medicine and Surgery. 2020;10(1):76.

[240] El-Sadek IA, Miyazawa A, Shen LTW, Makita S, Mukherjee P, Lichtenegger A, et al. Three-dimensional dynamics optical coherence tomography for tumor spheroid evaluation. Biomedical Optics Express. 2021 Nov;12(11):6844-63. Available from: https://opg.optica.org/boe/abstract.cfm?uri=boe-12-11-6844.

[241] Abd El-Sadek I, Shen LTW, Mori T, Makita S, Mukherjee P, Lichtenegger A, et al. Label-free drug response evaluation of human derived tumor spheroids using three-dimensional dynamic optical coherence tomography. Scientific Reports. 2023;13(1):15377.

[242] Abd El-Sadek I, Morishita R, Mori T, Makita S, Mukherjee P, Matsusaka S, et al. Label-free visualization and quantification of the drug-type-dependent response of tumor spheroids by dynamic optical coherence tomography. Scientific Reports. 2024;14(1):3366.

[243] Yang L, Ji P, Miranda Buzetta AA, Li H, Lockett MR, Zhou H, et al. Longitudinal tracking of perfluorooctanoic acid exposure on mammary epithelial cell spheroids by dynamic optical coherence tomography. Biomedical Optics Express. 2024 Sep;15(9):5115. Available from: https://opg.optica.org/abstract.cfm?URI=boe-15-9-5115.

[244] Kohlfaerber T, Ding S, Rahmanzadeh R, Jüngst T, Groll J, Schulz-Hildebrandt H, et al. Investigation of cell dynamics in 3D cell spheroids and cell interaction with 3D printed scaffolds by mOCT. Transactions on Additive Manufacturing Meets Medicine. 2019;1(1).

[245] Tan KH, Ang JLY, Yong ASK, Lim SZE, Kng JSJ, Liang K. Non-destructive viability assessment of cancer cell spheroids using dynamic optical coherence tomography with trypan blue validation. Biomedical Optics Express. 2024 Nov;15(11):6370-83. Available from: https://opg.optica.org/boe/abstract.cfm?uri=boe-15-11-6370.

[246] Wang L, Wang C, Li Q, Fu R, Xu C, Xu M. Quantitative evaluation of the site-dependent cell viability in three-dimensional hepatocyte spheroids based on dynamic optical coherence tomography. Journal of Biomedical Optics. 2025;30(3):035003-3.

[247] McIntosh JC, Yang L, Wang T, Zhou H, Lockett MR, Oldenburg AL. Tracking the invasion of breast cancer cells in paper-based 3D cultures by OCT motility analysis. Biomedical Optics Express. 2020;11(6):3181-94.

[248] Fujimoto JG, Pitris C, Boppart SA, Brezinski ME. Optical coherence tomography: an emerging technology for biomedical imaging and optical biopsy. Neoplasia. 2000;2(1-2):9-25.

[249] Thouvenin O, Boccara C, Fink M, Sahel J, Pâques M, Grieve K. Cell motility as contrast agent in retinal explant imaging with full-field optical coherence tomography. Investigative ophthalmology & visual science. 2017;58(11):4605-15.

[250] Münter M, Vom Endt M, Pieper M, Casper M, Ahrens M, Kohlfaerber T, et al. Dynamic contrast in scanning microscopic OCT. Optics letters. 2020;45(17):4766-9.

[251] Musial G, Kohlfaerber T, Ahrens M, Schulz-Hildebrandt H, Steven P, Hüttmann G. Dynamic contrast microscopic optical coherence tomography as a novel method for assessing corneal epithelium during exposure to benzalkonium chloride. Translational Vision Science & Technology. 2022;11(5):28-8.

[252] Mukherjee P, Miyazawa A, Fukuda S, Yamashita T, Lukmanto D, Okada K, et al. Label-free functional and structural imaging of liver microvascular complex in mice by Jones matrix optical coherence tomography. Scientific Reports. 2021;11(1):20054.

[253] Mukherjee P, Fukuda S, Lukmanto D, Yamashita T, Okada K, Makita S, et al. Label-free metabolic imaging of non-alcoholic-fatty-liver-disease (NAFLD) liver by volumetric dynamic optical coherence tomography. Biomedical Optics Express. 2022;13(7):4071-86.

[254] Kohlfaerber T, Pieper M, Münter M, Holzhausen C, Ahrens M, Idel C, et al. Dynamic microscopic optical coherence tomography to visualize the morphological and functional micro-anatomy of the airways. Biomedical Optics Express. 2022 Jun;13(6):3211-23. Available from: https://opg.optica.org/boe/abstract.cfm?uri=boe-13-6-3211.

[255] Umezu K, Xia T, Larina IV. Dynamic volumetric imaging and cilia beat mapping in the mouse male reproductive tract with optical coherence tomography. Biomedical Optics Express. 2022;13(6):3672-84.

[256] Liu CJ, Smith JT, Wang Y, Ouellette JN, Rogers JD, Oliner JD, et al. Assessing cell viability with dynamic optical coherence microscopy. Biomedical Optics Express. 2024;15(3):1408-17.

[257] Xu Z, Zhu H, Wang H. Segmentation of the urothelium in optical coherence tomography images with dynamic contrast. Journal of Biomedical Optics. 2021;26(8):086002-2.

[258] Leung HM, Wang ML, Osman H, Abouei E, MacAulay C, Follen M, et al. Imaging intracellular motion with dynamic micro-optical coherence tomography. Biomedical Optics Express. 2020;11(5):2768-78.

[259] Quénéhervé L, Olivier R, Gora MJ, Bossard C, Mosnier JF, a La Guillaume EB, et al. Full-field optical coherence tomography: novel imaging technique for extemporaneous high-resolution analysis of mucosal architecture in human gut biopsies. Gut. 2021;70(1):6-8.

[260] Yang H, Zhang S, Liu P, Cheng L, Tong F, Liu H, et al. Use of high-resolution full-field optical coherence tomography and dynamic cell imaging for rapid intraoperative diagnosis during breast cancer surgery. Cancer. 2020;126:3847-56.

[261] a la Guillaume EB, Apelian C, Dalimier E, Boccara C, Mansuet-Lupo A, Chassagnon G, et al. Lung biopsy assessment with dynamic cell optical imaging (Conference Presentation). In: Endoscopic Microscopy XIII. vol. 10470. SPIE; 2018. p. 104700C.

[262] Perwein MKE, Welzel J, De Carvalho N, Pellacani G, Schuh S. Dynamic optical coherence tomography: A non-invasive imaging tool for the distinction of nevi and melanomas. Cancers. 2022;15(1):20.

[263] Scholler J. Motion artifact removal and signal enhancement to achieve in vivo dynamic full field OCT. Optics Express. 2019;27(14):19562-72.

[264] Wei W, Tang P, Xie Z, Li Y, Wang RK. Dynamic imaging and quantification of subcellular motion with eigen-decomposition optical coherence tomography-based variance analysis. Journal of biophotonics. 2019;12(10):e201900076.

[265] Wang S, Burton JC, Behringer RR, Larina IV. In vivo micro-scale tomography of ciliary behavior in the mammalian oviduct. Scientific Reports. 2015;5(1):13216.

[266] Wang S, Syed R, Grishina OA, Larina IV. Prolonged in vivo functional assessment of the mouse oviduct using optical coherence tomography through a dorsal imaging window. Journal of biophotonics. 2018;11(5):e201700316.

[267] Wang S, Larina IV. In vivo imaging of the mouse reproductive organs, embryo transfer, and oviduct cilia dynamics using optical coherence tomography. Mouse Embryogenesis: Methods and Protocols. 2018:53-62.

[268] Xia T, Umezu K, Scully DM, Wang S, Larina IV. In vivo volumetric depth-resolved imaging of cilia metachronal waves using dynamic optical coherence tomography. Optica. 2023;10(11):1439-51.

[269] Zhang J, Mazlin V, Fei K, Boccara AC, Yuan J, Xiao P. Time-domain full-field optical coherence tomography (TD-FF-OCT) in ophthalmic imaging. Therapeutic Advances in Chronic Disease. 2023;14:20406223231170146.

[270] Yi M, Weaver D, Hajnoóczky G. Control of mitochondrial motility and distribution by the calcium signal: a homeostatic circuit. The Journal of cell biology. 2004;167(4):661-72.

[271] Egan MJ, Tan K, Reck-Peterson SL. Lis1 is an initiation factor for dynein-driven organelle transport. Journal of Cell Biology. 2012;197(7):971-82.

[272] Oldenburg AL, Ji P, Yu X, Yang L. Compressed intracellular motility via non-uniform temporal sampling in dynamic optical coherence tomography. Journal of Biomedical Optics. 2024;29(7):076002-2.

[273] Apelian C, Gastaud C, Boccara AC. Extracting relevant information for cancer diagnosis from dynamic full field OCT through image processing and learning. In: Optical Coherence Tomography and Coherence Domain Optical Methods in Biomedicine XXI. vol. 10053. SPIE; 2017. p. 102-8.

[274] Caujolle S, Cernat R, Silvestri G, Marques M, Bradu A, Feuchter T, et al. Speckle variance OCT for depth resolved assessment of the viability of bovine embryos. Biomedical Optics Express. 2017;8(11):5139-50.

[275] Liu Y, Abd El-Sadek I, Morishita R, Makita S, Mori T, Furukawa A, et al. Neural-network based high-speed volumetric dynamic optical coherence tomography. Biomedical Optics Express. 2024;15(5):3216-39.

[276] Morishita R, Abd El-Sadek I, Mukherjee P, Seesan T, Lim Y, Mori T, et al. Quantitative dynamic optical coherence tomography by multi-time-window signal intensity variance. In: Optical Coherence Tomography and Coherence Domain Optical Methods in Biomedicine XXVIII. vol. 12830. SPIE; 2024. p. 121-5.

[277] Yousefi S, Zhi Z, Wang RK. Eigendecomposition-based clutter filtering technique for optical microangiography. IEEE transactions on biomedical engineering. 2011;58(8):2316-23.

[278] Ammari H, Romero F, Shi C. A signal separation technique for sub-cellular imaging using dynamic optical coherence tomography. Multiscale Modeling & Simulation. 2017;15(3):1155-75.

[279] Klein T, Huber R. High-speed OCT light sources and systems. Biomedical optics express. 2017;8(2):828-59.

[280] Tan B, Hosseinaee Z, Han L, Kralj O, Sorbara L, Bizheva K. 250 kHz, 1.5 μm resolution SD-OCT for in-vivo cellular imaging of the human cornea. Biomedical optics express. 2018;9(12):6569-83.

[281] Chhetri RK, Kozek KA, Johnston-Peck AC, Tracy JB, Oldenburg AL. Imaging three-dimensional rotational diffusion of plasmon resonant gold nanorods using polarization-sensitive optical coherence tomography. Physical Review E—Statistical, Nonlinear, and Soft Matter Physics. 2011;83(4):040903.

[282] Thouvenin O, Grieve K, Xiao P, Apelian C, Boccara AC. En face coherence microscopy. Biomedical optics express. 2017;8(2):622-39.

[283] Chen K, Swanson S, Bizheva K. Line-field dynamic optical coherence tomography platform for volumetric assessment of biological tissues. Biomedical Optics Express. 2024;15(7):4162-75.

[284] Graner F, Glazier JA. Simulation of biological cell sorting using a two-dimensional extended Potts model. Physical review letters. 1992;69(13):2013.

[285] Wu FY. The potts model. Reviews of modern physics. 1982;54(1):235.

[286] Ising E. Beitrag zur theorie des ferromagnetismus. Zeitschrift für Physik. 1925;31(1):253-8.

[287] Lenz W. Beitrag zum Verständnis der magnetischen Erscheinungen in festen Körpern. Z Phys. 1920;21:613-5.

[288] Savill NJ, Hogeweg P. Modelling morphogenesis: from single cells to crawling slugs. Journal of theoretical biology. 1997;184(3):229-35.

[289] Glazier JA, Balter A, Popławski NJ. Magnetization to morphogenesis: a brief history of the Glazier-Graner-Hogeweg model. Single-cell-based models in biology and medicine. 2007:79-106.

[290] Glazier JA, Graner F. Simulation of the differential adhesion driven rearrangement of biological cells. Physical Review E. 1993;47(3):2128.

[291] Sottoriva A, Vermeulen L, Tavaré S. Modeling evolutionary dynamics of epigenetic mutations in hierarchically organized tumors. PLoS computational biology. 2011;7(5):e1001132.

[292] Starruß J, Bley T, Søgaard-Andersen L, Deutsch A. A new mechanism for collective migration in Myxococcus xanthus. Journal of Statistical Physics. 2007;128:269-86.

[293] Szabó A, Ünnep R, Méhes E, Twal W, Argraves S, Cao Y, et al. Collective cell motion in endothelial monolayers. Physical biology. 2010;7(4):046007.

[294] Bauer AL, Jackson TL, Jiang Y. A cell-based model exhibiting branching and anastomosis during tumor-induced angiogenesis. Biophysical journal. 2007;92(9):3105-21.

[295] Merks RM, Perryn ED, Shirinifard A, Glazier JA. Contact-inhibited chemotaxis in de novo and sprouting blood-vessel growth. PLoS computational biology. 2008;4(9):e1000163.

[296] Szabo A, Mehes E, Kosa E, Czirok A. Multicellular sprouting in vitro. Biophysical journal. 2008;95(6):2702-10.

[297] Merks RM, Brodsky SV, Goligorksy MS, Newman SA, Glazier JA. Cell elongation is key to in silico replication of in vitro vasculogenesis and subsequent remodeling. Developmental biology. 2006;289(1):44-54.

[298] Shirinifard A, Gens JS, Zaitlen BL, Popławski NJ, Swat M, Glazier JA. 3D multi-cell simulation of tumor growth and angiogenesis. PloS one. 2009;4(10):e7190.

[299] Kaura P, Mishra T, Verma N, Dalal IS, Sheraton V. Effects of combined chemotherapeutic drugs on the growth and survival of cancerous tumours–an in-silico study. Journal of Computational Science. 2021;54:101421.

[300] Nagai T, Kawasaki K, Nakamura K. Vertex dynamics of two-dimensional cellular patterns. Journal of the physical society of Japan. 1988;57(7):2221-4.

[301] Newman TJ. Modeling multi-cellular systems using sub-cellular elements. arXiv preprint q-bio/0504028. 2005.

[302] Zajac M, Jones GL, Glazier JA. Simulating convergent extension by way of anisotropic differential adhesion. Journal of Theoretical Biology. 2003;222(2):247-59.

[303] Marée AF, Jilkine A, Dawes A, Grieneisen VA, Edelstein-Keshet L. Polarization and movement of keratocytes: a multiscale modelling approach. Bulletin of mathematical biology. 2006;68:1169-211.

[304] Köhn-Luque A, De Back W, Starruß J, Mattiotti A, Deutsch A, Pérez-Pomares JM, et al. Early embryonic vascular patterning by matrix-mediated paracrine signalling: a mathematical model study. PLoS One. 2011;6(9):e24175.

[305] Harrison NC, Diez del Corral R, Vasiev B. Coordination of cell differentiation and migration in mathematical models of caudal embryonic axis extension. PloS one. 2011;6(7):e22700.

[306] Jiang Y, Pjesivac-Grbovic J, Cantrell C, Freyer JP. A multiscale model for avascular tumor growth. Biophysical journal. 2005;89(6):3884-94.

[307] Turner S, Sherratt JA. Intercellular adhesion and cancer invasion: a discrete simulation using the extended Potts model. Journal of theoretical biology. 2002;216(1):85-100.

[308] Cipra BA. An introduction to the Ising model. The American Mathematical Monthly. 1987;94(10):937-59.

[309] Metropolis N, Rosenbluth AW, Rosenbluth MN, Teller AH, Teller E. Equation of state calculations by fast computing machines. The journal of chemical physics. 1953;21(6):1087-92.

[310] Käfer J, Hayashi T, Marée AF, Carthew RW, Graner F. Cell adhesion and cortex contractility determine cell patterning in the Drosophila retina. Proceedings of the National Academy of Sciences. 2007;104(47):18549-54.

[311] Krieg M, Arboleda-Estudillo Y, Puech PH, Käfer J, Graner F, Müller D, et al. Tensile forces govern germ-layer organization in zebrafish. Nature cell biology. 2008;10(4):429-36.

[312] Merks R, Koolwijk P. Modeling Morphogenesis in silico and in vitro: TowardsQuantitative, Predictive, Cell-based Modeling. Mathematical Modelling of Natural Phenomena. 2009;4(4):149-71.

[313] Swat MH, Thomas GL, Belmonte JM, Shirinifard A, Hmeljak D, Glazier JA. Multiscale modeling of tissues using CompuCell3D. In: Methods in cell biology. vol. 110. Elsevier; 2012. p. 325-66.

[314] Suzuki Y. Invariant measures for the multitype voter model. Tokyo journal of mathematics. 1991;14(1):61-72.

[315] Madras NN. Lectures on monte carlo methods. vol. 16. American Mathematical Soc.; 2002.

[316] Deroulers C, Aubert M, Badoual M, Grammaticos B. Modeling tumor cell migration: from microscopic to macroscopic models. Physical Review E—Statistical, Nonlinear, and Soft Matter Physics. 2009;79(3):031917.

[317] Liggett TM, Liggett TM. Interacting particle systems. vol. 2. Springer; 1985.

[318] Simpson MJ, Towne C, McElwain DS, Upton Z. Migration of breast cancer cells: understanding the roles of volume exclusion and cell-to-cell adhesion. Physical Review E—Statistical, Nonlinear, and Soft Matter Physics. 2010;82(4):041901.

[319] Costa EC, Moreira AF, de Melo-Diogo D, Gaspar VM, Carvalho MP, Correia IJ. 3D tumor spheroids: an overview on the tools and techniques used for their analysis. Biotechnology Advances. 2016 Dec;34(8):1427-41. Available from: https://www.sciencedirect.com/science/article/pii/S0734975016301379.

[320] Baker BM, Chen CS. Deconstructing the third dimension – how 3D culture microenvironments alter cellular cues. Journal of Cell Science. 2012 Jul;125(13):3015-24. Available from: https://doi.org/10.1242/jcs.079509.

[321] Ma Hl, Jiang Q, Han S, Wu Y, Tomshine JC, Wang D, et al. Multicellular tumor spheroids as an in vivo–like tumor model for three-dimensional imaging of chemotherapeutic and nano material cellular penetration. Molecular imaging. 2012;11(6):7290-2012.

[322] Drexler W, Fujimoto JG. Optical coherence tomography: technology and applications. Springer Science & Business Media; 2008.

[323] Sharma M, Verma Y, Rao KD, Nair R, Gupta PK. Imaging growth dynamics of tumour spheroids using optical coherence tomography. Biotechnology Letters. 2007 Feb;29(2):273-8. Available from: https://link.springer.com/10.1007/s10529-006-9232-2.

[324] Jung Y, Nichols AJ, Klein OJ, Roussakis E, Evans CL. Label-free, longitudinal visualization of PDT response in vitro with optical coherence tomography. Israel journal of chemistry. 2012;52(8-9):728-44.

[325] Huang Y, Wang S, Guo Q, Kessel S, Rubinoff I, Chan LLY, et al. Optical Coherence Tomography Detects Necrotic Regions and Volumetrically Quantifies Multicellular Tumor Spheroids. Cancer Research. 2017 Nov;77(21):6011-20. Available from: https://aacrjournals.org/cancerres/article/77/21/6011/662613/Optical-Coherence-Tomography-Detects-Necrotic.

[326] Yan F, Mutembei B, Valerio T, Gunay G, Ha JH, Zhang Q, et al. Optical coherence tomography for multicellular tumor spheroid category recognition and drug screening classification via multi-spatial-superficial-parameter and machine learning. Biomedical Optics Express. 2024;15(4):2014-47.

[327] Boas D, Bizheva K, Siegel A. Using dynamic low-coherence interferometry to image Brownian motion within highly scattering media. Optics letters. 1998;23(5):319-21.

[328] Bizheva KK, Siegel AM, Boas DA. Path-length-resolved dynamic light scattering in highly scattering random media: The transition to diffusing wave spectroscopy. Physical Review E. 1998;58(6):7664.

[329] Rumpler M, Woesz A, Dunlop JWC, van Dongen JT, Fratzl P. The effect of geometry on three-dimensional tissue growth. Journal of The Royal Society Interface. 2008 Mar;5(27):1173-80. Available from: https://royalsocietypublishing.org/doi/full/10.1098/rsif.2008.0064.

[330] Tartagni O, Borók A, Mensà E, Bonyár A, Monti B, Hofkens J, et al. Microstructured soft devices for the growth and analysis of populations of homogenous multicellular tumor spheroids. Cellular and Molecular Life Sciences. 2023 Apr;80(4):93. Available from: https://link.springer.com/10.1007/s00018-023-04748-1.

[331] Matsumoto K, Yamada Y, Takahashi M, Todoroki T, Mizoguchi K, Misaki H, et al. Fluorometric determination of carnitine in serum with immobilized carnitine dehydrogenase and diaphorase. Clinical chemistry. 1990;36(12):2072-6.

[332] Belinsky M, Jaiswal AK. NAD (P) H: quinone oxidoreductase 1 (DT-diaphorase) expression in normal and tumor tissues. Cancer and Metastasis Reviews. 1993;12:103-17.

[333] Chikuba K, Yubisui T, Shirabe K, Takeshita M. Cloning and nucleotide sequence of a cDNA of the human erythrocyte NADPH-flavin reductase. Biochemical and biophysical research communications. 1994;198(3):1170-6.

[334] Elmore S. Apoptosis: a review of programmed cell death. Toxicologic pathology. 2007;35(4):495-516.

[335] Thavarajah R, Mudimbaimannar VK, Elizabeth J, Rao UK, Ranganathan K. Chemical and physical basics of routine formaldehyde fixation. Journal of Oral and Maxillofacial Pathology : JOMFP. 2012;16(3):400-5. Available from: https://www.ncbi.nlm.nih.gov/pmc/articles/PMC3519217/.

[336] Keyes M, Crook J, Morton G, Vigneault E, Usmani N, Morris WJ. Treatment options for localized prostate cancer. Canadian Family Physician. 2013;59(12):1269-74.

[337] Weiswald LB, Bellet D, Dangles-Marie V. Spherical cancer models in tumor biology. Neoplasia. 2015;17(1):1-15.

[338] Raitanen J, Barta B, Hacker M, Georg D, Balber T, Mitterhauser M. Comparison of Radiation response between 2D and 3D cell culture models of different human Cancer cell lines. Cells. 2023;12(3):360.

[339] Al-Ramadan A, Mortensen AC, Carlsson J, Nestor MV. Analysis of radiation effects in two irradiated tumor spheroid models. Oncology Letters. 2018;15(3):3008-16.

[340] Cristini V, Koay E, Wang Z. An introduction to physical oncology: How mechanistic mathematical modeling can improve cancer therapy outcomes. CRC Press; 2017.

[341] Deisboeck TS, Wang Z, Macklin P, Cristini V. Multiscale cancer modeling. Annual review of biomedical engineering. 2011;13(1):127-55.

[342] Glazier J, Balter A, Poplawski N, Anderson A, Chaplain M, Rejniak K. Single-cell-based models in biology and medicine. Birkhauser-Verlag, Basel, Switzerland, chapter Magnetization to ...; 2007.

[343] Wang Z, Butner JD, Kerketta R, Cristini V, Deisboeck TS. Simulating cancer growth with multiscale agent-based modeling. In: Seminars in cancer biology. vol. 30. Elsevier; 2015. p. 70-8.

[344] Buch K, Peters T, Nawroth T, Sänger M, Schmidberger H, Langguth P. Determination of cell survival after irradiation via clonogenic assay versus multiple MTT Assay-A comparative study. Radiation oncology. 2012;7:1-6.

[345] Brüningk SC, Rivens I, Box C, Oelfke U, Ter Haar G. 3D tumour spheroids for the prediction of the effects of radiation and hyperthermia treatments. Scientific Reports. 2020;10(1):1653.

[346] Kaida A, Miura M. Visualizing the effect of tumor microenvironments on radiation-induced cell kinetics in multicellular spheroids consisting of HeLa cells. Biochemical and Biophysical Research Communications. 2013;439(4):453-8.

[347] Chhetri RK, Phillips ZF, Troester MA, Oldenburg AL. Longitudinal Study of Mammary Epithelial and Fibroblast Co-Cultures Using Optical Coherence Tomography Reveals Morphological Hallmarks of Pre-Malignancy. PLOS ONE. 2012 Nov;7(11):e49148. Available from: https://journals.plos.org/plosone/article?id=10.1371/journal.pone.0049148.

[348] Carmichael J, DeGraff WG, Gazdar AF, Minna JD, Mitchell JB. Evaluation of a tetrazolium-based semiautomated colorimetric assay: assessment of radiosensitivity. Cancer research. 1987;47(4):943-6.

[349] Kim WH, Chon CY, Moon YM, Kang JK, Park IS, Choi HJ. Effect of anticancer drugs and desferrioxamine in combination with radiation on hepatoma cell lines. Yonsei medical journal. 1993;34(1):45-56.

[350] Gupta N, Lamborn K, Deen DF. A statistical approach for analyzing clonogenic survival data. Radiation research. 1996;145(5):636-40.

[351] Rajaee Z, Khoei S, Mahdavi SR, Ebrahimi M, Shirvalilou S, Mahdavian A. Evaluation of the effect of hyperthermia and electron radiation on prostate cancer stem cells. Radiation and environmental biophysics. 2018;57:133-42.

[352] Cho YM, Kim YS, Kang MJ, Farrar WL, Hurt EM. Long-term recovery of irradiated prostate cancer increases cancer stem cells. The Prostate. 2012;72(16):1746-56.

[353] Fazeli GR, KHOUEI S, NIKOUFAR A, Goliaei B. Reduced DNA damage in tumor spheroids compared to monolayer cultures exposed to ionizing radiation. INTERNATIONAL JOURNAL OF RADIATION RESEARCH. 2007.

[354] Koch J, Moench D, Maass A, Gromoll C, Hehr T, Leibold T, et al. Three dimensional cultivation increases chemo-and radioresistance of colorectal cancer cell lines. PLoS One. 2021;16(1):e0244513.

[355] Durand RE, Sutherland RM. Dependence of the radiation response of an in vitro tumor model on cell cycle effects. Cancer Research. 1973;33(2):213-9.

[356] Liu H, Adler AS, Segal E, Chang HY. A transcriptional program mediating entry into cellular quiescence. PLoS Genetics. 2007;3(6):e91.

[357] Mittler F, Obeïd P, Rulina AV, Haguet V, Gidrol X, Balakirev MY. High-content monitoring of drug effects in a 3D spheroid model. Frontiers in oncology. 2017;7:293.

[358] Elliott MR, Ravichandran KS. The dynamics of apoptotic cell clearance. Developmental cell. 2016;38(2):147-60.

[359] Lammering G, Valerie K, Lin PS, Hewit TH, Schmidt-Ullrich RK. Radiation-induced activation of a common variant of EGFR confers enhanced radioresistance. Radiotherapy and oncology. 2004;72(3):267-73.

[360] Xu W, Luo T, Li P, Zhou C, Cui D, Pang B, et al. RGD-conjugated gold nanorods induce radiosensitization in melanoma cancer cells by downregulating $\alpha v\beta 3$ expression. International Journal of Nanomedicine. 2012:915-24.

[361] Schweigerer L, Rave-Fränk M, Schmidberger H, Hecht M. Sublethal irradiation promotes invasiveness of neuroblastoma cells. Biochemical and biophysical research communications. 2005;330(3):982-8.

[362] Hamis S, Kohandel M, Dubois LJ, Yaromina A, Lambin P, Powathil GG. Combining hypoxia-activated prodrugs and radiotherapy in silico: Impact of treatment scheduling and the intra-tumoural oxygen landscape. PLoS computational biology. 2020;16(8):e1008041.

[363] Mao X, McManaway S, Jaiswal JK, Patel PB, Wilson WR, Hicks KO, et al. An agent-based model for drug-radiation interactions in the tumour microenvironment: Hypoxia-activated prodrug SN30000 in multicellular tumour spheroids. PLoS computational biology. 2018;14(10):e1006469.

[364] Sánchez-Reyes A. A simple model of radiation action in cells based on a repair saturation mechanism. Radiation research. 1992;130(2):139-47.

[365] Stewart RD. Two-lesion kinetic model of double-strand break rejoining and cell killing. Radiation research. 2001;156(4):365-78.

[366] Cleri F. Agent-based model of multicellular tumor spheroid evolution including cell metabolism. The European Physical Journal E. 2019;42:1-15.

[367] Kempf H, Hatzikirou H, Bleicher M, Meyer-Hermann M. In silico analysis of cell cycle synchronisation effects in radiotherapy of tumour spheroids. PLoS computational biology. 2013;9(11):e1003295.

[368] Kempf H, Bleicher M, Meyer-Hermann M. Spatio-temporal dynamics of hypoxia during radiotherapy. PLoS One. 2015;10(8):e0133357.

[369] Powathil GG, Adamson DJ, Chaplain MA. Towards predicting the response of a solid tumour to chemotherapy and radiotherapy treatments: clinical insights from a computational model. PLoS computational biology. 2013;9(7):e1003120.

[370] Powathil GG, Swat M, Chaplain MA. Systems oncology: towards patient-specific treatment regimes informed by multiscale mathematical modelling. In: Seminars in cancer biology. vol. 30. Elsevier; 2015. p. 13-20.

[371] Powathil GG, Munro AJ, Chaplain MA, Swat M. Bystander effects and their implications for clinical radiation therapy: Insights from multiscale in silico experiments. Journal of theoretical biology. 2016;401:1-14.

[372] Testa U, Castelli G, Pelosi E. Cellular and molecular mechanisms underlying prostate cancer development: Therapeutic implications. Medicines. 2019 Jul;6(3):82.

[373] Thoma CR, Zimmermann M, Agarkova I, Kelm JM, Krek W. 3D cell culture systems modeling tumor growth determinants in cancer target discovery. Advanced Drug Delivery Reviews. 2014 Apr;69-70:29-41.

[374] Friedrich J, Seidel C, Ebner R, Kunz-Schughart LA. Spheroid-based drug screen: considerations and practical approach. Nature Protocols. 2009 Mar;4(3):309-24.

[375] Gong X, Lin C, Cheng J, Su J, Zhao H, Liu T, et al. Generation of Multicellular Tumor Spheroids with Microwell-Based Agarose Scaffolds for Drug Testing. PLOS ONE. 2015 Jun;10(6):e0130348.

[376] Sheraton MV, Chiew GGY, Melnikov V, Tan E, Luo KQ, Verma N, et al. Emergence of spatio-temporal variations in chemotherapeutic drug efficacy: in-vitro and in-Silico 3D tumour spheroid studies. BMC cancer. 2020;20:1-16.

[377] Cancino-Marentes ME, Hernández-Flores G, Ortiz-Lazareno PC, Villaseñor-García MM, Orozco-Alonso E, Sierra-Díaz E, et al. Sensitizing the cytotoxic action of Docetaxel induced by Pentoxifylline in a PC3 prostate cancer cell line. BMC urology. 2021;21:1-10.

[378] Michalska M, Schultze-Seemann S, Bogatyreva L, Hauschke D, Wetterauer U, Wolf P. In vitro and in vivo effects of a recombinant anti-PSMA immunotoxin in combination with docetaxel against prostate cancer. Oncotarget. 2016;7(16):22531.

[379] Cai X, Duan X, Tang T, Cui S, Wu T. JMJD2A participates in cytoskeletal remodeling to regulate castration-resistant prostate cancer docetaxel resistance. BMC Cancer. 2023 May;23:423.

[380] Lange R, Heine Rt, Van Wieringen WN, Tromp AM, Paap M, Bloemendal HJ, et al. Cytotoxic effects of the therapeutic radionuclide rhenium-188 combined with taxanes in human prostate carcinoma cell lines. Cancer Biotherapy and Radiopharmaceuticals. 2017;32(1):16-23.

[381] Cisse O, Quraishi M, Gulluni F, Guffanti F, Mavrommati I, Suthanthirakumaran M, et al. Downregulation of class II phosphoinositide 3-kinase PI3K-C2β delays cell division and potentiates the effect of docetaxel on cancer cell growth. Journal of Experimental & Clinical Cancer Research. 2019;38:1-19.

[382] Oprea-Lager DE, van Kanten MP, van Moorselaar RJ, van den Eertwegh AJ, van de Ven PM, Bijnsdorp IV, et al. [18 F] Fluoromethylcholine as a Chemotherapy Response Read-Out in Prostate Cancer Cells. Molecular Imaging and Biology. 2015;17:319-27.

[383] Buck SAJ, Van Hemelryk A, De Ridder C, Stuurman D, Erkens-Schulze S, Van 'T Geloof S, et al. Darolutamide Added to Docetaxel Augments Antitumor Effect in Models of Prostate Cancer through Cell Cycle Arrest at the G1–S Transition. Molecular Cancer Therapeutics. 2024 May;23:711-20.

[384] Beier AMK, Ebersbach C, Siciliano T, Scholze J, Hofmann J, Hönscheid P, et al. Targeting the glutamine metabolism to suppress cell proliferation in mesenchymal docetaxel-resistant prostate cancer. Oncogene. 2024 Jun;43(26):2038-50.

[385] Lai X, Friedman A. Mathematical modeling in scheduling cancer treatment with combination of VEGF inhibitor and chemotherapy drugs. Journal of Theoretical Biology. 2019;462:490-8.

[386] Gordon K. Mathematical modelling of cell-cycle-dependent chemotherapy drugs: implications for cancer treatment [PhD thesis]. Nethergate, Dundee DD1 4HN: University of Dundee; 2006.

[387] Lee DH, Park SW. Systemic Chemotherapy in Metastatic Castration-Resistant Prostate Cancer. Management of Advanced Prostate Cancer. 2018:167-73.

[388] Bruno R, Hille D, Riva A, Vivier N, ten Bokkel Huinnink WW, Van Oosterom AT, et al. Population pharmacokinetics/pharmacodynamics of docetaxel in phase II studies in patients with cancer. Journal of clinical oncology. 1998;16(1):187-96.

[389] Karshafian R, Almasri F, Giles A, Czarnota GJ. Enhancing chemotherapy by ultrasound and microbubbles: Effect of acoustic pressure and treatment order in in vitro suspension of reast and prostate cancer cells. In: 2010 IEEE International Ultrasonics Symposium. IEEE; 2010. p. 1582-5.

[390] Mathur A, Abd Elmageed ZY, Liu X, Kostochka ML, Zhang H, Abdel-Mageed AB, et al. Subverting ER-stress towards apoptosis by nelfinavir and curcumin coexposure

augments docetaxel efficacy in castration resistant prostate cancer cells. PloS one. 2014;9(8):e103109.

[391] Bromma K, Beckham W, Chithrani DB. Utilizing two-dimensional monolayer and three-dimensional spheroids to enhance radiotherapeutic potential by combining gold nanoparticles and docetaxel. Cancer Nanotechnology. 2023;14(1):80.

[392] Fujiike AY, de Oliveira LCB, Ribeiro DL, Pereira ÉR, Okuyama NCM, Dos Santos AGP, et al. Effects of docetaxel on metastatic prostate (DU-145) carcinoma cells cultured as 2D monolayers and 3D multicellular tumor spheroids. Journal of Toxicology and Environmental Health, Part A. 2024;87(6):227-44.

[393] Brown JS, Amend SR, Austin RH, Gatenby RA, Hammarlund EU, Pienta KJ. Updating the definition of cancer. Molecular Cancer Research. 2023;21(11):1142-7.

[394] Almasri F, Karshafian R. Synergistic enhancement of cell death by triple combination therapy of docetaxel, ultrasound and microbubbles, and radiotherapy on PC3 a prostate cancer cell line. Heliyon. 2022;8(8).

[395] Linke D, Donix L, Peitzsch C, Erb HH, Dubrovska A, Pfeifer M, et al. Comprehensive evaluation of multiple approaches targeting ABCB1 to resensitize docetaxel-resistant prostate cancer cell lines. International Journal of Molecular Sciences. 2022;24(1):666.

[396] Pilling A, Kim SH, Hwang C. Androgen receptor negatively regulates mitotic checkpoint signaling to induce docetaxel resistance in castration-resistant prostate cancer. The Prostate. 2022;82(2):182-92.

[397] Li YF, Ji HH, Zhang ZL, Zhang TT, Gan W, Zhang SF. Targeting MRP4 expression by anti-androgen treatment reverses MRP4-mediated docetaxel resistance in castration-resistant prostate cancer. Oncology letters. 2017;14(2):1748-56.

[398] Hurtubise A, Momparler RL. Evaluation of antineoplastic action of 5-aza-2'-deoxycytidine (Dacogen) and docetaxel (Taxotere) on human breast, lung and prostate carcinoma cell lines. Anti-cancer drugs. 2004;15(2):161-7.

[399] Yan J, Tang D. Prostate cancer stem-like cells proliferate slowly and resist etoposide-induced cytotoxicity via enhancing DNA damage response. Experimental cell research. 2014;328(1):132-42.

[400] Zemskova M, Sahakian E, Bashkirova S, Lilly M. The PIM1 kinase is a critical component of a survival pathway activated by docetaxel and promotes survival of docetaxel-treated prostate cancer cells. Journal of Biological Chemistry. 2008;283(30):20635-44.

[401] McDermott N, Meunier A, Mooney B, Nortey G, Hernandez C, Hurley S, et al. Fractionated radiation exposure amplifies the radioresistant nature of prostate cancer cells. Scientific reports. 2016;6(1):34796.

[402] Hernández-Vargas H, Palacios J, Moreno-Bueno G. Molecular profiling of docetaxel cytotoxicity in breast cancer cells: uncoupling of aberrant mitosis and apoptosis. Oncogene. 2007;26(20):2902-13.

[403] Monteverde M, Tonissi F, Fischel JL, Etienne-Grimaldi MC, Milano G, Merlano M, et al. Combination of docetaxel and vandetanib in docetaxel-sensitive or resistant PC3 cell line. In: Urologic Oncology: Seminars and Original Investigations. vol. 31. Elsevier; 2013. p. 776-86.

[404] Scholpa N, Kolli R, Moore M, Arnold R, Glenn T, Cummings B. Nephrotoxicity of epigenetic inhibitors used for the treatment of cancer. Chemico-biological interactions. 2016;258:21-9.

[405] Chen C, Cai Z, Zhuo Y, Xi M, Lin Z, Jiang F, et al. Overexpression of SLC6A1 associates with drug resistance and poor prognosis in prostate cancer. BMC cancer. 2020;20:1-10.

[406] Pereira S, Egbu R, Jannati G, Al-Jamal W. Docetaxel-loaded liposomes: The effect of lipid composition and purification on drug encapsulation and in vitro toxicity. International journal of pharmaceutics. 2016;514(1):150-9.

[407] Chambers KF, Mosaad EM, Russell PJ, Clements JA, Doran MR. 3D cultures of prostate cancer cells cultured in a novel high-throughput culture platform are more resistant to chemotherapeutics compared to cells cultured in monolayer. PloS one. 2014;9(11):e111029.

[408] Souza AG, Silva IBB, Campos-Fernandez E, Barcelos LS, Souza JB, Marangoni K, et al. Comparative assay of 2D and 3D cell culture models: proliferation, gene expression and anticancer drug response. Current pharmaceutical design. 2018;24(15):1689-94.

[409] Edmondson R, Adcock AF, Yang L. Influence of matrices on 3D-cultured prostate cancer cells' drug response and expression of drug-action associated proteins. PloS one. 2016;11(6):e0158116.

[410] Bromma K, Dos Santos N, Barta I, Alexander A, Beckham W, Krishnan S, et al. Enhancing nanoparticle accumulation in two dimensional, three dimensional, and

xenograft mouse cancer cell models in the presence of docetaxel. Scientific reports. 2022;12(1):13508.

[411] Grayson KA, Hope JM, Wang W, Reinhart-King CA, King MR. Taxanes sensitize prostate cancer cells to TRAIL-induced apoptotic synergy via endoplasmic reticulum stress. Molecular cancer therapeutics. 2021;20(5):833-45.

[412] Stebbing A. Hormesis—the stimulation of growth by low levels of inhibitors. Science of the total environment. 1982;22(3):213-34.

[413] Schulz H. Ueber mefegifte. Pflügers Archiv fur die gesamte Physiologic. 1888;42:517.

[414] Southam CM, Chrlich J. Effects of extract of Western Bed-Cedar heart-wood on certain wood-decaying fungi in culture. Phytopathology. 1943;33:517.

[415] Calabrese EJ. Cancer biology and hormesis: human tumor cell lines commonly display hormetic (biphasic) dose responses. Critical reviews in toxicology. 2005;35(6):463-582.

[416] Anderson LM. Cancer biology and hormesis: comments on Calabrese (2005). Critical Reviews in Toxicology. 2005;35(6):583-6.

[417] Sagan LA. On radiation, paradigms, and hormesis. Science. 1989;245(4918):574-4.

[418] Shibamoto Y, Nakamura H. Overview of biological, epidemiological, and clinical evidence of radiation hormesis. International journal of molecular sciences. 2018;19(8):2387.

[419] Chang X, Tamauchi S, Nakagawa A, Xinyuan W, Yoshida K, Yokoi A, et al. Chemotherapeutic hormesis induced by the tumor microenvironment in refractory ovarian cancer. Scientific Reports. 2025;15(1):596.

[420] Yoshimasu T, Oura S, Hirai I, Tamaki T, Kokawa Y, Hata K, et al. Data acquisition for the histoculture drug response assay in lung cancer. The Journal of thoracic and cardiovascular surgery. 2007;133(2):303-8.

[421] Yoshimasu T, Ohashi T, Oura S, Kokawa Y, Kawago M, Hirai Y, et al. A theoretical model for the hormetic dose-response curve for anticancer agents. Anticancer Research. 2015;35(11):5851-5.

[422] Ohashi T, Yoshimasu T, Oura S, Kokawa Y, Kawago M, Hirai Y, et al. Class III beta-tubulin expression in non-small cell lung cancer: a predictive factor for paclitaxel response. Anticancer research. 2015;35(5):2669-74.

[423] Xu AP, Xu LB, Smith ER, Fleishman JS, Chen ZS, Xu XX. Cancer nuclear envelope rupture and repair in taxane resistance. Medical Review. 2024;4(6):522-30.

[424] Hinow P, Gerlee P, McCawley LJ, Quaranta V, Ciobanu M, Wang S, et al. A spatial model of tumor-host interaction: application of chemotherapy. Mathematical biosciences and engineering: MBE. 2009;6(3):521.

[425] Demetriades M, Zivanovic M, Hadjicharalambous M, Ioannou E, Ljujic B, Vucicevic K, et al. Interrogating and quantifying in vitro cancer drug pharmacodynamics via agent-based and bayesian monte carlo modelling. Pharmaceutics. 2022;14(4):749.

[426] Colli P, Gomez H, Lorenzo G, Marinoschi G, Reali A, Rocca E. Optimal control of cytotoxic and antiangiogenic therapies on prostate cancer growth. Mathematical Models and Methods in Applied Sciences. 2021;31(07):1419-68.

[427] Pourhasanzade F, Sabzpoushan S. A cellular automata model of chemotherapy effects on tumour growth: targeting cancer and immune cells. Mathematical and Computer Modelling of Dynamical Systems. 2019;25(1):63-89.

[428] Xie H, Jiao Y, Fan Q, Hai M, Yang J, Hu Z, et al. Modeling three-dimensional invasive solid tumor growth in heterogeneous microenvironment under chemotherapy. PloS one. 2018;13(10):e0206292.

[429] Powathil GG, Gordon KE, Hill LA, Chaplain MA. Modelling the effects of cell-cycle heterogeneity on the response of a solid tumour to chemotherapy: biological insights from a hybrid multiscale cellular automaton model. Journal of theoretical biology. 2012;308:1-19.

[430] Jarrett AM, Shah A, Bloom MJ, McKenna MT, Hormuth DA, Yankeelov TE, et al. Experimentally-driven mathematical modeling to improve combination targeted and cytotoxic therapy for HER2+ breast cancer. Scientific reports. 2019;9(1):12830.

[431] Ghaffari Laleh N, Loeffler CML, Grajek J, Staňková K, Pearson AT, Muti HS, et al. Classical mathematical models for prediction of response to chemotherapy and immunotherapy. PLoS computational biology. 2022;18(2):e1009822.

[432] Pawlik TM, Keyomarsi K. Role of cell cycle in mediating sensitivity to radiotherapy. International Journal of Radiation Oncology*Biology*Physics. 2004;59(4):928-42.

APPENDICES

Appendix A

Prostate tumor spheroid growth CPM

In the CC3D platform, each CPM is governed by a CC3D file, an XML file, a main Python file, and any number of Python files called "Steppables" that are implemented at a chosen frequency, given in number of MCS. Three Steppable files of interest govern growth, mitosis, and output data. Each of these files for the prostate tumor spheroid growth CPM are provided with a brief description below. The full model code is also available on Github at https://github.com/skswanso/CPM.git.

The CC3D file simply points towards the locations of the other modeling files, relative to its own file location.

```
<Simulation version="4.1.0">
   <XMLScript Type="XMLScript">Simulation/model.xml</XMLScript>
   <PythonScript Type="PythonScript">Simulation/model.py</PythonScript>
   <PythonScript Type="PythonScript">Simulation/Growth.py</PythonScript>
   <PythonScript Type="PythonScript">Simulation/Mitosis.py</PythonScript>
   <PythonScript Type="PythonScript">Simulation/Output.py</PythonScript>
</Simulation>
```

The XML file of each model contains specific parameters required by CC3D, and has been extended here to further centralize and store all parameter values, which are accessed by the relevant Python file.

```
<CompuCell3D Revision="20190906" Version="4.1.0">

<!-- Automation ****************************************************** -->
    <Automation>
        <InitialCondition>"X:/IC/
   InVitro_gel_1000_cells_1000_cell_gap_IDs_ceiling_81_162x162x81/"</
   InitialCondition>
```

```
        <WaitSeconds>
            <StartAttempts>60</StartAttempts>
            <QueueAttempts>600</QueueAttempts>
            <DeleteIC>3600</DeleteIC>
        </WaitSeconds>
    </Automation>

<!-- Output ************************************************************ -->
    <Output>
        <Path>
            <CSV>"X:/Output/2025-07-07/"</CSV>
            <CC3D>"X:/Output/2025-07-07/"</CC3D>
        </Path>
        <Frequency>
            <CollectData>10</CollectData>
            <WriteData>10</WriteData>
            <Lattice>400</Lattice>
        </Frequency>
        <ExtendMCS>0</ExtendMCS>
        <StopDistance>5</StopDistance>
    </Output>

<!-- Potts model properties ************************************************ -->
    <Potts>
        <Dimensions x="162" y="162" z="81" />
        <Steps>3605</Steps>
        <Flip2DimRatio>1</Flip2DimRatio>
        <Boundary_x>Periodic</Boundary_x>
        <Boundary_y>Periodic</Boundary_y>
        <Boundary_z>Periodic</Boundary_z>
        <CellMotility>
            <MotilityParameters CellType="Normoxic" Motility="10" />
            <MotilityParameters CellType="Hypoxic" Motility="10" />
            <MotilityParameters CellType="Necrotic" Motility="10" />
            <MotilityParameters CellType="Gap" Motility="10" />
        </CellMotility>
        <NeighborOrder>3</NeighborOrder>
    </Potts>

<!-- Growth ************************************************************ -->
    <Growth>
        <Frequency>10</Frequency>
        <Tumour>
            <Volume>
                <Target>160</Target>
```

```
                <Lambda>10</Lambda>
                <MaxChange>0.19</MaxChange>
                <HalfSat>10</HalfSat>
            </Volume>
            <Surface>
                <Target>480</Target>
                <Lambda>2</Lambda>
                <MaxChange>0.58</MaxChange>
                <HalfSat>10</HalfSat>
            </Surface>
            <OxygenThreshold Hypoxic="5" Necrotic="1" />
            <NecroticLambda>10000</NecroticLambda>
        </Tumour>
    </Growth>

<!-- Mitosis ********************************************************* -->
    <Mitosis>
        <Frequency>10</Frequency>
        <DoublingVolume>
            <Normoxic>260</Normoxic>
            <Hypoxic>260</Hypoxic>
        </DoublingVolume>
    </Mitosis>

<!-- Basic simulation properties ********************************** -->
    <Metadata>
        <NumberOfProcessors>4</NumberOfProcessors>
        <DebugOutputFrequency>500</DebugOutputFrequency>
    </Metadata>

<!-- Plugins ********************************************************* -->
    <Plugin Name="CellType">
        <CellType TypeId="0" TypeName="Medium" />
        <CellType TypeId="1" TypeName="Normoxic" />
        <CellType TypeId="2" TypeName="Hypoxic" />
        <CellType TypeId="3" TypeName="Necrotic" />
        <CellType Freeze="" TypeId="4" TypeName="Gel" />
        <CellType TypeId="5" TypeName="Gap" />
    </Plugin>

    <Plugin Name="Contact">
        <Energy Type1="Medium" Type2="Medium">0</Energy>
        <Energy Type1="Normoxic" Type2="Medium">1</Energy>
        <Energy Type1="Normoxic" Type2="Normoxic">6</Energy>

```

```
        <Energy Type1="Hypoxic" Type2="Medium">1</Energy>
        <Energy Type1="Hypoxic" Type2="Normoxic">6</Energy>
        <Energy Type1="Hypoxic" Type2="Hypoxic">6</Energy>

        <Energy Type1="Necrotic" Type2="Medium">0</Energy>
        <Energy Type1="Necrotic" Type2="Normoxic">0</Energy>
        <Energy Type1="Necrotic" Type2="Hypoxic">0</Energy>
        <Energy Type1="Necrotic" Type2="Necrotic">0</Energy>

        <Energy Type1="Gap" Type2="Medium">1</Energy>
        <Energy Type1="Gap" Type2="Normoxic">6</Energy>
        <Energy Type1="Gap" Type2="Hypoxic">6</Energy>
        <Energy Type1="Gap" Type2="Necrotic">0</Energy>
        <Energy Type1="Gap" Type2="Gap">6</Energy>

        <Energy Type1="Gel" Type2="Medium">0</Energy>
        <Energy Type1="Gel" Type2="Normoxic">1</Energy>
        <Energy Type1="Gel" Type2="Hypoxic">1</Energy>
        <Energy Type1="Gel" Type2="Necrotic">0</Energy>
        <Energy Type1="Gel" Type2="Gap">1</Energy>
        <Energy Type1="Gel" Type2="Gel">0</Energy>

        <NeighborOrder>5</NeighborOrder>
    </Plugin>

    <Plugin Name="ExternalPotential">
        <Lambda x="0.0" y="0.0" z="10000.0" />
    </Plugin>

<!-- Other plugin declarations ************************************ -->
    <Plugin Name="Volume" />

    <Plugin Name="Surface" />

    <Plugin Name="CenterOfMass" />

    <Plugin Name="NeighborTracker" />

<!-- Steppables ************************************************** -->

    <Steppable Type="KernelDiffusionSolver">
    <DiffusionField>
        <Kernel>35</Kernel>
        <CoarseGrainFactor>3</CoarseGrainFactor>
        <DiffusionData>
```

```
            <FieldName>Oxygen</FieldName>
            <DiffusionConstant>3440</DiffusionConstant>
        </DiffusionData>

        <SecretionData>
        <Uptake MaxUptake="24" RelativeUptakeRate="1" Type="Hypoxic" />
        <Uptake MaxUptake="24" RelativeUptakeRate="1" Type="Normoxic" />
        <ConstantConcentration Type="Medium">10</ConstantConcentration>
        <ConstantConcentration Type="Gap">10</ConstantConcentration>
        </SecretionData>
    </DiffusionField>
    </Steppable>

    <Steppable Type="PIFInitializer">
        <PIFName>Simulation/InitialCondition/Tumour.piff</PIFName>
    </Steppable>

</CompuCell3D>
```

The control of each Steppable python file is managed through the main Python file.

```
import os
import inspect
import xml.etree.ElementTree as ET
from cc3d.CompuCellSetup import register_steppable
from Growth import GrowthSteppable
from Mitosis import MitosisSteppable
from Output import OutputSteppable

# Get file name from current directory and trial text file.
currentFile = inspect.getframeinfo(inspect.currentframe()).filename
currentDir = os.path.dirname(os.path.abspath(currentFile))
project = os.path.basename(os.path.dirname(currentDir))
trialFile = f'{currentDir}/Trial_number.txt'
with open(trialFile, 'r') as trial_file:
    trial = trial_file.readline().strip()
name = f'{project}_trial-{trial}'

# Read model xml file for Steppable frequencies.
modelName = os.path.splitext(os.path.basename(currentFile))[0]
xmlModelPath = f'{currentDir}/{modelName}.xml'
xmlModelTree = ET.parse(xmlModelPath)
xmlModelRoot = xmlModelTree.getroot()
growthFreq = int(xmlModelRoot.find('Growth/Frequency').text)
mitosisFreq = int(xmlModelRoot.find('Mitosis/Frequency').text)
outputFreq = int(xmlModelRoot.find('Output/Frequency/CollectData').text)
```

```
26
27 # Register GrowthSteppable.
28 register_steppable(steppable=GrowthSteppable(xmlModelPath,
29                                               frequency=growthFreq))
30
31 # Register MitosisSteppable.
32 register_steppable(steppable=MitosisSteppable(xmlModelPath,
33                                                frequency=mitosisFreq))
34
35 # Register OutputSteppable.
36 register_steppable(steppable=OutputSteppable(xmlModelPath, name,
37                                               frequency=outputFreq))
38
39 CompuCellSetup.run()
```

The Growth Steppable controls conversion between cell types and implements cell growth by increasing cell target volumes and surface areas.

```
1  from cc3d.core.PySteppables import *
2  import xml.etree.ElementTree as ET
3
4  class GrowthSteppable(SteppableBasePy):
5      def __init__(self, xmlModelpath, frequency=1):
6          SteppableBasePy.__init__(self, frequency)
7
8          self.growthFreq = frequency
9
10         # Initialize parameter values from model xml file.
11         xmlModelTree = ET.parse(xmlModelpath)
12         xmlModelRoot = xmlModelTree.getroot()
13         tumour = xmlModelRoot.find('Growth/Tumour')
14
15         # Indicate if the simulation "restarts" with existing fields.
16         if xmlModelRoot.find('.//ConcentrationFileName') is not None:
17             self.doTransient = False
18         else:
19             self.doTransient = True
20
21         # Tumour cell target and lambda volumes and surfaces.
22         self.tumTargetVolume = float(tumour.find('Volume/Target').text)
23         self.tumLambdaVolume = float(tumour.find('Volume/Lambda').text)
24         self.tumTargetSurface = float(tumour.find('Surface/Target').text)
25         self.tumLambdaSurface = float(tumour.find('Surface/Lambda').text)
26
27         # Thresholds for tumour differentiation.
28         self.hypoOxyThresh = float(
```

```
            tumour.find('OxygenThreshold').get('Hypoxic')
            )
        self.necOxyThresh = float(
            tumour.find('OxygenThreshold').get('Necrotic')
            )

        # Michaelis-Menten parameters for tumour growth.
        self.tumVmax = float(tumour.find('Volume/MaxChange').text)
        self.tumOv = float(tumour.find('Volume/HalfSat').text)
        self.tumSmax = float(tumour.find('Surface/MaxChange').text)
        self.tumOs = float(tumour.find('Surface/HalfSat').text)

        # Necrotic volume and surface lambda to freeze cell size.
        self.necLambda = float(tumour.find('NecroticLambda').text)

    def start(self):
        for cell in self.cellList:
            # Initialize target and lambda cell volumes and surfaces.
            if (cell.type == self.NORMOXIC or
                cell.type == self.HYPOXIC or
                cell.type == self.GAP
                ):
                cell.targetVolume = self.tumTargetVolume
                cell.lambdaVolume = self.tumLambdaVolume
                cell.targetSurface = self.tumTargetSurface
                cell.lambdaSurface = self.tumLambdaSurface
            if (cell.type == self.NECROTIC):
                cell.targetVolume = self.tumTargetVolume
                cell.lambdaVolume = self.necLambda
                cell.targetSurface = self.tumTargetSurface
                cell.lambdaSurface = self.necLambda

    def step(self, mcs):
        fieldOxygen = self.field.Oxygen

        for cell in self.cellList:
            # Tumour growth and conversion (after transient period).
            if (cell.type == self.NORMOXIC or cell.type == self.HYPOXIC
                    and (mcs > 100 or (not self.doTransient))):
                # Find oxygen concentration at cell COM.
                conOxygen = fieldOxygen[cell.xCOM, cell.yCOM, cell.zCOM]

                # Cell conversion.
                if conOxygen < self.necOxyThresh:
                    cell.type = self.NECROTIC
```

```
                    cell.lambdaVolume = self.necLambda
                    cell.lambdaSurface = self.necLambda
                elif conOxygen < self.hypoOxyThresh:
                    cell.type = self.HYPOXIC
                else:
                    cell.type = self.NORMOXIC

                # Growth equation.
                cell.targetVolume += self.growthFreq * (
                    self.tumVmax*conOxygen / (self.tumOv + conOxygen)
                    )
                cell.targetSurface += self.growthFreq * (
                    self.tumSmax*conOxygen / (self.tumOs + conOxygen)
                    )
```

The Mitosis Steppable manages cell divison.

```
from cc3d.core.PySteppables import *
import xml.etree.ElementTree as ET
import numpy as np

class MitosisSteppable(MitosisSteppableBase):
    def __init__(self, xmlModelPath, frequency=1):
        MitosisSteppableBase.__init__(self, frequency)

        self.frequency = frequency

        # Initialize parameter values from model xml file.
        xmlModelTree = ET.parse(xmlModelPath)
        xmlModelRoot = xmlModelTree.getroot()
        celltype = xmlModelRoot.find('Plugin[@Name="CellType"]')
        doubVol = xmlModelRoot.find('Mitosis/DoublingVolume')
        tumour = xmlModelRoot.find('Growth/Tumour')

        # Get cell type index from xml file because
        # self.CELLTYPE has not been initialized yet.
        NORMOXIC = int(celltype.find(
            'CellType[@TypeName="Normoxic"]').get('TypeId')
            )
        HYPOXIC = int(celltype.find(
            'CellType[@TypeName="Hypoxic"]').get('TypeId')
            )

        # Doubling volumes in the form {cell.type: doublingVolume, ...}.
        # Uses cancer and vascular modules for cell type index because
        # self.CELLTYPE has not been initialized yet.
```

```
        self.doubVolDic = {
            NORMOXIC: float(doubVol.find('Normoxic').text),
            HYPOXIC: float(doubVol.find('Hypoxic').text)
            }

        # Tumour cell volumes and surfaces.
        self.tumTargetVolume = float(tumour.find('Volume/Target').text)
        self.tumLambdaVolume = float(tumour.find('Volume/Lambda').text)
        self.tumTargetSurface = float(tumour.find('Surface/Target').text)
        self.tumLambdaSurface = float(tumour.find('Surface/Lambda').text)

    def start(self):
        # Initialize doublingTime writing.
        for cell in self.cell_list_by_type(self.NORMOXIC, self.HYPOXIC):
            cell.dict['Timer'] = 0
            cell.dict['writeDoublingTime'] = False

    def step(self, mcs):
        cellsToDivide = []
        for cell in self.cell_list_by_type(self.NORMOXIC, self.HYPOXIC):
            cell.dict['Timer'] += self.frequency
            doublingVolume = self.doubVolDic[cell.type]
            if cell.volume > doublingVolume:
                cellsToDivide.append(cell)
                cell.dict['doublingTime'] = cell.dict['Timer']
                cell.dict['writeDoublingTime'] = True

        for cell in cellsToDivide:
            self.divide_cell_random_orientation(cell)

    def update_attributes(self):
        # Set child cell type and parent values of tumour cells.
        self.parentCell.targetVolume = self.tumTargetVolume
        self.parentCell.lambdaVolume = self.tumLambdaVolume
        self.parentCell.targetSurface = self.tumTargetSurface
        self.parentCell.lambdaSurface = self.tumLambdaSurface

        # Reset doubTime writing in child.
        self.parentCell.dict['Timer'] = 0
        self.childCell.dict['Timer'] = 0
        self.childCell.dict['writeDoublingTime'] = False

        # Always set child attribute to be the same as the parent's.
        self.childCell.type = self.parentCell.type
        self.childCell.targetVolume = self.parentCell.targetVolume
```

```
        self.childCell.lambdaVolume = self.parentCell.lambdaVolume
        self.childCell.targetSurface = self.parentCell.targetSurface
        self.childCell.lambdaSurface = self.parentCell.lambdaSurface
```

Finally, the Output Steppable collects, calculates and manages storage of output data.

```
from cc3d.core.PySteppables import *
import csv
import os
import xml.etree.ElementTree as ET
import socket
from datetime import datetime

class OutputSteppable(SteppableBasePy):

    def __init__(self, xmlModelPath, name, frequency=1):
        SteppableBasePy.__init__(self, frequency)

        # Create computer-datetime stamp.
        computer = socket.gethostname()
        start = datetime.now().strftime('%Y-%m-%d-%H%M')
        stamp = f'{computer}_{start}'

        # Read output dirs from model xml file and create file paths.
        xmlModelTree = ET.parse(xmlModelPath)
        xmlModelRoot = xmlModelTree.getroot()
        csvDir = xmlModelRoot.find(
            'Output/Path/CSV'
            ).text.replace('"', '')
        cc3dDir = xmlModelRoot.find(
            'Output/Path/CC3D'
            ).text.replace('"', '')
        self.csvOutInitial = f'{csvDir}_INC_{name}_{stamp}.csv'
        self.cc3dOutInitial = f'{cc3dDir}_INC_{name}'  # Automated stamp.
        self.csvOutFinal = f'{csvDir}{name}_{stamp}.csv'
        self.cc3dOutFinal = f'{cc3dDir}{name}_{stamp}'

        # Create (nested) csv output directory if it does not exist.
        print('\nCreating csv output directory if needed...')
        for ind in range(1, len(csvDir.split('/'))):
            component = '/'.join(csvDir.split('/')[:ind])
            if not os.path.isdir(f'{component}'):
                print(f'\t{component}')
                os.mkdir(f'{component}')

        # Initialize and check writing frequency from model xml file.
```

```
        self.writeFreq = int(
            xmlModelRoot.find('Output/Frequency/WriteData').text)
        if self.writeFreq % frequency != 0:
            msg = f'Writing frequency {self.writeFreq} not a multiple of'
            raise ValueError(f'{msg} output frequency {frequency}')
        self.outputPerWrite = int(self.writeFreq/frequency)
        self.writeIndex = 0

        # Initialize parameters to control when simulation ends.
        self.frequency = frequency
        self.nMCS = int(xmlModelRoot.find('Potts/Steps').text)
        self.extendMCS = int(xmlModelRoot.find('Output/ExtendMCS').text)
        self.stopDistance = int(
            xmlModelRoot.find('Output/StopDistance').text
            )
        self.border = [
            float(xmlModelRoot.find('Potts/Dimensions').get('x')),
            float(xmlModelRoot.find('Potts/Dimensions').get('y')),
            float(xmlModelRoot.find('Potts/Dimensions').get('z'))
            ]

        # Time step.
        self.mcsLBL = 'MCS'

        # Number of cell types of interest.
        self.normLBL = 'Normoxic cell number'
        self.hypoLBL = 'Hypoxic cell number'
        self.necLBL = 'Necrotic cell number'

        # Volumes of interest.
        self.tumvolLBL = 'Tumour volume'
        self.totvolLBL = 'Total volume'
        self.gapvolLBL = 'Internal gap volume'

        # Surface areas of interest.
        self.extAreaLBL = 'External surface area'

        # Oxygenation.
        self.normoxyLBL = 'Avg Normoxic oxygen'
        self.hypooxyLBL = 'Avg Hypoxic oxygen'

        # Speed.
        self.tumSpeedLBL = 'Average Tumour Cell Speed'

        # Doubling times.
```

```
        self.tumdoubLBL = 'Avg tumour cell doubling time'

        # Column labels, in the following order.
        self.headers = [
            self.mcsLBL,
            self.normLBL, self.hypoLBL, self.necLBL,
            self.tumvolLBL, self.totvolLBL, self.gapvolLBL,
            self.extAreaLBL,
            self.normoxyLBL, self.hypooxyLBL,
            self.tumSpeedLBL,
            self.tumdoubLBL,
            ]

        # For each output MCS, appends a list of dictionaries with column
        # labels as keys with their corresponding values.
        self.outputArr = []

        # Keeps track of initialization for restarts, since will need to
        # handle the first writing after a restart differently.
        self.isInitialized = None

    def start(self):
        # Will be initialized after starting simulation from first MCS.
        # If simulation started from restart, no initialization and first
        # restart step writing to file will write column headers and
        # handle a variable number of output steps.
        self.isInitialized = True

    def step(self, mcs):
        # Record cell type numbers and tissue type sizes.
        normNum = 0
        hypoNum = 0
        necNum = 0
        tumVol = 0
        totVol = 0
        gapVol = 0
        extArea = 0
        normOxy = 0
        hypoOxy = 0
        tumSpeed = 0
        tumDoubTime = 0
        tumDoubNum = 0

        fieldOxygen = self.field.Oxygen

```

```
        # DEBUG
        print('\nCollecting output data for: MCS {0}\n'.format(mcs))

        # Flag gap cells as external if they touch medium, else internal.
        for cell in self.cellList:
            if cell.type == self.GAP:
                cell.dict['isInternal'] = True
                neighborList = self.get_cell_neighbor_data_list(cell)
                for neighbor, commonSurfaceArea in neighborList:
                    # If neighbor is not medium, gap is external.
                    if not neighbor:
                        cell.dict['isInternal'] = False
                        break

        # Track the final conditions; NEW: final COM as well
        for cell in self.cellList:

            # Get total volume and external surface area.
            if (cell.type == self.NORMOXIC or
                cell.type == self.HYPOXIC or
                cell.type == self.NECROTIC):
                totVol += cell.volume
                # Add to external area if medium or ext gap neighbor.
                neighborList = self.get_cell_neighbor_data_list(cell)
                for neighbor, commonSurfaceArea in neighborList:
                    if not neighbor:
                        extArea += commonSurfaceArea
                    else:
                        if (neighbor.type == self.GAP and
                            not neighbor.dict['isInternal']):
                            extArea += commonSurfaceArea

            if cell.type == self.NORMOXIC:
                normNum += 1
                tumVol += cell.volume
                normOxy += fieldOxygen[cell.xCOM, cell.yCOM, cell.zCOM]
                tumSpeed += self.vector_norm(
                    self.invariant_distance_vector(
                        p1=[cell.xCOMPrev, cell.yCOMPrev, cell.zCOMPrev],
                        p2=[cell.xCOM, cell.yCOM, cell.zCOM]))
                if cell.dict['writeDoublingTime']:
                    tumDoubTime += cell.dict['doublingTime']
                    cell.dict['writeDoublingTime'] = False
                    tumDoubNum += 1

```

```
            elif cell.type == self.HYPOXIC:
                hypoNum += 1
                tumVol += cell.volume
                hypoOxy += fieldOxygen[cell.xCOM, cell.yCOM, cell.zCOM]
                tumSpeed += self.vector_norm(
                    self.invariant_distance_vector(
                        p1=[cell.xCOMPrev, cell.yCOMPrev, cell.zCOMPrev],
                        p2=[cell.xCOM, cell.yCOM, cell.zCOM]))
                if cell.dict['writeDoublingTime']:
                    tumDoubTime += cell.dict['doublingTime']
                    cell.dict['writeDoublingTime'] = False
                    tumDoubNum += 1

            elif cell.type == self.NECROTIC:
                necNum += 1

            elif cell.type == self.GAP:
                if cell.dict['isInternal']:
                    gapVol += cell.volume
            else:
                pass  # Allow gel.

        #  Average the oxygen concentrations, doubling times, and speed.
        if normNum > 0:
            normOxy /= normNum
        if hypoNum > 0:
            hypoOxy /= hypoNum
        if normNum + hypoNum > 0:
            tumSpeed /= normNum + hypoNum
        if tumDoubNum > 0:
            tumDoubTime /= tumDoubNum

        # Update output array; NEW: add direction
        self.outputArr.append({
            self.mcsLBL: mcs,
            self.normLBL: normNum,
            self.hypoLBL: hypoNum,
            self.necLBL: necNum,
            self.tumvolLBL: tumVol,
            self.totvolLBL: totVol,
            self.gapvolLBL: gapVol,
            self.extAreaLBL: extArea,
            self.normoxyLBL: normOxy,
            self.hypooxyLBL: hypoOxy,
            self.tumSpeedLBL: tumSpeed,
```

```
            self.tumdoubLBL: tumDoubTime,
            })

        # Write to file.
        if mcs % self.writeFreq == 0:
            with open(self.csvOutInitial, 'a+', newline='') as f:
                dictWriter = csv.DictWriter(f, fieldnames=self.headers)

                # If first MCS or it has been restarted, need to write
                # headers to csv file and write the first output step or
                # the number of output steps collected since the restart.
                if mcs == 0 or not self.isInitialized:
                    dictWriter.writeheader()
                    numOut = len(self.outputArr)
                    dictWriter.writerows(self.outputArr[:numOut])
                    self.writeIndex += numOut
                    self.isInitialized = True

                # Otherwise, write same number of lines to csv file.
                else:
                    start = self.writeIndex
                    finish = self.writeIndex + self.outputPerWrite
                    dictWriter.writerows(self.outputArr[start:finish])
                    self.writeIndex += self.outputPerWrite

            # DEBUG
            print('Wrote to output file: {0}\n'.format(
                self.csvOutInitial
                ))

            # End simulation if the tumour has completely disappeared.
            if normNum + hypoNum + necNum == 0:
                print('Tumour has disappeared, so simulation will end\n')
                self.nMCS = mcs
                # Rename simulation as dead.
                csvBase = f'DEAD_{os.path.basename(self.csvOutFinal)}'
                csvDir = os.path.dirname(self.csvOutFinal)
                self.csvOutFinal = f'{csvDir}/{csvBase}'
                cc3dBase = f'DEAD_{os.path.basename(self.cc3dOutFinal)}'
                cc3dDir = os.path.dirname(self.cc3dOutFinal)
                self.cc3dOutFinal = f'{cc3dDir}/{cc3dBase}'
                self.finish()
                self.stop_simulation()

    def finish(self):
```

```
266         """Rename CC3D data folder and output csv file with MCS."""
267         self.cc3dOutFinal += f'_MCS-{self.nMCS}'
268         self.csvOutFinal = self.csvOutFinal.split('.')[0]
269         self.csvOutFinal += f'_MCS-{self.nMCS}.csv'
270 
271         # Rename CC3D data folder and output csv file.
272         if os.path.isdir(self.cc3dOutInitial):
273             os.rename(self.cc3dOutInitial, self.cc3dOutFinal)
274         if os.path.isfile(self.csvOutInitial):
275             os.rename(self.csvOutInitial, self.csvOutFinal)
```

Appendix B

Prostate tumor spheroid radiation treatment CPM

The CPM of radiation treatment modifies the prostate tumor spheroid growth CPM given in Appendix A. The full model code is also available on Github at https://github.com/skswanso/CPM.git.

A Radiation Steppable was added to identify cells that survive treatment.

```
from cc3d.core.PySteppables import *
import xml.etree.ElementTree as ET
import numpy as np

class RadiationSteppable(SteppableBasePy):
    def __init__(self, xmlModelPath, frequency=1):
        SteppableBasePy.__init__(self, frequency)

        self.frequency = frequency

        # Initialize parameter values from model xml file.
        xmlModelTree = ET.parse(xmlModelPath)
        xmlModelRoot = xmlModelTree.getroot()
        rad = xmlModelRoot.find('Treatment/Radiation')

        # Linear quadratic model parameters for radiation survival.
        self.alpha = float(rad.find('Alpha').text)
        self.beta = float(rad.find('Beta').text)
        self.dose = float(rad.find('Dose').text)
        self.TreatmentMCS = int(rad.find('TreatmentMCS').text)

```

```
22      def start(self):
23          # Initialize cell survival flag.
24          for cell in self.cell_list_by_type(self.NORMOXIC, self.HYPOXIC):
25              cell.dict['survivedRadiation'] = True
26
27      def step(self, mcs):
28          # If rand > probability of survival, kill cell.
29          if mcs == self.TreatmentMCS:
30              for cell in self.cell_list_by_type(
31                  self.NORMOXIC, self.HYPOXIC
32                  ):
33                  survival_prob = np.exp(
34                      - self.dose * (self.alpha + self.beta * self.dose))
35                  rand = np.random.random()
36                  if rand > survival_prob:
37                      cell.dict['survivedRadiation'] = False
```

The following files from the prostate tumor spheroid growth CPM were also modified to include and record the effects of radiation treatment.

The CC3D file additionally points towards the Radiation Steppable on line 7.

```
1 <Simulation version="4.1.0">
2    <XMLScript Type="XMLScript">Simulation/model.xml</XMLScript>
3    <PythonScript Type="PythonScript">Simulation/model.py</PythonScript>
4    <PythonScript Type="PythonScript">Simulation/Growth.py</PythonScript>
5    <PythonScript Type="PythonScript">Simulation/Mitosis.py</PythonScript>
6    <PythonScript Type="PythonScript">Simulation/Output.py</PythonScript>
7    <PythonScript Type="PythonScript">Simulation/Radiation.py</
     PythonScript>
8 </Simulation>
```

The XML file defines an *Apoptotic* cell type with the same characteristics as *Necrotic* cells. It also adds a `Treatment` section.

```
1 <CompuCell3D Revision="20190906" Version="4.1.0">
2
3 <!-- Automation ************************************************** -->
4     <Automation>
5         <InitialCondition>"X:/IC/
     InVitro_gel_1000_cells_1000_cell_gap_IDs_ceiling_81_162x162x81/"</
     InitialCondition>
6         <WaitSeconds>
7             <StartAttempts>60</StartAttempts>
8             <QueueAttempts>600</QueueAttempts>
9             <DeleteIC>3600</DeleteIC>
```

```
        </WaitSeconds>
    </Automation>

<!-- Output ********************************************************** -->
    <Output>
        <Path>
            <CSV>"X:/Output/2025-07-07/"</CSV>
            <CC3D>"X:/Output/2025-07-07/"</CC3D>
        </Path>
        <Frequency>
            <CollectData>10</CollectData>
            <WriteData>10</WriteData>
            <Lattice>1200</Lattice>
        </Frequency>
        <ExtendMCS>0</ExtendMCS>
        <StopDistance>5</StopDistance>
    </Output>

<!-- Potts model properties ************************************** -->
    <Potts>
        <Dimensions x="162" y="162" z="81" />
        <Steps>2405</Steps>
        <Flip2DimRatio>1</Flip2DimRatio>
        <Boundary_x>Periodic</Boundary_x>
        <Boundary_y>Periodic</Boundary_y>
        <Boundary_z>Periodic</Boundary_z>
        <CellMotility>
            <MotilityParameters CellType="Normoxic" Motility="10" />
            <MotilityParameters CellType="Hypoxic" Motility="10" />
            <MotilityParameters CellType="Necrotic" Motility="10" />
            <MotilityParameters CellType="RadApoptotic" Motility="10" />
            <MotilityParameters CellType="Gap" Motility="10" />
        </CellMotility>
        <NeighborOrder>3</NeighborOrder>
    </Potts>

<!-- Growth ****************************************************** -->
    <Growth>
        <Frequency>10</Frequency>
        <Tumour>
            <Volume>
                <Target>160</Target>
                <Lambda>10</Lambda>
                <MaxChange>0.19</MaxChange>
                <HalfSat>10</HalfSat>
```

```
            </Volume>
            <Surface>
                <Target>480</Target>
                <Lambda>2</Lambda>
                <MaxChange>0.58</MaxChange>
                <HalfSat>10</HalfSat>
            </Surface>
            <OxygenThreshold Hypoxic="5" Necrotic="1" />
            <NecroticLambda>10000</NecroticLambda>
        </Tumour>
    </Growth>

<!-- Mitosis ********************************************************* -->
    <Mitosis>
        <Frequency>10</Frequency>
        <DoublingVolume>
            <Normoxic>260</Normoxic>
            <Hypoxic>260</Hypoxic>
        </DoublingVolume>
    </Mitosis>

<!-- Treatment ******************************************************* -->
    <Treatment>
        <Radiation>
            <Alpha>0.236</Alpha>
            <Beta>0.040</Beta>
            <Dose>1</Dose>
            <TreatmentMCS>1200</TreatmentMCS>
        </Radiation>
    </Treatment>

<!-- Basic simulation properties ************************************** -->
    <Metadata>
        <NumberOfProcessors>4</NumberOfProcessors>
        <DebugOutputFrequency>500</DebugOutputFrequency>
    </Metadata>

<!-- Plugins ********************************************************* -->
    <Plugin Name="CellType">
        <CellType TypeId="0" TypeName="Medium" />
        <CellType TypeId="1" TypeName="Normoxic" />
        <CellType TypeId="2" TypeName="Hypoxic" />
        <CellType TypeId="3" TypeName="Necrotic" />
        <CellType TypeId="4" TypeName="RadApoptotic" />
        <CellType Freeze="" TypeId="5" TypeName="Gel" />
```

```
        <CellType TypeId="6" TypeName="Gap" />
    </Plugin>

    <Plugin Name="Contact">
        <Energy Type1="Medium" Type2="Medium">0</Energy>
        <Energy Type1="Normoxic" Type2="Medium">1</Energy>
        <Energy Type1="Normoxic" Type2="Normoxic">6</Energy>

        <Energy Type1="Hypoxic" Type2="Medium">1</Energy>
        <Energy Type1="Hypoxic" Type2="Normoxic">6</Energy>
        <Energy Type1="Hypoxic" Type2="Hypoxic">6</Energy>

        <Energy Type1="Necrotic" Type2="Medium">0</Energy>
        <Energy Type1="Necrotic" Type2="Normoxic">0</Energy>
        <Energy Type1="Necrotic" Type2="Hypoxic">0</Energy>
        <Energy Type1="Necrotic" Type2="Necrotic">0</Energy>

        <Energy Type1="RadApoptotic" Type2="Medium">0</Energy>
        <Energy Type1="RadApoptotic" Type2="Normoxic">0</Energy>
        <Energy Type1="RadApoptotic" Type2="Hypoxic">0</Energy>
        <Energy Type1="RadApoptotic" Type2="Necrotic">0</Energy>
        <Energy Type1="RadApoptotic" Type2="RadApoptotic">0</Energy>

        <Energy Type1="Gap" Type2="Medium">1</Energy>
        <Energy Type1="Gap" Type2="Normoxic">6</Energy>
        <Energy Type1="Gap" Type2="Hypoxic">6</Energy>
        <Energy Type1="Gap" Type2="Necrotic">0</Energy>
        <Energy Type1="Gap" Type2="RadApoptotic">0</Energy>
        <Energy Type1="Gap" Type2="Gap">6</Energy>

        <Energy Type1="Gel" Type2="Medium">0</Energy>
        <Energy Type1="Gel" Type2="Normoxic">1</Energy>
        <Energy Type1="Gel" Type2="Hypoxic">1</Energy>
        <Energy Type1="Gel" Type2="Necrotic">0</Energy>
        <Energy Type1="Gel" Type2="RadApoptotic">0</Energy>
        <Energy Type1="Gel" Type2="Gap">1</Energy>
        <Energy Type1="Gel" Type2="Gel">0</Energy>

        <NeighborOrder>5</NeighborOrder>
    </Plugin>

    <Plugin Name="ExternalPotential">
        <Lambda x="0.0" y="0.0" z="10000.0" />
    </Plugin>

```

```
<!-- Other plugin declarations ************************************ -->
    <Plugin Name="Volume" />

    <Plugin Name="Surface" />

    <Plugin Name="CenterOfMass" />

    <Plugin Name="NeighborTracker" />

<!-- Steppables ********************************************************* -->

    <Steppable Type="KernelDiffusionSolver">
    <DiffusionField>
        <Kernel>35</Kernel>
        <CoarseGrainFactor>3</CoarseGrainFactor>
        <DiffusionData>
            <FieldName>Oxygen</FieldName>
            <DiffusionConstant>3440</DiffusionConstant>
        </DiffusionData>

        <SecretionData>
        <Uptake MaxUptake="24" RelativeUptakeRate="1" Type="Hypoxic" />
        <Uptake MaxUptake="24" RelativeUptakeRate="1" Type="Normoxic" />
        <ConstantConcentration Type="Medium">10</ConstantConcentration>
        <ConstantConcentration Type="Gap">10</ConstantConcentration>
        </SecretionData>
    </DiffusionField>
    </Steppable>

    <Steppable Type="PIFInitializer">
        <PIFName>Simulation/InitialCondition/Tumour.piff</PIFName>
    </Steppable>

</CompuCell3D>
```

The main Python file additionally registers the Radiation Steppable.

```
import os
import inspect
import xml.etree.ElementTree as ET
from cc3d.CompuCellSetup import register_steppable
from Growth import GrowthSteppable
from Mitosis import MitosisSteppable
from Output import OutputSteppable
from Radiation import RadiationSteppable

```

```
# Get file name from current directory and trial text file.
currentFile = inspect.getframeinfo(inspect.currentframe()).filename
currentDir = os.path.dirname(os.path.abspath(currentFile))
project = os.path.basename(os.path.dirname(currentDir))
trialFile = f'{currentDir}/Trial_number.txt'
with open(trialFile, 'r') as trial_file:
    trial = trial_file.readline().strip()
name = f'{project}_trial-{trial}'

# Read model xml file for Steppable frequencies.
modelName = os.path.splitext(os.path.basename(currentFile))[0]
xmlModelPath = f'{currentDir}/{modelName}.xml'
xmlModelTree = ET.parse(xmlModelPath)
xmlModelRoot = xmlModelTree.getroot()
growthFreq = int(xmlModelRoot.find('Growth/Frequency').text)
mitosisFreq = int(xmlModelRoot.find('Mitosis/Frequency').text)
outputFreq = int(xmlModelRoot.find('Output/Frequency/CollectData').text)
radFreq = int(xmlModelRoot.find('Treatment/Radiation/TreatmentMCS').text)

# Register GrowthSteppable.
register_steppable(steppable=GrowthSteppable(xmlModelPath,
                                             frequency=growthFreq))

# Register MitosisSteppable.
register_steppable(steppable=MitosisSteppable(xmlModelPath,
                                              frequency=mitosisFreq))

# Register OutputSteppable.
register_steppable(steppable=OutputSteppable(xmlModelPath, name,
                                             frequency=outputFreq))

# Register RadiationSteppable.
register_steppable(steppable=RadiationSteppable(xmlModelPath,
                                                frequency=radFreq))

CompuCellSetup.run()
```

The `start` function of the Growth Steppable was modified to initialize *Apoptotic* cells with the same volume and surface area values as *Necrotic* cells.

```
from cc3d.core.PySteppables import *
import xml.etree.ElementTree as ET

class GrowthSteppable(SteppableBasePy):
    def __init__(self, xmlModelpath, frequency=1):
        SteppableBasePy.__init__(self, frequency)
```

```
7
8           self.growthFreq = frequency
9
10          # Initialize parameter values from model xml file.
11          xmlModelTree = ET.parse(xmlModelpath)
12          xmlModelRoot = xmlModelTree.getroot()
13          tumour = xmlModelRoot.find('Growth/Tumour')
14
15          # Indicate if the simulation "restarts" with existing fields.
16          if xmlModelRoot.find('.//ConcentrationFileName') is not None:
17              self.doTransient = False
18          else:
19              self.doTransient = True
20
21          # Tumour cell target and lambda volumes and surfaces.
22          self.tumTargetVolume = float(tumour.find('Volume/Target').text)
23          self.tumLambdaVolume = float(tumour.find('Volume/Lambda').text)
24          self.tumTargetSurface = float(tumour.find('Surface/Target').text)
25          self.tumLambdaSurface = float(tumour.find('Surface/Lambda').text)
26
27          # Thresholds for tumour differentiation.
28          self.hypoOxyThresh = float(
29              tumour.find('OxygenThreshold').get('Hypoxic')
30              )
31          self.necOxyThresh = float(
32              tumour.find('OxygenThreshold').get('Necrotic')
33              )
34
35          # Michaelis-Menten parameters for tumour growth.
36          self.tumVmax = float(tumour.find('Volume/MaxChange').text)
37          self.tumOv = float(tumour.find('Volume/HalfSat').text)
38          self.tumSmax = float(tumour.find('Surface/MaxChange').text)
39          self.tumOs = float(tumour.find('Surface/HalfSat').text)
40
41          # Necrotic volume and surface lambda to freeze cell size.
42          self.necLambda = float(tumour.find('NecroticLambda').text)
43
44      def start(self):
45          for cell in self.cellList:
46              # Initialize target and lambda cell volumes and surfaces.
47              if (cell.type == self.NORMOXIC or
48                  cell.type == self.HYPOXIC or
49                  cell.type == self.GAP
50                  ):
51                  cell.targetVolume = self.tumTargetVolume
```

```
                cell.lambdaVolume = self.tumLambdaVolume
                cell.targetSurface = self.tumTargetSurface
                cell.lambdaSurface = self.tumLambdaSurface
            if (cell.type == self.NECROTIC or
                cell.type == self.RADAPOPTOTIC
                ):
                cell.targetVolume = self.tumTargetVolume
                cell.lambdaVolume = self.necLambda
                cell.targetSurface = self.tumTargetSurface
                cell.lambdaSurface = self.necLambda

    def step(self, mcs):
        fieldOxygen = self.field.Oxygen

        for cell in self.cellList:

            # Tumour growth and conversion (after transient period).
            if (cell.type == self.NORMOXIC or cell.type == self.HYPOXIC
                    and (mcs > 100 or (not self.doTransient))):
                # Find oxygen concentration at cell COM.
                conOxygen = fieldOxygen[cell.xCOM, cell.yCOM, cell.zCOM]

                # Cell conversion.
                if conOxygen < self.necOxyThresh:
                    cell.type = self.NECROTIC
                    cell.lambdaVolume = self.necLambda
                    cell.lambdaSurface = self.necLambda
                elif conOxygen < self.hypoOxyThresh:
                    cell.type = self.HYPOXIC
                else:
                    cell.type = self.NORMOXIC

                # Growth equation.
                cell.targetVolume += self.growthFreq * (
                    self.tumVmax*conOxygen / (self.tumOv + conOxygen)
                    )
                cell.targetSurface += self.growthFreq * (
                    self.tumSmax*conOxygen / (self.tumOs + conOxygen)
                    )
```

The Mitosis Steppable `step` function was modified to only perform cell division if the cell survived treatment, otherwise the cell becomes *Apoptotic*.

```
from cc3d.core.PySteppables import *
import xml.etree.ElementTree as ET

```

```
class MitosisSteppable(MitosisSteppableBase):
    def __init__(self, xmlModelPath, frequency=1):
        MitosisSteppableBase.__init__(self, frequency)

        self.frequency = frequency

        # Initialize parameter values from model xml file.
        xmlModelTree = ET.parse(xmlModelPath)
        xmlModelRoot = xmlModelTree.getroot()
        celltype = xmlModelRoot.find('Plugin[@Name="CellType"]')
        doubVol = xmlModelRoot.find('Mitosis/DoublingVolume')
        tumour = xmlModelRoot.find('Growth/Tumour')

        # Get cell type index from xml file because
        # self.CELLTYPE has not been initialized yet.
        NORMOXIC = int(celltype.find(
            'CellType[@TypeName="Normoxic"]').get('TypeId')
            )
        HYPOXIC = int(celltype.find(
            'CellType[@TypeName="Hypoxic"]').get('TypeId')
            )

        # Doubling volumes in the form {cell.type: doublingVolume, ...}.
        # Uses cancer and vascular modules for cell type index because
        # self.CELLTYPE has not been initialized yet.
        self.doubVolDic = {
            NORMOXIC: float(doubVol.find('Normoxic').text),
            HYPOXIC: float(doubVol.find('Hypoxic').text)
            }

        # Tumour cell volumes and surfaces.
        self.tumTargetVolume = float(tumour.find('Volume/Target').text)
        self.tumLambdaVolume = float(tumour.find('Volume/Lambda').text)
        self.tumTargetSurface = float(tumour.find('Surface/Target').text)
        self.tumLambdaSurface = float(tumour.find('Surface/Lambda').text)

    def start(self):
        # Initialize doublingTime writing.
        for cell in self.cell_list_by_type(self.NORMOXIC, self.HYPOXIC):
            cell.dict['Timer'] = 0
            cell.dict['writeDoublingTime'] = False

    def step(self, mcs):
        cellsToDivide = []
        for cell in self.cell_list_by_type(self.NORMOXIC, self.HYPOXIC):
```

```
            cell.dict['Timer'] += self.frequency
            doublingVolume = self.doubVolDic[cell.type]
            if cell.volume > doublingVolume:

                # Divide only if cell survived radiation, else kill it.
                if cell.dict['survivedRadiation']:
                    cellsToDivide.append(cell)
                    cell.dict['doublingTime'] = cell.dict['Timer']
                    cell.dict['writeDoublingTime'] = True
                else:
                    cell.type = self.RADAPOPTOTIC

        for cell in cellsToDivide:
            self.divide_cell_random_orientation(cell)

    def update_attributes(self):
        # Set child cell type and parent values of tumour cells.
        self.parentCell.targetVolume = self.tumTargetVolume
        self.parentCell.lambdaVolume = self.tumLambdaVolume
        self.parentCell.targetSurface = self.tumTargetSurface
        self.parentCell.lambdaSurface = self.tumLambdaSurface

        # Reset timers and set false condition to write doubTime in child
    .
        self.parentCell.dict['Timer'] = 0
        self.childCell.dict['Timer'] = 0
        self.childCell.dict['writeDoublingTime'] = False

        # Always set child attribute to be the same as the parent's.
        self.childCell.type = self.parentCell.type
        self.childCell.targetVolume = self.parentCell.targetVolume
        self.childCell.lambdaVolume = self.parentCell.lambdaVolume
        self.childCell.targetSurface = self.parentCell.targetSurface
        self.childCell.lambdaSurface = self.parentCell.lambdaSurface

        # Set radiation survival attribute of child cell.
        self.childCell.dict['survivedRadiation'] = True
```

Finally, the Output Steppable was modified throughout the `start` and `step` functions to track *Apoptotic* cells.

```
from cc3d.core.PySteppables import *
import csv
import os
import xml.etree.ElementTree as ET
import socket
```

```
from datetime import datetime

class OutputSteppable(SteppableBasePy):

    def __init__(self, xmlModelPath, name, frequency=1):
        SteppableBasePy.__init__(self, frequency)

        # Create computer-datetime stamp.
        computer = socket.gethostname()
        start = datetime.now().strftime('%Y-%m-%d-%H%M')
        stamp = f'{computer}_{start}'

        # Read output dirs from model xml file and create file paths.
        xmlModelTree = ET.parse(xmlModelPath)
        xmlModelRoot = xmlModelTree.getroot()
        csvDir = xmlModelRoot.find(
            'Output/Path/CSV'
            ).text.replace('"', '')
        cc3dDir = xmlModelRoot.find(
            'Output/Path/CC3D'
            ).text.replace('"', '')
        self.csvOutInitial = f'{csvDir}_INC_{name}_{stamp}.csv'
        self.cc3dOutInitial = f'{cc3dDir}_INC_{name}'  # Automated stamp.
        self.csvOutFinal = f'{csvDir}{name}_{stamp}.csv'
        self.cc3dOutFinal = f'{cc3dDir}{name}_{stamp}'

        # Create (nested) csv output directory if it does not exist.
        print('\nCreating csv output directory if needed...')
        for ind in range(1, len(csvDir.split('/'))):
            component = '/'.join(csvDir.split('/')[:ind])
            if not os.path.isdir(f'{component}'):
                print(f'\t{component}')
                os.mkdir(f'{component}')

        # Initialize and check writing frequency from model xml file.
        self.writeFreq = int(
            xmlModelRoot.find('Output/Frequency/WriteData').text)
        if self.writeFreq % frequency != 0:
            msg = f'Writing frequency {self.writeFreq} not a multiple of'
            raise ValueError(f'{msg} output frequency {frequency}')
        self.outputPerWrite = int(self.writeFreq/frequency)
        self.writeIndex = 0

        # Initialize parameters to control when simulation ends.
        self.frequency = frequency
```

```
        self.nMCS = int(xmlModelRoot.find('Potts/Steps').text)
        self.extendMCS = int(xmlModelRoot.find('Output/ExtendMCS').text)
        self.stopDistance = int(
            xmlModelRoot.find('Output/StopDistance').text
            )
        self.border = [
            float(xmlModelRoot.find('Potts/Dimensions').get('x')),
            float(xmlModelRoot.find('Potts/Dimensions').get('y')),
            float(xmlModelRoot.find('Potts/Dimensions').get('z'))
            ]

        # Time step.
        self.mcsLBL = 'MCS'

        # Number of cell types of interest.
        self.normLBL = 'Normoxic cell number'
        self.hypoLBL = 'Hypoxic cell number'
        self.necLBL = 'Necrotic cell number'
        self.liveRadApopLBL = 'Live radiation apoptotic cell number'
        self.radApopLBL = 'Radiation apoptotic cell number'

        # Volumes of interest.
        self.tumvolLBL = 'Tumour volume'
        self.totvolLBL = 'Total volume'
        self.gapvolLBL = 'Internal gap volume'

        # Surface areas of interest.
        self.extAreaLBL = 'External surface area'

        # Oxygenation.
        self.normoxyLBL = 'Avg Normoxic oxygen'
        self.hypooxyLBL = 'Avg Hypoxic oxygen'

        # Speed.
        self.tumSpeedLBL = 'Average Tumour Cell Speed'

        # Doubling times.
        self.tumdoubLBL = 'Avg tumour cell doubling time'

        # Column labels, in the following order.
        self.headers = [
            self.mcsLBL,
            self.normLBL, self.hypoLBL, self.necLBL,
            self.liveRadApopLBL, self.radApopLBL,
            self.tumvolLBL, self.totvolLBL, self.gapvolLBL,
```

```
            self.extAreaLBL,
            self.normoxyLBL, self.hypooxyLBL,
            self.tumSpeedLBL,
            self.tumdoubLBL,
            ]

        # For each output MCS, appends a list of dictionaries with column
        # labels as keys with their corresponding values.
        self.outputArr = []

        # Keeps track of initialization for restarts, since will need to
        # handle the first writing after a restart differently.
        self.isInitialized = None

    def start(self):
        # Will be initialized after starting simulation from first MCS.
        # If simulation started from restart, no initialization and first
        # restart step writing to file will write column headers and
        # handle a variable number of output steps.
        self.isInitialized = True

    def step(self, mcs):
        # Record cell type numbers and tissue type sizes.
        normNum = 0
        hypoNum = 0
        necNum = 0
        liveRadApopNum = 0
        radApopNum = 0
        tumVol = 0
        totVol = 0
        gapVol = 0
        extArea = 0
        normOxy = 0
        hypoOxy = 0
        tumSpeed = 0
        tumDoubTime = 0
        tumDoubNum = 0

        fieldOxygen = self.field.Oxygen

        # DEBUG
        print('\nCollecting output data for: MCS {0}\n'.format(mcs))

        # Flag gap cells as external if they touch medium, else internal.
        for cell in self.cellList:
```

```
            if cell.type == self.GAP:
                cell.dict['isInternal'] = True
                neighborList = self.get_cell_neighbor_data_list(cell)
                for neighbor, commonSurfaceArea in neighborList:
                    # If neighbor is not medium, gap is external.
                    if not neighbor:
                        cell.dict['isInternal'] = False
                        break

        # Track the final conditions.
        for cell in self.cellList:

            # Get total volume and external surface area.
            if (cell.type == self.NORMOXIC or
                cell.type == self.HYPOXIC or
                cell.type == self.NECROTIC or
                cell.type == self.RADAPOPTOTIC):
                totVol += cell.volume
                # Add to external area if medium or ext gap neighbor.
                neighborList = self.get_cell_neighbor_data_list(cell)
                for neighbor, commonSurfaceArea in neighborList:
                    if not neighbor:
                        extArea += commonSurfaceArea
                    else:
                        if (neighbor.type == self.GAP and
                            not neighbor.dict['isInternal']):
                            extArea += commonSurfaceArea

            if cell.type == self.NORMOXIC:
                normNum += 1
                tumVol += cell.volume
                normOxy += fieldOxygen[cell.xCOM, cell.yCOM, cell.zCOM]
                tumSpeed += self.vector_norm(
                    self.invariant_distance_vector(
                        p1=[cell.xCOMPrev, cell.yCOMPrev, cell.zCOMPrev],
                        p2=[cell.xCOM, cell.yCOM, cell.zCOM]))
                if cell.dict['writeDoublingTime']:
                    tumDoubTime += cell.dict['doublingTime']
                    cell.dict['writeDoublingTime'] = False
                    tumDoubNum += 1
                if not cell.dict['survivedRadiation']:
                    liveRadApopNum += 1

            elif cell.type == self.HYPOXIC:
                hypoNum += 1
```

```
                tumVol += cell.volume
                hypoOxy += fieldOxygen[cell.xCOM, cell.yCOM, cell.zCOM]
                tumSpeed += self.vector_norm(
                    self.invariant_distance_vector(
                        p1=[cell.xCOMPrev, cell.yCOMPrev, cell.zCOMPrev],
                        p2=[cell.xCOM, cell.yCOM, cell.zCOM]))
                if cell.dict['writeDoublingTime']:
                    tumDoubTime += cell.dict['doublingTime']
                    cell.dict['writeDoublingTime'] = False
                    tumDoubNum += 1
                if not cell.dict['survivedRadiation']:
                    liveRadApopNum += 1

            elif cell.type == self.NECROTIC:
                necNum += 1

            elif cell.type == self.RADAPOPTOTIC:
                radApopNum += 1

            elif cell.type == self.GAP:
                if cell.dict['isInternal']:
                    gapVol += cell.volume
            else:
                pass  # Allow gel.

        #  Average the oxygen concentrations, doubling times, and speed.
        if normNum > 0:
            normOxy /= normNum
        if hypoNum > 0:
            hypoOxy /= hypoNum
        if normNum + hypoNum > 0:
            tumSpeed /= normNum + hypoNum
        if tumDoubNum > 0:
            tumDoubTime /= tumDoubNum

        # Update output array.
        self.outputArr.append({
            self.mcsLBL: mcs,
            self.normLBL: normNum,
            self.hypoLBL: hypoNum,
            self.liveRadApopLBL: liveRadApopNum,
            self.radApopLBL: radApopNum,
            self.necLBL: necNum,
            self.tumvolLBL: tumVol,
            self.totvolLBL: totVol,
```

```
231             self.gapvolLBL: gapVol,
232             self.extAreaLBL: extArea,
233             self.normoxyLBL: normOxy,
234             self.hypooxyLBL: hypoOxy,
235             self.tumSpeedLBL: tumSpeed,
236             self.tumdoubLBL: tumDoubTime,
237             })
238 
239         # Write to file.
240         if mcs % self.writeFreq == 0:
241             with open(self.csvOutInitial, 'a+', newline='') as f:
242                 dictWriter = csv.DictWriter(f, fieldnames=self.headers)
243 
244                 # If first MCS or it has been restarted, need to write
245                 # headers to csv file and write the first output step or
246                 # the number of output steps collected since the restart.
247                 if mcs == 0 or not self.isInitialized:
248                     dictWriter.writeheader()
249                     numOut = len(self.outputArr)
250                     dictWriter.writerows(self.outputArr[:numOut])
251                     self.writeIndex += numOut
252                     self.isInitialized = True
253 
254                 # Otherwise, write same number of lines to csv file.
255                 else:
256                     start = self.writeIndex
257                     finish = self.writeIndex + self.outputPerWrite
258                     dictWriter.writerows(self.outputArr[start:finish])
259                     self.writeIndex += self.outputPerWrite
260 
261             # DEBUG
262             print('Wrote to output file: {0}\n'.format(
263                 self.csvOutInitial
264                 ))
265 
266             # End the simulation if the tumour has completely disappeared
    .
267             if normNum + hypoNum + radApopNum + necNum == 0:
268                 print('Tumour has disappeared, so simulation will end\n')
269                 self.nMCS = mcs
270                 # Rename simulation as dead.
271                 csvBase = f'DEAD_{os.path.basename(self.csvOutFinal)}'
272                 csvDir = os.path.dirname(self.csvOutFinal)
273                 self.csvOutFinal = f'{csvDir}/{csvBase}'
274                 cc3dBase = f'DEAD_{os.path.basename(self.cc3dOutFinal)}'
```

```
                cc3dDir = os.path.dirname(self.cc3dOutFinal)
                self.cc3dOutFinal = f'{cc3dDir}/{cc3dBase}'
                self.finish()
                self.stop_simulation()

    def finish(self):
        """Rename CC3D data folder and output csv file with MCS."""
        self.cc3dOutFinal += f'_MCS-{self.nMCS}'
        self.csvOutFinal = self.csvOutFinal.split('.')[0]
        self.csvOutFinal += f'_MCS-{self.nMCS}.csv'

        # Rename CC3D data folder and output csv file.
        if os.path.isdir(self.cc3dOutInitial):
            os.rename(self.cc3dOutInitial, self.cc3dOutFinal)
        if os.path.isfile(self.csvOutInitial):
            os.rename(self.csvOutInitial, self.csvOutFinal)
```

Appendix C

Prostate tumor spheroid DTX treatment CPM

The CPM of DTX chemotherapy treatment also modifies the prostate tumor spheroid growth CPM given in Appendix A. The full model code is also available on Github at https://github.com/skswanso/CPM.git.

There are no changes to the CC3D file

```
<Simulation version="4.1.0">
   <XMLScript Type="XMLScript">Simulation/model.xml</XMLScript>
   <PythonScript Type="PythonScript">Simulation/model.py</PythonScript>
   <PythonScript Type="PythonScript">Simulation/Growth.py</PythonScript>
   <PythonScript Type="PythonScript">Simulation/Mitosis.py</PythonScript>
   <PythonScript Type="PythonScript">Simulation/Output.py</PythonScript>
</Simulation>
```

and the main Python file.

```
import os
import inspect
import xml.etree.ElementTree as ET
from cc3d.CompuCellSetup import register_steppable
from Growth import GrowthSteppable
from Mitosis import MitosisSteppable
from Output import OutputSteppable

# Get file name from current directory and trial text file.
currentFile = inspect.getframeinfo(inspect.currentframe()).filename
currentDir = os.path.dirname(os.path.abspath(currentFile))
```

```
project = os.path.basename(os.path.dirname(currentDir))
trialFile = f'{currentDir}/Trial_number.txt'
with open(trialFile, 'r') as trial_file:
    trial = trial_file.readline().strip()
name = f'{project}_trial-{trial}'

# Read model xml file for Steppable frequencies.
modelName = os.path.splitext(os.path.basename(currentFile))[0]
xmlModelPath = f'{currentDir}/{modelName}.xml'
xmlModelTree = ET.parse(xmlModelPath)
xmlModelRoot = xmlModelTree.getroot()
growthFreq = int(xmlModelRoot.find('Growth/Frequency').text)
mitosisFreq = int(xmlModelRoot.find('Mitosis/Frequency').text)
outputFreq = int(xmlModelRoot.find('Output/Frequency/CollectData').text)

# Register GrowthSteppable.
register_steppable(steppable=GrowthSteppable(xmlModelPath,
                                             frequency=growthFreq))

# Register MitosisSteppable.
register_steppable(steppable=MitosisSteppable(xmlModelPath,
                                              frequency=mitosisFreq))

# Register OutputSteppable.
register_steppable(steppable=OutputSteppable(xmlModelPath, name,
                                             frequency=outputFreq))

CompuCellSetup.run()
```

The XML file defines an *Apoptotic* cell type on line 98 with the same cell motility (line 40) and contact energy (lines 103-136) as *Necrotic* cells. It also contains a `Treatment` section on lines 76-84 and defines the PDE governing DTX on lines 173-185.

```
<CompuCell3D Revision="20190906" Version="4.1.0">

<!-- Automation ************************************************** -->
    <Automation>
        <InitialCondition>"X:/IC/
    InVitro_gel_1000_cells_1000_cell_gap_IDs_ceiling_81_162x162x81/"</
    InitialCondition>
        <WaitSeconds>
            <StartAttempts>60</StartAttempts>
            <QueueAttempts>600</QueueAttempts>
            <DeleteIC>3600</DeleteIC>
        </WaitSeconds>
    </Automation>
```

```
12
13 <!-- Output ************************************************************ -->
14     <Output>
15         <Path>
16             <CSV>"X:/Output/2025-07-07/"</CSV>
17             <CC3D>"X:/Output/2025-07-07/"</CC3D>
18         </Path>
19         <Frequency>
20             <CollectData>10</CollectData>
21             <WriteData>10</WriteData>
22             <Lattice>1200</Lattice>
23         </Frequency>
24         <ExtendMCS>0</ExtendMCS>
25         <StopDistance>5</StopDistance>
26     </Output>
27
28 <!-- Potts model properties ************************************************ -->
29     <Potts>
30         <Dimensions x="162" y="162" z="81" />
31         <Steps>3605</Steps>
32         <Flip2DimRatio>1</Flip2DimRatio>
33         <Boundary_x>Periodic</Boundary_x>
34         <Boundary_y>Periodic</Boundary_y>
35         <Boundary_z>Periodic</Boundary_z>
36         <CellMotility>
37             <MotilityParameters CellType="Normoxic" Motility="10" />
38             <MotilityParameters CellType="Hypoxic" Motility="10" />
39             <MotilityParameters CellType="Necrotic" Motility="10" />
40             <MotilityParameters CellType="DrugApoptotic" Motility="10" />
41             <MotilityParameters CellType="Gap" Motility="10" />
42         </CellMotility>
43         <NeighborOrder>3</NeighborOrder>
44     </Potts>
45
46 <!-- Growth ************************************************************** -->
47     <Growth>
48         <Frequency>10</Frequency>
49         <Tumour>
50             <Volume>
51                 <Target>160</Target>
52                 <Lambda>10</Lambda>
53                 <MaxChange>0.19</MaxChange>
54                 <HalfSat>10</HalfSat>
55             </Volume>
56             <Surface>
```

```
                <Target>480</Target>
                <Lambda>2</Lambda>
                <MaxChange>0.58</MaxChange>
                <HalfSat>10</HalfSat>
            </Surface>
            <OxygenThreshold Hypoxic="5" Necrotic="1" />
            <NecroticLambda>10000</NecroticLambda>
        </Tumour>
    </Growth>

<!-- Mitosis ********************************************************* -->
    <Mitosis>
        <Frequency>10</Frequency>
        <DoublingVolume>
            <Normoxic>260</Normoxic>
            <Hypoxic>260</Hypoxic>
        </DoublingVolume>
    </Mitosis>

<!-- Treatment ******************************************************* -->
    <Treatment>
        <Drug>
            <a>0.87</a>
            <b>1.89</b>
            <c>0.13</c>
            <TreatmentMCS>1200</TreatmentMCS>
        </Drug>
    </Treatment>

<!-- Basic simulation properties ********************************** -->
    <Metadata>
        <NumberOfProcessors>4</NumberOfProcessors>
        <DebugOutputFrequency>500</DebugOutputFrequency>
    </Metadata>

<!-- Plugins ********************************************************* -->
    <Plugin Name="CellType">
        <CellType TypeId="0" TypeName="Medium" />
        <CellType TypeId="1" TypeName="Normoxic" />
        <CellType TypeId="2" TypeName="Hypoxic" />
        <CellType TypeId="3" TypeName="Necrotic" />
        <CellType TypeId="4" TypeName="DrugApoptotic" />
        <CellType Freeze="" TypeId="5" TypeName="Gel" />
        <CellType TypeId="6" TypeName="Gap" />
    </Plugin>
```

```
102
103     <Plugin Name="Contact">
104         <Energy Type1="Medium" Type2="Medium">0</Energy>
105         <Energy Type1="Normoxic" Type2="Medium">1</Energy>
106         <Energy Type1="Normoxic" Type2="Normoxic">6</Energy>
107
108         <Energy Type1="Hypoxic" Type2="Medium">1</Energy>
109         <Energy Type1="Hypoxic" Type2="Normoxic">6</Energy>
110         <Energy Type1="Hypoxic" Type2="Hypoxic">6</Energy>
111
112         <Energy Type1="Necrotic" Type2="Medium">0</Energy>
113         <Energy Type1="Necrotic" Type2="Normoxic">0</Energy>
114         <Energy Type1="Necrotic" Type2="Hypoxic">0</Energy>
115         <Energy Type1="Necrotic" Type2="Necrotic">0</Energy>
116
117         <Energy Type1="DrugApoptotic" Type2="Medium">0</Energy>
118         <Energy Type1="DrugApoptotic" Type2="Normoxic">0</Energy>
119         <Energy Type1="DrugApoptotic" Type2="Hypoxic">0</Energy>
120         <Energy Type1="DrugApoptotic" Type2="Necrotic">0</Energy>
121         <Energy Type1="DrugApoptotic" Type2="DrugApoptotic">0</Energy>
122
123         <Energy Type1="Gap" Type2="Medium">1</Energy>
124         <Energy Type1="Gap" Type2="Normoxic">6</Energy>
125         <Energy Type1="Gap" Type2="Hypoxic">6</Energy>
126         <Energy Type1="Gap" Type2="Necrotic">0</Energy>
127         <Energy Type1="Gap" Type2="DrugApoptotic">0</Energy>
128         <Energy Type1="Gap" Type2="Gap">6</Energy>
129
130         <Energy Type1="Gel" Type2="Medium">0</Energy>
131         <Energy Type1="Gel" Type2="Normoxic">1</Energy>
132         <Energy Type1="Gel" Type2="Hypoxic">1</Energy>
133         <Energy Type1="Gel" Type2="Necrotic">0</Energy>
134         <Energy Type1="Gel" Type2="DrugApoptotic">0</Energy>
135         <Energy Type1="Gel" Type2="Gap">1</Energy>
136         <Energy Type1="Gel" Type2="Gel">0</Energy>
137
138         <NeighborOrder>5</NeighborOrder>
139     </Plugin>
140
141     <Plugin Name="ExternalPotential">
142         <Lambda x="0.0" y="0.0" z="10000.0" />
143     </Plugin>
144
145 <!-- Other plugin declarations ************************************ -->
146     <Plugin Name="Volume" />
```

```
147
148     <Plugin Name="Surface" />
149
150     <Plugin Name="CenterOfMass" />
151
152     <Plugin Name="NeighborTracker" />
153
154 <!-- Steppables ************************************************** -->
155
156     <Steppable Type="KernelDiffusionSolver">
157         <DiffusionField>
158             <Kernel>35</Kernel>
159             <CoarseGrainFactor>3</CoarseGrainFactor>
160             <DiffusionData>
161                 <FieldName>Oxygen</FieldName>
162                 <DiffusionConstant>3440</DiffusionConstant>
163             </DiffusionData>
164
165             <SecretionData>
166             <Uptake MaxUptake="24" RelativeUptakeRate="1" Type="Hypoxic"
    />
167             <Uptake MaxUptake="24" RelativeUptakeRate="1" Type="Normoxic"
     />
168             <ConstantConcentration Type="Medium">10</
    ConstantConcentration>
169             <ConstantConcentration Type="Gap">10</ConstantConcentration>
170             </SecretionData>
171         </DiffusionField>
172
173         <DiffusionField>
174             <Kernel>35</Kernel>
175             <CoarseGrainFactor>3</CoarseGrainFactor>
176             <DiffusionData>
177                 <FieldName>Drug</FieldName>
178                 <DiffusionConstant>1080</DiffusionConstant>
179             </DiffusionData>
180       <SecretionData>
181             <ConstantConcentration Type="Medium">1</ConstantConcentration
    >
182             <ConstantConcentration Type="Gap">1</ConstantConcentration>
183             </SecretionData>
184         </DiffusionField>
185     </Steppable>
186
187     <Steppable Type="PIFInitializer">
```

```
        <PIFName>Simulation/InitialCondition/Tumour.piff</PIFName>
    </Steppable>

</CompuCell3D>
```

The Mitosis Steppable `step` function was modified to check the concentration of DTX at the center of the cell if treatment has begun. If the cell survived treatment, it perform cell divisions, otherwise the cell becomes *Apoptotic* (lines 62-78).

```
from cc3d.core.PySteppables import *
import xml.etree.ElementTree as ET
import numpy as np

class MitosisSteppable(MitosisSteppableBase):
    def __init__(self, xmlModelPath, frequency=1):
        MitosisSteppableBase.__init__(self, frequency)

        self.frequency = frequency

        # Initialize parameter values from model xml file.
        xmlModelTree = ET.parse(xmlModelPath)
        xmlModelRoot = xmlModelTree.getroot()
        celltype = xmlModelRoot.find('Plugin[@Name="CellType"]')
        doubVol = xmlModelRoot.find('Mitosis/DoublingVolume')
        tumour = xmlModelRoot.find('Growth/Tumour')
        drug = xmlModelRoot.find('Treatment/Drug')

        # Get cell type index from xml file because
        # self.CELLTYPE has not been initialized yet.
        NORMOXIC = int(celltype.find(
            'CellType[@TypeName="Normoxic"]').get('TypeId')
            )
        HYPOXIC = int(celltype.find(
            'CellType[@TypeName="Hypoxic"]').get('TypeId')
            )

        # Doubling volumes in the form {cell.type: doublingVolume, ...}.
        # Uses cancer and vascular modules for cell type index because
        # self.CELLTYPE has not been initialized yet.
        self.doubVolDic = {
            NORMOXIC: float(doubVol.find('Normoxic').text),
            HYPOXIC: float(doubVol.find('Hypoxic').text)
            }

        # Tumour cell volumes and surfaces.
        self.tumTargetVolume = float(tumour.find('Volume/Target').text)
```

```
        self.tumLambdaVolume = float(tumour.find('Volume/Lambda').text)
        self.tumTargetSurface = float(tumour.find('Surface/Target').text)
        self.tumLambdaSurface = float(tumour.find('Surface/Lambda').text)

        # Drug treatment time and curve fit.
        self.TreatmentMCS = int(drug.find('TreatmentMCS').text)
        self.druga = float(drug.find('a').text)
        self.drugb = float(drug.find('b').text)
        self.drugc = float(drug.find('c').text)

    def start(self):
        # Initialize doublingTime writing.
        for cell in self.cell_list_by_type(self.NORMOXIC, self.HYPOXIC):
            cell.dict['Timer'] = 0
            cell.dict['writeDoublingTime'] = False

    def step(self, mcs):
        cellsToDivide = []
        for cell in self.cell_list_by_type(self.NORMOXIC, self.HYPOXIC):
            cell.dict['Timer'] += self.frequency
            doublingVolume = self.doubVolDic[cell.type]
            if cell.volume > doublingVolume:

                # If treatment has started, check drug concentration.
                if mcs >= self.TreatmentMCS:
                    # Find drug concentration and survival probability.
                    fieldDrug = self.field.Drug
                    conDrug = fieldDrug[cell.xCOM, cell.yCOM, cell.zCOM]
                    psur = (
                        self.druga*np.exp(-self.drugb*conDrug) +
                        self.drugc
                        )
                    rand = np.random.random()
                    # If rand < probability of survival, cell divides.
                    if rand < psur:
                        cellsToDivide.append(cell)
                    else:
                        cell.type = self.DRUGAPOPTOTIC

                else:
                    cellsToDivide.append(cell)

        # Divide and update cells.
        for cell in cellsToDivide:
            self.divide_cell_random_orientation(cell)
```

```
            cell.dict['doublingTime'] = cell.dict['Timer']
            cell.dict['writeDoublingTime'] = True

    def update_attributes(self):
        # Set child cell type and parent values of tumour cells.
        self.parentCell.targetVolume = self.tumTargetVolume
        self.parentCell.lambdaVolume = self.tumLambdaVolume
        self.parentCell.targetSurface = self.tumTargetSurface
        self.parentCell.lambdaSurface = self.tumLambdaSurface

        # Reset doubTime writing in child.
        self.parentCell.dict['Timer'] = 0
        self.childCell.dict['Timer'] = 0
        self.childCell.dict['writeDoublingTime'] = False

        # Always set child attribute to be the same as the parent's.
        self.childCell.type = self.parentCell.type
        self.childCell.targetVolume = self.parentCell.targetVolume
        self.childCell.lambdaVolume = self.parentCell.lambdaVolume
        self.childCell.targetSurface = self.parentCell.targetSurface
        self.childCell.lambdaSurface = self.parentCell.lambdaSurface
```

The remaining changes to the Growth and Output Steppables are identical to those of the CPM of radiation treatment given in Appendix B, with the cell type `RadApoptotic` replaced by `DrugApoptotic`.

```
from cc3d.core.PySteppables import *
import xml.etree.ElementTree as ET

class GrowthSteppable(SteppableBasePy):
    def __init__(self, xmlModelpath, frequency=1):
        SteppableBasePy.__init__(self, frequency)

        self.growthFreq = frequency

        # Initialize parameter values from model xml file.
        xmlModelTree = ET.parse(xmlModelpath)
        xmlModelRoot = xmlModelTree.getroot()
        tumour = xmlModelRoot.find('Growth/Tumour')

        # Indicate if the simulation "restarts" with existing fields.
        if xmlModelRoot.find('.//ConcentrationFileName') is not None:
            self.doTransient = False
        else:
            self.doTransient = True

```

```
        # Tumour cell target and lambda volumes and surfaces.
        self.tumTargetVolume = float(tumour.find('Volume/Target').text)
        self.tumLambdaVolume = float(tumour.find('Volume/Lambda').text)
        self.tumTargetSurface = float(tumour.find('Surface/Target').text)
        self.tumLambdaSurface = float(tumour.find('Surface/Lambda').text)

        # Thresholds for tumour differentiation.
        self.hypoOxyThresh = float(
            tumour.find('OxygenThreshold').get('Hypoxic')
            )
        self.necOxyThresh = float(
            tumour.find('OxygenThreshold').get('Necrotic')
            )

        # Michaelis-Menten parameters for tumour growth.
        self.tumVmax = float(tumour.find('Volume/MaxChange').text)
        self.tumOv = float(tumour.find('Volume/HalfSat').text)
        self.tumSmax = float(tumour.find('Surface/MaxChange').text)
        self.tumOs = float(tumour.find('Surface/HalfSat').text)

        # Necrotic volume and surface lambda to freeze cell size.
        self.necLambda = float(tumour.find('NecroticLambda').text)

    def start(self):
        for cell in self.cellList:
            # Initialize target and lambda cell volumes and surfaces.
            if (cell.type == self.NORMOXIC or
                cell.type == self.HYPOXIC or
                cell.type == self.GAP
                ):
                cell.targetVolume = self.tumTargetVolume
                cell.lambdaVolume = self.tumLambdaVolume
                cell.targetSurface = self.tumTargetSurface
                cell.lambdaSurface = self.tumLambdaSurface
            if (cell.type == self.NECROTIC or
                cell.type == self.DRUGAPOPTOTIC
                ):
                cell.targetVolume = self.tumTargetVolume
                cell.lambdaVolume = self.necLambda
                cell.targetSurface = self.tumTargetSurface
                cell.lambdaSurface = self.necLambda

    def step(self, mcs):
        fieldOxygen = self.field.Oxygen

```

```
        for cell in self.cellList:

            # Tumour growth and conversion (after transient period).
            if (cell.type == self.NORMOXIC or cell.type == self.HYPOXIC
                    and (mcs > 100 or (not self.doTransient))):
                # Find oxygen concentration at cell COM.
                conOxygen = fieldOxygen[cell.xCOM, cell.yCOM, cell.zCOM]

                # Cell conversion.
                if conOxygen < self.necOxyThresh:
                    cell.type = self.NECROTIC
                    cell.lambdaVolume = self.necLambda
                    cell.lambdaSurface = self.necLambda
                elif conOxygen < self.hypoOxyThresh:
                    cell.type = self.HYPOXIC
                else:
                    cell.type = self.NORMOXIC

                # Growth equation.
                cell.targetVolume += self.growthFreq * (
                    self.tumVmax*conOxygen / (self.tumOv + conOxygen)
                    )
                cell.targetSurface += self.growthFreq * (
                    self.tumSmax*conOxygen / (self.tumOs + conOxygen)
                    )
```

The modified Output Steppable is given below.

```
from cc3d.core.PySteppables import *
import csv
import os
import xml.etree.ElementTree as ET
import socket
from datetime import datetime

class OutputSteppable(SteppableBasePy):

    def __init__(self, xmlModelPath, name, frequency=1):
        SteppableBasePy.__init__(self, frequency)

        # Create computer-datetime stamp.
        computer = socket.gethostname()
        start = datetime.now().strftime('%Y-%m-%d-%H%M')
        stamp = f'{computer}_{start}'

        # Read output directories from model xml file and create file
```

```
    paths.
        xmlModelTree = ET.parse(xmlModelPath)
        xmlModelRoot = xmlModelTree.getroot()
        csvDir = xmlModelRoot.find(
            'Output/Path/CSV'
            ).text.replace('"', '')
        cc3dDir = xmlModelRoot.find(
            'Output/Path/CC3D'
            ).text.replace('"', '')
        self.csvOutInitial = f'{csvDir}_INC_{name}_{stamp}.csv'
        self.cc3dOutInitial = f'{cc3dDir}_INC_{name}'  # Automated stamp.
        self.csvOutFinal = f'{csvDir}{name}_{stamp}.csv'
        self.cc3dOutFinal = f'{cc3dDir}{name}_{stamp}'

        # Create (nested) csv output directory if it does not exist.
        print('\nCreating csv output directory if needed...')
        for ind in range(1, len(csvDir.split('/'))):
            component = '/'.join(csvDir.split('/')[:ind])
            if not os.path.isdir(f'{component}'):
                print(f'\t{component}')
                os.mkdir(f'{component}')

        # Initialize and check writing frequency from model xml file.
        self.writeFreq = int(
            xmlModelRoot.find('Output/Frequency/WriteData').text)
        if self.writeFreq % frequency != 0:
            msg = f'Writing frequency {self.writeFreq} is not a multiple
    of'
            raise ValueError(f'{msg} output frequency {frequency}')
        self.outputPerWrite = int(self.writeFreq/frequency)
        self.writeIndex = 0

        # Initialize parameters to control when simulation ends.
        self.frequency = frequency
        self.nMCS = int(xmlModelRoot.find('Potts/Steps').text)
        self.extendMCS = int(xmlModelRoot.find('Output/ExtendMCS').text)
        self.stopDistance = int(xmlModelRoot.find('Output/StopDistance').
    text)
        self.border = [
            float(xmlModelRoot.find('Potts/Dimensions').get('x')),
            float(xmlModelRoot.find('Potts/Dimensions').get('y')),
            float(xmlModelRoot.find('Potts/Dimensions').get('z'))
            ]

        # Time step.
```

```
61          self.mcsLBL = 'MCS'
62
63          # Number of cell types of interest.
64          self.normLBL = 'Normoxic cell number'
65          self.hypoLBL = 'Hypoxic cell number'
66          self.necLBL = 'Necrotic cell number'
67          self.drugApopLBL = 'Drug apoptotic cell number'
68
69          # Volumes of interest.
70          self.tumvolLBL = 'Tumour volume'
71          self.totvolLBL = 'Total volume'
72          self.gapvolLBL = 'Internal gap volume'
73
74          # Surface areas of interest.
75          self.extAreaLBL = 'External surface area'
76
77          # Drug concentration.
78          self.tumDrugLBL = 'Avg tumour drug concentration'
79
80          # Oxygenation.
81          self.normoxyLBL = 'Avg Normoxic oxygen'
82          self.hypooxyLBL = 'Avg Hypoxic oxygen'
83
84          # Speed.
85          self.tumSpeedLBL = 'Average Tumour Cell Speed'
86
87          # Doubling times.
88          self.tumdoubLBL = 'Avg tumour cell doubling time'
89
90          # Column labels, in the following order.
91          self.headers = [
92              self.mcsLBL,
93              self.normLBL, self.hypoLBL, self.necLBL, self.drugApopLBL,
94              self.tumvolLBL, self.totvolLBL, self.gapvolLBL,
95              self.extAreaLBL,
96              self.tumDrugLBL, self.normoxyLBL, self.hypooxyLBL,
97              self.tumSpeedLBL,
98              self.tumdoubLBL,
99              ]
100
101         # For each output MCS, appends a list of dictionaries with column
102         # labels as keys with their corresponding values.
103         self.outputArr = []
104
105         # Keeps track of initialization for restarts, since will need to
```

```
106         # handle the first writing after a restart differently.
107         self.isInitialized = None
108 
109     def start(self):
110         # Will be initialized after starting simulation from first MCS.
111         # If simulation started from restart, no initialization and first
112         # restart step writing to file will write column headers and
113         # handle a variable number of output steps.
114         self.isInitialized = True
115 
116     def step(self, mcs):
117         # Record cell type numbers and tissue type sizes.
118         normNum = 0
119         hypoNum = 0
120         necNum = 0
121         drugApopNum = 0
122         tumVol = 0
123         totVol = 0
124         gapVol = 0
125         extArea = 0
126         tumDrug = 0
127         normOxy = 0
128         hypoOxy = 0
129         tumSpeed = 0
130         tumDoubTime = 0
131         tumDoubNum = 0
132 
133         fieldDrug = self.field.Drug
134         fieldOxygen = self.field.Oxygen
135 
136         # DEBUG
137         print('\nCollecting output data for: MCS {0}\n'.format(mcs))
138 
139         # Flag gap cells as external if they touch medium, else internal.
140         for cell in self.cellList:
141             if cell.type == self.GAP:
142                 cell.dict['isInternal'] = True
143                 neighborList = self.get_cell_neighbor_data_list(cell)
144                 for neighbor, commonSurfaceArea in neighborList:
145                     # If neighbor is not medium, gap is external.
146                     if not neighbor:
147                         cell.dict['isInternal'] = False
148                         break
149 
150         # Track the final conditions.
```

```
        for cell in self.cellList:

            # Get total volume and external surface area.
            if (cell.type == self.NORMOXIC or
                cell.type == self.HYPOXIC or
                cell.type == self.NECROTIC or
                cell.type == self.DRUGAPOPTOTIC):
                totVol += cell.volume
                tumDrug += fieldDrug[cell.xCOM, cell.yCOM, cell.zCOM]
                # Add to external area if medium or ext gap neighbor.
                neighborList = self.get_cell_neighbor_data_list(cell)
                for neighbor, commonSurfaceArea in neighborList:
                    if not neighbor:
                        extArea += commonSurfaceArea
                    else:
                        if (neighbor.type == self.GAP and
                            not neighbor.dict['isInternal']):
                            extArea += commonSurfaceArea

            if cell.type == self.NORMOXIC:
                normNum += 1
                tumVol += cell.volume
                normOxy += fieldOxygen[cell.xCOM, cell.yCOM, cell.zCOM]
                tumSpeed += self.vector_norm(
                    self.invariant_distance_vector(
                        p1=[cell.xCOMPrev, cell.yCOMPrev, cell.zCOMPrev],
                        p2=[cell.xCOM, cell.yCOM, cell.zCOM]))
                if cell.dict['writeDoublingTime']:
                    tumDoubTime += cell.dict['doublingTime']
                    cell.dict['writeDoublingTime'] = False
                    tumDoubNum += 1

            elif cell.type == self.HYPOXIC:
                hypoNum += 1
                tumVol += cell.volume
                hypoOxy += fieldOxygen[cell.xCOM, cell.yCOM, cell.zCOM]
                tumSpeed += self.vector_norm(
                    self.invariant_distance_vector(
                        p1=[cell.xCOMPrev, cell.yCOMPrev, cell.zCOMPrev],
                        p2=[cell.xCOM, cell.yCOM, cell.zCOM]))
                if cell.dict['writeDoublingTime']:
                    tumDoubTime += cell.dict['doublingTime']
                    cell.dict['writeDoublingTime'] = False
                    tumDoubNum += 1

```

```
            elif cell.type == self.NECROTIC:
                necNum += 1

            elif cell.type == self.DRUGAPOPTOTIC:
                drugApopNum += 1

            elif cell.type == self.GAP:
                if cell.dict['isInternal']:
                    gapVol += cell.volume
                else:
                    pass  # Allow gel.

        #  Average the oxygen concentrations, doubling times, and speed.
        if normNum + hypoNum + necNum + drugApopNum > 0:
            tumDrug /= normNum + hypoNum + necNum + drugApopNum
        if normNum > 0:
            normOxy /= normNum
        if hypoNum > 0:
            hypoOxy /= hypoNum
        if normNum + hypoNum > 0:
            tumSpeed /= normNum + hypoNum
        if tumDoubNum > 0:
            tumDoubTime /= tumDoubNum

        # Update output array.
        self.outputArr.append({
            self.mcsLBL: mcs,
            self.normLBL: normNum,
            self.hypoLBL: hypoNum,
            self.drugApopLBL: drugApopNum,
            self.necLBL: necNum,
            self.tumvolLBL: tumVol,
            self.totvolLBL: totVol,
            self.gapvolLBL: gapVol,
            self.extAreaLBL: extArea,
            self.tumDrugLBL: tumDrug,
            self.normoxyLBL: normOxy,
            self.hypooxyLBL: hypoOxy,
            self.tumSpeedLBL: tumSpeed,
            self.tumdoubLBL: tumDoubTime,
            })

        # Write to file.
        if mcs % self.writeFreq == 0:
            with open(self.csvOutInitial, 'a+', newline='') as f:
```

```
                dictWriter = csv.DictWriter(f, fieldnames=self.headers)

                # If first MCS or it has been restarted, need to write
                # headers to csv file and write the first output step or
                # the number of output steps collected since the restart.
                if mcs == 0 or not self.isInitialized:
                    dictWriter.writeheader()
                    numOut = len(self.outputArr)
                    dictWriter.writerows(self.outputArr[:numOut])
                    self.writeIndex += numOut
                    self.isInitialized = True

                # Otherwise, write same number of lines to csv file.
                else:
                    start = self.writeIndex
                    finish = self.writeIndex + self.outputPerWrite
                    dictWriter.writerows(self.outputArr[start:finish])
                    self.writeIndex += self.outputPerWrite

            # DEBUG
            print('Wrote to output file: {0}\n'.format(
                self.csvOutInitial
                ))

            # End simulation if the tumour has completely disappeared.
            if normNum + hypoNum + drugApopNum + necNum == 0:
                print('Tumour has disappeared, so simulation will end\n')
                self.nMCS = mcs
                # Rename simulation as dead.
                csvBase = f'DEAD_{os.path.basename(self.csvOutFinal)}'
                csvDir = os.path.dirname(self.csvOutFinal)
                self.csvOutFinal = f'{csvDir}/{csvBase}'
                cc3dBase = f'DEAD_{os.path.basename(self.cc3dOutFinal)}'
                cc3dDir = os.path.dirname(self.cc3dOutFinal)
                self.cc3dOutFinal = f'{cc3dDir}/{cc3dBase}'
                self.finish()
                self.stop_simulation()

    def finish(self):
        """Rename CC3D data folder and output csv file with MCS."""
        self.cc3dOutFinal += f'_MCS-{self.nMCS}'
        self.csvOutFinal = self.csvOutFinal.split('.')[0]
        self.csvOutFinal += f'_MCS-{self.nMCS}.csv'

        # Rename CC3D data folder and output csv file.
```

```
286         if os.path.isdir(self.cc3dOutInitial):
287             os.rename(self.cc3dOutInitial, self.cc3dOutFinal)
288         if os.path.isfile(self.csvOutInitial):
289             os.rename(self.csvOutInitial, self.csvOutFinal)
```